

**UNIVERSITY OF SÃO PAULO
POLYTECHNIC SCHOOL
GRADUATE PROGRAM IN CIVIL ENGINEERING**

RUBENS AUGUSTO AMARO JUNIOR

Numerical modeling of fluid-structure interaction (FSI):
time-consistent pressure computation, rigid bodies contact and coupled particle-mesh methods

Revised Version

São Paulo

2021

RUBENS AUGUSTO AMARO JUNIOR

Numerical modeling of fluid-structure interaction (FSI):

time-consistent pressure computation, rigid bodies contact and coupled particle-mesh methods

Revised Version

Thesis presented to the Graduate Program in
Civil Engineering at the Polytechnic School of
University of São Paulo to obtain the degree of
Doctor of Science.

Advisor: Prof. Dr. Liang-Yee Cheng

São Paulo

2021

Autorizo a reprodução e divulgação total ou parcial deste trabalho, por qualquer meio convencional ou eletrônico, para fins de estudo e pesquisa, desde que citada a fonte.

Este exemplar foi revisado e corrigido em relação à versão original, sob responsabilidade única do autor e com a anuência de seu orientador.

São Paulo, _____ de _____ de _____

Assinatura do autor: _____

Assinatura do orientador: _____

Catálogo-na-publicação

Amaro Junior, Rubens Augusto

Numerical modeling of fluid-structure interaction (FSI): time-consistent pressure computation, rigid bodies contact and coupled particle-mesh methods / R. A. Amaro Junior -- versão corr. -- São Paulo, 2021.
209 p.

Tese (Doutorado) - Escola Politécnica da Universidade de São Paulo.
Departamento de Engenharia de Construção Civil.

1.Pressure oscillation 2.Solid contact 3.Hydroelasticity 4.Particle-based method 5.Finite element method I.Universidade de São Paulo. Escola Politécnica. Departamento de Engenharia de Construção Civil II.t.

AMARO JR, R. A. **Numerical modeling of fluid-structure interaction (FSI):** time-consistent pressure computation, rigid bodies contact and coupled particle-mesh methods. 2021. Thesis (Doctoral degree in Science) - Polytechnic School, University of São Paulo, São Paulo, 2021.

Approved on:

Doctoral Committee

Prof. Dr. _____
Institution _____
Judgement _____
Signature _____

Prof. Dr. _____
Institution _____
Judgement _____
Signature _____

Prof. Dr. _____
Institution _____
Judgement _____
Signature _____

Prof. Dr. _____
Institution _____
Judgement _____
Signature _____

ACKNOWLEDGMENTS

I would like to express my heartfelt gratitude to prof. Dr. Liang-Yee Cheng, who give me the honor of supervising my PhD study. His vast knowledge and incisive insight have inspired me since I met him. He always encouraged me and patiently helped me during our discussions on various issues of this research at different stages. I will be grateful for the rest of my life and words are not enough to express my gratitude.

This work cannot be accomplished without the help of my colleagues of the MPS/TPN-USP group, prof. Dr. Fernando Akira Kurokawa, Dr. Marcio Michiharu Tsukamoto, Dr. Fabio Kenji Motezuki, Dr. Cezar Augusto Bellezi, Dr. Davi Teodoro Fernandes, MSc Gabriel Henrique de Souza Ribeiro, Eng. Lucas Soares Pereira, Eng. Eric Henrique Favero, Eng. Stella Vieira Rosa and Eng. Pedro Henrique Saggioratto Osello. Our valuable discussions as well as their constructive suggestions make this work possible. I would also express my gratitude to Dr. Pedro Cardozo de Mello for his valuable help in the execution of some experiments.

A would like to give my special thanks to prof. Dr. Ahmad Shakibaeinia for his support during my experience abroad at Polytechnique Montréal, Canada. The sandwich PhD period was a unique experience. Besides his sincere involvement to help me, I am really honored for the opportunity to collaborate with his team. The nice and productive talks with their students was very helpful during this period, so I give my thankfulness to Andrea Mellado-Cusicahua, Abdellah Mahdi, Mojtaba Jandaghian, Maryam Shademani, Faroogh Garoosi and Mohammad Pilvar. It was a pleasure to work with this group.

I am also very thankful to prof. Dr. Alfredo Gay Neto for offering me his support, and for providing me with the source code of finite element platform Giraffe (Generic Interface Readily Accessible for Finite Elements), essential for the conclusion of this work.

I would like to acknowledge the Coordenação de Aperfeiçoamento de Pessoal de Nível Superior - Brasil (CAPES) Finance Code 001 for providing scholarship support during my PhD study, and for providing scholarship as a Visiting Student - Process: PDSE - 88881.188463/2018-01.

I must also say thank to Office of Naval Research Global (ONR Global) that partially supported this study under the Award Number: N62909-16-1-2181.

At last, I would like to express my deepest gratitude to my friends and my family, especially my parents Heloisa and Rubens, who encouraged and supported me strongly.

ABSTRACT

AMARO JR, R. A. Numerical modeling of fluid-structure interaction (FSI): time-consistent pressure computation, rigid bodies contact and coupled particle-mesh methods. 2021. Thesis (Doctoral degree) - Polytechnic School, University of São Paulo, São Paulo, 2021.

This thesis is devoted to developing efficient computational solutions based on meshless particle-based methods for complex fluid-structure interaction (FSI) in free-surface flow from two different ways, namely, the truly incompressible and weakly-compressible approaches. Overall, the main contributions of this thesis can be summarized into three distinct parts:

- I. Proposal of a new approach from the viewpoint of the momentum conservation regarding particle-level collisions to derive new source terms of pressure Poisson equation (PPE) of the moving particle semi-implicit (MPS) method. The new source terms depend directly on the spatial discretization and are independent to the time step, i.e., a direct consequence is the time-consistent computation of the pressure. The effectiveness of the proposed approach, namely time-scale correction of particle-level impulses (TCPI), is demonstrated through the simulations of hydrostatic and hydrodynamic problems.
- II. A numerical solid contact model adopting a penalty-based method, that uses a nonlinear spring and dashpot concept, is proposed for the incompressible MPS. To address some geometrical anomalies such as non-smooth modeling of a plane, which may occur when using particles to represent the shell of the rigid bodies, an approach based on the faces of the bodies and contact force computed taken into account the normal vectors of solid walls is derived. The improvements on stability and accuracy computations are investigated by problems involving free-surface flow interacting with multiple bodies.
- III. Development of a 3D coupled particle-mesh model. An improved weakly-compressible moving particle semi-implicit (WC-MPS) to solve transient violent free-surface flows is coupled with a geometrically exact shell model for nonlinear structural dynamic. Besides enhancements on the stability and accuracy of WC-MPS, a stable repulsive Lennard-Jones force, discrete divergence operators with proper modifications, and a simple technique to avoid false interaction between particles placed at opposite sides of thin shell are introduced in the explicitly represented polygon (ERP) wall boundary model. Hydroelastic simulations are conducted to verify the robustness and accuracy of the coupled model.

Keywords: Hydrodynamic loads. Pressure oscillation. Computational fluid dynamics. Solid contact. Hydroelasticity. Particle-based method. Finite element method.

RESUMO

AMARO JR, R. A. Modelagem numérica da interação fluido-estrutura: cálculo de pressão consistente no tempo, contato entre corpos rígidos e acoplamento entre métodos de partícula e malha. 2021. Tese (Doutorado) - Escola Politécnica, Universidade de São Paulo, São Paulo, 2021.

Esta tese é dedicada ao desenvolvimento de modelos computacionais eficientes e baseados nos métodos de partículas sem malha para o complexo fenômeno de interação fluido-estrutura (IFS) em escoamentos com presença de superfície livre considerando as abordagens incompressíveis e fracamente compressíveis. As principais contribuições desta tese podem ser resumidas em três partes distintas:

- I. Proposta de uma nova abordagem do ponto de vista da conservação da quantidade de movimento relativa às colisões no nível de partículas, obtendo novos termos fonte para equação de Poisson para a pressão (EPP) no método de partículas *moving particle semi-implicit* (MPS). Os novos termos fonte dependem diretamente da resolução espacial e são independentes do passo de tempo, ou seja, resultam no cálculo consistente no tempo da pressão. A eficiência da abordagem proposta, denominada *time-scale correction of particle-level impulses* (TCPI), é demonstrada através de simulações de problemas hidrostáticos e hidrodinâmicos.
- II. Um modelo numérico de contato entre sólidos que adota o método das penalidades, usando um modelo não linear de mola-amortecedor, é proposto para o MPS incompressível. Visando eliminar algumas anomalias geométricas, como a modelagem não suave de um plano que pode ser induzida pelo uso de partículas para representar as faces dos corpos rígidos, é proposta uma abordagem baseada nas faces dos corpos e na força de contato calculada levando-se em conta os vetores normais de paredes sólidas. As melhorias na estabilidade e precisão numéricas são investigadas através de vários problemas envolvendo escoamentos com presença de superfície livre interagindo com múltiplos corpos rígidos.
- III. Desenvolvimento de um modelo 3D acoplado de partícula-malha. O método de partículas *weakly-compressible moving particle semi-implicit* (WC-MPS) é aprimorado e utilizado nos escoamentos com superfície livre e acoplado a um modelo de casca geometricamente exato para simular a dinâmica estrutural não linear. Além de aprimoramentos na estabilidade e precisão do WC-MPS, uma força estável e repulsiva de Lennard-Jones,

operadores discretos de divergente com modificações apropriadas e uma técnica simples para evitar a interação errônea entre partículas posicionadas em lados opostos das paredes finas são introduzidos no modelo *explicitly represented polygon (ERP) wall boundary*. Simulações envolvendo hidroelasticidade são realizadas para verificar a robustez e precisão do modelo acoplado.

Palavras-chave: Carregamentos hidrodinâmicos. Oscilação de pressão. Dinâmica dos fluidos computacionais. Contato entre sólidos. Hidroelasticidade. Método de partículas. Método dos elementos finitos.

CONTENTS

LIST OF FIGURES	13
LIST OF TABLES	20
LIST OF SYMBOLS AND NOTATIONS	22
LIST OF ABBREVIATIONS.....	28
CHAPTER 1 INTRODUCTION	31
1.1 BACKGROUND AND MOTIVATION	32
1.2 PARTICLE-BASED METHODS.....	35
1.3 OUTLINE OF THE THESIS	37
CHAPTER 2 REVIEW OF INCOMPRESSIBLE MOVING PARTICLE SEMI-IMPLICIT (MPS) AND WEAKLY-COMPRESSIBLE MPS (WC-MPS) METHODS.....	39
2.1 BACKGROUND	40
2.2 NUMERICAL METHOD	40
2.2.1 GOVERNING EQUATIONS	40
2.2.2 NUMERICAL OPERATORS.....	41
2.2.2.1 Particle number density.....	42
2.2.2.2 Gradient.....	42
2.2.2.3 Divergence	43
2.2.2.4 Rotational	43
2.2.2.5 Laplacian.....	43
2.2.2.6 Pressure gradient	45
2.2.2.7 Divergence of velocity	46
2.2.2.8 Laplacian of velocity and pressure.....	46
2.2.3 NUMERICAL MODELING OF THE BOUNDARY CONDITIONS	46
2.2.3.1 Rigid wall.....	46
2.2.3.2 Free surface	47
2.2.4 ALGORITHM.....	48
2.3 INCOMPRESSIBLE MOVING PARTICLE SEMI-IMPLICIT (MPS)	50
2.4 WEAKLY-COMPRESSIBLE MOVING PARTICLE SEMI-IMPLICIT (WC-MPS).....	54
2.5 STABILIZATION TECHNIQUE	56
2.6 NEIGHBOR SEARCH.....	56

CHAPTER 3 TIME-CONSISTENCY AND STABILITY OF THE PARTICLE-BASED HYDRODYNAMIC PRESSURE	58
3.1 BACKGROUND	59
3.2 RELATED WORK.....	61
3.3 NUMERICAL METHOD.....	63
3.3.1 MOVING PARTICLE SEMI-IMPLICIT (MPS) METHOD.....	63
3.4 TIME-SCALE CORRECTION OF PARTICLE-LEVEL IMPULSES (TCPI).....	64
3.4.1 CALIBRATION OF THE PROPAGATION SPEED OF THE PERTURBATIONS cs	70
3.5 CASES OF STUDY	75
3.6 RESULTS AND DISCUSSIONS.....	76
3.6.1 2D HYDROSTATIC TANK.....	76
3.6.2 2D WATER JET.....	80
3.6.3 2D DAM BREAKING.....	86
3.6.4 3D SLOSHING IN PRISMATIC TANK.....	91
3.7 CONCLUDING REMARKS	96
CHAPTER 4 RIGID BODIES CONTACT FOR PARTICLE-BASED METHODS	98
4.1 BACKGROUND	99
4.2 RELATED WORK.....	100
4.3 NUMERICAL METHOD.....	101
4.3.1 MOVING PARTICLE SEMI-IMPLICIT (MPS) METHOD.....	101
4.3.2 RIGID BODY DYNAMICS.....	102
4.3.3 TIME STEP.....	103
4.3.4 VALIDATION OF THE HYDRODYNAMIC MODELING.....	104
4.3.4.1 3D dam breaking.....	104
4.3.4.2 Fluid-structure interaction verification.....	106
4.4 SOLID-SOLID CONTACT MODEL	108
4.4.1 CONTACT FORCE.....	108
4.4.1.1 Normal forces between closest particles.....	108
4.4.1.2 Tangential forces between closest particles.....	109
4.4.1.3 Contact forces between rigid bodies.....	110
4.4.2 CONTACT TORQUES.....	110
4.4.3 IMPROVED CONTACT NORMAL VECTOR.....	111

4.4.4	IMPROVED DISTANCE OF CONTACT	112
4.4.5	VALIDATION OF THE SOLID-SOLID CONTACT MODEL.....	114
4.4.5.1	Collision energy and linear momentum	114
4.4.5.2	Frictional force	116
4.5	ALGORITHM	118
4.6	RESULTS AND DISCUSSIONS.....	119
4.6.1	3D DAM-BREAK FLOW HITTING ONE CUBE.....	119
4.6.2	3D DAM-BREAK FLOW HITTING STACKED CUBES.....	122
4.6.2.1	Three stacked cubes aligned vertically.....	124
4.6.2.2	Six cubes stacked in triangle formation (pyramid)	127
4.7	CONCLUDING REMARKS	129
 CHAPTER 5 3D COUPLED WC-MPS-FE PARTICLE-MESH MODEL FOR FSI		
	PHENOMENA	131
5.1	BACKGROUND	132
5.2	RELATED WORKS	134
5.3	NUMERICAL METHODS	136
5.3.1	WEAKLY COMPRESSIBLE MPS (WC-MPS) METHOD - FLUID SUBDOMAIN	137
5.3.1.1	Explicitly represented polygon (ERP) wall boundary model.....	137
5.3.1.1.1	Divergence of the velocity - Free-slip boundary condition.....	140
5.3.1.1.2	Divergence of the velocity - No-slip boundary condition.....	140
5.3.1.2	Particle interaction across zero-thickness walls	141
5.3.2	FINITE ELEMENT METHOD (FEM) – SOLID SUBDOMAIN	142
5.3.2.1	Kinematic description	142
5.3.2.2	Strain measures	144
5.3.2.3	Weak form of the equations of motion.....	144
5.3.2.4	Time integration scheme	146
5.3.2.5	Triangular shell finite element	147
5.3.3	COUPLING SCHEME.....	148
5.4	ALGORITHM	150
5.5	VERIFICATION OF THE WC-MPS METHOD	151
5.5.1	3D PLATE SUBJECT TO GRAVITY.....	152
5.5.2	DYNAMIC PRESSURE UNDER DAM-BREAK EVENT	154

5.6	VERIFICATION OF THE GEOMETRICALLY EXACT SHELL MODEL	158
5.6.1	STATIC RESPONSE OF PLATE CLAMPED AT ALL EDGES UNDER UNIFORM PRESSURE.....	158
5.6.2	DYNAMIC RESPONSE OF PLATE CLAMPED AT ONE EDGE AND SUBJECTED TO INITIAL VELOCITY DISTRIBUTION PERPENDICULAR TO THE PLATE	161
5.7	RESULTS AND DISCUSSIONS.....	163
5.7.1	SQUARE PLATE CLAMPED AT ALL EDGES AND UNDER HYDROSTATIC PRESSURE	164
5.7.2	VERTICAL PLATE CLAMPED AT THE BOTTOM SUBJECT TO HYDROSTATIC PRESSURE.....	167
5.7.3	WATER COLUMN WITH AN ELASTIC GATE CLAMPED AT TOP EDGE.....	170
5.7.4	DAM BREAKING HITTING AN ELASTIC PLATE CLAMPED AT ONE EDGE.....	176
5.8	CONCLUDING REMARKS	181
	CHAPTER 6 FINAL CONSIDERATIONS	182
6.1	CONCLUSIONS	183
6.1.1	TIME-CONSISTENCY AND STABILITY OF THE PARTICLE-BASED HYDRODYNAMIC PRESSURE ..	183
6.1.2	RIGID BODIES CONTACT FOR PARTICLE-BASED METHODS	184
6.1.3	3D COUPLED WC-MPS-FE PARTICLE-MESH MODEL FOR FSI PHENOMENA	184
6.2	PERSPECTIVES OF FUTURE WORKS.....	185
6.2.1	TIME-CONSISTENCY AND STABILITY OF THE PARTICLE-BASED HYDRODYNAMIC PRESSURE ..	185
6.2.2	RIGID BODIES CONTACT FOR PARTICLE-BASED METHODS	185
6.2.3	3D COUPLED WC-MPS-FE PARTICLE-MESH MODEL FOR FSI PHENOMENA	185
	CHAPTER 7 REFERENCES	187

LIST OF FIGURES

FIGURE 1.1 - FLUID-STRUCTURE INTERACTION PROBLEMS. NATURE OF THE FLOW (STAGNANT OR FLOWING FLUID) AND THE INTERACTION STRENGTH (WEAK OR STRONG COUPLING).	33
FIGURE 1.2 - (A) PHYSICAL WAVE, (B) MESH-BASED AND (C) PARTICLE-BASED REPRESENTATION.....	35
FIGURE 1.3 - MAIN CONTRIBUTIONS AND RESPECTIVE CHAPTERS	37
FIGURE 2.1 - GRAPHICAL REPRESENTATION OF THE WEIGHT FUNCTION ω_{ij} AND ITS RANGE OF INFLUENCE r_e IN 2D SPACE. THE REFERENCE PARTICLE i (CENTRAL SPHERE) HAS ITS PHYSICAL PROPERTIES INFLUENCED BY THEIR NEIGHBORHOOD \mathbb{P}_i	41
FIGURE 2.2 - GRAPHICAL REPRESENTATION OF A CIRCULAR CONTROL VOLUME Ω WITH RADIUS r_e	44
FIGURE 2.3 - BOUNDARY CONDITIONS IN 2D SPACE. (A) FLUID PARTICLES AND SOLID WALL MODELED BY WALL AND DUMMY PARTICLES. (B) FREE-SURFACE PARTICLES: RESULTANT WEIGHTED DEVIATION VECTOR.....	47
FIGURE 2.4 - SCHEMATIC DIAGRAM DURING A TIME STEP USING THE MPS OR WC-MPS.	49
FIGURE 2.5 – SCHEMATIC REPRESENTATION OF THE CELL INDEX METHOD. ENTIRE DOMAIN DIVIDED INTO CELLS OF SIZE l_{cell} AND CANDIDATES AND NEIGHBOR PARTICLES IN THE COMPACT SUPPORT OF RADIUS r_e	57
FIGURE 3.1 - SKETCH OF CONTINUOUS (TOP) AND DISCRETE (BOTTOM) EVOLUTION OF A VOLUME OF FLUID ON AN INCLINED PANEL.....	65
FIGURE 3.2 - SKETCH OF PHYSICAL AND NUMERICAL IMPACT PRESSURE AT TWO SUCCESSIVE OBSERVATION POINTS. ADAPTED FROM CHENG AND ARAI (2002).	66
FIGURE 3.3 - A) 1D PARTICLE ARRANGEMENT. (B) PRESSURE OF PARTICLE AT $Y = 4$. CASES SIMULATED WITH $l_0 = 0.1M$ AND $\Delta t = 5 \times 10^{-3}, 2.5 \times 10^{-3}, 1.25 \times 10^{-3}, 6.25 \times 10^{-4}$ AND $3.13 \times 10^{-4}S$	67
FIGURE 3.4 - CALIBRATION OF THE PROPAGATION SPEED OF THE PERTURBATIONS. MAIN DIMENSIONS OF THE HYDROSTATIC TANK AND SENSOR POSITION (SH_1). COLOR SCALE IS REPRESENTATIVE OF THE PRESSURE FIELD IN THE INITIAL CONFIGURATION.	71
FIGURE 3.5 - PROPAGATION SPEED OF THE PERTURBATIONS cs . (A) TCPI-PND AND (B) TCPI-PND-DF SOURCE TERM.	74
FIGURE 3.6 - 2D HYDROSTATIC TANK. MAIN DIMENSIONS AND SENSOR POSITION (SH_1). CONTOURS ARE REPRESENTATIVE OF THE PRESSURE FIELD IN THE INITIAL CONFIGURATION.....	76
FIGURE 3.7 - HYDROSTATIC PRESSURE AT SENSOR SH_1 . SOURCE TERMS WITH THE ZERO VARIATION OF THE PARTICLE NUMBER DENSITY O-PND AND TCPI-PND.	78
FIGURE 3.8 - HYDROSTATIC PRESSURE AT SENSOR SH_1 . SOURCE TERMS WITH THE ZERO VARIATION OF THE PARTICLE NUMBER DENSITY O-PND-DF AND TCPI-PND-DF.	79

FIGURE 3.9 - 2D HYDROSTATIC TANK. STANDARD DEVIATION (STD) OF PRESSURE. (A) ORIGINAL O-PND AND O-PND-DF, (B) PROPOSED TCPI-PND AND TCPI-PND-DF SOURCE TERMS	80
FIGURE 3.10 - 2D WATER JET. MAIN DIMENSIONS, SHAPE OF THE WATER JET AFTER REACH THE STEADY STATE AND SENSOR POSITION (SW_1). PRESSURE FIELD IN STEADY STATE FLOW.	81
FIGURE 3.11 - HYDRODYNAMIC PRESSURE AT SENSOR SW_1 . SOURCE TERMS WITH THE ZERO VARIATION OF THE PARTICLE NUMBER DENSITY O-PND AND TCPI-PND.	82
FIGURE 3.12 - HYDRODYNAMIC PRESSURE AT SENSOR SW_1 . SOURCE TERMS WITH THE ZERO VARIATION OF THE PARTICLE NUMBER DENSITY AND VELOCITY-DIVERGENCE-FREE CONDITION O-PND-DF AND TCPI-PND-DF.	83
FIGURE 3.13 - 2D WATER JET PRESSURE FIELD. ORIGINAL O-PND AND O-PND-DF, AND PROPOSED TCPI-PND AND TCPI-PND-DF SOURCE TERMS. DISTANCE BETWEEN PARTICLES $l_0 = 0.01M$ AND TIME STEP $\Delta t = 5 \times 10^{-4}S$. EVOLUTION OF WATER JET PROFILE AT TIMES $t = 1.0$ AND $2.0S$ ($\tau = 3.33$ AND 6.66). THE ORANGE SQUARES REPRESENT THE FREE-SURFACE STEADY STATE ANALYTICAL SOLUTION (SEE EQ. (3.21)).	84
FIGURE 3.14 - 2D WATER JET. STANDARD DEVIATION (STD) OF PRESSURE. (A) ORIGINAL O-PND AND O-PND-DF, (B) PROPOSED TCPI-PND AND TCPI-PND-DF SOURCE TERMS.	85
FIGURE 3.15 - 2D WATER JET. STANDARD DEVIATION (STD) OF PRESSURE IN SPATIAL-TIME REGION. THE MAGNITUDE OF STD IS REPRESENTED BY THE CIRCLE'S DIAMETER AND CROSS MARKERS REPRESENT FAILED SIMULATIONS. (A) O-PND AND TCPI-PND, (B) O-PND-DF AND TCPI-PND-DF SOURCE TERMS. UNDERLYING COLORS ARE USED TO IDENTIFY THE REGION IN WHICH THE O-PND-DF COMPUTATIONS FAILED.	86
FIGURE 3.16 - 2D DAM BREAKING. MAIN DIMENSIONS AND SENSOR POSITION (LOBOVSKÝ ET AL., 2014). PRESSURE FIELD IN THE INITIAL CONFIGURATION (SEE EQ. (3.22)).....	87
FIGURE 3.17 - 2D DAM BREAKING. PRESSURE AT SENSOR SD_1 . SOURCE TERMS WITH THE ZERO VARIATION OF THE PARTICLE NUMBER DENSITY AND VELOCITY-DIVERGENCE-FREE CONDITION O-PND AND TCPI-PND.....	88
FIGURE 3.18 - 2D DAM BREAKING. PRESSURE AT SENSOR SD_1 . SOURCE TERMS WITH THE ZERO VARIATION OF THE PARTICLE NUMBER DENSITY AND VELOCITY-DIVERGENCE-FREE CONDITION O-PND-DF AND TCPI-PND-DF.....	89
FIGURE 3.19 - 2D DAM BREAKING. ORIGINAL O-PND AND PROPOSED TCPI-PND SOURCE TERMS. DISTANCE BETWEEN PARTICLES $l_0 = 0.005M$ AND TIME STEP $\Delta t = 5 \times 10^{-5}S$. EVOLUTION OF FREE-SURFACE PROFILE AT TIMES $t = 0.50, 1.00, 1.50$ AND $2.0S$ ($\tau = 2.86, 5.72, 8.58$ AND 11.44)	90
FIGURE 3.20 - 2D DAM BREAKING. ORIGINAL O-PND-DF AND PROPOSED TCPI-PND-DF SOURCE TERMS. DISTANCE BETWEEN PARTICLES $l_0 = 0.005M$ AND TIME STEP $\Delta t = 5 \times 10^{-5}S$. EVOLUTION OF FREE-SURFACE PROFILE AT TIMES $t = 0.50, 1.00, 1.50$ AND $2.0S$ ($\tau = 2.86, 5.72, 8.58$ AND 11.44).....	91

FIGURE 3.21 - 2D DAM BREAKING. NORMALIZED ROOT MEAN SQUARE DEVIATION (NRMSD) OF PRESSURE. (A) ORIGINAL O-PND AND O-PND-DF, (B) PROPOSED TCPI-PND AND TCPI-PND-DF SOURCE TERMS.	91
FIGURE 3.22 - SCHEMATIC VIEW OF 3D SLOSHING. MAIN DIMENSIONS OF TANK, FILLING HEIGHT AND SENSOR POSITION P_1	92
FIGURE 3.23 - 3D SLOSHING IN PRISMATIC TANK. PRESSURE AT SENSOR P_1 . SOURCE TERMS WITH THE ZERO VARIATION OF THE PARTICLE NUMBER DENSITY (O-PND AND TCPI-PND) AND VELOCITY-DIVERGENCE-FREE CONDITION (O-PND-DF AND TCPI-PND-DF). CASES SIMULATED WITH $l_0 = 0.01M$	93
FIGURE 3.24 - EXPERIMENTAL AND NUMERICAL SIMULATIONS OF 3D SLOSHING. ORIGINAL O-PND AND PROPOSED TCPI-PND-DF SOURCE TERMS. DISTANCE BETWEEN PARTICLES $l_0 = 0.01M$ AND TIME STEP $\Delta t = 1 \times 10^{-4}S$. EVOLUTION OF FREE-SURFACE PROFILE AT TIMES $t = 6.75, 8.50, 9.00, 10.60, 12.15$ AND $14.0S$ ($\tau_s = 5.40, 6.80, 7.20, 8.48, 9.72$ AND 11.20).	95
FIGURE 3.25 - 3D SLOSHING IN PRISMATIC TANK. NORMALIZED ROOT MEAN SQUARE DEVIATION (NRMSD) OF PRESSURE. ORIGINAL O-PND AND O-PND-DF, AND PROPOSED TCPI-PND AND TCPI-PND-DF SOURCE TERMS. DISTANCE BETWEEN PARTICLES OF $l_0 = 0.01M$	96
FIGURE 4.1 - RIGID BODY REPRESENTED BY A COLLECTION OF SOLID WALL AND INTERNAL (DUMMY) PARTICLES IN 2D SPACE.	103
FIGURE 4.2 - (A) INITIAL GEOMETRY AND MAIN DIMENSIONS OF THE 3D DAM BREAKING. (B) PRESSURE SENSORS P_1 AND P_2 ON THE BLOCK.	104
FIGURE 4.3 – PRESSURE COMPUTED BY PRESENT MPS AND MEASURED BY KLEEFSMAN ET AL. (2005) AT PRESSURE SENSORS (A) P_1 AND (B) P_2	105
FIGURE 4.4 - MAIN DIMENSIONS AND INITIAL POSITION OF THE FLOATING BLOCK WITH AN ASYMMETRIC MASS DISTRIBUTION IMMERSSED IN A VISCOUS FLOW.	106
FIGURE 4.5 - (A) HORIZONTAL, (B) VERTICAL AND (C) ROTATIONAL TIME SERIES OF THE SOLID COMPUTED WITH PRESENT MPS FOR THE RESOLUTIONS $L/l_0 = 25, 50$ AND 100 , AND RIEMMAN-SPH, δ -SPH, EXPLICIT ISPH AND FVPM IN BARCAROLO ET AL. (2013) FOR RESOLUTION OF $L/l_0 = 100$	107
FIGURE 4.6 - SCHEMATIC REPRESENTATION OF RECTANGULAR PARALLELEPIPED GEOMETRY AND RESPECTIVE WALL PARTICLE MODEL. FEATURES HIGHLIGHT AS: FACE PARTICLE (YELLOW CIRCLE), EDGE PARTICLE (BLUE CIRCLE), VERTEX PARTICLE (RED CIRCLE), AND NEIGHBORS (GRAY CIRCLE) WITHIN THE RADIUS OF $1.1 \times l_0$	111
FIGURE 4.7 - WALL PARTICLES OF TWO RIGID BODIES AND THE DISTANCE OF CONTACT VECTOR \mathbf{r}_{kl} , \perp BETWEEN PARTICLE k AND THE CLOSEST WALL PARTICLE l	112
FIGURE 4.8 - CUTOFF RADIUS ADOPTED FOR SELECT CANDIDATE PAIRS OF PARTICLES IN CONTACT IN (A) 2D AND (B) 3D SPACE.	113
FIGURE 4.9 - INITIAL CONFIGURATION AND MAIN DIMENSIONS OF A COLLISION BETWEEN THREE RIGID CUBES.	114

FIGURE 4.10 - HORIZONTAL VELOCITIES OF THE CUBES (V_1 , V_2 AND V_3) AND DIMENSIONLESS ENERGY (U/U_0) AND LINEAR MOMENTUM (Q/Q_0) COMPUTED ONLY WITH (A) THE NEAREST PARTICLES DISTANCE CRITERION AND (B) THE COMBINATION OF CONTACT NORMAL (\mathbf{nc}) AND DISTANCE OF CONTACT (\mathbf{rkl}, \perp) VECTORS.	115
FIGURE 4.11 - EVOLUTION OF THE COLLISION BETWEEN 3 CUBES BY USING THE PROPOSED CONTACT MODEL.	116
FIGURE 4.12 - MAIN DIMENSIONS OF THE SLOPED SURFACE AND THE SLIDING BLOCK.	116
FIGURE 4.13 - POSITION OF THE SLIDING BLOCK COMPUTED USING (A) THE NEAREST PARTICLES DISTANCE CRITERION AND (B) THE COMBINATION OF CONTACT NORMAL (\mathbf{nc}) AND DISTANCE OF CONTACT (\mathbf{rkl}, \perp) VECTORS. SYMBOLS REPRESENT ANALYTICAL SOLUTIONS, AND SOLID LINES ARE COMPUTED RESULTS.	117
FIGURE 4.14 - VELOCITY OF THE SLIDING BLOCK COMPUTED USING (A) THE NEAREST PARTICLES DISTANCE CRITERION AND (B) THE COMBINATION OF CONTACT NORMAL (\mathbf{nc}) AND DISTANCE OF CONTACT (\mathbf{rkl}, \perp) VECTORS. SYMBOLS REPRESENT ANALYTICAL SOLUTIONS, AND SOLID LINES ARE COMPUTED RESULTS.	118
FIGURE 4.15 - SCHEMATIC DIAGRAM OF THE FSI NUMERICAL ALGORITHM.	119
FIGURE 4.16 - THE COORDINATE SYSTEM, INITIAL GEOMETRY AND MAIN DIMENSIONS OF THE 3D DAM BREAKING WITH ONE CUBE (CANELAS ET AL., 2016).....	120
FIGURE 4.17 - 3D DAM BREAKING WITH ONE CUBE. LONGITUDINAL MOTION OBTAINED BY EXPERIMENTAL TEST (CANELAS ET AL., 2016) AND PRESENT MPS MODELING.....	122
FIGURE 4.18 - INITIAL GEOMETRY AND MAIN DIMENSIONS OF THE 3D DAM BREAKING WITH (A) THREE CUBES STACKED AND ALIGNED VERTICALLY AND (B) SIX CUBES IN TRIANGLE FORMATION (PYRAMID).....	123
FIGURE 4.19 - SNAPSHOTS OF THE NUMERICAL SIMULATIONS OF 3D DAM BREAKING WITH THREE CUBES. INITIAL PARTICLE DISTANCE $l_0 = 10 \text{ mm}$	124
FIGURE 4.20 - SNAPSHOTS OF THE 3D DAM BREAKING WITH THREE CUBES. (A) EXPERIMENT (CANELAS ET AL., 2016) AND THE SIMULATIONS CARRIED IN THE PRESENT STUDY WITH (B) $l_0 = 10 \text{ mm}$ AND (C) $l_0 = 7.5 \text{ mm}$	125
FIGURE 4.21 - 3D DAM BREAKING WITH THREE CUBES. MOTION OF THE CUBE ON THE BASE ALONG THE LONGITUDINAL DIRECTION. EXPERIMENT, SPH SIMULATION (CANELAS ET AL., 2016) AND THE PRESENT MPS SIMULATIONS.	126
FIGURE 4.22 - 3D DAM BREAKING WITH THREE CUBES. MOTION OF THE TOP CUBE ALONG THE (A) LONGITUDINAL AND (B) VERTICAL DIRECTION. EXPERIMENT, SPH SIMULATION (CANELAS ET AL., 2016) AND THE PRESENT MPS SIMULATIONS.	126
FIGURE 4.23 - SNAPSHOTS OF THE NUMERICAL SIMULATIONS OF 3D DAM BREAKING WITH SIX CUBES. INITIAL PARTICLE DISTANCE $l_0 = 10 \text{ mm}$	127
FIGURE 4.24 - SNAPSHOTS OF THE 3D DAM BREAKING WITH SIX CUBES. (A) EXPERIMENT (CANELAS ET AL., 2016) AND THE PRESENT SIMULATIONS WITH (B) $l_0 = 10 \text{ mm}$ AND (C) $l_0 = 7.5 \text{ mm}$	128

FIGURE 4.25 - 3D DAM BREAKING WITH SIX CUBES. MOTION OF THE TOP CUBE ALONG THE (A) LONGITUDINAL AND (B) VERTICAL DIRECTION. EXPERIMENT, SPH SIMULATION (CANELAS ET AL., 2016) AND THE PRESENT MPS SIMULATIONS.	128
FIGURE 5.1 - ERP MODEL. CONTRIBUTION OF FLUID PARTICLES AND POLYGON WALLS TO THE CALCULATION OF NUMERICAL OPERATORS.	138
FIGURE 5.2 - NEIGHBORING PARTICLE DETECTION IN THE PRESENCE OF ZERO-THICKNESS WALLS.....	142
FIGURE 5.3 - SHELL DESCRIPTION AND BASIC KINEMATICAL CONFIGURATIONS THROUGH TIME EVOLUTION (ADAPTED FROM MOREIRA (2009)).	143
FIGURE 5.4 - SIX-NODE TRIANGULAR ELEMENT IN REFERENCE AND DEFORMED CONFIGURATIONS. NODES, SUBAREAS AND BARYCENTRIC COORDINATE.	147
FIGURE 5.5 - SCHEMATIC DIAGRAM OF THE WC-MPS-FEM NUMERICAL ALGORITHM.	151
FIGURE 5.6 - HYDROSTATIC WATER COLUMN OF HEIGHT $HF = 0.2M$ IN A TANK OF HEIGHT $HT = 0.22M$ AND SQUARE BOTTOM OF SIDE LENGTH $Lp = 0.2M$. CONTROL VOLUME OF SQUARE CROSS SECTION OF SIDE $l0$ AND HEIGHT $HF = 0.2M$	152
FIGURE 5.7 - NON-DIMENSIONAL PRESSURE (Cp) AT THE PARTICLES IN THE CONTROL VOLUME (SEE FIGURE 5.6) BETWEEN THE INSTANTS $t = 0.7$ AND $1.0S$. COMPARISON BETWEEN THE ANALYTICAL AND NUMERICAL RESULTS COMPUTED WITH THE WF-WC-MPS AND CD-WC-MPS METHODS	154
FIGURE 5.8 - SCHEMATIC DRAWING OF THE TANK OF LENGTH $LT = 1.61M$, WIDTH $WT = 0.15M$ AND HEIGHT $HT = 0.6M$, INITIAL WATER COLUMN OF HEIGHT $HF = 0.3M$ AND LENGTH $LF = 0.6M$, AND THE SENSORS S2, PLACED AT THE HEIGHT $HS2 = 0.015M$ AND S4, PLACED AT THE HEIGHT $HS4 = 0.08M$ (LOBOVSKÝ ET AL., 2014). THE SECTION A1-A1 DENOTES THE MIDDLE CROSS-SECTIONAL VIEW.....	155
FIGURE 5.9 - DAM BREAK. SNAPSHOTS OF THE EXPERIMENT (LOBOVSKÝ ET AL., 2014) AND NUMERICAL SIMULATIONS (MIDDLE CROSS-SECTIONAL VIEW A1-A1, SEE FIGURE 5.8) AT THE INSTANTS $T = 0.40, 0.80, 1.20, 1.60, 2.00, 2.40S$ (NON-DIMENSIONAL TIMES $\tau = 1.58, 2.57, 3.27, 6.67$). WF-WC-MPS AND CD-WC-MPS USING THE PARTICLE DISTANCE $l0 = 5MM$. THE COLORS ON THE FLUID PARTICLES ARE RELATED TO ITS PRESSURE MAGNITUDE.	156
FIGURE 5.10 - COMPARISON BETWEEN THE EXPERIMENTAL (LOBOVSKÝ ET AL., 2014) AND NUMERICAL PRESSURES COMPUTED WITH WF-WC-MPS AND CD-WC-MPS. PRESSURES AT SENSORS S2 AND S4.	157
FIGURE 5.11 - SQUARE PLATE OF SIDE LENGTH $Lp = 0.2M$ AND THICKNESS $e = 0.002M$, CLAMPED AT ALL EDGES AND UNDER UNIFORM PRESSURE $P = 2000 PA$	159
FIGURE 5.12 - PLATE'S MID-SPAN VERTICAL DISPLACEMENT. ANALYTICAL AND NUMERICAL RESULTS COMPUTED WITH THE PRESENT FEM FOR DIFFERENT NUMBER OF ELEMENTS $4 \times 4, 8 \times 8, 16 \times 16, 32 \times 32$	160
FIGURE 5.13 - SQUARE PLATE OF SIDE LENGTH $Lp = 0.2M$ AND THICKNESS $e = 0.002M$, CLAMPED AT ONE EDGE AND SUBJECTED TO INITIAL ($t = 0$) VELOCITY DISTRIBUTION v_{yx} PERPENDICULAR TO THE PLATE.....	162

FIGURE 5.14 - SQUARE PLATE OF SIDE LENGTH $L_p = 0.2\text{M}$, CLAMPED AT ALL EDGES AND UNDER HYDROSTATIC WATER COLUMN OF HEIGHT $H_F = 0.2\text{M}$ IN A TANK OF HEIGHT $H_T = 0.22\text{M}$. THE SECTION A2-A2 IS THE MIDDLE CROSS-SECTIONAL VIEW.	164
FIGURE 5.15 - (A) PRESSURE FIELD IN THE FLUID AND THE FIELD OF THE DISPLACEMENT IN THE ELASTIC PLATE AT $t = 2.0\text{S}$ USING $l_0 = 5\text{MM}$ (MIDDLE CROSS-SECTIONAL VIEW A2-A2, SEE FIGURE 5.14). (B) TIME HISTORY OF THE PLATE'S MID-SPAN VERTICAL DISPLACEMENT. ANALYTICAL AND NUMERICAL RESULTS COMPUTED WITH THE PRESENT WC-MPS-FE FOR DIFFERENT PARTICLE DISTANCES $l_0 = 20, 10, 5\text{MM}$	166
FIGURE 5.16 - SQUARE PLATE OF SIDE LENGTH $L_P = 0.20\text{M}$, CLAMPED AT ONE EDGE AND UNDER HYDROSTATIC WATER COLUMN OF HEIGHT $H_F = 0.18\text{M}$ IN A CUBIC TANK OF SIDE LENGTH $L_T = 0.2\text{M}$. THE SECTION A3-A3 IS THE MIDDLE CROSS-SECTIONAL VIEW.	168
FIGURE 5.17 - (A) PRESSURE FIELD IN THE FLUID AND THE FIELD OF THE DISPLACEMENT IN THE ELASTIC PLATE AT $t = 1.0\text{S}$ USING $l_0 = 5\text{MM}$ (MIDDLE CROSS-SECTIONAL VIEW A3-A3, SEE FIGURE 5.16). (B) TIME SERIES OF HORIZONTAL DISPLACEMENT OF THE ELASTIC PLATE'S TIP. ANALYTICAL AND NUMERICAL RESULTS COMPUTED WITH THE PRESENT WC-MPS-FE FOR DIFFERENT PARTICLE DISTANCES $l_0 = 20, 10, 5\text{MM}$	169
FIGURE 5.18 - SCHEMATIC DRAWING OF THE TANK OF LENGTH $L_T = 0.5\text{M}$, WIDTH $W_T = 0.1\text{M}$ AND HEIGHT $H_T = 0.146\text{M}$, WATER COLUMN OF HEIGHT $H_F = 0.14\text{M}$ AND LENGTH $L_F = 0.1\text{M}$, AND A CLAMPED ELASTIC GATE OF HEIGHT $H_P = 0.079\text{M}$ AND WIDTH $W_P = 0.098\text{M}$ (ANTOCI ET AL., 2007). THE SECTION A4-A4 IS THE MIDDLE CROSS-SECTIONAL VIEW.	170
FIGURE 5.19 - WATER COLUMN WITH A CLAMPED GATE. SNAPSHOTS OF THE NUMERICAL SIMULATIONS WC-MPS-FE FOR THE PARTICLE DISTANCE $l_0 = 2.5\text{MM}$ AT THE INSTANTS $T = 0.04, 0.08, 0.12, 0.16, 0.20, 0.24\text{S}$. THE COLOR SCALE OF THE FLUID PARTICLES IS RELATED TO ITS NON-DIMENSIONAL VELOCITY $v/(2gH_F)$ AND THE COLOR SCALE ON THE ELASTIC PLATE REFERS TO ITS DISPLACEMENT.	172
FIGURE 5.20 - WATER COLUMN WITH A CLAMPED GATE. SNAPSHOTS OF THE EXPERIMENT (ANTOCI ET AL., 2007) AND NUMERICAL SIMULATIONS (MIDDLE CROSS-SECTIONAL VIEW A4-A4, SEE FIGURE 5.18) WITH WC-MPS-FE FOR THE PARTICLE DISTANCE $l_0 = 2.5\text{MM}$ AT THE INSTANTS $T = 0.40, 0.80, 1.20, 1.60, 2.00, 2.40\text{S}$. THE COLORS ON THE FLUID PARTICLES ARE RELATED TO ITS PRESSURE MAGNITUDE.	173
FIGURE 5.21 - TIME SERIES OF THE HORIZONTAL DISPLACEMENTS OF THE FREE END OF THE ELASTIC PLATE IN THE DAM-BREAK FLOW WITH AN INITIAL WATER COLUMN OF HEIGHT $H_F = 0.14\text{M}$. EXPERIMENTAL DATA FROM ANTOCI ET AL. (2007), NUMERICAL RESULTS OF SPH-FEM WITH LINEAR AND NON-LINEAR (MOONEY-RIVLIN) ELASTICITY (YANG ET AL., 2012) AND PRESENT WC-MPS-FE WITH LINEAR ELASTICITY FOR DIFFERENT PARTICLE DISTANCES $l_0 = 10, 5, 2.5\text{MM}$	175
FIGURE 5.22 - TIME SERIES OF THE VERTICAL DISPLACEMENTS OF THE FREE END OF THE ELASTIC PLATE IN THE DAM-BREAK FLOW WITH AN INITIAL WATER COLUMN OF HEIGHT $H_F = 0.14\text{M}$. EXPERIMENTAL DATA FROM ANTOCI ET AL. (2007), NUMERICAL RESULTS OF SPH-FEM WITH LINEAR AND NON-LINEAR (MOONEY-RIVLIN) ELASTICITY (YANG ET AL.,	

2012) AND PRESENT WC-MPS-FE WITH LINEAR ELASTICITY FOR DIFFERENT PARTICLE DISTANCES $l_0 = 10, 5, 2.5\text{MM}$	175
FIGURE 5.23 - SCHEMATIC DRAWING OF THE TANK OF LENGTH $LT = 0.8\text{M}$, WIDTH $WT = 0.2\text{M}$ AND HEIGHT $HT = 0.6\text{M}$, WATER COLUMN OF HEIGHT $HF = 0.4\text{M}$ AND LENGTH $LF = 0.2\text{M}$, CLAMPED ELASTIC PLATE OF HEIGHT $HP = 0.1\text{M}$ AND WIDTH $WP = 0.1995\text{M}$ AND A GATE SUBJECTED TO A UPWARD MOTION $y_g(t)$ (LIAO ET AL., 2015). THE ELASTIC PLATE IS LOCATED $LP = 0.6\text{M}$ DOWNSTREAM. THE SECTION A5-A5 REPRESENTS THE MIDDLE CROSS-SECTIONAL VIEW.	176
FIGURE 5.24 - DAM BREAKING HITTING A CLAMPED PLATE. SNAPSHOTS OF THE NUMERICAL SIMULATIONS WC-MPS-FE FOR THE PARTICLE DISTANCE $l_0 = 5\text{MM}$ AT THE INSTANTS $T = 0.05, 0.25, 0.35, 0.45, 0.60, 0.80\text{S}$. THE COLORS ON THE FLUID PARTICLES ARE RELATED TO ITS NON-DIMENSIONAL VELOCITY $v/(2gHF)$ AND THE COLOR ON THE ELASTIC PLATE REFERS TO ITS DISPLACEMENT.	178
FIGURE 5.25 - DAM BREAKING HITTING A CLAMPED PLATE. SNAPSHOTS OF THE EXPERIMENT (LIAO ET AL., 2015) AND NUMERICAL SIMULATIONS (MIDDLE CROSS-SECTIONAL VIEW A5-A5, SEE FIGURE 5.23) WITH WC-MPS-FE FOR THE PARTICLE DISTANCE $l_0 = 5\text{MM}$ AT THE INSTANTS $T = 0.25, 0.28, 0.30, 0.55, 0.60, 0.80\text{S}$. THE COLORS ON THE FLUID PARTICLES ARE RELATED TO ITS PRESSURE MAGNITUDE.	180
FIGURE 5.26 - TIME SERIES OF THE HORIZONTAL DISPLACEMENT OF THE FREE END OF THE ELASTIC PLATE IN THE DAM-BREAK FLOW WITH AN INITIAL WATER COLUMN OF HEIGHT $HF = 0.4\text{M}$. EXPERIMENTAL DATA FROM LIAO ET AL. (2015), NUMERICAL RESULTS OF SINGLE-PHASE AND MULTI-PHASE SPH (SUN ET AL., 2019), SINGLE-PHASE MPS (KHAYYER ET AL., 2019), AND PRESENT SINGLE-PHASE WC-MPS-FE FOR DIFFERENT INITIAL PARTICLE DISTANCES $l_0 = 20, 10, 5\text{MM}$	181

LIST OF TABLES

TABLE 1.1 COMPARISON BETWEEN EULERIAN AND LAGRANGIAN DESCRIPTIONS.	36
TABLE 1.2 TYPICAL PARTICLE-BASED METHODS.	37
TABLE 3.1: NUMERICAL OPERATORS APPLIED IN THE PROBLEMS PRESENTED IN THIS CHAPTER.	63
TABLE 3.2: DESCRIPTION OF THE ORIGINAL AND PROPOSED SOURCE TERMS APPLIED IN THIS STUDY.	70
TABLE 3.3: STANDARD DEVIATION OF PRESSURE (<i>Stdp</i>) AND NORMALIZED ROOT MEAN SQUARE DEVIATION OF THE FREE-SURFACE HEIGHT (<i>NRMSDH</i>) FOR THE SIMULATIONS USING THE PROPOSED SOURCE TERM TCPI-PND.	73
TABLE 3.4: STANDARD DEVIATION OF PRESSURE (<i>Stdp</i>) AND NORMALIZED ROOT MEAN SQUARE DEVIATION OF THE FREE-SURFACE HEIGHT (<i>NRMSDH</i>) FOR THE SIMULATIONS USING THE PROPOSED SOURCE TERM TCPI-PND-DF.	73
TABLE 3.5: NUMERICAL PARAMETERS ADOPTED FOR THE SIMULATIONS USING ORIGINAL (O- PND OR O-PND-DF) AND PROPOSED (TCPI-PND OR TCPI -PND-DF) SOURCE TERMS.	76
TABLE 4.1: NUMERICAL OPERATORS APPLIED IN THE PROBLEMS PRESENTED IN THIS CHAPTER.	102
TABLE 4.2 - SLIDING BLOCK. NUMERICAL PARAMETERS AND MATERIAL PROPERTIES.	116
TABLE 4.3 - 3D DAM BREAKING WITH ONE CUBE. NUMERICAL AND MATERIALS PROPERTIES.	121
TABLE 4.4 - 3D DAM BREAKING WITH ONE CUBE. SPATIAL AND TEMPORAL DISCRETIZATION.	121
TABLE 4.5 - 3D DAM BREAKING WITH MULTIPLE CUBES. MATERIALS PROPERTIES.	123
TABLE 4.6 - 3D DAM BREAKING WITH MULTIPLE CUBES. NUMERICAL PARAMETERS.	123
TABLE 5.1 - PHYSICAL PROPERTIES OF THE FLUID.	152
TABLE 5.2 - HYDROSTATIC TANK. SIMULATION PARAMETERS OF THE FLUID.	153
TABLE 5.3 - HYDROSTATIC TANK. COMPUTATIONAL TIME.	153
TABLE 5.4 - DAM BREAK. SIMULATION PARAMETERS OF THE FLUID.	155
TABLE 5.5 - DAM BREAK. COMPUTATIONAL TIME.	155
TABLE 5.6 - SQUARE PLATE CLAMPED AT ALL EDGES AND UNDER UNIFORM PRESSURE. PHYSICAL PROPERTIES OF THE ELASTIC PLATE.	159
TABLE 5.7 - SQUARE PLATE CLAMPED AT ALL EDGES AND UNDER UNIFORM PRESSURE. SIMULATION PARAMETERS OF THE ELASTIC PLATE.	159
TABLE 5.8 - SQUARE PLATE CLAMPED AT ALL EDGES AND UNDER UNIFORM PRESSURE. COMPUTATIONAL TIME.	160
TABLE 5.9 - ANALYTICAL AND NUMERICAL PLATE'S MID-SPAN VERTICAL DISPLACEMENT COMPUTED WITH THE PRESENT FEM FOR DIFFERENT NUMBER OF ELEMENTS 4×4, 8×8, 16×16, 32×32.	161

TABLE 5.10 - SQUARE PLATE CLAMPED AT ONE EDGE AND SUBJECTED TO INITIAL VELOCITY. PHYSICAL PROPERTIES OF THE ELASTIC PLATE.	161
TABLE 5.11 - SQUARE PLATE CLAMPED AT ONE EDGE AND SUBJECTED TO INITIAL VELOCITY. SIMULATION PARAMETERS OF THE ELASTIC PLATE.	162
TABLE 5.12 - SQUARE PLATE CLAMPED AT ONE EDGE AND SUBJECTED TO INITIAL VELOCITY. ANALYTICAL AND NUMERICAL RESULTS FROM THE PARTICLE METHODS SPH (GRAY ET AL., 2001; ANTOCI ET AL., 2007; RAFIEE & THIAGARAJAN, 2009), MPS (HWANG ET AL., 2014) AND PRESENT FEM.	163
TABLE 5.13 - SQUARE PLATE CLAMPED AT ALL EDGES AND UNDER HYDROSTATIC WATER COLUMN. PHYSICAL PROPERTIES OF THE FLUID AND ELASTIC PLATE.	164
TABLE 5.14 - SQUARE PLATE CLAMPED AT ALL EDGES AND UNDER HYDROSTATIC WATER COLUMN. SIMULATION PARAMETERS OF THE FLUID AND ELASTIC PLATE.	165
TABLE 5.15 - SQUARE PLATE CLAMPED AT ALL EDGES AND UNDER HYDROSTATIC WATER COLUMN. COMPUTATIONAL TIME.	165
TABLE 5.16 - SQUARE PLATE CLAMPED AT ALL EDGES AND UNDER HYDROSTATIC WATER COLUMN. ANALYTICAL AND NUMERICAL RESULTS COMPUTED WITH THE PRESENT WC-MPS-FE FOR DIFFERENT PARTICLE DISTANCES $l_0 = 20, 10, 5\text{MM}$	167
TABLE 5.17 - SQUARE PLATE CLAMPED AT ONE EDGE AND UNDER HYDROSTATIC WATER COLUMN. PHYSICAL PROPERTIES OF THE FLUID AND ELASTIC PLATE.	167
TABLE 5.18 - SQUARE PLATE CLAMPED AT ONE EDGE AND UNDER HYDROSTATIC WATER COLUMN. SIMULATION PARAMETERS OF THE FLUID AND ELASTIC PLATE.	168
TABLE 5.19 - SQUARE PLATE CLAMPED AT ONE EDGE AND UNDER HYDROSTATIC WATER COLUMN. COMPUTATIONAL TIME.	168
TABLE 5.20 - SQUARE PLATE CLAMPED AT ALL EDGES AND UNDER HYDROSTATIC WATER COLUMN. ANALYTICAL AND NUMERICAL RESULTS COMPUTED WITH THE PRESENT WC-MPS-FE FOR DIFFERENT PARTICLE DISTANCES $l_0 = 20, 10, 5\text{MM}$	170
TABLE 5.21 - WATER COLUMN WITH A CLAMPED GATE. PHYSICAL PROPERTIES OF THE FLUID AND ELASTIC PLATE.	171
TABLE 5.22 - WATER COLUMN WITH A CLAMPED GATE. SIMULATION PARAMETERS OF THE FLUID AND ELASTIC PLATE.	171
TABLE 5.23 - WATER COLUMN WITH A CLAMPED GATE. COMPUTATIONAL TIME.	171
TABLE 5.24 - DAM BREAKING HITTING A CLAMPED PLATE. PHYSICAL PROPERTIES OF THE FLUID AND ELASTIC PLATE.	177
TABLE 5.25 - DAM BREAKING HITTING A CLAMPED PLATE. SIMULATION PARAMETERS OF THE FLUID AND ELASTIC PLATE.	177
TABLE 5.26 - DAM BREAKING HITTING A CLAMPED PLATE. COMPUTATIONAL TIME.	177

LIST OF SYMBOLS AND NOTATIONS

Latin letters

A	area of a finite element
A_{CS}	dimensionless constant related to the velocity of the perturbations
A_{fe}	amplitude motion at the free end of elastic plate
A_F	non-dimensional number used in equation of stabilization technique
A_x, A_y	sloshing amplitude motion
\mathbf{a}	current director of a point in the middle surface
\mathbf{a}^r	shell director in the reference configuration r
\mathbf{A}	skew-symmetric tensor of Rodrigues rotation vector $\boldsymbol{\alpha}$
\mathbf{b}	body force per unit reference volume
C	Courant number
c_n	normal damping constant
c_0	numerical speed of sound in the reference density
c_s	propagation velocity of the perturbations
c_t	tangential damping constant
C_i	particle concentration (volume fraction) at particle i
C_p	non-dimensional pressure coefficient
C_{PS}	non-dimensional pressure coefficient
C_r	Courant number
C_{rep}	non-dimensional repulsive constant
\mathbb{C}	a given configuration
dim	number of spatial dimensions
$d\mathbf{a}$	body face area vector
D	diffusive term
\mathbb{D}_i	neighboring dummy particles of the particle i
e	thickness
e_T	thickness of Plexiglass tank
E	Young's modulus
E_{min}	minimum Young's modulus
$\mathbf{e}_{\{\cdot\}}$	orthonormal component
\mathbf{E}_3	skew-symmetric tensor of orthonormal component \mathbf{e}_3

\mathbb{E}	identification of a given finite element
\mathbf{f}_c	contact force between rigid bodies vector
\mathbf{f}_{ext}	external force on the rigid body vector
\mathbf{f}_g	gravitational force vector
\mathbf{f}_h	hydrodynamic force vector
\mathbf{f}_n	normal component vector
\mathbf{f}_t	tangential component vector
\mathbf{f}^c	Coulomb friction law vector
\mathbf{f}^d	damping force vector
\mathbf{f}^r	repulsion force vector
$\mathbf{f}_i^{\text{rep}}$	repulsive force vector
\mathbf{F}_n	numerical impact force vector
\mathbf{F}_p	physical impact force vector
\mathcal{F}_b	body force per unit mass vector
g	absolute value of gravitational acceleration
\mathbf{g}	gravitational acceleration vector
h	shell thickness in the reference configuration
h_{max}	maximum surface height
h_o	initial fluid column height
H_F	water column height
H_{jet}	water jet height
H_T	tank height
i, j	identification number of particles
i', j'	identification number of mirror particles
\mathbf{I}	identity matrix
\mathbf{I}_s	inertia matrix of rigid body
\mathbf{J}	impulse
k_n	normal stiffness constant
k_t	tangential stiffness constant
K	kinetic energy
l_0	initial distance between two adjacent particles
l_{cell}	domain cells size
L	length

L_F	water column length
L_p	square plate side length
L_T	tank length
L_{wall}	wall length
m	mass
m_s	mass of rigid body
Ma	Mach number
$\bar{\mathbf{m}}$	external moments per unit area
\mathbf{m}^r	back-rotated cross sectional moments per unit length
n	particle number density
n^t	particle number density at the instant t
n^0	initial particle number density
n^*	particle number density obtained in the prediction step
n_v	number of values computed during a time interval
n_1, n_2	integer repulsive coefficients
N	number of particles
\hat{N}	number of particles inside the limited search domain
N_c	number of pairs of particles belonging to two different bodies that are in contact
N_{ij}	number of particles belonging on the perimeter of the circle Ω
\mathbf{n}_c	contact normal vector
\mathbf{n}_k	normal vector of the wall at the wall particle k
$\mathbf{n}_i^{\text{wall}}$	normal vector of the wall pointing to the particle i
$\bar{\mathbf{n}}$	external forces per unit area
\mathbf{n}^r	back-rotated cross sectional forces per unit length
\mathbf{N}	matrix of element shape functions
P	pressure
\hat{P}	minimum pressure belonging to the neighborhood of a particle
P_{atm}	atmospheric pressure
P_{fs}	pressure at free-surface particles
P_n	numerical impact pressure
P_p	physical impact pressure
P_s	pressure at the stagnation point (null velocity)
\mathbb{P}_E	neighboring particles of the finite element E

\mathbb{P}_i	neighboring particles of the particle i
\mathbf{p}	nine-dimensional vector associated with each nodal degree-of-freedom
$\bar{\mathbf{q}}$	generalized external forces vector
\mathbf{Q}	rotation tensor
\mathcal{Q}	linear momentum
r	initial reference configuration
r_e	effective radius
\mathbf{r}	position vector
\mathbf{r}_{ck}	position vector between the CM of the rigid body p and the particle k
\mathbf{r}_{CM}	position vector of the solid center of mass
r_p	distance between pair of closest particles belonging to two different bodies
\mathbf{r}_s	position vector from the center of mass of the rigid body
\mathbf{r}_\perp	distance of contact vector
$\mathbf{r}_i^{\mathbb{E}}$	closest point on the finite element \mathbb{E} to particle i
$\mathbf{r}_i^{\text{wall}}$	closest point on the polygon to particle i
\mathbf{R}^{ref}	transformation matrix
\mathbb{R}^{dim}	dim -dimensional real space
\mathbf{s}	vector perpendicular to the position vector \mathbf{r}
t	time
t_c	duration of a typical contact among rigid bodies
T_s	sloshing period
\mathbf{t}	tangential contact vector
\mathbf{t}_s	surface traction per unit reference area
\mathbf{T}_h	torque vector due hydrodynamic force
\mathbf{T}_c	contact torque vector
\mathbf{T}_{ext}	external torque on the rigid body vector
u_{max}	maximum velocity
u_w	velocity of wave front
U	total energy
U_E	elastic energy
U_K	kinetic energy
\mathbf{u}	velocity vector
\mathbf{u}_s	velocity vector at the center of mass of the rigid body

$\mathbf{u}_i^{\text{wall}}$	velocity vector of the wall at the point where the force of particle i is applied
\mathbf{v}	velocity
V_{in}	inflow velocity
\mathbb{V}_i	virtual neighborhood of a particle i
x_s, y_s	water jet contour shape
\mathbf{x}	material point position vector
W_{jet}	width of water jet
W_T	tank width
\mathbf{z}	current position of a point in the middle surface

Greek letters

α_c	artificial compressibility factor
α_1	fluid particles collision distance coefficient
α_2	fluid particles coefficient of restitution
α_3	fluid particles collision coefficient
$\boldsymbol{\alpha}$	Rodrigues rotation vector
β	PND free surface constant
β_N	Newmark coefficient
β_R	Rayleigh damping
γ	relaxation coefficient
γ_N	Newmark coefficient
γ_p	polytrophic index
Γ	auxiliar coefficient of original source term
δ	overlap (penetration) between two wall particles belonging to two different bodies
δ^t	relative sliding
δt	physical time interval between collisions at successive panels
δT	virtual variation of the kinetic energy
δW_{ext}	external virtual work
δW_{int}	internal virtual work
Δt	numerical time step
Δt_f	numerical time step used in the fluid domain
Δt_s	numerical time step used in the solid domain
$\boldsymbol{\varepsilon}$	strain vector

ϵ	correction coefficient
ζ	thickness coordinate of orthonormal component
ζ	point on the reference middle surface
$\boldsymbol{\eta}_\alpha$	translational strain vector
$\boldsymbol{\theta}$	Euler rotation vector
$\boldsymbol{\kappa}_\alpha^r$	back-rotated specific rotation vector
λ	correction parameter of the Laplacian model of the MPS method
μ	kinetic friction coefficient
ν	Poisson's ratio
ν_k	kinematic viscosity
ξ_n	contact ratio
ξ_1, ξ_2	coordinates of orthonormal component
$\boldsymbol{\xi}$	position of any shell material point
Π	auxiliar coefficient of improved source term
ρ_f	fluid density
ρ_s	solid density
ρ^0	reference density
ϱ	weight free surface constant
$\boldsymbol{\sigma}$	stress vector
τ	non-dimensional time
τ_s	non-dimensional time
τ_u	non-dimensional time
$\boldsymbol{\tau}^r$	back-rotated stress vector
ϕ	arbitrary function
$\boldsymbol{\chi}$	displacement vector
ω	weight function
Ω	circle domain
Ω_p	domain with solid wall particles
Ω_s	solid subdomain
$\boldsymbol{\omega}$	angular velocity vector
$\boldsymbol{\omega}_s$	angular velocity vector of rigid body

LIST OF ABBREVIATIONS

AABB	Axis-aligned bounding box
ALE	Arbitrary Lagrangian Eulerian
CAPES	Coordenação de Aperfeiçoamento de Pessoal de Nível Superior
CD-WC-MPS	WC-MPS using the smoothed Continuity equation with Diffusive term
CFD	Computational fluid dynamics
CFL	Courant Friedrichs Lewy
CM	Center of mass
CPM	Consistent particle method
CPS	Conventional parallel staggered
CPU	Central processing unit
CSS	Conventional sequential staggered
δ-SPH	Delta smoothed particle hydrodynamics
DEM	Discrete element method
DPD	Dissipative particle dynamics
DS	Dynamic stabilization
DSMC	Direct simulation Monte Carlo
EMPS	Explicit moving particle simulation
EOS	Equation of state
EPP	Equação de Poisson para a pressão
ERP	Explicitly represented polygon
FDM	Finite difference method
FE	Finite element
FEM	Finite element method
FLIC	Fluid-in-cell
FSI	Fluid-structure interaction
FVM	Finite volume method
FVPM	Finite volume particle method
Giraffe	Generic Interface Readily Accessible for Finite Elements
GPU	Graphical processing unit
HPC	High-performance computing
IFS	Interação fluido-estrutura
ISPH	Incompressible smoothed particle hydrodynamics

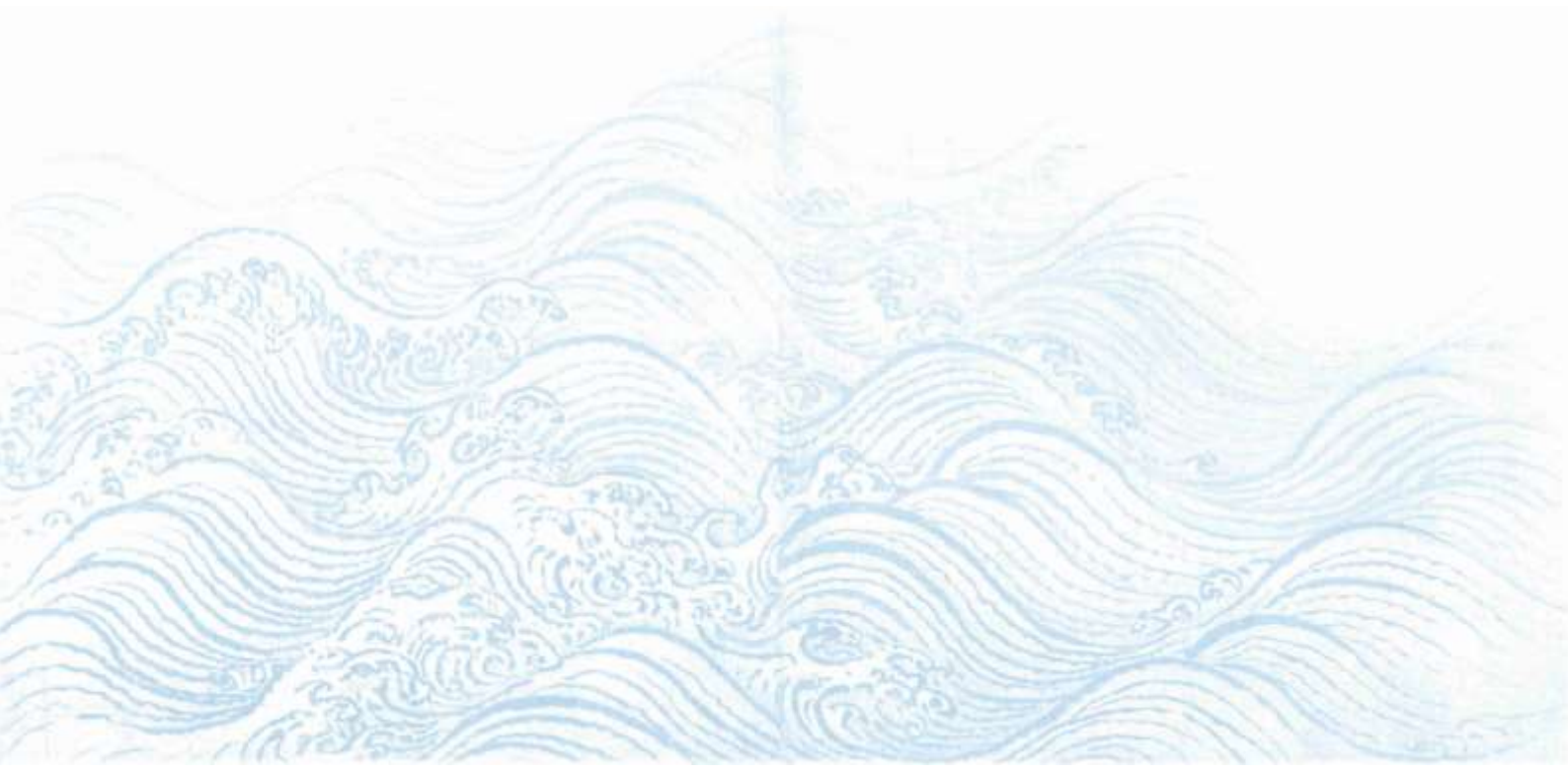
ISPH-DF	Incompressible smoothed particle hydrodynamics with free divergence
KFBI	Kernel function-based interpolation
LBE	Lattice Boltzmann equation
LBM	Lattice Boltzmann method
LES	Large eddy simulation
LGCA	Lattice gas cellular automata
MAC	Marker-and-cell
MC	Monte Carlo
MD	Molecular dynamics
MM	Meshless method
MPI	Message passing interface
MPM	Material point method
MPS	Moving particle semi-implicit
NPCD	Neighborhood particles centroid deviation
NRMSD	Normalized root mean square deviation
O-PND	Original PND deviation
O-PND-DF	Original PND deviation and divergence-free condition
ONR	Office of Naval Research
OpenMP	Open multi-processing
PFEM	Particle finite element method
PIC	Particle-in-cell
PND	Particle number density
PPE	Pressure Poisson equation
PST	Particle stabilizing term
RMSD	Root mean square deviation
TCPI	Time-scale correction of particle-level impulses
TCPI-PND	Proposed PND deviation
TCPI-PND-DF	Proposed PND deviation and divergence-free condition
TPN-USP	Numerical Offshore Tank of USP
S-PIB	Striped-point-in-box
SDF	Signed distance function
Shd	Free-surface height deviation
SPH	Smoothed particle hydrodynamics
SPS	Sub particle-scale

Std	Standard deviation
WC-MPS	Weakly-compressible moving particle semi-implicit
WF-WC-MPS	WC-MPS adopting the Weight Function

CHAPTER 1

INTRODUCTION

This chapter is divided into three parts. The first part illustrates the relevance of fluid-structure interaction problems and the importance of a reliable computational model, which motivates the present work on the adoption of truly incompressible moving particle semi-implicit (MPS) (Koshizuka & Oka, 1996) and weakly-compressible moving particle semi-implicit (WC-MPS) (Shakibaeinia & Jin, 2010) particle-based methods to address violent free-surface flow. Following, a brief review on the meshless (or meshfree) particle-based methods is introduced. Finally, the outline of the thesis is listed.



1.1 BACKGROUND AND MOTIVATION

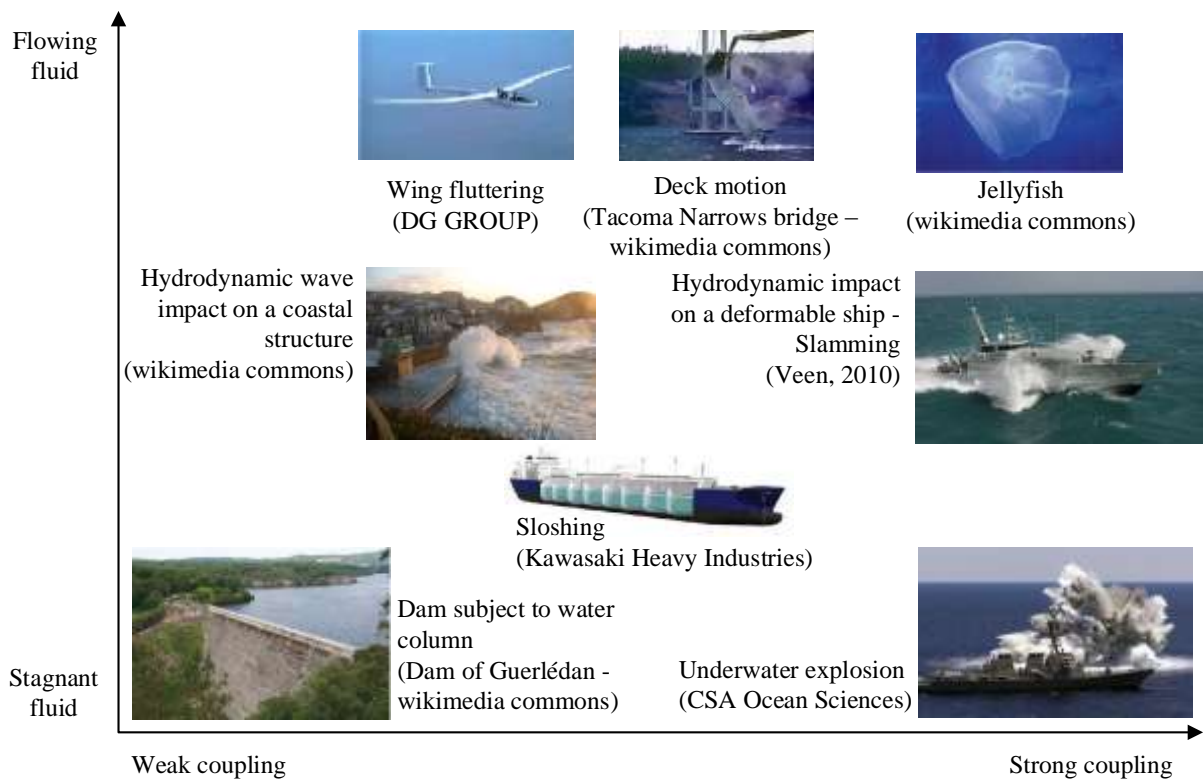
Fluid-structure interaction (FSI) is a class of phenomena involving the coupling between the motions of a structure and a fluid, i.e., a mutual dependence in which the flow behavior depends on the shape and motion of the structure, whereas the motion and deformation of the structure depend on the fluid loads acting on it (Bazilevs et al., 2013). It has attracted increasing interest due to wide range of applications in several areas, including civil (wave loads on coastal structures, wind on suspension bridges, flooding impacts, building drainage), ocean (wave energy converters, free-surface phenomena in reservoirs), mechanical (deflection of wind-turbine blades, nuclear reactors), aerospace (fluttering of aircraft wings, dynamics of spacecraft parachutes), automotive (inflation of automobile airbags, moving fuel-storage tanks), environmental (fish swimming, bird/insect flying), biomedical engineering (arterial dynamics in cerebral aneurysms, behavior of biological tissues and organs), and others.

FSI problems can be classified using two criteria according to the physics of the phenomenon (Gaugain, 2013). The first criterion is based on the physical nature of the fluid flow (Axisa & Antunes, 2006). The fluid is defined as stagnant if the flow is negligible or non-existent, i.e., the governing equations describe small motions of the fluid and the structure around an equilibrium rest state, generally leading to linear problems. Otherwise, the fluid is denominated as flowing, i.e., the governing equations express larger motions of the fluid and/or the structure, describing their behavior in terms of the current state of the system and generally leading to nonlinear problems.

The second criterion contemplates the coupling strength, which may be characterized by the intensity of the physical interactions or exchanges between the two media. If the effect of one media is dominant over the other, then it is defined by a weak coupling. On the other hand, a strong coupling is described by high levels of exchange between the two media, i.e., the fluid has a significant influence on the structure, and vice versa.

Figure 1.1 shows some FSI problems according to the above criteria.

Figure 1.1 - Fluid-structure interaction problems. Nature of the flow (stagnant or flowing fluid) and the interaction strength (weak or strong coupling).



Source: adapted by the author from Gaugain (2013).

Due to the intrinsic complexity of FSI problems, analytical or even semi-analytical solutions are available only for a restricted range of cases covering simple geometry and physics. Experimental tests using scaled models provide meaningful data to understand the physics of complex cases. Notwithstanding, experiments are generally expensive, demand time consuming experimental setting, are restricted by scale effects and the reproducibility data acquisition is frequently limited. Numerical methods represent an economical alternative to simulate more complex scenarios and even, in some situations, are the unique possibility to face them in detail with minimum assumptions.

In this context, many numerical methods have been proposed. Grid or mesh-based methods, e.g., finite difference (FD), finite volume (FV) and finite element (FE) methods, have been widely applied to solve such problem. However, these methods suffer from some limitation, which restrict their applications in many FSI problems, especially for those in the presence of violent free-surface flow, e.g., and multiple solids with large motion and deformations. Free-surface flow problems are characterized by large boundary deformations, fragmentation, merging, or moving interface, and numerical treatments like free surface tracking or

remeshing techniques are required by mesh-based methods, which increase the computational complexity. Due to the easy implementation and flexibility, the meshless particle-based methods (Li & Kam, 2004; Liu & Liu, 2015) provide new perspectives for the modeling of free-surface flow. In these methods, all the physical domain is represented by a set of nodal points (particles), without additional mesh constraints.

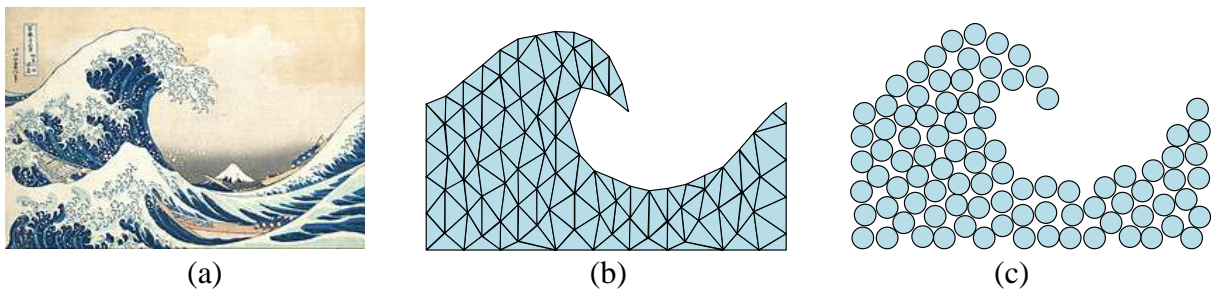
A vast number of research studies have been conducted on development and improvements of meshless methods, but several key aspects, e.g., consistency, stability, adaptivity, coupling to other models, and boundary conditions, remain not comprehensively resolved. Within this context, the objective of this work is to develop efficient computational solutions based on meshless particle methods for complex FSI in free-surface flow. Initially, the unstable nature of pressure computation of the incompressible projection-based particle methods is investigated. Based on the viewpoint of momentum conservation in particle-level collisions, a correction of the mismatch between numerical and physical time scales is introduced to derive consistent formulations in time domain for the pressure Poisson equation (PPE), named as time-scale correction of particle-level impulses (TCPI). To demonstrate their effectiveness, the MPS method is adopted and four phenomena, including hydrostatic and hydrodynamic, are studied. After that, a numerical solid contact model is proposed for the MPS. The model adopts a penalty-based method that uses a nonlinear spring and dashpot concept, thus reproducing the macroscopic properties of the multiple bodies interactions. By using this model, several problems involving free-surface flow interacting with multiple bodies are investigated. Finally, a novel 3D fluid-structure coupling between an improved WC-MPS and finite element (FE) methods is developed to take advantage of the so-called explicitly represented polygon (ERP) wall boundary model (Mitsume et al., 2015). The WC-MPS is used to model the fluid domain, whereas nonlinear structural dynamic is modeled following a geometrically exact shell model. Since a significant range of FSI problems involves thin and complex flexible structures, the particles-based modeling of fluid and solid domains requires extremely fine resolutions, which in turn lead to considerable high computational effort. By adopting the shell to modeling the thin solid, the computational cost as well as required memory can be drastically reduced, since the fluid spatial resolution is not affected, without compromising the accuracy of the solution. Consequently, the proposed model expands its application to wider range of FSI problems. Simulations of quasi-hydrostatic and hydrodynamic FSI problems are conducted to verify the robustness and accuracy of the proposed model. In the current work, the MPS and WC-MPS codes have been developed in

C++ for CPU (Central Processing Unit) and take advantage of the parallel computing in shared memory systems using OpenMP® 3.0 (Dagum & Menon, 1998).

1.2 PARTICLE-BASED METHODS

Particle-based methods (or particle methods) in general refers to a special class of meshless methods that adopt a finite number of discrete nodal points (particles) to represent the state and to solve the governing equations of a physical system (Liu & Liu, 2015). The mesh and particle representations for a continuum physical domain, here represented by a breaking wave, are illustrated in Figure 1.2. Each point (particle) moves accordingly with its own mass and the internal/external forces are evaluated by the interaction with their neighboring particles (Idelsohn & Oñate, 2006). Also, each particle can be directly associated to discrete physical variable such as mass, velocity, position, pressure, vorticity, energy, charge, etc., or be used to represent a part of the continuum domain. Instead of the Eulerian description, in which the physical variables are determined at fixed spatial locations as the medium advances through time, particle methods adopt the Lagrangian description, where the particles follow the motion of the physical medium. Table 1.1 summarizes the main features of both descriptions.

Figure 1.2 - (a) Physical wave, (b) mesh-based and (c) particle-based representation.



Source: The Great Wave at Kanagawa carved by Katsushika Hokusai, distributed under a CC-BY 2.0 license, and the author.

These methods have been applied in many fields from very small atomistic to very large astronomical scale problems of solid and fluid mechanics, for example, microflow (Hoogerbrugge & Koelman, 1992; Karunasena et al., 2014), chemical (Liu et al., 2019; Pan et al., 2019), nuclear (Vorobyev et al., 2011; Wang et al., 2017), ocean and civil engineering (Gotoh & Khayyer, 2018; Ye et al., 2019), automotive (Chiron et al., 2019; Guo et al., 2020), biology and medicine (Zhang et al., 2019), swarm robot control (Pimenta et al., 2013; Maningo et al., 2017), astrophysical (Rasio, 2000), among others. Some typical particle-based methods are presented in Table 1.2.

Since there is no grid or mesh to connect the particles, the particle-based methods are expected to be more adaptive, versatile, and robust compared to mesh-based methods (Liu & Liu, 2015). Consequently, they can be very effective in modeling complex problems involving large deformations, discontinuous physics, complex-shaped bodies, and moving boundaries. The advantages of the particle-based methods are especially evident when simulating nonlinear hydrodynamic phenomena such as violent FSI in wave-break process, which is the focus of the present work.

Table 1.1 Comparison between Eulerian and Lagrangian descriptions.

Description	Eulerian	Lagrangian
Node	Fixed in the space	Attached on the moving material
Track	Mass, momentum, and energy flux across grid nodes and mesh cell boundary	Motion of any point on materials
Moving boundary and interface	Difficult to track	Easy to track
Complex geometry	Difficult to model with good accuracy	Easy to model
Large deformation and fragmentation	Easy to handle	Difficult to handle (mesh-based) Easy to handle (meshless)

Source: adapted by author from Liu and Liu (2003).

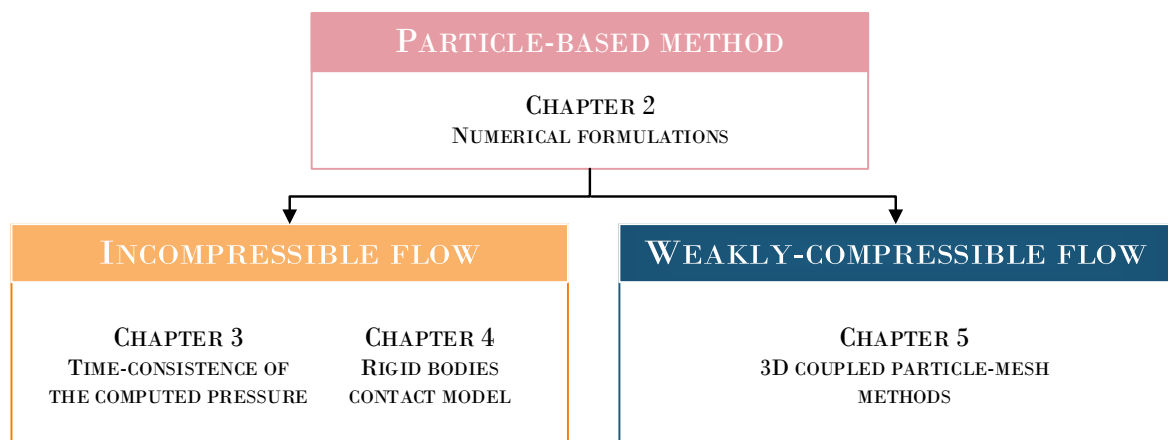
Table 1.2 Typical particle-based methods.

Particle-based methods	References
Monte Carlo (MC)	(Metropolis & Ulam, 1949)
Molecular dynamics (MD)	(Alder & Wainright, 1957)
Particle-in-cell (PIC)	(Evans & Harlow, 1957)
Direct simulation Monte Carlo (DSMC)	(Bird, 1963)
Marker-and-cell (MAC)	(Harlow & Welch, 1965)
Fluid-in-cell (FLIC)	(Gentry et al., 1966)
Vortex methods	(Chorin & Bernard, 1973)
Smoothed particle hydrodynamics (SPH)	(Gingold & Monaghan, 1977; Lucy, 1977)
Discrete element method (DEM)	(Cundall & Strack, 1979)
Lattice gas cellular automata (LGCA)	(Frisch et al., 1986)
Lattice Boltzmann equation (LBE)	(McNamara & Zanetti, 1988)
Dissipative particle dynamics (DPD)	(Hoogerbrugge & Koelman, 1992)
Material point method (MPM)	(Sulsky et al., 1994)
Moving particle semi- implicit (MPS)	(Koshizuka & Oka, 1996)
Finite volume particle method (FVPM)	(Hietel et al., 2000; Ismagilov, 2006)
Consistent particle method (CPM)	(Koh et al., 2012)

Source: adapted by author from Liu and Liu (2015).

1.3 OUTLINE OF THE THESIS

Figure 1.3 - Main contributions and respective chapters



Source: the author.

The main contributions of the thesis on the context of truly incompressible or weakly-compressible particle-based methods are shown in Figure 1.3 and organized as follows:

Chapter 2 provides the numerical formulations related to the incompressible MPS and the weakly-compressible MPS, namely WC-MPS, adopted in the present work.

Chapter 3 examines the unstable nature of pressure computation of the incompressible projection-based particle methods. New source terms dependent directly on the spatial discretization and independent to the time step are proposed for the MPS. The source terms, consistent in time domain, are established through numerical simulations of hydrostatic and hydrodynamic benchmark tests.

Chapter 4 concentrates on the development of a numerical solid-solid contact model for the particle-based methods. The proposed solid contact model is explained in detail and several FSI problems with free-surface flow and multiple bodies are simulated in order to demonstrate the features of the proposed model in the context of the MPS method.

Chapter 5 presents a novel 3D fluid-structure coupling between WC-MPS and FE methods. The main features and the numerical formulations adopted to free-surface flow and elastic thin-walled structures are introduced comprehensively, including the polygon wall boundary model representation and the improvements on the stability and accuracy of the computation. The flexible applicability, robustness and accuracy of the implemented coupling are demonstrated by solving quasi-hydrostatic and hydrodynamic complex free-surface problems with thin solids.

Finally, Chapter 6 explores some conclusions and few recommendations for future research based on the results and discussions from this work.

CHAPTER 2

REVIEW OF INCOMPRESSIBLE MOVING PARTICLE SEMI- IMPLICIT (MPS) AND WEAKLY-COMPRESSIBLE MPS (WC- MPS) METHODS

The moving particle semi-implicit (MPS) is a purely meshfree method, in which the continuum is represented by a set of particles (points), that interact with each other within a compact support, and the differential operators of the governing equations are approximated by local weighted summations. Currently, the MPS adopts fully explicit algorithms using an equation of state, the so-called explicit MPS (E-MPS) and weakly-compressible MPS (WC-MPS), and semi-implicit algorithms by solving a linear system of pressure Poisson equations (PPE), namely MPS. This chapter explores previous and proposed formulations related to the incompressible and weakly-compressible MPS methods.



2.1 BACKGROUND

The moving-particle semi-implicit (MPS) is a numerical method originally developed by Koshizuka and Oka (1996), for modeling incompressible free-surface flows. As a particle method, MPS represents the continuum with a set of mobile particles (without any connectivity) over which the flow governing equations are solved. The particles containing a set of continuum material properties, interact with each other within a range controlled by a weight function (also referred to as kernel function), and move in a Lagrangian system according to the particle interactions and external forces. Fluid particles moves in a natural way so that free surface, fluid-fluid interfaces or moving boundaries do not need to be explicitly tracked. Moreover, as a meshfree method, MPS can effectively avoid the mesh tangling and consequently re-meshing process is not required. In this way, MPS is very effective for the simulations of incompressible flow involving large deformation of free surfaces, fragmentation, and merging, or involving complex shaped multi-bodies, multi-phase flows, and multi-physic problems.

A semi-implicit algorithm, which divides each time step into prediction and correction steps, was originally used for the temporal integration of the governing equations in the MPS method for incompressible flows with free surfaces (Koshizuka & Oka, 1996). In the semi-implicit algorithm, an implicit pressure Poisson equation (PPE) was formulated to keep the particle number density as a constraint condition of incompressibility. On the other hand, the MPS method was also used by assuming a slightly compressible approach with a fully explicit algorithm (Shakibaeinia & Jin, 2010). In order to couple the continuity and momentum equations, an equation of state (EOS) is explicitly calculated providing the pressure of the particles.

2.2 NUMERICAL METHOD

2.2.1 GOVERNING EQUATIONS

The governing equations for incompressible viscous flow are expressed by the conservation laws of mass and momentum:

$$\frac{D\rho}{Dt} = -\rho_f \nabla \cdot \mathbf{u} = 0, \quad (2.1)$$

$$\frac{D\mathbf{u}}{Dt} = -\frac{\nabla P}{\rho_f} + \nu_k \nabla^2 \mathbf{u} + \mathcal{F}_b, \quad (2.2)$$

where ρ_f is the fluid density, \mathbf{u} is the velocity vector, P is the pressure, ν_k is the kinematic viscosity and \mathcal{F}_b is the external body force per unit mass vector.

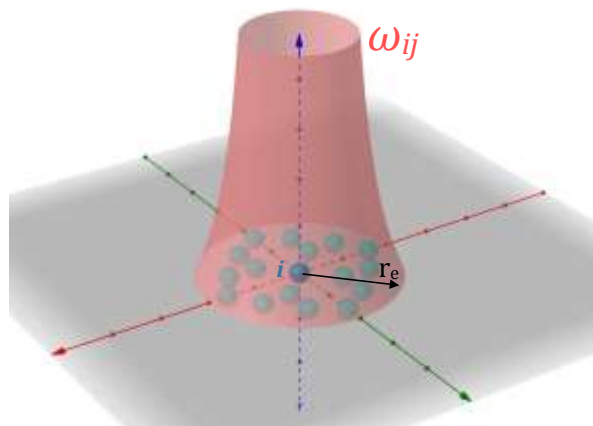
2.2.2 NUMERICAL OPERATORS

In the MPS method, the differential operators of the governing equations of continuum are replaced by discrete operators derived based on a weight function, as shown in Figure 2.1. For a given particle i , the influence of a neighbor particle j is defined by the weight function ω_{ij} :

$$\omega_{ij} = \begin{cases} \frac{r_e}{\|\mathbf{r}_{ij}\|} - 1 & \|\mathbf{r}_{ij}\| \leq r_e \\ 0 & \|\mathbf{r}_{ij}\| > r_e \end{cases}, \quad (2.3)$$

where r_e is the effective radius that limits the range of the neighborhood \mathbb{P}_i of the particle i and $\|\mathbf{r}_{ij}\| = \|\mathbf{r}_j - \mathbf{r}_i\|$ represents the distance between the particles i and j . More accurate results are expected by the adoption of larger effective radius r_e since more neighboring particles are inside the support for a target particle. Nevertheless, numerical accuracy and stabilization are limited with increasing r_e , as demonstrated by Koshizuka and Oka (1996) and Yoon et al. (1999). Following Koshizuka and Oka (1996), in the present work, the effective radius $r_e = 2.1l_0$ is used for the particle number density (see Eq. (2.4)), gradient operator (see Eq. (2.15)) and divergence operator (see Eq. (2.16)) for both 2D and 3D simulations, whereas the radius $r_e = 4.0l_0$ and $r_e = 2.1l_0$ are used for the Laplacian operator (see Eq. (2.24)) in 2D and 3D simulations, respectively. l_0 is the initial distance between two adjacent particles.

Figure 2.1 - Graphical representation of the weight function ω_{ij} and its range of influence r_e in 2D space. The reference particle i (central sphere) has its physical properties influenced by their neighborhood \mathbb{P}_i .



Source: the author.

2.2.2.1 PARTICLE NUMBER DENSITY

The summation of the weight of all the particles in the neighborhood \mathbb{P}_i of the particle i is defined as its particle number density n_i , which is proportional to the fluid density:

$$n_i = \sum_{j \in \mathbb{P}_i} \omega_{ij}. \quad (2.4)$$

2.2.2.2 GRADIENT

A Taylor expansion of an arbitrary quantity ϕ_j around a particle i can be expressed as:

$$\phi_j = \phi_i + \nabla\phi|_i \cdot (\mathbf{r}_j - \mathbf{r}_i) + \mathcal{O}(\|\mathbf{r}_j - \mathbf{r}_i\|^2). \quad (2.5)$$

Eliminating the second order term, we can obtain the following relationship:

$$\nabla\phi|_i \cdot (\mathbf{r}_j - \mathbf{r}_i) = \phi_j - \phi_i. \quad (2.6)$$

With some algebraic manipulations we have

$$\nabla\phi|_i \cdot \frac{(\mathbf{r}_j - \mathbf{r}_i)}{\|\mathbf{r}_j - \mathbf{r}_i\|} = \frac{\phi_j - \phi_i}{\|\mathbf{r}_j - \mathbf{r}_i\|}, \quad (2.7)$$

$$\left[\nabla\phi|_i \cdot \frac{(\mathbf{r}_j - \mathbf{r}_i)}{\|\mathbf{r}_j - \mathbf{r}_i\|} \right] \frac{(\mathbf{r}_j - \mathbf{r}_i)}{\|\mathbf{r}_j - \mathbf{r}_i\|} = \frac{\phi_j - \phi_i}{\|\mathbf{r}_j - \mathbf{r}_i\|} \frac{(\mathbf{r}_j - \mathbf{r}_i)}{\|\mathbf{r}_j - \mathbf{r}_i\|}, \quad (2.8)$$

$$\nabla\phi|_i \left[\frac{(\mathbf{r}_j - \mathbf{r}_i)}{\|\mathbf{r}_j - \mathbf{r}_i\|} \otimes \frac{(\mathbf{r}_j - \mathbf{r}_i)}{\|\mathbf{r}_j - \mathbf{r}_i\|} \right] = \frac{\phi_j - \phi_i}{\|\mathbf{r}_j - \mathbf{r}_i\|} \frac{(\mathbf{r}_j - \mathbf{r}_i)}{\|\mathbf{r}_j - \mathbf{r}_i\|}, \quad (2.9)$$

where \otimes designates the tensor product.

Integrating Eq. (2.9) over \mathbb{R}^{dim} , where $dim = 1, 2, 3$ is the number of spatial dimensions, we find:

$$\nabla\phi|_i \int_{\mathbb{R}^{dim}} \frac{(\mathbf{r}_j - \mathbf{r}_i)}{\|\mathbf{r}_j - \mathbf{r}_i\|} \otimes \frac{(\mathbf{r}_j - \mathbf{r}_i)}{\|\mathbf{r}_j - \mathbf{r}_i\|} d\mathbf{r} = \int_{\mathbb{R}^{dim}} \frac{\phi_j - \phi_i}{\|\mathbf{r}_j - \mathbf{r}_i\|} \frac{(\mathbf{r}_j - \mathbf{r}_i)}{\|\mathbf{r}_j - \mathbf{r}_i\|} d\mathbf{r}. \quad (2.10)$$

Considering that the integrals over \mathbb{R}^{dim} are restricted to the compact domain \mathbb{P}_i , the integrals are approximated by a discrete weighted summation:

$$\nabla\phi|_i \left[\frac{1}{n^0} \sum_{j \in \mathbb{P}_i} \frac{(\mathbf{r}_j - \mathbf{r}_i)}{\|\mathbf{r}_j - \mathbf{r}_i\|} \otimes \frac{(\mathbf{r}_j - \mathbf{r}_i)}{\|\mathbf{r}_j - \mathbf{r}_i\|} \omega_{ij} \right] = \frac{1}{n^0} \sum_{j \in \mathbb{P}_i} \frac{\phi_j - \phi_i}{\|\mathbf{r}_j - \mathbf{r}_i\|} \frac{(\mathbf{r}_j - \mathbf{r}_i)}{\|\mathbf{r}_j - \mathbf{r}_i\|} \omega_{ij}, \quad (2.11)$$

$$\nabla\phi|_i = \left[\frac{1}{n^0} \sum_{j \in \mathbb{P}_i} \frac{(\mathbf{r}_j - \mathbf{r}_i)}{\|\mathbf{r}_j - \mathbf{r}_i\|} \otimes \frac{(\mathbf{r}_j - \mathbf{r}_i)}{\|\mathbf{r}_j - \mathbf{r}_i\|} \omega_{ij} \right]^{-1} \left(\frac{1}{n^0} \sum_{j \in \mathbb{P}_i} \frac{\phi_j - \phi_i}{\|\mathbf{r}_j - \mathbf{r}_i\|} \frac{(\mathbf{r}_j - \mathbf{r}_i)}{\|\mathbf{r}_j - \mathbf{r}_i\|} \omega_{ij} \right). \quad (2.12)$$

In the original MPS, the first term of the right-hand side of Eq. (2.12) is approximated by a correction coefficient related to the number of spatial dimensions $dim = 1, 2, 3$:

$$\left[\frac{1}{n^0} \sum_{j \in \mathbb{P}_i} \frac{(\mathbf{r}_j - \mathbf{r}_i)}{\|\mathbf{r}_j - \mathbf{r}_i\|} \otimes \frac{(\mathbf{r}_j - \mathbf{r}_i)}{\|\mathbf{r}_j - \mathbf{r}_i\|} \omega_{ij} \right] \approx \frac{1}{dim} \mathbf{I}, \quad (2.13)$$

where \mathbf{I} is the identity matrix, and the gradient of an arbitrary function ϕ in the particle i is approximated by:

$$\langle \nabla \phi \rangle_i = \frac{dim}{n^0} \sum_{j \in \mathbb{P}_i} \frac{\phi_j - \phi_i}{\|\mathbf{r}_j - \mathbf{r}_i\|} \frac{(\mathbf{r}_j - \mathbf{r}_i)}{\|\mathbf{r}_j - \mathbf{r}_i\|} \omega_{ij}, \quad (2.14)$$

$$\langle \nabla \phi \rangle_i = \frac{dim}{n^0} \sum_{j \in \mathbb{P}_i} \frac{\phi_j - \phi_i}{\|\mathbf{r}_{ij}\|^2} \mathbf{r}_{ij} \omega_{ij}, \quad (2.15)$$

where $\langle \ \rangle_i$ denotes discrete form, and n^0 is the initial value of n_i for a complete support of regular distributed neighbor particles.

2.2.2.3 DIVERGENCE

Based on a procedure similar to that used to obtain the gradient operator, the divergence of an arbitrary vector $\boldsymbol{\phi}_i$ was originally approximated by:

$$\langle \nabla \cdot \boldsymbol{\phi} \rangle_i = \frac{dim}{n^0} \sum_{j \in \mathbb{P}_i} \frac{\boldsymbol{\phi}_j - \boldsymbol{\phi}_i}{\|\mathbf{r}_{ij}\|^2} \cdot \mathbf{r}_{ij} \omega_{ij}. \quad (2.16)$$

2.2.2.4 ROTATIONAL

The rotational of an arbitrary vector $\boldsymbol{\phi}_i$ can be derived in a similar way of the gradient, and was originally approximated by:

$$\langle \nabla \times \boldsymbol{\phi} \rangle_i = \frac{dim}{n^0} \sum_{j \in \mathbb{P}_i} \frac{\boldsymbol{\phi}_j - \boldsymbol{\phi}_i}{\|\mathbf{r}_{ij}\|} \cdot \frac{\mathbf{s}_{ij}}{\|\mathbf{s}_{ij}\|} \omega_{ij}, \quad (2.17)$$

where \mathbf{s}_{ij} is a vector perpendicular to \mathbf{r}_{ij} .

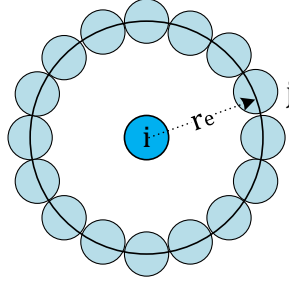
2.2.2.5 LAPLACIAN

The Laplacian operator of MPS can be derived following the works of Isshiki (2011) and Ng et al. (2014). Considering a 2D space, the Gauss divergence theorem is applied on a circular control volume, as depicted in Figure 2.2:

$$\int_{\Omega} \nabla^2 \phi \, d\Omega = \int_{\partial\Omega} \frac{\partial \phi}{\partial r} \, dl, \quad (2.18)$$

where Ω is a circle of radius r , and $\partial\Omega$ is the circular boundary. Here, the subscript i denotes the center of Ω and j are points uniformly distributed on $\partial\Omega$, the perimeter of Ω .

Figure 2.2 - Graphical representation of a circular control volume Ω with radius r_e .



Source: the author.

Assuming that r_{ij} is small, we have:

$$\langle \nabla^2 \phi \rangle_i \pi \| \mathbf{r}_{ij} \|^2 = \epsilon'(r_{ij}) \sum_{j \in \partial \Omega} \frac{\phi_j - \phi_i}{N_{ij}} \frac{2\pi \| \mathbf{r}_{ij} \|^2}{N_{ij}}, \quad (2.19)$$

where $\epsilon'(r_{ij})$ denotes a correction coefficient, and N_{ij} is the number of particles belonging to $\partial \Omega$.

Eq. (2.19) can be rewritten as:

$$N_{ij} \langle \nabla^2 \phi \rangle_i \| \mathbf{r}_{ij} \|^2 = \epsilon'(r_{ij}) \dim \sum_{j \in \partial \Omega} (\phi_j - \phi_i). \quad (2.20)$$

The introducing of the weight ω_{ij} on both sides of Eq. (2.20) yields:

$$N_{ij} \langle \nabla^2 \phi \rangle_i \| \mathbf{r}_{ij} \|^2 \omega_{ij} = \epsilon'(r_{ij}) \dim \sum_{j \in \partial \Omega} (\phi_j - \phi_i) \omega_{ij}. \quad (2.21)$$

Considering $\epsilon'(r_{ij})$ approximately a constant $\epsilon(r_e)$, Eq. (2.21) applied over the compact support \mathbb{P}_i , i.e., summing from $\| \mathbf{r}_{ij} \| = 0$ to $\| \mathbf{r}_{ij} \| = r_e$, gives:

$$\langle \nabla^2 \phi \rangle_i \sum_{j \in \mathbb{P}_i} \| \mathbf{r}_{ij} \|^2 \omega_{ij} = \epsilon(r_e) \dim \sum_{j \in \mathbb{P}_i} (\phi_j - \phi_i) \omega_{ij}, \quad (2.22)$$

$$\langle \nabla^2 \phi \rangle_i = \frac{\epsilon(r_e) \dim}{\sum_{j \in \mathbb{P}_i} \omega_{ij} \| \mathbf{r}_{ij} \|^2} \sum_{j \in \mathbb{P}_i} (\phi_j - \phi_i) \omega_{ij}. \quad (2.23)$$

The correction constant $\epsilon(r_e)$ is approximated by 2 in MPS to compensate for the error generated due to the one-sided differencing scheme applied for the approximation of radial derivative at the circular boundary $\partial \Omega$ (Ng et al., 2014). Consequently, Eq. (2.23) can be rewritten as:

$$\langle \nabla^2 \phi \rangle_i = \frac{2 \dim}{\lambda_i n^0} \sum_{j \in \mathbb{P}_i} (\phi_j - \phi_i) \omega_{ij}. \quad (2.24)$$

with

$$\lambda_i = \frac{\sum_{j \in \mathbb{P}_i} \omega_{ij} \|\mathbf{r}_{ij}\|^2}{\sum_{j \in \mathbb{P}_i} \omega_{ij}}. \quad (2.25)$$

Here, λ_i is a correction parameter by which the variance increase is equal to that of the analytical solution:

$$\lambda = \frac{\left(\int_{\mathbb{R}^{dim}} \omega(\mathbf{r}) \|\mathbf{r}\|^2 d\mathbf{r} \right)}{\left(\int_{\mathbb{R}^{dim}} \omega(\mathbf{r}) d\mathbf{r} \right)}. \quad (2.26)$$

In order to solve the Eqs. (2.1) and (2.2), the differential operators, namely pressure gradient, divergence of velocity and Laplacian of velocity, need to be approximated in MPS. The formulations adopted in this work are presented below.

2.2.2.6 PRESSURE GRADIENT

To prevent instability issue due to the particle clustering, avoiding unstable behavior when attracting forces act between particles, the pressure gradient reads (Koshizuka & Oka, 1996):

$$\langle \nabla P \rangle_i = \frac{dim}{n^0} \sum_{j \in \mathbb{P}_i} \frac{P_j - \hat{P}_i}{\|\mathbf{r}_{ij}\|^2} \mathbf{r}_{ij} \omega_{ij}, \quad (2.27)$$

where \hat{P}_i is the minimum pressure belonging the neighborhood of the i -th particle, i.e., $\hat{P}_i = \min_{j \in \mathbb{P}_i} (P_j, P_i)$. This pressure gradient can be decomposed into the following form:

$$\langle \nabla P \rangle_i = \frac{dim}{n^0} \sum_{j \in \mathbb{P}_i} \frac{P_j - P_i}{\|\mathbf{r}_{ij}\|^2} \mathbf{r}_{ij} \omega_{ij} + \frac{dim}{n^0} (P_i - \hat{P}_i) \sum_{j \in \mathbb{P}_i} \frac{\mathbf{r}_{ij}}{\|\mathbf{r}_{ij}\|^2} \omega_{ij}. \quad (2.28)$$

As reported by Duan et al. (2017), the first part of Eq. (2.28) corresponds to the original gradient model (see Eq. (2.15)) and the second part is a particle stabilizing term (PST), which forces particles from regions of high concentration to regions of low concentration, since $P_i - \hat{P}_i$ always give positive values. Therefore, PST is essential to avoid non-uniform distribution of particles and prevent numerical instability in MPS.

As previous reported by some authors (Khayyer et al., 2017; Wang et al., 2017), the energy conservation properties of particle-based methods are shown to be directly related to Taylor series consistency of pressure gradient models. In this way, instead the 0th order gradient, see Eq. (2.27), higher order and conservative operators were proposed.

Wang et al. (2017) proposed the 1st order pressure gradient based on a Taylor series expansion:

$$\langle \nabla P \rangle_i = \left[\sum_{j \in \mathbb{P}_i} \omega_{ij} \frac{\mathbf{r}_{ij}}{\|\mathbf{r}_{ij}\|} \otimes \frac{\mathbf{r}_{ij}^T}{\|\mathbf{r}_{ij}\|} \right]^{-1} \left[\sum_{j \in \mathbb{P}_i} \frac{P_j - \hat{P}_i}{\|\mathbf{r}_{ij}\|^2} \mathbf{r}_{ij} \omega_{ij} \right]. \quad (2.29)$$

In order to produce an antisymmetric momentum equation, Jandaghian and Shakibaeinia (2020) proposed the following pressure gradient:

$$\langle \nabla P \rangle_i = \frac{dim}{n^0} \sum_{j \in \mathbb{P}_i} \left(\frac{n_i}{n_j} P_j + \frac{n_j}{n_i} P_i \right) \frac{\mathbf{r}_{ij}}{\|\mathbf{r}_{ij}\|^2} \omega_{ij}. \quad (2.30)$$

2.2.2.7 DIVERGENCE OF VELOCITY

With respect to the divergence of the velocity, the original formulation reads:

$$\langle \nabla \cdot \mathbf{u} \rangle_i = \frac{dim}{n^0} \sum_{j \in \mathbb{P}_i} \frac{(\mathbf{u}_j - \mathbf{u}_i) \cdot \mathbf{r}_{ij}}{\|\mathbf{r}_{ij}\|^2} \omega_{ij}, \quad (2.31)$$

whereas in (Jandaghian & Shakibaeinia, 2020) it is approximated by:

$$\langle \nabla \cdot \mathbf{u} \rangle_i = \frac{dim}{n^0} \sum_{j \in \mathbb{P}_i} \left(\frac{n_j}{n_i} \right) \frac{(\mathbf{u}_j - \mathbf{u}_i) \cdot \mathbf{r}_{ij}}{\|\mathbf{r}_{ij}\|^2} \omega_{ij}. \quad (2.32)$$

2.2.2.8 LAPLACIAN OF VELOCITY AND PRESSURE

Finally, the original Laplacian of velocity (vector) and pressure (scalar) are approximated by:

$$\langle \nabla^2 \mathbf{u} \rangle_i = \frac{2dim}{\lambda^0 n^0} \sum_{j \in \mathbb{P}_i} (\mathbf{u}_j - \mathbf{u}_i) \omega_{ij}, \quad (2.33)$$

$$\langle \nabla^2 P \rangle_i = \frac{2dim}{\lambda^0 n^0} \sum_{j \in \mathbb{P}_i} (P_j - P_i) \omega_{ij}. \quad (2.34)$$

2.2.3 NUMERICAL MODELING OF THE BOUNDARY CONDITIONS

2.2.3.1 RIGID WALL

Solid wall boundary is originally modeled using some layers of fixed particles, see Figure 2.3(a). In this work we adopted three layers of particles so that we ensure a good balance between accuracy and computational cost of the numerical operators using the effective radius $2.1l_0 \leq r_e \leq 4.0l_0$. The particles that form the layer in contact with the fluid are denominated wall particles, of which the pressure is computed together with the fluid particles. The particles that form two other layers are denominated dummy particles. Dummy particles are used to assure the correct calculation of the particle number density of the wall particles. Pressure is not calculated in the dummy particles, although this pressure can be extrapolated, which is explained later. As boundary condition of rigid wall of fixed or moving bodies, zero relative velocity of the fluid and the wall is imposed.

2.2.3.2 FREE SURFACE

In the particle-based methods, the kinematic boundary condition of a free surface is directly satisfied by the motion of the free-surface particles. On the other hand, the dynamic boundary condition is imposed by applying the Dirichlet condition $P_{fs} = P_{atm} = 0$, where P_{fs} is the pressure at free-surface particles and P_{atm} stands for the atmospheric pressure.

In order to identify the free-surface particles, the neighborhood particles centroid deviation (NCPD) technique (Tsukamoto et al., 2016) is used in all the simulations carried out in the present study. Figure 2.3(b) shows the main idea behind the NCPD method, i.e., the resultant weighted deviation vector. In the NCPD technique, a particle is defined as a free-surface one and its pressure is set to zero when

$$\begin{cases} n_i < \beta \cdot n^0 \\ \sigma_i > \varrho \cdot l_0 \end{cases} \quad (2.35)$$

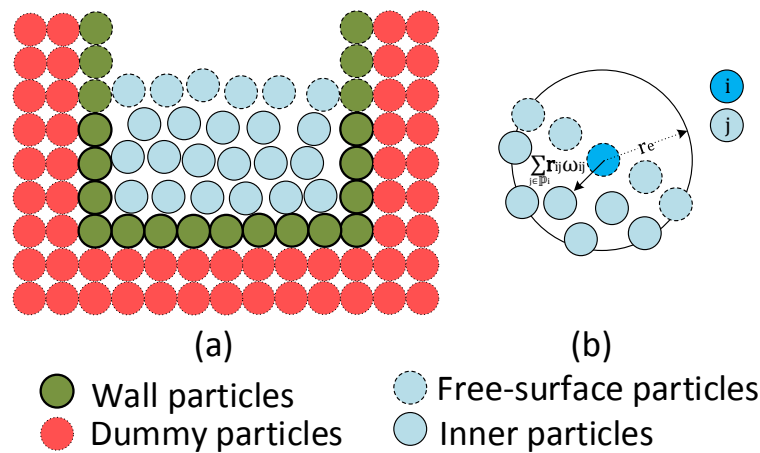
The deviation σ_i is calculated as:

$$\sigma_i = \frac{|\sum_{j \in \mathbb{P}_i} (\omega_{ij} \mathbf{r}_{ij})|}{\sum_{j \in \mathbb{P}_i} \omega_{ij}} = \frac{\sqrt{(\sum_{j \in \mathbb{P}_i} \omega_{ij} x_{ij})^2 + (\sum_{j \in \mathbb{P}_i} \omega_{ij} y_{ij})^2 + (\sum_{j \in \mathbb{P}_i} \omega_{ij} z_{ij})^2}}{\sum_{j \in \mathbb{P}_i} \omega_{ij}}, \quad (2.36)$$

where $x_{ij} = (x_j - x_i)$, $y_{ij} = (y_j - y_i)$ and $z_{ij} = (z_j - z_i)$.

The constant β_1 can be chosen in the range $\beta_1 \in [0.80, 0.99]$ (Koshizuka & Oka, 1996) and ϱ_1 higher of 0.2, $\varrho_1 \in [0.2, \infty)$ (Tsukamoto et al., 2016). The values of $\beta_1 = 0.98$ and $\varrho_1 = 0.2$ are used for all simulations performed herein. The particles that are not assigned as free surface are called inner particles in present work.

Figure 2.3 - Boundary conditions in 2D space. (a) Fluid particles and solid wall modeled by wall and dummy particles. (b) Free-surface particles: resultant weighted deviation vector.



Source: the author.

As the particles defined as free surface have the pressure fixed by zero following the Dirichlet dynamic boundary condition, and its neighbor is not enough to proper calculation of the differential operators, the pressure gradient is not taken into account for these particles. Thus, a collision model is required to adjust the distances between free-surface particles. The collision model is applied after the explicit first stage of the MPS method, and a repulsive variation of velocity for fluid particles is enforced by:

$$\Delta \mathbf{u}_i = \begin{cases} \sum_{j \in \mathbb{P}_i} \frac{(1 + \alpha_2) \mathbf{r}_{ij} \cdot \mathbf{u}_{ij}}{\alpha_3} \frac{\mathbf{r}_{ij}}{\|\mathbf{r}_{ij}\|} & \|\mathbf{r}_{ij}\| \leq \alpha_1 l_o \quad \text{and} \quad \mathbf{r}_{ij} \cdot \mathbf{u}_{ij} < 0, \\ 0 & \text{otherwise} \end{cases}, \quad (2.37)$$

where, according to Lee et al. (2011), values of $\alpha_1 \geq 0.8$ and $\alpha_2 \leq 0.2$ increase the spatial stability in simulations. For all cases analyzed herein, the coefficients α_1 and α_2 are set to 0.8 and 0.2, respectively. If the neighbor particle j is fluid then $\alpha_3 = 2$, otherwise $\alpha_3 = 1$.

2.2.4 ALGORITHM

At first, predictions of the particle's velocity and position are carried out explicitly by using viscosity and external forces terms of the momentum conservation (Eq. (2.2)):

$$\mathbf{u}_i^* = \mathbf{u}_i^t + [\nu_f \langle \nabla^2 \mathbf{u} \rangle_i + \mathcal{F}_b]^t \Delta t, \quad (2.38)$$

$$\mathbf{r}_i^* = \mathbf{r}_i^t + \mathbf{u}_i^* \Delta t. \quad (2.39)$$

After the prediction of velocities and positions of the fluid particles, a collision model is applied to fluid particles located in the free surface, avoiding clustering of particles, and the contribution $\Delta \mathbf{u}^*$, see Eq. (2.37), is added:

$$\mathbf{u}_i^{**} = \mathbf{u}_i^* + \Delta \mathbf{u}_i^*, \quad (2.40)$$

$$\mathbf{r}_i^{**} = \mathbf{r}_i^* + \Delta \mathbf{u}_i^* \Delta t, \quad (2.41)$$

The term $\Delta \mathbf{u}_i^*$ is set to zero when i is an inner particle.

Then the pressures of all fluid and wall particles can be calculated by (1) or (2):

- (1) solving the pressure Poisson equation (PPE) implicitly in the original incompressible MPS (Koshizuka & Oka, 1996);
- (2) an equation of state (EOS) explicitly computed in the weakly-compressible moving particle semi-implicit (WC-MPS) (Shakibaenia & Jin, 2010).

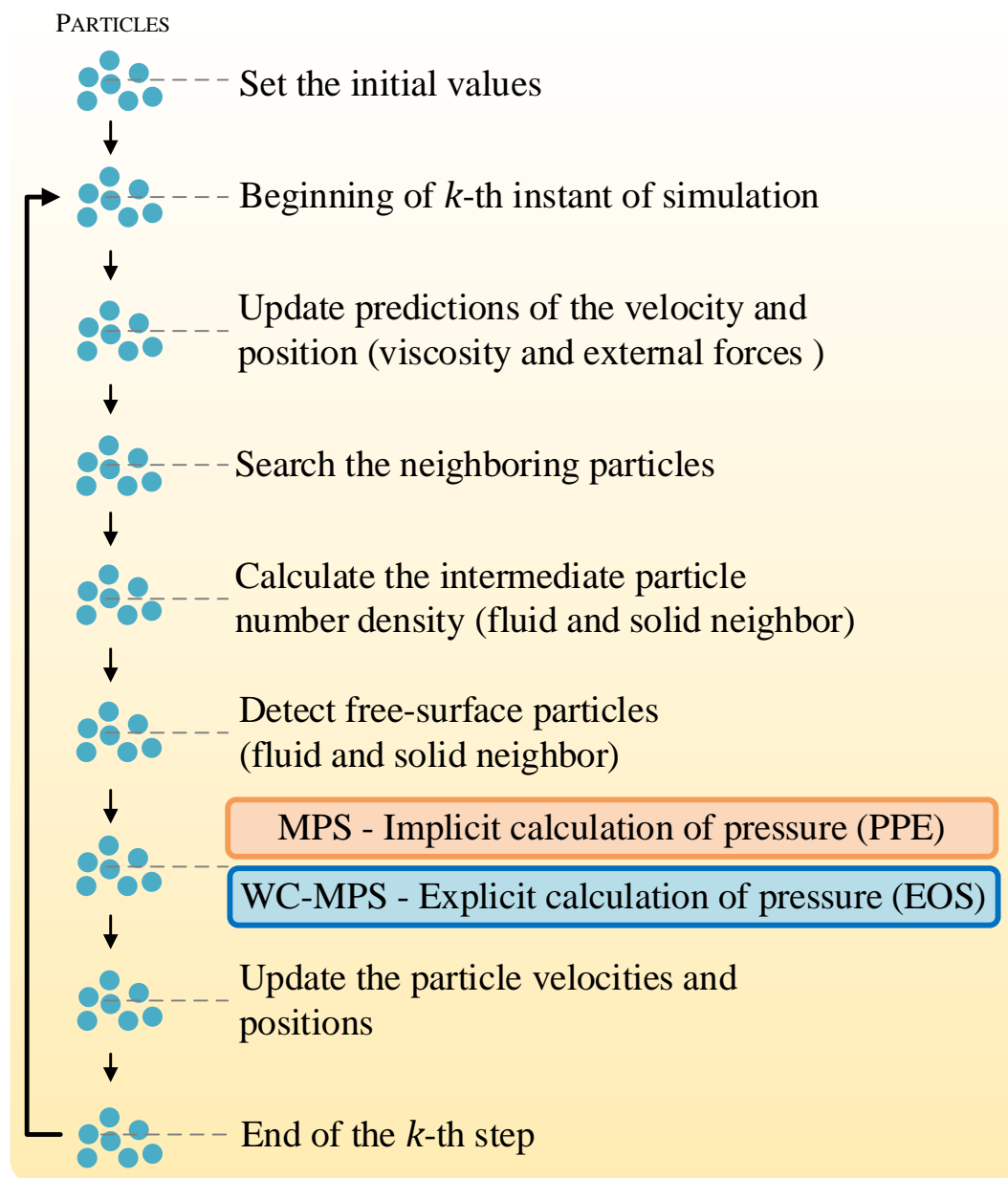
Finally, the velocity of the fluid particles is updated by using the pressure gradient term of the momentum conservation (see Eq. (2.2)) and the new positions of the particles can be obtained:

$$\mathbf{u}_i^{t+\Delta t} = \mathbf{u}_i^{**} - \frac{\Delta t}{\rho_f} \langle \nabla P \rangle_i^{t+\Delta t}, \quad (2.42)$$

$$\mathbf{r}_i^{t+\Delta t} = \mathbf{r}_i^{**} + (\mathbf{u}_i^{t+\Delta t} - \mathbf{u}_i^{**})\Delta t. \quad (2.43)$$

Figure 2.4 shows a schematic diagram of the calculation procedures for one time step using the MPS or WC-MPS methods.

Figure 2.4 - Schematic diagram during a time step using the MPS or WC-MPS.



Source: the author.

2.3 INCOMPRESSIBLE MOVING PARTICLE SEMI-IMPLICIT (MPS)

To solve the incompressible viscous flow, a semi-implicit algorithm is used in the original MPS method, which is similar to the projection method (Harlow & Welch, 1965; Chorin, 1967; Temam, 1969). The theory behind the projection method is the Helmholtz-Hodge decomposition, which states that any vector field can be decomposed into a divergence-free component and the gradient of a curl-free component. One of the critical points in this semi-implicit algorithm is to solve a pressure Poisson equation (PPE), that leads to the numerical computation of a very large linear system in every time step. In this way, significant progress has been made in the implementation of particle-based methods in massive parallel processing in clusters of central processing units (CPUs) comprising thousands of compute nodes with each node containing multiple cores (Fernandes et al., 2015; Guo et al., 2018), or the emerging hardware such as graphics processing units (GPUs) (Hori et al., 2011; Chow et al., 2018).

Taking the divergence of both side of Eq. (2.42), we obtain the following equation:

$$\langle \nabla \cdot \mathbf{u} \rangle_i^{t+\Delta t} = \langle \nabla \cdot \mathbf{u} \rangle_i^{**} - \langle \nabla \cdot \frac{\Delta t}{\rho_f} \langle \nabla P \rangle \rangle_i^{t+\Delta t}. \quad (2.44)$$

Considering the incompressible constraint of Eq. (2.1) at the final of the step $t + \Delta t$, i.e., $\langle \nabla \cdot \mathbf{u} \rangle_i^{t+\Delta t} = 0$, Eq. (2.44) is rewritten as a pressure Poisson equation (PPE):

$$\langle \nabla^2 P \rangle_i^{t+\Delta t} = \frac{\rho_f}{\Delta t} \langle \nabla \cdot \mathbf{u} \rangle_i^{**}. \quad (2.45)$$

After the prediction of velocities and positions, Eq. (2.1) can be approximated by:

$$\left. \frac{D\rho}{Dt} \right|_i^{**} + \rho_f \langle \nabla \cdot \mathbf{u} \rangle_i^{**} = \frac{\rho_i^{**} - \rho_f}{\Delta t} + \rho_f \langle \nabla \cdot \mathbf{u} \rangle_i^{**} = 0, \quad (2.46)$$

where the material derivative of fluid density $\frac{D\rho}{Dt}$ was approximated by the forward Euler method.

The relation between the fluid density ρ_i^{**} and the particle number density n_i^{**} at the particle i is given by (Koshizuka et al., 1998):

$$\frac{n_i^{**}}{n^0} = \frac{\rho_i^{**}}{\rho_f} = \frac{\rho_i^{**}}{\rho^0}, \quad (2.47)$$

where n^0 stands for the constant particle number density computed considering a fully compact support with an initial regular arrangement of particles and $\rho^0 = \rho_f$ is the reference density. Using Eq. (2.47) in Eq. (2.46), we have:

$$\langle \nabla \cdot \mathbf{u} \rangle_i^{**} = -\frac{1}{\Delta t} \frac{n_i^{**} - n^0}{n^0}. \quad (2.48)$$

Then, by substituting the Eq. (2.48) for the right-hand side of Eq. (2.45), the pressures of all fluid and wall particles can be calculated by solving the PPE considering the particle number density (PND) criterion as follows (Koshizuka & Oka, 1996):

$$\langle \nabla^2 P \rangle_i^{t+\Delta t} = \frac{\rho_f}{\Delta t^2} \frac{n^0 - n_i^{**}}{n^0}, \quad (2.49)$$

where Δt is the time step, n_i^{**} stands for the particle number density calculated based on the displacement of particles obtained in the explicit calculations.

A relaxation coefficient $\gamma < 1.0$ is normally introduced to the PPE:

$$\langle \nabla^2 P \rangle_i^{t+\Delta t} = \gamma \frac{\rho_f}{\Delta t^2} \frac{n^0 - n_i^{**}}{n^0}. \quad (2.50)$$

The idea behind the adoption of relaxation or damping coefficients is to enforce the incompressibility condition in a robust way, while suppressing spurious oscillations in the discrete PPE. Besides a detailed description, Henshaw and Kreiss (1995) and Li (2020) showed that the accuracy of a numerical method can be assured by adopting a properly tuned damping coefficient if using split-step strategy, the so-called split-step finite-difference scheme (Henshaw & Petersson, 2003), in the same manner as projection methods.

Another incompressible condition was proposed by Tanaka and Matsunaga (2010):

$$\langle \nabla^2 P \rangle_i^{t+\Delta t} = \gamma \frac{\rho_f}{\Delta t^2} \left(\frac{n^0 - n_i^t}{n^0} \right) + (1 - \gamma) \frac{\rho_f}{\Delta t} \langle \nabla \cdot \mathbf{u} \rangle_i^{**}. \quad (2.51)$$

The first term of the right-hand side refers to the accumulative density deviations, i.e., the deviation of particle number density at the current instant (n_i^t) from that obtained for a fully filled compact support at the initial of the simulation (n^0). On the other hand, the second term, i.e., the divergence of velocity, designates the instantaneous time variation of particle density at the current instant t (Gotoh et al., 2014) and here is calculated by Eq. (2.31).

Eqs. (2.50) and (2.51) are solved as a linear matrix system in the form of $[\mathbf{A}]\mathbf{x} = \mathbf{b}$, as follows:

$$\frac{2dim}{\lambda^0 n^0} \begin{bmatrix} -\sum_{j \in \mathbb{P}_1} \omega_{1,j} & \cdots & \omega_{1,i-1} & \omega_{1,i} & \omega_{1,i+1} & \cdots & \omega_{1,N} \\ \vdots & \ddots & \vdots & \vdots & \vdots & \ddots & \vdots \\ \omega_{i-1,1} & \cdots & -\sum_{j \in \mathbb{P}_{i-1}} \omega_{i-1,j} & \omega_{i-1,i} & \omega_{i-1,i+1} & \cdots & \omega_{i-1,N} \\ \omega_{i,1} & \cdots & \omega_{i,i-1} & -\sum_{j \in \mathbb{P}_i} \omega_{i,j} & \omega_{i,i+1} & \cdots & \omega_{i,N} \\ \omega_{i+1,1} & \cdots & \omega_{i+1,i-1} & \omega_{i+1,i} & -\sum_{j \in \mathbb{P}_{i+1}} \omega_{i+1,j} & \cdots & \omega_{i+1,N} \\ \vdots & \ddots & \vdots & \vdots & \vdots & \ddots & \vdots \\ \omega_{N,1} & \cdots & \omega_{N,i-1} & \omega_{N,i} & \omega_{N,i+1} & \cdots & -\sum_{j \in \mathbb{P}_N} \omega_{N,j} \end{bmatrix} \begin{bmatrix} P_1 \\ \vdots \\ P_{i-1} \\ P_i \\ P_{i+1} \\ \vdots \\ P_N \end{bmatrix}^{t+\Delta t} = \begin{bmatrix} b_1 \\ \vdots \\ b_{i-1} \\ b_i \\ b_{i+1} \\ \vdots \\ b_N \end{bmatrix}, \quad (2.52)$$

where the source term of Eq. (2.50) reads:

$$\begin{Bmatrix} b_1 \\ \vdots \\ b_{i-1} \\ b_i \\ b_{i+1} \\ \vdots \\ b_N \end{Bmatrix} = \gamma \frac{\rho_f}{\Delta t^2 n^0} \begin{Bmatrix} n^0 - n_1^{**} \\ \vdots \\ n^0 - n_{i-1}^{**} \\ n^0 - n_i^{**} \\ n^0 - n_{i+1}^{**} \\ \vdots \\ n^0 - n_N^{**} \end{Bmatrix}, \quad (2.53)$$

and the source term of Eq. (2.51) is:

$$\begin{Bmatrix} b_1 \\ \vdots \\ b_{i-1} \\ b_i \\ b_{i+1} \\ \vdots \\ b_N \end{Bmatrix} = \gamma \frac{\rho_f}{\Delta t^2 n^0} \begin{Bmatrix} n^0 - n_1^t \\ \vdots \\ n^0 - n_{i-1}^t \\ n^0 - n_i^t \\ n^0 - n_{i+1}^t \\ \vdots \\ n^0 - n_N^t \end{Bmatrix} + (1 - \gamma) \frac{\rho_f \dim}{\Delta t n^0} \left\{ \begin{array}{l} \sum_{j \in \mathbb{P}_1} \frac{(\mathbf{u}_j - \mathbf{u}_1) \cdot (\mathbf{r}_j - \mathbf{r}_1)}{\|\mathbf{r}_j - \mathbf{r}_1\|^2} \omega_{1j} \\ \vdots \\ \sum_{j \in \mathbb{P}_{i-1}} \frac{(\mathbf{u}_j - \mathbf{u}_{i-1}) \cdot (\mathbf{r}_j - \mathbf{r}_{i-1})}{\|\mathbf{r}_j - \mathbf{r}_{i-1}\|^2} \omega_{i-1j} \\ \sum_{j \in \mathbb{P}_i} \frac{(\mathbf{u}_j - \mathbf{u}_i) \cdot (\mathbf{r}_j - \mathbf{r}_i)}{\|\mathbf{r}_j - \mathbf{r}_i\|^2} \omega_{ij} \\ \sum_{j \in \mathbb{P}_{i+1}} \frac{(\mathbf{u}_j - \mathbf{u}_{i+1}) \cdot (\mathbf{r}_j - \mathbf{r}_{i+1})}{\|\mathbf{r}_j - \mathbf{r}_{i+1}\|^2} \omega_{i+1j} \\ \vdots \\ \sum_{j \in \mathbb{P}_N} \frac{(\mathbf{u}_j - \mathbf{u}_N) \cdot (\mathbf{r}_j - \mathbf{r}_N)}{\|\mathbf{r}_j - \mathbf{r}_N\|^2} \omega_{Nj} \end{array} \right\}^{**}. \quad (2.54)$$

With certain boundary conditions, the above linear system of equations may be efficiently solved by using an iterative method, such as the conjugate gradient (CG), Jacobi, and generalized minimum residual (GMRES) methods. In the present work, the conjugate gradient (CG) method is used to solve the linear equation of PPE in a CPU-based code.

The nonhomogeneous Neumann boundary condition of pressure is applied at rigid walls and the pressure of a dummy particle j can be approximated by:

$$P_j = P_i + \|\mathbf{r}_{ij}\| \left. \frac{\partial P}{\partial n} \right|_{\partial \Omega_{\text{wall}}}, \quad (2.55)$$

with the following simplified relation (Matsunaga et al., 2020):

$$\left. \frac{\partial P}{\partial n} \right|_{\partial \Omega_{\text{wall}}} = \rho \mathbf{n}|_{\partial \Omega_{\text{wall}}} \cdot \mathbf{g} \approx \rho \frac{\mathbf{r}_{ij}}{\|\mathbf{r}_{ij}\|} \cdot \mathbf{g}. \quad (2.56)$$

Then, Eq. (2.55) is included in the PPE.

For simplicity and to be more clear with our explanation, only one row of the linear system (2.52), i.e., equations related to a target i -th particle, will hereafter be written. The inclusion of Eq. (2.55) in the PPE using the source term of Eq. (2.50) is rewritten as:

$$\frac{2 \dim}{\lambda^0 n^0} \sum_{j \in \mathbb{P}_i} (P_j^{t+\Delta t} - P_i^{t+\Delta t}) \omega_{ij} = - \frac{2 \dim}{\lambda^0 n^0} \sum_{j \in \mathbb{D}_i} \rho \mathbf{r}_{ij}^{**} \cdot \mathbf{g} \omega_{ij} + \gamma \frac{\rho_f}{\Delta t^2} \left(\frac{n^0 - n_i^{**}}{n^0} \right), \quad (2.57)$$

and adopting the source term of Eq. (2.51) reads:

$$\frac{2dim}{\lambda^0 n^0} \sum_{j \in \mathbb{P}_i} (P_j^{t+\Delta t} - P_i^{t+\Delta t}) \omega_{ij} = -\frac{2dim}{\lambda^0 n^0} \sum_{j \in \mathbb{D}_i} \rho \mathbf{r}_{ij}^{**} \cdot \mathbf{g} \omega_{ij} + \gamma \frac{\rho_f}{\Delta t^2} \left(\frac{n^0 - n_i^t}{n^0} \right) + (1 - \gamma) \frac{\rho_f}{\Delta t} \frac{dim}{n^0} \sum_{j \in \mathbb{P}_i} \frac{\mathbf{u}_{ij}^{**} \cdot \mathbf{r}_{ij}^{**}}{\|\mathbf{r}_{ij}^{**}\|^2} \omega_{ij}, \quad (2.58)$$

where \mathbb{D}_i stands for the neighboring dummy particles.

Finally, in order to improve the stability of the computation method it is possible to introduce a slight linear compressibility in the PPE. Ikeda (1999) proposed the following deviation of particle number density:

$$\left. \frac{1}{\Delta t} \frac{D\rho}{Dt} \right|_i^{**} \approx -\frac{\rho_f}{\Delta t^2} \left(\frac{n^{t+\Delta t} - n_i^{**}}{n^0} \right), \quad (2.59)$$

with the linear relation

$$n^{t+\Delta t} = n^0 + \frac{n^0}{\rho_f} \frac{\partial \rho}{\partial P} P^{t+\Delta t}. \quad (2.60)$$

Let us define the artificial compressibility factor

$$\alpha_c = \frac{1}{\rho_f} \frac{\partial \rho}{\partial P}. \quad (2.61)$$

Substituting Eqs. (2.60) and (2.61) into Eq. (2.59), the Eq. (2.57) becomes:

$$\begin{aligned} & \frac{2dim}{\lambda^0 n^0} \sum_{j \in \mathbb{P}_i} \left[P_j^{t+\Delta t} - \left(1 + \alpha_c \frac{\rho_f \lambda^0 n^0}{\Delta t^2 2dim} \right) P_i^{t+\Delta t} \right] \omega_{ij} = \\ & -\frac{2dim}{\lambda^0 n^0} \sum_{j \in \mathbb{D}_i} \rho \mathbf{r}_{ij}^{**} \cdot \mathbf{g} \omega_{ij} + \gamma \frac{\rho_f}{\Delta t^2} \left(\frac{n^0 - n_i^{**}}{n^0} \right), \end{aligned} \quad (2.62)$$

and the Eq. (2.58) can be expressed as:

$$\begin{aligned} & \frac{2dim}{\lambda^0 n^0} \sum_{j \in \mathbb{P}_i} \left[P_j^{t+\Delta t} - \left(1 + \alpha_c \frac{\rho_f \lambda^0 n^0}{\Delta t^2 2dim} \right) P_i^{t+\Delta t} \right] \omega_{ij} = \\ & -\frac{2dim}{\lambda^0 n^0} \sum_{j \in \mathbb{D}_i} \rho \mathbf{r}_{ij}^{**} \cdot \mathbf{g} \omega_{ij} + \gamma \frac{\rho_f}{\Delta t^2} \left(\frac{n^0 - n_i^t}{n^0} \right) + (1 - \gamma) \frac{\rho_f}{\Delta t} \frac{dim}{n^0} \sum_{j \in \mathbb{P}_i} \frac{\mathbf{u}_{ij}^{**} \cdot \mathbf{r}_{ij}^{**}}{\|\mathbf{r}_{ij}^{**}\|^2} \omega_{ij}. \end{aligned} \quad (2.63)$$

The introduction of α_c leads to a diagonal dominant matrix. Generally, this diagonal dominance results in a faster convergence of the iterative solver and make the simulation more stable. The coefficient α_c should be selected as small as possible, but keep in mind that it implies in slight compressibility.

2.4 WEAKLY-COMPRESSIBLE MOVING PARTICLE SEMI-IMPLICIT (WC-MPS)

In the present work, an enhanced weakly-compressible moving particle semi-implicit (WC-MPS) method is adopted to solve the hydrodynamic equations of Newtonian free-surface flow. Instead of the solution of simultaneous linear equations in the PPE, an equation of state in a fully explicit form is solved in the WC-MPS. In this sense, while the solver of the linear system in incompressible MPS might be very costly in each time step, the absence of a linear system to be solved in WC-MPS reduces remarkably computational costs per time step. However, whereas the time step of hydrodynamics simulations is limited by the maximum computed velocity in the incompressible MPS, the time step is limited by the speed of sound in WC-MPS, and generally lower time steps are required. Therefore, compared to the semi-implicit MPS, the fully explicit WC-MPS simulations typically require a larger number of temporal integrations for each physical time. Moreover, thanks to its fully explicit algorithm, the implementation of parallel computing technique is relatively straightforward in explicit particle methods and easy to obtain a high-performance efficiency by applying GPU calculations.

For fully explicit methods, the directly calculation using the weight function, see Eq. (2.4), inevitably leads to a more noisy particle number density estimation given that one is more sensitive to small changes in the local distribution of the particles (Price, 2012). Consequently, since the pressure is directly evaluated from the n_i in the WC-MPS, a smoother particle number density field leads to a smoother pressure field. In this way, aiming to overcome excessive non-physical pressure oscillations, here the particle number density n_i is obtained by using the continuity equation (2.1) including a diffusive term, similar to that originally proposed by Molteni and Colagrossi (2009) on the so-called delta-SPH (δ -SPH) method, and recently adapted for the WC-MPS in Jandaghian and Shakibaeinia (2020).

The relation between the fluid density ρ_i and the particle number density n_i at the particle i is given by (Koshizuka et al., 1998):

$$\frac{n_i}{n^0} = \frac{\rho_i}{\rho^0}, \quad (2.64)$$

where n^0 stands for the constant particle number density computed considering a fully compact support with an initial cubic arrangement of particles and ρ^0 denotes for the reference fluid density.

Substituting Eq. (2.64) into the discrete version of Eq. (2.1), we obtain:

$$\frac{1}{n_i} \frac{Dn_i}{Dt} = -\langle \nabla \cdot \mathbf{u} \rangle_i. \quad (2.65)$$

Inspired by the work of Fernández-Gutiérrez and Zohdi (2020), a diffusive term D_i related to the Laplacian of the pressure is added in the smoothed continuity equation as follows:

$$\frac{1}{n_i} \frac{Dn_i}{Dt} = -\langle \nabla \cdot \mathbf{u} \rangle_i + D_i, \quad (2.66)$$

with D_i given by:

$$D_i = \frac{\Delta t}{\rho} \frac{2dim}{\lambda^0 n^0} \sum_{j \in \mathbb{P}_i} [P_j - P_i - (-\rho_f \mathbf{g} \cdot \mathbf{r}_{ij})] \omega_{ij}, \quad (2.67)$$

where Δt denotes the time step, $dim = 1, 2, 3$ is the number of spatial dimensions, \mathbf{g} represents the gravity acceleration vector and λ^0 refers to a correction parameter that provide consistency between the variance increase of above Laplacian to that of the analytical solution. In Eq. (2.67), $P_j - P_i$ quantifies the dynamic pressures, whereas $-\rho_f \mathbf{g} \cdot \mathbf{r}_{ij}$ denotes the hydrostatic component.

As pointed out in Fernández-Gutiérrez and Zohdi (2020), physically, D_i smooths the natural density field from the pressure jump, effectively suppressing the induced sound wave, and no tuning parameter is required in Eq. (2.66). It should be highlighted that the effectiveness of this pure numerical correction shall reduce by increasing the spatial resolution (Antuono et al., 2012; Meringolo et al., 2019).

With respect to the divergence of the velocity in Eq. (2.66), it is approximated by Eq. (2.32). Instead of the fully incompressible model considered in the original MPS, the WC-MPS assumes a slightly compressible flow. Then, in order to couple the continuity (2.1) and momentum (2.2) equations, the Tait's equation of state (EOS) is explicitly calculated providing the pressure of a i -th fluid particle (Shakibaeinia & Jin, 2010):

$$p_i^{t+\Delta t} = \frac{\rho_f c_0^2}{\gamma_p} \left[\left(\frac{n_i^*}{n^0} \right)^{\gamma_p} - 1 \right], \quad (2.68)$$

where $c_0 = \sqrt{\partial P / \partial \rho}$ stands for the speed of sound in the reference density, the polytropic index $\gamma_p = 7$ is a typical value adopted for fluid phase and n_i^* is the particle number density calculated after the prediction process. An artificial speed of sound is usually used to prevent numerical instabilities and extremely small time steps. Following the previous work of Monaghan (1994), c_0 is chosen about ten times the maximum velocity to keep the density variations less than 1%, i.e., Mach number $Ma < 0.1$.

2.5 STABILIZATION TECHNIQUE

To reduce the discrepancy between the particle number densities n_i^{**} and n^0 , then improving the numerical stabilization and maintaining the incompressibility in the particle methods, the particle shifting governed by Fick's law of diffusion, as proposed by Lind et al. (2012) in SPH, can be adopted as:

$$\Delta \mathbf{r}_i^{\text{new}} = \begin{cases} -F_i \langle \nabla C \rangle_i^{\text{new}} & \text{inner particle} \\ 0 & \text{otherwise} \end{cases}, \quad (2.69)$$

where $F_i = A_F l_0^2 C_r Ma$. A_F is a dimensionless number in the range $A_F \in [1, 6]$, C_r denotes the Courant number and Ma represents the Mach number.

Then, at the end of each time step, $\Delta \mathbf{r}_i^{\text{new}}$ is imposed to inner fluid particles, i.e., no free-surface, and the final position is adjusted as:

$$\mathbf{r}_i^{t+\Delta t} = \mathbf{r}_i^{\text{new}} - \Delta \mathbf{r}_i^{\text{new}}. \quad (2.70)$$

In MPS, the particle concentration (volume fraction) at a target particle i can be obtained as:

$$C_i = \frac{\sum_{j \in \mathbb{P}_i} \omega_{ij}}{n^0}. \quad (2.71)$$

The gradient of the concentration is approximated by (Jandaghian & Shakibaeinia, 2020):

$$\langle \nabla C \rangle_i = \frac{dim}{n^0} \sum_{j \in \mathbb{P}_i} \frac{C_i + C_j}{\|\mathbf{r}_{ij}\|^2} \mathbf{r}_{ij} \omega_{ij}. \quad (2.72)$$

Although this particle shifting technique can be used in both incompressible and weakly-compressible particle methods, we adopted this stabilization technique only for the WC-MPS. With the exception of the quasi-hydrostatic simulations where we adopted $A_F = 1$ to reach a quasi-static state, we adopted $A_F = 2$ for all dynamic simulations, as recommended in Skillen et al. (2013).

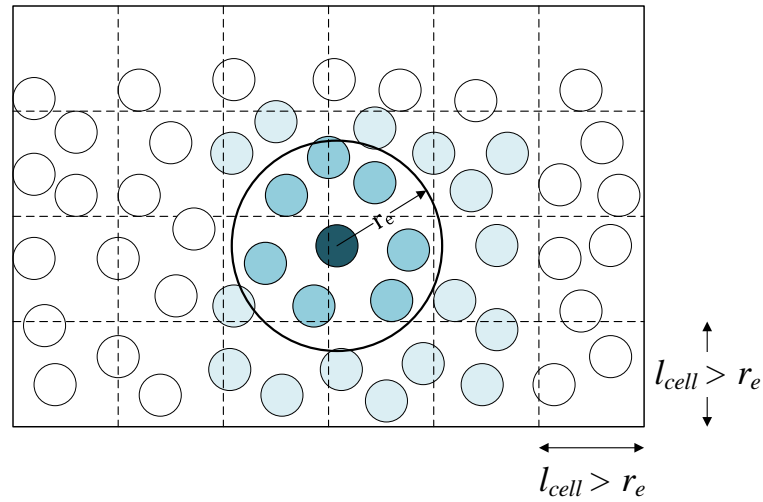
2.6 NEIGHBOR SEARCH

An efficient algorithm for searching neighbor particles is essential in almost all particle-based simulation methods. Since it is a $O(N^2)$ combinatory problem, where N states the number of particles, usually it becomes the bottleneck of the simulation time. To reduce the computational time in the present MPS, it was adopted the cell index method (Quentrec & Brot, 1975).

The main idea of the cell index method is to take advantage of the local compact support of the range of influence for each particle and divide the entire domain into cells with dimensions l_{cell} slightly larger than effective radius r_e , as shown in Figure 2.5. Therefore, the

search of each particle's neighbor can be limited in a small region close to it, thus reducing the problem to $O(N\hat{N})$, where \hat{N} is the quantity of particles inside the limited search domain. Particle's neighbors are stored in a list for each time step of the simulation.

Figure 2.5 – Schematic representation of the cell index method. Entire domain divided into cells of size l_{cell} and candidates and neighbor particles in the compact support of radius r_e .



Source: the author.

CHAPTER 3

TIME-CONSISTENCY AND STABILITY OF THE PARTICLE-BASED HYDRODYNAMIC PRESSURE

One of the critical points in the numerical assessment of hydrodynamic impact loads is accurate and stable computation of the pressure in particle-based methods. Due to discrete approximations adopted by the numerical methods, high frequencies unphysical pressure oscillations, caused by unstable or even non-converging numerical computation, are generally obtained. The aim of this research work is to investigate the unstable nature of pressure computation focusing on extremely flexible but compute-intensive incompressible flow modeling through the projection-based particle methods. A new approach from the viewpoint of the momentum conservation regarding particle-level collisions is proposed to derive new source terms of pressure Poisson equation (PPE). This results in stable pressure computations with drastic reduction of the spurious pressure oscillation and pressure magnitudes almost independent to time step. Moreover, in comparison to the other strategies, no additional computational effort is required, its implementation is extremely simple, and the only numerical parameter is the propagation speed of the perturbations, of which the calibration is much more straightforward due to its physical meaning. Simulations were carried out using moving particle semi-implicit (MPS) method improved by the proposed approach, although other projection-based particle methods such as the incompressible smoothed particle hydrodynamics (ISPH) method can also be used. The comparisons of the computed results with theoretical and experimental ones confirmed the effectiveness of the proposed approach.

3.1 BACKGROUND

Many numerical methods have been proposed to predict hydrodynamic loads to solve multidisciplinary problems in hydraulic, coastal, marine and offshore areas. Grid or mesh-based methods are generally applied for such problems. However, these methods suffer from some limitations, especially for interface problems, e.g., violent free-surface flow, and numerical treatments like free surface tracking or remeshing techniques are required, resulting in a very time-consuming activity. Due to the easy implementation and flexibility to model highly complex problems, the meshless methods have opened new perspectives in recent years, especially to solve violent free-surface flows and strong fluid-solid interaction problems. An important class of meshless method is the particle-based methods, where the behavior of a physical problem is represented by a collection of points (particles). In the particle-based method, each particle moves accordingly with its own mass and the internal/external forces are evaluated by the interaction with the neighboring particles (Idelsohn & Oñate, 2006).

Numerical methods dealing with problems associated with strongly nonlinear interactions between water waves and structures are mainly based on solving either the fully nonlinear potential flow theory or the Navier-Stokes equations (Ma et al., 2016). In general, particle-based methods applied to free-surface flows that solve the Navier-Stokes equations can be categorized into two groups: weakly compressible and incompressible projection-based methods (Gotoh & Khayyer, 2016). The former such as smoothed particle hydrodynamics (SPH) (Gingold & Monaghan, 1977; Lucy, 1977) or weakly compressible moving particle semi-implicit (WC-MPS) (Shakibaeinia & Jin, 2010) methods solve an appropriate equation of state in a fully explicit form. The latter such as moving particle semi-implicit (MPS) (Koshizuka & Oka, 1996) or incompressible smoothed particle hydrodynamics (ISPH) (Cummins & Rudman, 1999; Lo & Shao, 2002) methods solve a pressure Poisson equation (PPE) through a Helmholtz-Hodge decomposition (Bhatia et al., 2013) and application of the projection method (Harlow & Welch, 1965; Chorin, 1967; Temam, 1969). Incompressible projection-based particle methods are generally expected to provide higher accuracy in terms of hydrodynamic pressure calculation and volume conservation (Lee et al., 2008; Gotoh et al., 2013). Therefore, they are preferable in many applications focused on hydrodynamic load assessment. However, as the main challenges of these methods, compute-intensive and unstable pressure computation can be mentioned.

To achieve accurate and stable computations, substantial efforts have been carried out, as previously detailed by Khayyer and Gotoh (2016), Ye et al. (2019) and Li et al. (2020). These efforts covering at least one of the following approaches:

- i.) regularization for particle distribution;
- ii.) high-order and/or modified discrete differential operators;
- iii.) improved free-surface particle detection;
- iv.) new formulations for the source term of PPE;
- v.) background mesh.

Although several efforts have been undertaken to enhance the computation of the hydrodynamic pressure, the source terms of previous works depend on the time step and, in practice, the computed pressure peak magnitudes are sensitive to time step, with an inconsistent behavior of increasing magnitude as the time step decreases, as illustrated later in Figure 3.2.

Within this context and aiming to provide a practical engineering tool for more time-stable assessment of loads due to extremely nonlinear hydrodynamic phenomena, an improvement on the pressure computation of the incompressible projection-based particle methods is proposed in the present work. Based on a novel viewpoint of momentum conservation in particle-level collisions, a correction of the mismatch between numerical and physical time scales is introduced to derive new formulations for the PPE. This leads to original source terms that depends directly on the spatial discretization and independent to time step, which results in stable computations of the pressure. Furthermore, the proposed formulation preserves advantages of the original meshless particle-based numerical methods such as their flexibility, very easy in coding implementation, no additional computational effort on the already compute-intensive method and easy to incorporate the approaches already mentioned to improve the stability and accuracy of pressure assessment. To demonstrate the effectiveness of the new PPE source terms derived from the proposed approach, namely time-scale correction of particle-level impulses (TCPI), the MPS method is adopted and four phenomena are studied: hydrostatic condition, water jet hitting a perpendicular flat wall, dam breaking, and liquid sloshing inside a prismatic tank. The computed pressures from MPS with original and proposed source terms are compared to show the effectiveness of the proposed improvement. The numerical results are also compared against the analytical and experimental ones available in the literature or conducted in the Numerical Offshore Tank of USP (TPN-USP).

3.2 RELATED WORK

In the context of a particle regularization procedure to improve non-uniform particle distribution, several methods have been proposed. Monaghan (1992) proposed the XSPH scheme which helps the particles to move with a velocity close to that of their neighboring particles, improving the smoothness of velocity field. Afterwards, Monaghan (2005) highlighted the fact that the XSPH scheme does not conserve energy and proposed an implicit XSPH to resolve this issue. Xu et al. (2009) proposed the particle shifting method, which slightly shifts the particles to prevent anisotropic particle structures, posteriorly extended by Lind et al. (2012), allowing applications to free-surface flows. Tsuruta et al. (2013) presented the so-called dynamic stabilization (DS) scheme which produces radial and anti-symmetric inter-particle forces and thus, at least, preserves both linear and angular momentum exactly. An optimized particle shifting scheme was presented in the context of the SPH method by Khayyer et al. (2017). Despite better distribution, the updating process of particles is computationally expensive, which is not practical (Wang & Zhang, 2018).

Instead of directly avoiding non-uniform particle distribution, modifications and corrections have been made on discrete differential operators considering irregular particle distribution. Discrete differential operators models have been proposed to assure momentum conservation (Khayyer & Gotoh, 2008; Tanaka & Masunaga, 2010), by changing the conventional operation of subtraction in the gradient operator. The so-called higher order Laplacian model was developed by Khayyer and Gotoh (2010; 2012), by directly taking the divergence of a gradient model. Higher order approximations for differential operators were proposed based on a Taylor series expansion, giving a combination of these operators and corrective matrix (Randles & Libersky, 1996; Suzuki, 2008; Tamai & Koshizuka, 2014; Duan et al., 2018; Liu et al., 2018). However, generally these formulations are complex and demands additional computational cost to the already compute-intensive methods, aside from the considerable coding implementation effort required.

Despite not being a definitive solution itself, the improvement of the free-surface particle detection techniques contributes significantly to more stable pressure computations by avoiding misdetection of free surface inside the fluid domain and the consequent mis imposition of the boundary condition for the pressure calculation. Among available fluid interface particle detection techniques, we can mention the techniques based on the sum of a weight function (Koshizuka & Oka, 1996), amount of neighborhood particles (Tanaka & Masunaga, 2010), gradient vector of a property of the particles (Itori et al., 2011), relative

distance between particles (Gotoh et al., 2009), a combination of the criteria based on the weight function and the amount of neighborhood particles (Lee et al., 2011) or the weighted distribution of neighboring particles (Tsukamoto et al., 2016), threshold angles between adjacent connecting lines of a given particle and its neighbor particles (Sun et al., 2019), or a combination of purely geometric sphere covering tests based on interval analysis with an adaptive spatial subdivision (Sandim et al., 2020).

Regarding the source term of PPE, one of the considerable improvements was the combination of two error mitigating parts, the zero variation of the density and the velocity-divergence-free condition (Hirokazu, 1999; Zhang et al., 2006; Tanaka & Masunaga, 2010), which corresponds to the accumulative and instantaneous density deviations, respectively. In Hu and Adams (2007), both the zero variation of density and velocity-divergence-free constraints of the incompressibility condition were enforced through the resolution of two PPEs and via application of a fractional time-step integration algorithm. Khayyer and Gotoh (2009) and Khayyer et al. (2009) introduced a higher order source term, which allows a slight compressibility. The authors also proposed a different formulation for the calculation of density variation by the total differentiation of the weight function. Kondo and Koshizuka (2011) proposed a multi-term source consisting of one main part and two error-compensating parts. With proper selection of the coefficients multiplied by the error compensating parts, unphysical pressure oscillation was suppressed. Khayyer and Gotoh (2011) and Gotoh et al. (2014) introduced a modified source term comprising of a set of high order error compensating, similar the work of Kondo and Koshizuka (2011), but with dynamic coefficients as functions of the instantaneous flow field. Zheng et al. (2014) proposed a new formulation of incompressible flows based on Rankine source solution. The PPE was modified into a form that does not require any direct approximations for function derivatives, then leading to a more robust numerical method, of which the main advantage corresponding to absence of the need to approximate second-order derivatives in the PPE. Ngo-Cong et al. (2015) proposed a novel numerical approach for incompressible smoothed particle hydrodynamics by solving the PPE on a set of so-called moving integrated radial basis function networks.

Apart from aforementioned improvements, some researchers have used background meshes to mitigate problems due to the particles maldistribution. Hwang (2011) and Ng et al. (2016) proposed an accurate MPS based on an embedded pressure mesh, namely moving particle pressure mesh (MPPM) and unstructured moving particle pressure mesh (UMPPM), to handle the continuity constraint. In both works, the main idea is to consider the pressure as Eulerian

variable, which is in contrast with the original MPS whereby the pressure and velocity are computed on the Lagrangian particles. A background mesh scheme was proposed by Wang et al. (2019) aiming to an accurate, smooth, and spatially continuous source term for the PPE. The source terms are first calculated at background mesh nodes with the interpolated velocities at fixed and regular neighboring nodes. Then, the computed source terms at mesh nodes are extrapolated to the nearest neighboring particles. Different from the last two works, the imaginary background meshes are only used for the calculation of the source terms of PPE, while the calculations of other equations are performed in the Lagrangian framework. The enhancement effectiveness of the stability and accuracy of pressure calculation is showed through several benchmark tests. The incorporation of a background mesh into Lagrangian particle-based methods seems a promising direction to solve challenging issues related to accurate and stable computations, however it can lead to complex data interpolations.

3.3 NUMERICAL METHOD

3.3.1 MOVING PARTICLE SEMI-IMPLICIT (MPS) METHOD

To solve the incompressible viscous flow, the semi-implicit algorithm of the incompressible MPS method, already detailed in the previous Chapter 2, is adopted herein. The numerical operators adopted to solve the problems studied in this chapter are listed in Table 3.1.

Table 3.1: Numerical operators applied in the problems presented in this chapter.

Numerical operator	Equation
Weight function	$\omega_{ij} = \begin{cases} \frac{r_e}{\ \mathbf{r}_{ij}\ } - 1 & \ \mathbf{r}_{ij}\ \leq r_e \\ 0 & \ \mathbf{r}_{ij}\ > r_e \end{cases}$
Particle number density	$n_i = \sum_{j \in \mathbb{P}_i} \omega_{ij}$
Pressure gradient	$\langle \nabla P \rangle_i = \frac{dim}{n^0} \sum_{j \in \mathbb{P}_i} \frac{P_j - \hat{P}_i}{\ \mathbf{r}_{ij}\ ^2} \mathbf{r}_{ij} \omega_{ij}$
Divergent of velocity	$\langle \nabla \cdot \mathbf{u} \rangle_i = \frac{dim}{n^0} \sum_{j \in \mathbb{P}_i} \frac{\mathbf{u}_j - \mathbf{u}_i}{\ \mathbf{r}_{ij}\ ^2} \cdot \mathbf{r}_{ij} \omega_{ij}$
Laplacian of velocity	$\langle \nabla^2 \mathbf{u} \rangle_i = \frac{2dim}{\lambda_i n^0} \sum_{j \in \mathbb{P}_i} (\mathbf{u}_j - \mathbf{u}_i) \omega_{ij}$

Source: the author.

3.4 TIME-SCALE CORRECTION OF PARTICLE-LEVEL IMPULSES (TCPI)

In explicit numerical schemes, especially for phenomena dominated by advection effects, the propagation of perturbations is limited by the Courant-Friedrichs-Lewy (CFL) condition (Courant et al., 1967) for numerical stability, which establishes the relation between the propagation velocity of the perturbations c_s and the numerical parameters:

$$C_r = \frac{c_s \Delta t}{l_0} < 1.0, \quad (3.1)$$

where C_r is the Courant number, Δt is the numerical time step and l_0 is the spatial resolution. For time discontinuous phenomena, such as impulsive load due to a collision or impact, this condition leads to a mismatch between physical δt and numerical time Δt durations of the events.

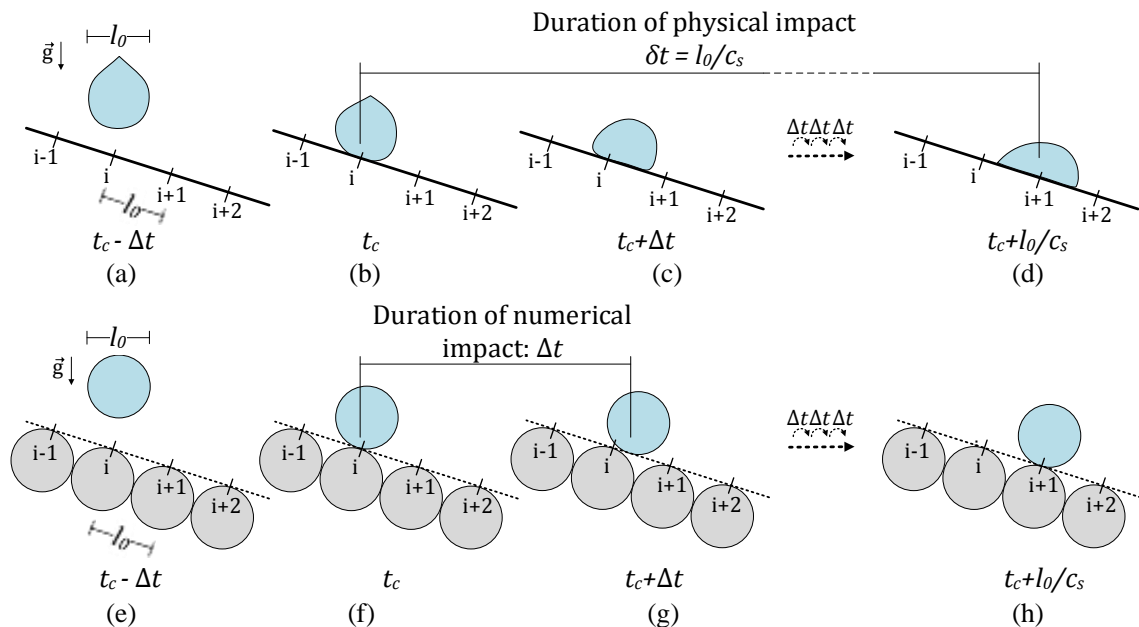
In order to understand this issue, let us consider, for example, the case of successive collisions or impacts at progressive speed c_s of a portion of continuum through a sequence of panels. A visualization is provided in Figure 3.1 adopting as an example the collision of a volume of fluid on an inclined panel. For sake of clarity, the resolution of the numerical modeling l_0 is adopted as the characteristic dimension. The fluid contact is first established with the point i at the instant t_c . Then, the volume of fluid slides down between the points i and $i+1$, covering the distance l_0 during the physical interval $\delta t = l_0/c_s$.

If the characteristic dimension of the problem is l_0 (Figure 3.1(a)), the intervals between the collisions detected at successive panels is $\delta t = l_0/c_s$ (Figure 3.1(b)-(d)). In addition to this, after the portion of the continuum collides one of the panels (Figure 3.1(b)), the contact will occur continuously and smoothly across the panel to reaches the next one (Figure 3.1(d)). In this way, physically, the order of the duration of the collision or impact associated to the space interval l_0 covered by the panel is about δt .

Now, considering l_0 as the minimal spatial resolution in case of the numerical modeling of the time discontinuous phenomena (Figure 3.1(e)), the collision or impact between particles or grids, which are discrete representation of continuous spatial domain, is detected at the time step Δt associated to the instant when the event occurs (Figure 3.1(f)-(g)). Moreover, in the numerical computation, apart from the change of the status prior and after the time discontinuous phenomena at the time step when the event occurs, the event is also processed within the time step when the contact was detected. This is because of the discrete time and space approximation, instead of continuous contact of a particle across another particle or panel (Figure 3.1(b)-(d)), the next event of contact will only occur when it reaches the

following one. As a result, despite the physical interval between collisions of a particle to successive particles or grids at a progressive speed c_s remains $\delta t = l_0/c_s$, numerically the duration of the collision or impact lasts about the numerical time step Δt (Figure 3.1(f)-(g)). Considering the stability criterion shown in Eq. (3.1), it is clear that $\Delta t < \delta t$. This means that the successive collisions or impacts that physically must last δt are numerically shortened to Δt when the numerical stability criterion is satisfied. Figure 3.1 illustrates this mismatch between physical δt and numerical Δt duration of collision or impact.

Figure 3.1 - Sketch of continuous (top) and discrete (bottom) evolution of a volume of fluid on an inclined panel.



Source: the author.

Since the conservation of the momentum is assured by the governing equations, the impulse \mathbf{J} of a collision or impact due to loads computed numerically or recorded physically should be the same, and can be obtained by the integrating the loads considering respective time interval:

$$\mathbf{J} = \int_t^{t+\Delta t} \mathbf{F}_n dt, \quad (3.2)$$

$$\mathbf{J} = \int_t^{t+\delta t} \mathbf{F}_p dt, \quad (3.3)$$

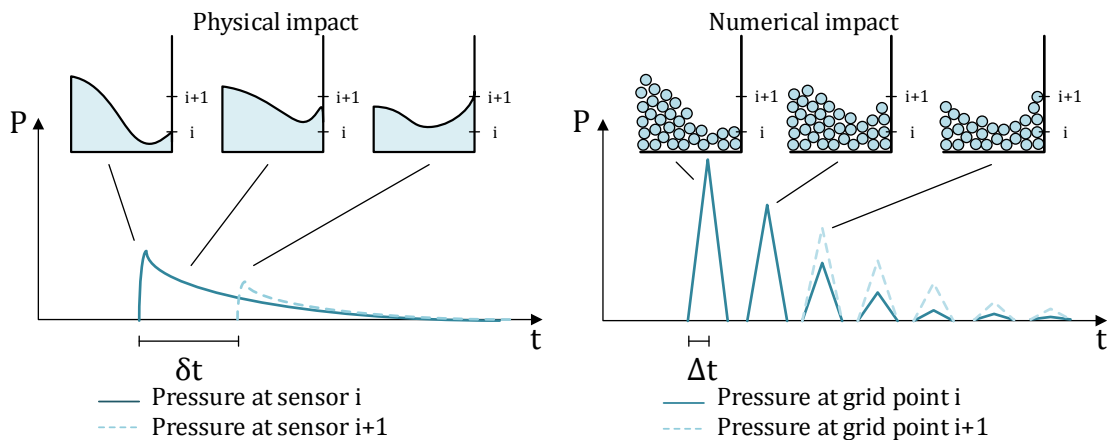
where, \mathbf{F}_n and \mathbf{F}_p are collision or impact loads computed numerically and recorded physically, respectively.

Thus, the relation between \mathbf{F}_n and \mathbf{F}_p , or the respectively pressures P_n and P_p , becomes:

$$\frac{\mathbf{F}_n}{\mathbf{F}_p} \propto \frac{P_n}{P_p} \propto \frac{\delta t}{\Delta t} = \frac{l_0/c_s}{C_r l_0/c_s} = \frac{1}{C_r} \rightarrow P_n \propto \frac{P_p}{C_r} \text{ or } \Delta t \propto C_r \delta t . \quad (3.4)$$

The Eq. (3.4) shows clearly that, in the explicit schemes, the imposition of the stability criteria leads to much higher magnitude for numerical pulses than the physical ones, with the magnitude amplification coefficient of $1/C_r$. In the other words, as the duration of the numerical impulses is much shorter than the physical ones, each of these discrete impacts is accompanied by a large increase in the magnitude of the impulsive loads. The same fact was observed in Marrone et. al, (2015), where the impact of two identical water jets was simulated by using an incompressible mesh-based level-set finite volume method. They highlighted that the computed pressure is proportional to $I_p/\Delta t$, being I_p the pressure impulse, i.e., the pressure impact becomes singular with the decrease of Δt (Meringolo et al., 2017). Moreover, a volume of fluid (VOF) model was used to simulate a dam break event in Mokrani and Abadie (2016) and, as presented in Figure 8 of their work, the computed pressure peak evolves quasi linearly with respect to the inverse of Δt . Actually, instead of abruptly rise and smoothly decaying pulses recorded physically, generally a sequence of spikes with amplified peaks is computed (see, e.g., Belytschko and Mullen (1981)), as sketched in Figure 3.2. This is a phenomenon pointed out by Cheng and Arai (2002) as one of causes of large amplitude spurious oscillations obtained in the numerical computation of impact pressure using mesh-based methods.

Figure 3.2 - Sketch of physical and numerical impact pressure at two successive observation points. Adapted from Cheng and Arai (2002).

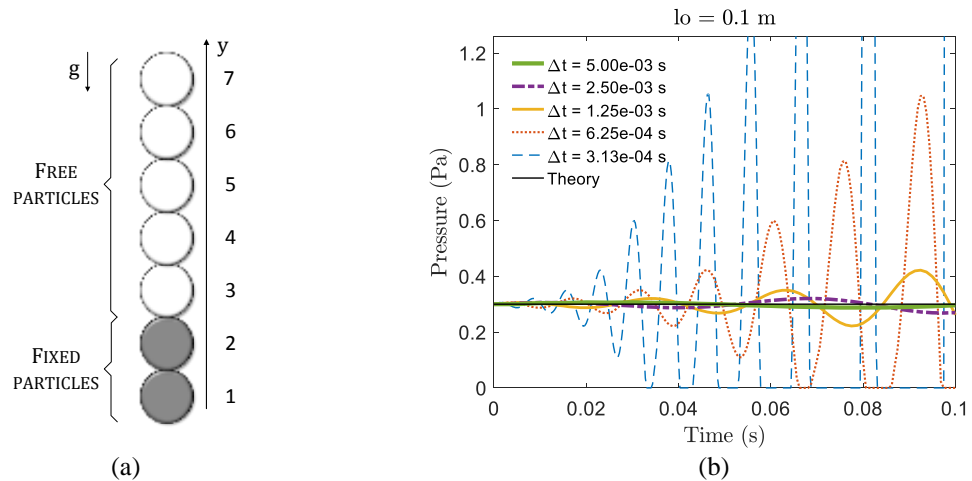


Source: the author.

Besides the dilemma of the numerical stability criterion that results in the unstable computation of the time discontinuous phenomena, the solution is inconsistent in time domain, with peak values very sensitive to Δt , because the magnitude of the unstable oscillating numerical collision loads $P_n \rightarrow \infty$ when the numerical time step $\Delta t \rightarrow 0$.

As a verification of the unstable and time-inconsistent behavior in the particle-based computation, an idealized scenario of a hydrostatic problem in which fluid particles are arranged at one-dimensional (1D) regular intervals (see Figure 3.3(a)) is taken to illustrate that the magnitude of the computed pressure is proportional to $1/\Delta t$. Particles are governed by the equations of inviscid incompressible flow. The source term with PND deviation (see Eq. (2.50)) is used here. The initial distance between particles l_0 is set to 0.1m, the effective radius $r_e = 2.1l_0$ is used for all operators and the relaxation coefficient $\gamma = 0.1$ is adopted. We assigned fluid density $\rho_f = 1\text{kg/m}^3$ and $g = 1\text{m/s}^2$. Particles at $y = 1$ and $y = 2$ are fixed whereas the remaining particles are free to move. As a Dirichlet boundary condition, pressures of particles at $y = 6$ and $y = 7$ are set to $\rho_f g l_0$ and 0, respectively.

Figure 3.3 - a) 1D particle arrangement. (b) Pressure of particle at $y = 4$. Cases simulated with $l_0 = 0.1\text{m}$ and $\Delta t = 5 \times 10^{-3}$, 2.5×10^{-3} , 1.25×10^{-3} , 6.25×10^{-4} and $3.13 \times 10^{-4}\text{s}$.



Source: the author.

Figure 3.3(b) gives the computed pressure of particle at $y = 4$ for different time steps. It is clear the dependence of the magnitude of pressure fluctuations with respect to Δt . Instead of a better result that might be obtained by using a smaller Δt , high-frequency pressure oscillations with higher peak magnitudes were computed.

Since the essence of the spurious oscillations and the time-inconsistent behavior are caused by the mismatch between the numerical and physical times, in the duration of collisions or

impacts, following Eq. (3.4), a possible solution to mitigate these issues of the numerical modeling is the application of the Courant number $C_r = \Delta t / \delta t$ as correction factor, i.e., the scale between the numerical time step and physical time interval, to compute the impulsive loads.

Now focusing on Lagrangian particle-based methods, in which particle-level collisions may occur, the correction of the mismatch between numerical and physical intervals is introduced to derive a new formulation for the PPE, by using the correction factor C_r to improve the stability and time-consistency of the computed pressure. Instead of using the numerical time step Δt in the source term (see Eq. (2.49)), the physical interval δt is adopted to adjust both the magnitude and duration of the impulses, so that:

$$\langle \nabla^2 P \rangle_i^{t+\Delta t} = \frac{\rho_f}{\delta t^2} \left(\frac{n^0 - n_i^{**}}{n^0} \right). \quad (3.5)$$

This is the same as applying the correction factor to the relaxation coefficient (see Eq. (3.4))

$$\gamma = C_r^2 = \left(\frac{c_s \Delta t}{l_0} \right)^2 \quad (3.6)$$

in Eq. (2.50). Rewriting the PPE, we have:

$$\langle \nabla^2 P \rangle_i^{t+\Delta t} = \frac{c_s^2 \Delta t^2}{l_0^2} \frac{\rho_f}{\Delta t^2} \left(\frac{n^0 - n_i^{**}}{n^0} \right), \quad (3.7)$$

resulting in:

$$\langle \nabla^2 P \rangle_i^{t+\Delta t} = c_s^2 \frac{\rho_f}{l_0^2} \left(\frac{n^0 - n_i^{**}}{n^0} \right). \quad (3.8)$$

Observe that the last equation is independent to Δt . This is an important aspect because it suggests that for a given spatial resolution l_0 , the computed pressure is independent of Δt , which is a strong indication that it might solve the inconsistency in time domain.

Also, instead of pressure relaxation coefficient γ that requires empirically calibration and adjustment, in the proposed source term the only numerical parameter is the propagation speed of the perturbations c_s , of which the calibration is much more straightforward due to its physical meaning (see Eq. (3.1)) regarding the particle-level collision dynamics.

Here it is important to explain an important feature of the replacement of the numerical time step Δt by the spatial resolution l_0 . With the traditional Δt based PPE source terms and fixed relaxation coefficients, the reduction of Δt leads to larger pressure oscillations and there is no change in the spatial resolution of the numerical model. The proposed PPE is based on δt , which, by introducing the correction factor, leads to l_0 in the source term. Since the reduction of l_0 means the use of a higher resolution model, the mass of the particles as well as the

numerical error are also reduced so that the error in the computed impulses does not increase with the reduction of l_0 . Furthermore, as previous explained, the reduction of l_0 means that the physical time $\delta t = l_0/c_s$ is smaller, and the error of the computed impulsive load, which is related to the amplitude of the oscillations and the mismatch between δt and Δt , might be reduced.

At this point, one should remind that the reduction of δt associated to the reduction of l_0 might also demand the reduction of Δt because the relation $\delta t/\Delta t > 1.0$ must be assured due to Courant condition. In summary, using the proposed source term Eq. (3.8), a smaller increase of the pressure oscillation with the reduction of l_0 should be expected, but it would be much smaller than that due to the reduction of Δt when using Eq. (2.50).

Another incompressible condition considered in the source term is that the divergence of the velocity field should be zero. As proposed by Tanaka e Matsunaga (2010), PPE can be rewritten as:

$$\langle \nabla^2 P \rangle_i^{t+\Delta t} = \gamma \frac{\rho_f}{\Delta t^2} \left(\frac{n^0 - n_i^t}{n^0} \right) + \frac{\rho_f}{\Delta t} \nabla \cdot \mathbf{u}^{**}. \quad (3.9)$$

The first term of the right-hand side represents the deviation of particle number density at instant t from the theoretical constant one (n^0), i.e., the accumulative density deviations. The second term corresponds to the instantaneous time variation of particle density at instant t (Gotoh et al., 2014).

Similarly to the previous procedure of introduction a relaxation coefficient γ to reduce spurious pressure oscillation and improve the time-consistency, by using the physical time interval δt , the first term and the second term of the right side are multiplied by C_r^2 and C_r , respectively:

$$\langle \nabla^2 P \rangle_i^{t+\Delta t} = \frac{c_s^2 \Delta t^2}{l_0^2} \frac{\rho_f}{\Delta t^2} \left(\frac{n^0 - n_i^t}{n^0} \right) + \frac{c_s \Delta t}{l_0} \frac{\rho_f}{\Delta t} \nabla \cdot \mathbf{u}^{**}, \quad (3.10)$$

that results in:

$$\langle \nabla^2 P \rangle_i^{t+\Delta t} = c_s^2 \frac{\rho_f}{l_0^2} \left(\frac{n^0 - n_i^t}{n^0} \right) + c_s \frac{\rho_f}{l_0} \nabla \cdot \mathbf{u}^{**}. \quad (3.11)$$

Eq. (3.11) is also independent to time step Δt , which strongly indicates that it might be a time-consistent formulation.

The coefficients that multiply the particle number density deviation and the divergence-free condition can be expressed by:

$$\Gamma_1 = \frac{\gamma}{\Delta t^2}, \quad \Gamma_2 = \frac{1}{\Delta t}, \quad \Pi_1 = \frac{c_s^2}{l_0^2}, \quad \Pi_2 = \frac{c_s}{l_0}. \quad (3.12)$$

Therefore, the Eqs. (3.8) and (3.11) can be rewritten as:

$$\langle \nabla^2 P \rangle_i^{t+\Delta t} = \rho_f \Gamma_1 \left(\frac{n^0 - n_i^t}{n^0} \right) + \rho_f \Gamma_2 \nabla \cdot \mathbf{u}^{**}, \quad (3.13)$$

$$\langle \nabla^2 P \rangle_i^{t+\Delta t} = \rho_f \Pi_1 \left(\frac{n^0 - n_i^t}{n^0} \right) + \rho_f \Pi_2 \nabla \cdot \mathbf{u}^{**}. \quad (3.14)$$

The classifications of original and improved source terms are summarized in Table 3.2.

Table 3.2: Description of the original and proposed source terms applied in this study.

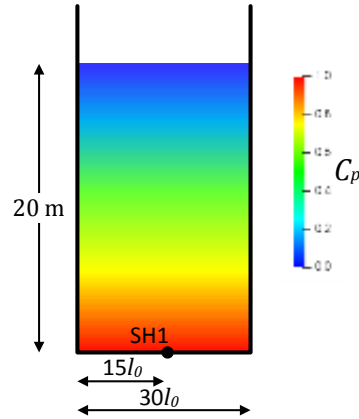
Source term	Abbreviation
Original PND deviation Eq. (2.50)	O-PND
Proposed PND deviation Eq. (3.8)	TCPI-PND
Original PND deviation and divergence-free condition Eq. (3.9)	O-PND-DF
Proposed PND deviation and divergence-free condition Eq. (3.11)	TCPI-PND-DF

Source: the author.

3.4.1 CALIBRATION OF THE PROPAGATION SPEED OF THE PERTURBATIONS c_s

In this section, one is intended to find the range of the speed of the perturbations c_s that enables stable simulations. For this purpose, the fluid volume variation and the pressure time series computed by the proposed source terms TCPI-PND and TCPI-PND-DF are analyzed considering hydrostatic condition. Figure 3.4 illustrates the tank dimensions of length $L_T = 30 \times l_0$, initial water level height $H_F = 20\text{m}$, and the position of the pressure sensor SH_1 located at the tank bottom. Even in the hydrostatic case, where particles are initially at rest, the source term of PPE is not zero for all particles so that particle motions are induced after the corrections of particle velocity and position (Kondo & Koshizuka, 2011). Furthermore, the error on total fluid volume and pressure oscillation tend to increase as the time advances. Hence, the analysis of variations on surface height and hydrostatic pressure seems an appropriate procedure to find stable coefficients $\Pi_1 = c_s^2/l_0^2$ and $\Pi_2 = c_s/l_0$.

Figure 3.4 - Calibration of the propagation speed of the perturbations. Main dimensions of the hydrostatic tank and sensor position (SH₁). Color scale is representative of the pressure field in the initial configuration.



Source: the author.

Assuming the fluid as weakly compressible, the pressure P can be related to the density field ρ by a linear equation of state:

$$P \sim c_s^2 \rho. \quad (3.15)$$

Regarding the particle-level collisions in the prediction step of the semi-implicit algorithm used in the projection-based methods, the predominant pressure scale is proportional to potential due to the gravitational effect $\rho g l_0$. Using this value in Eq. (3.15), the following relation is obtained:

$$c_s \sim \sqrt{g l_0}, \quad (3.16)$$

where $g = 9.81 \text{ m/s}^2$ is the gravity.

In order to certify the above relation, several initial distances between particles $l_0 = 1.0, 0.4, 0.1$ and 0.02 m , with respective ratios $H_F/l_0 = 20, 50, 200$ and 1000 , time steps $\Delta t = l_0/20, l_0/50$ and $l_0/80$, and the propagation velocity of the perturbations ranging from $c_s = 0.5$ to 40 m/s , were adopted to simulate an hydrostatic tank during 50 seconds.

The oscillation of the dimensionless pressure $C_p = P/\rho g H_F$ is quantified by its standard deviation (Std_p) at sensor SH₁ given by:

$$Std_p = \sqrt{\frac{1}{m-1} \sum_{i=1}^m |C_{p_i} - \bar{C}_p|^2}, \quad (3.17)$$

where m is the number of values computed during a time interval and \bar{C}_p is the mean of the computed results C_p .

The variation of the fluid volume is verified by the normalized root mean square deviation of the free-surface height ($NRMSD_H$) related to its initial one H_F , here calculated as:

$$NRMSD_H = \frac{1}{H_F} RMSD_H = \frac{1}{H_F} \sqrt{\frac{1}{m} \sum_{i=1}^m |H_i - H_F|^2}, \quad (3.18)$$

where $RMSD_H$ denotes the root mean square deviation, H_i is the computed height of the free-surface particle at the center of the tank and m denotes the number of values computed during a time interval. Both deviations are computed during the last 10 seconds, i.e., the time interval between 40 and 50s.

The deviations Std_p and $NRMSD_H$ of the results obtained using TCPI-PND are shown in Table 3.3 while those computed using TCPI-PND-DF are presented in Table 3.4. In order to obtain the velocity \tilde{c}_s that provides a good compromise between the minimum Std_p and $NRMSD_H$ for each distance between particles l_0 , the following weighted interpolation was adopted:

$$\tilde{c}_s = 0.5 \sum_{i=1}^n \left[\left(\frac{\alpha_{Si}}{\sum_{i=1}^n \alpha_{Si}} + \frac{\alpha_{Ni}}{\sum_{i=1}^n \alpha_{Ni}} \right) c_{Si} \right], \quad (3.19)$$

with

$$\alpha_{Si} = \frac{\max_{i \in n} |Std_{p_i}|}{Std_{p_i}} - 1 \quad \text{and} \quad \alpha_{Ni} = \frac{\max_{i \in n} |NRMSD_{H_i}|}{NRMSD_{H_i}} - 1, \quad (3.20)$$

where n is the number of c_s values considered for each initial distance l_0 . The calculated values of \tilde{c}_s are also given in Table 3.3 and Table 3.4.

Table 3.3: Standard deviation of pressure (Std_p) and normalized root mean square deviation of the free-surface height ($NRMSD_H$) for the simulations using the proposed source term TCPI-PND.

		$l_0/\Delta t = 20 \text{ m/s}$		$l_0/\Delta t = 50 \text{ m/s}$			$l_0/\Delta t = 80 \text{ m/s}$		
l_0 [m]	c_s [m/s]	Std_p	$NRMSD_H$	c_s [m/s]	Std_p	$NRMSD_H$	c_s [m/s]	Std_p	$NRMSD_H$
1.0	15	0.010	0.048	40	0.084	0.029	40	0.029	0.027
	10	0.005	0.065	30	0.012	0.029	30	0.013	0.027
	5	0.009	0.165	20	0.009	0.095	20	0.010	0.034
	1	0.027	0.227	10	0.006	0.047	10	0.015	0.041
		$\bar{c}_s = 11.20 \text{ m/s}$		$\bar{c}_s = 24.06 \text{ m/s}$			$\bar{c}_s = 26.68 \text{ m/s}$		
0.4	15	0.024	0.012	30	0.055	0.007	30	0.086	0.007
	10	0.016	0.017	20	0.038	0.007	20	0.056	0.007
	5	0.017	0.023	15	0.033	0.009	15	0.055	0.008
	1	0.064	0.721	10	0.032	0.021	10	0.049	0.045
		$\bar{c}_s = 11.18 \text{ m/s}$		$\bar{c}_s = 18.30 \text{ m/s}$			$\bar{c}_s = 18.35 \text{ m/s}$		
0.1	10	0.081	0.004	15	0.282	0.032	15	0.473	0.011
	7.5	0.072	0.004	10	0.339	0.007	10	0.289	0.008
	5	0.082	0.005	7.5	0.244	0.011	7.5	0.331	0.010
	1	0.046	0.021	5	0.210	0.396	5	0.272	0.086
		$\bar{c}_s = 4.86 \text{ m/s}$		$\bar{c}_s = 8.02 \text{ m/s}$			$\bar{c}_s = 6.96 \text{ m/s}$		
0.02	5	0.806	0.003	5	0.616	0.009	5	0.418	0.017
	4	0.675	0.006	4	0.525	0.014	4	0.386	0.085
	3	0.541	0.141	3	0.437	0.017	3	0.262	0.147
	2	0.406	0.016	2	0.261	0.100	2	0.333	0.075
		$\bar{c}_s = 3.46 \text{ m/s}$		$\bar{c}_s = 3.31 \text{ m/s}$			$\bar{c}_s = 3.71 \text{ m/s}$		

Source: the author.

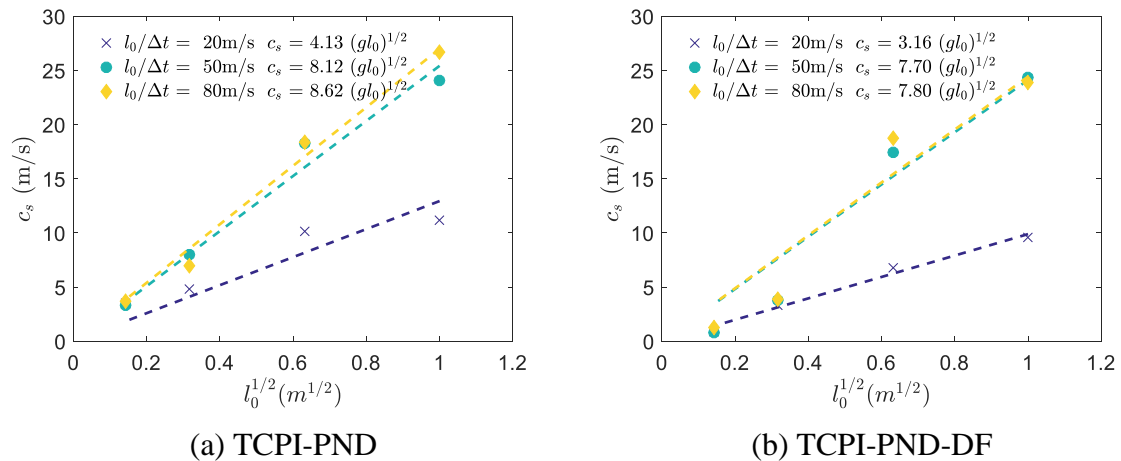
Table 3.4: Standard deviation of pressure (Std_p) and normalized root mean square deviation of the free-surface height ($NRMSD_H$) for the simulations using the proposed source term TCPI-PND-DF.

		$l_0/\Delta t = 20 \text{ m/s}$		$l_0/\Delta t = 50 \text{ m/s}$			$l_0/\Delta t = 80 \text{ m/s}$		
l_0 [m]	c_s [m/s]	Std_p	$NRMSD_H$	c_s [m/s]	Std_p	$NRMSD_H$	c_s [m/s]	Std_p	$NRMSD_H$
1.0	15	0.013	0.042	40	0.026	0.029	40	0.021	0.023
	10	0.004	0.063	30	0.013	0.030	30	0.012	0.024
	5	0.004	0.075	20	0.007	0.034	20	0.009	0.032
	1	0.014	0.477	10	0.007	0.058	10	0.006	0.064
		$\bar{c}_s = 9.56 \text{ m/s}$		$\bar{c}_s = 24.33 \text{ m/s}$			$\bar{c}_s = 23.86 \text{ m/s}$		
0.4	15	0.023	0.011	30	0.042	0.008	30	0.057	0.007
	10	0.016	0.010	20	0.030	0.010	20	0.035	0.008
	5	0.019	0.021	15	0.022	0.009	15	0.032	0.009
	1	0.006	0.115	10	0.024	0.009	10	0.027	0.011
		$\bar{c}_s = 6.80 \text{ m/s}$		$\bar{c}_s = 17.40 \text{ m/s}$			$\bar{c}_s = 18.77 \text{ m/s}$		
0.1	7.5	0.052	0.004	10	0.078	0.006	10	0.100	0.008
	5	0.041	0.004	7.5	0.057	0.006	7.5	0.082	0.008
	1	0.027	0.009	5	0.072	0.006	5	0.087	0.007
	0.5	0.015	0.021	1	0.030	0.009	1	0.031	0.034
		$\bar{c}_s = 3.30 \text{ m/s}$		$\bar{c}_s = 3.81 \text{ m/s}$			$\bar{c}_s = 3.85 \text{ m/s}$		
0.02	2	0.341	0.012	2	0.325	0.014	2	0.302	0.080
	1	0.243	0.015	1	0.031	0.003	1.5	0.040	0.004
	0.5	0.010	0.011	0.5	0.002	0.055	1	0.003	0.039
		$\bar{c}_s = 0.97 \text{ m/s}$		$\bar{c}_s = 0.83 \text{ m/s}$			$\bar{c}_s = 1.25 \text{ m/s}$		

Source: the author.

The computed values of \tilde{c}_s and the best linear fit solution based on the least-square method, for each ratio $l_0/\Delta t = 20, 50$ and 80m/s , were determined for both source terms and are illustrated in Figure 3.5.

Figure 3.5 - Propagation speed of the perturbations c_s . (a) TCPI-PND and (b) TCPI-PND-DF source term.



Source: the author.

According to Figure 3.5(a) and Figure 3.5(b), the linear relation between c_s and $l_0^{1/2}$ given by Eq. (3.16) was numerically confirmed by the computed values of \tilde{c}_s using TCPI-PND and TCPI-PND-DF, respectively. Besides the linear relation computed for all ratios $l_0/\Delta t$, lower values of \tilde{c}_s were computed for the lower ratio $l_0/\Delta t = 20\text{m/s}$, while higher and very close values of \tilde{c}_s were computed for the ratios $l_0/\Delta t = 50$ and 80m/s . This suggests that, for a given particle-based model, as smaller Δt are used, the optimal propagation speed of perturbation \tilde{c}_s converges to the same value related to l_0 .

The computed values given in Figure 3.5(a) and Figure 3.5(b) indicate that Eq. (3.16) can be approximated by $c_s = A_{cs}\sqrt{gl_0}$, with $A_{cs} \sim 10$. Indeed, considering these results and our experience, one may suggest the adoption of dimensionless constant $1 \leq A_{cs} \leq 30$ to provide stable simulations by using both source terms TCPI-PND and TCPI-PND-DF. However, it is important to keep in mind that these relations were obtained by the hydrostatic pressure condition to support a more general condition dominated by gravitational forces, e.g., water wave motions. Hence, aiming to improve the numerical accuracy, an in-depth calibration for each simulation is recommended.

3.5 CASES OF STUDY

In order to evaluate the performance of the source terms derived from the proposed TCPI approach, four phenomena were considered. First, a 2D hydrostatic case is simulated and the pressure of the particle on the bottom of the tank computed by the proposed source terms is compared to original ones and analytical results. After that, three simulations covering dynamic cases are considered. The first one is 2D water jet impact on a flat wall. The analytical pressure at the stagnation point is compared against the pressure computed from the original and proposed source terms. The second one consisting of a 2D dam-break problem and the last one corresponds to liquid sloshing inside a 3D prismatic tank. The computed pressure at the sensor located on side wall obtained by the proposed source terms is compared to original ones and against experimental results.

The relaxation coefficient γ needs to be calibrated based on the specificities of each case. In this sense, the definition of the value of the coefficient is carried out carefully to achieve the best results for the original formulations. As pointed out in previous works (Tanaka & Masunaga, 2010; Lee et al., 2011), a suitable relaxation coefficient range can be obtained from a hydrostatic pressure calculation. As the range $0.005 < \gamma < 0.05$ seems reasonable from the results of computed hydrostatic pressures (Tanaka & Masunaga, 2010; Lee et al., 2011), $\gamma = 0.01$ was adopted for the simulations using the original source terms. The propagation speed of the perturbations used for the simulations with the proposed source terms can be obtained by Eq. (3.6) as $c_s = \sqrt{\gamma} \cdot \left(\frac{l_0}{\Delta t}\right)$. By adopting $\gamma = 0.01$ and $l_0/\Delta t = 20\text{m/s}$, the value of $c_s = 2\text{m/s}$ is obtained, which is in agreement with the recommended range given in section 3.4.1. Since our main goal here is to demonstrate the numerical robustness and stability of the proposed source terms, we used only the value of $c_s = 2\text{m/s}$ for all l_0 , although the optimum c_s is directly related to $l_0^{1/2}$, as previous detailed in section 3.4.1. The numerical parameters used for all the simulations analyzed herein are presented in Table 3.5. Three particle distances $l_0 = 0.010, 0.005$ and 0.002 m and three time steps $\Delta t = l_0/20, l_0/50$ and $l_0/100$ were considered.

Table 3.5: Numerical parameters adopted for the simulations using original (O-PND or O-PND-DF) and proposed (TCPI-PND or TCPI -PND-DF) source terms.

l_0 [m]	Δt [s]	$l_0/\Delta t$ [m/s]	γ	c_s [m/s]	Γ_1 [s ⁻²]	Π_1 [s ⁻²]	Γ_2 [s ⁻¹]	Π_2 [s ⁻¹]
0.010	5.0×10^{-4}	20	0.01	2	4.0×10^4	4.0×10^4	2.0×10^3	2.0×10^2
	2.0×10^{-4}	50			2.5×10^5		5.0×10^3	
	1.0×10^{-4}	100			1.0×10^6		1.0×10^4	
0.005	2.5×10^{-4}	20			1.6×10^5	1.6×10^5	4.0×10^3	4.0×10^2
	1.0×10^{-4}	50			1.0×10^6		1.0×10^4	
	5.0×10^{-5}	100			4.0×10^6		2.0×10^4	
0.002	1.0×10^{-4}	20			1.0×10^6	1.0×10^6	1.0×10^4	1.0×10^3
	4.0×10^{-5}	50			6.3×10^6		2.5×10^4	
	2.0×10^{-5}	100			2.5×10^7		5.0×10^4	

* $\Gamma_1 = \gamma/\Delta t^2$, $\Gamma_2 = 1/\Delta t$, $\Pi_1 = c_s^2/l_0^2$, $\Pi_2 = c_s/l_0$.

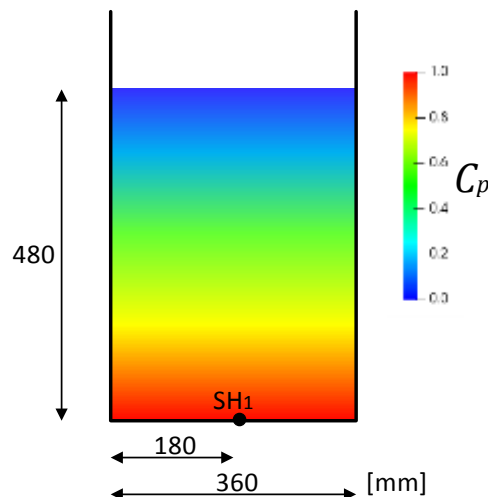
Source: the author.

3.6 RESULTS AND DISCUSSIONS

3.6.1 2D HYDROSTATIC TANK

The first test case consists of a 2D hydrostatic condition with tank of length $L_T = 0.36\text{m}$ and $H_F = 0.48\text{m}$ of column water height. Figure 3.6 gives the main dimensions and the initial hydrostatic pressure field, as well as the position of the pressure sensor SH₁. The fluid properties are density of $\rho_f = 1000\text{kg/m}^3$ and kinematic viscosity of $\nu_k = 1.0 \times 10^{-6} \text{ m}^2/\text{s}$. The hydrostatic pressures at SH₁ computed for 10 seconds using different source terms were analyzed.

Figure 3.6 - 2D hydrostatic tank. Main dimensions and sensor position (SH₁). Contours are representative of the pressure field in the initial configuration.



Source: the author.

The hydrostatic pressure is represented by the non-dimensional pressure coefficient $C_p = P/\rho_f g H_F$, and the dimensionless time (τ) is defined as $\tau = t\sqrt{g/H_F}$, where $g = 9.81\text{m/s}^2$ is the gravity acceleration and $H_F = 0.48\text{m}$ denotes the water column height.

At first, the time histories of raw pressure coefficients at sensor SH₁ computed using the original (O-PND) and proposed (TCPI-PND) sources terms are plotted together in Figure 3.7 to show the effects of the numerical parameters. It is important to point out that all the time histories shown in the present work are plot of raw results, without any filtering technique, which is a usual procedure to suppress the high frequency spurious numerical oscillation. The theoretical pressure coefficient $C_p = 1$, represented by the blue solid line, is also shown. Figure 3.7 shows that, when original formulation O-PND is applied, the decrease of time step, i.e., increase of the ratio $l_0/\Delta t$, leads to remarkable magnification of the magnitude of pressure oscillations whereas the application of formulation proposed herein TCPI-PND ensures a much lower amplification of the pressure oscillation due to the decrease of time step. On the other hand, Figure 3.7 shows that, for constant value $c_s = 2\text{m/s}$ adopted here, the pressure oscillations increase asymptotically as l_0 decreases from 0.010 to 0.002m.

Regarding the increasing pressure oscillation when l_0 decreases, for both original and proposed source terms, it is interesting to remind that the setting of the c_s is based on the fine-tuned numerical coefficients of the original source term, which also depends on l_0 , and Δt (Tsukamoto et al., 2020). In this way, further improvements on the stability of the pressure computation for higher spatial resolution cases might be expected for an in-depth tuning of the parameter c_s to the respective l_0 .

Figure 3.7 - Hydrostatic pressure at sensor SH₁. Source terms with the zero variation of the particle number density O-PND and TCPI-PND.

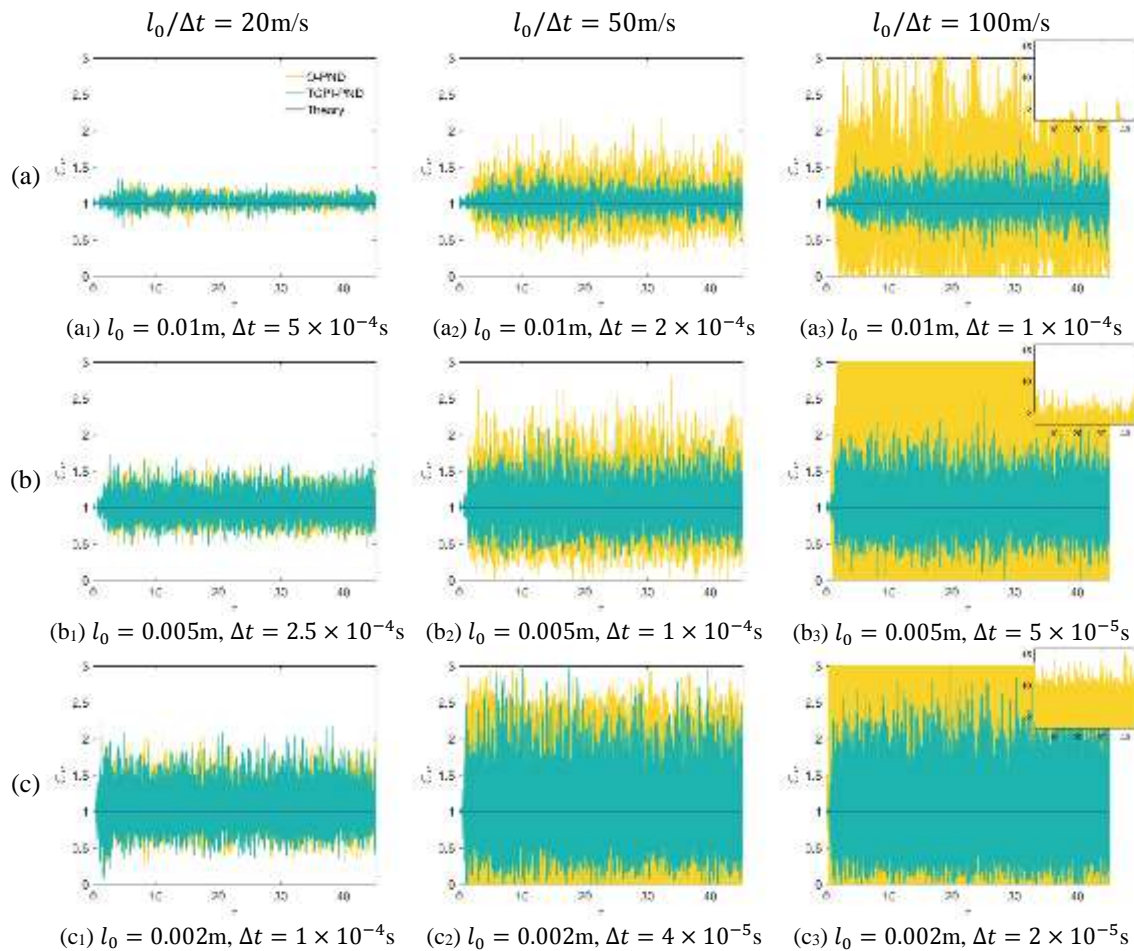
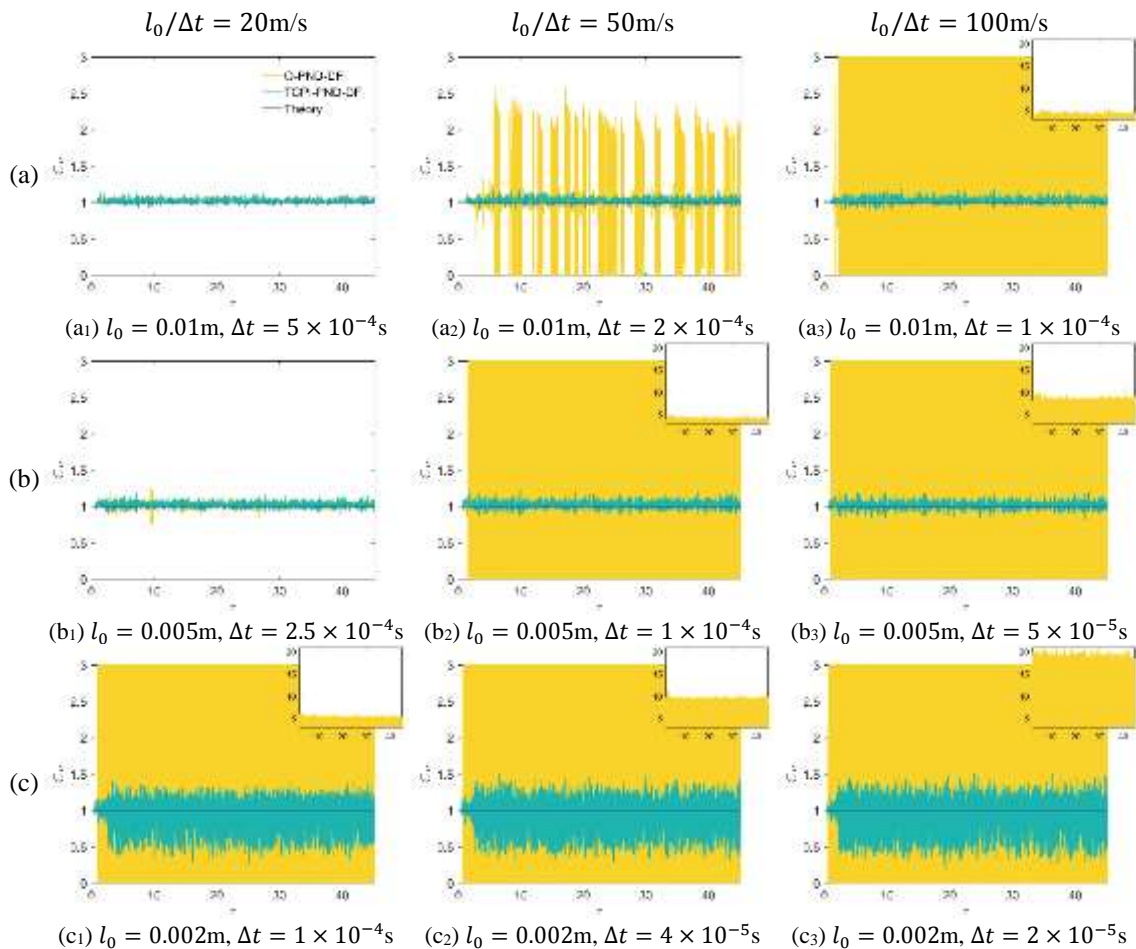


Figure 3.8 shows comparisons of the time histories of the raw pressure coefficient at sensor SH₁ computed by the source terms O-PND-DF and TCPI-PND-DF taken into account the numerical parameters listed in Table 3.5. Computed pressures and theoretical pressure coefficient $C_p = 1$ are also presented in Figure 3.8.

Similar to the previous simulations, the decrease of time step leads to very high pressure oscillations computed by O-PND-DF, showing the time stability issue. On the other hand, the pressure oscillations computed by TCPI-PND-DF remains almost constant, especially for $l_0 = 0.01$ and 0.005m , where very similar oscillation's amplitudes are achieved for both particle distances. On the other hand, meanwhile the pressure oscillations computed by O-PND-DF is highly sensible to $l_0/\Delta t$ and the coefficient Π_2 or Γ_2 , the pressures computed using TCPI-PND-DF are very stable with almost negligible oscillations and independent to the $l_0/\Delta t$ or the numerical parameters. For $l_0 = 0.002\text{m}$, the results from TCPI-PND-DF

shows higher oscillations although are much lower than those computed by O-PND-DF. The results show remarkable improvement on the stability and the possibility of straightforward calibration provided by using c_s through the application of the proposed approach, and the potential of the time-scale correction of particle-level impulses to improve the existing source terms.

Figure 3.8 - Hydrostatic pressure at sensor SH₁. Source terms with the zero variation of the particle number density O-PND-DF and TCPI-PND-DF.

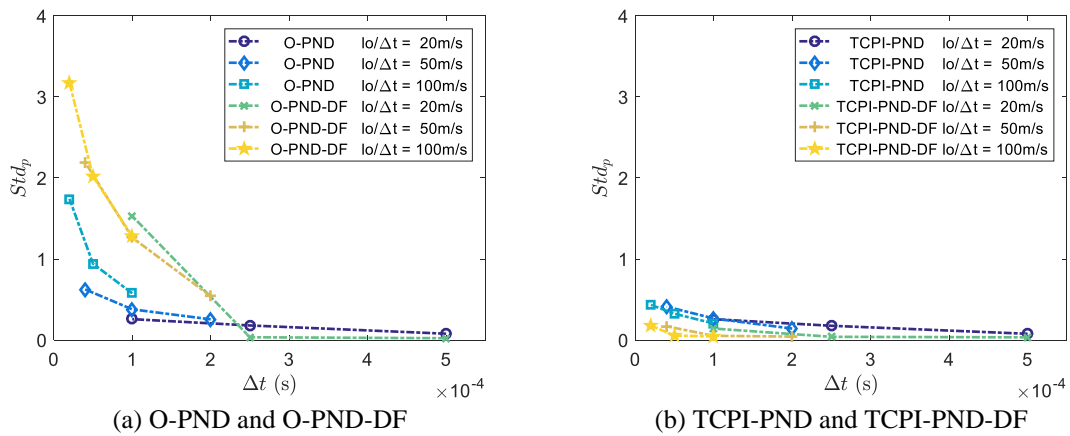


Source: the author.

In order to quantify the computed pressure oscillation, the standard deviations (Std), see Eq. (3.17), of the pressure coefficient for O-PND, O-PND-DF, TCPI-PND and TCPI-PND-DF in relation to the theoretical value ($C_p = 1$) are plotted in Figure 3.9. Figure 3.9(a) shows how the original source terms O-PND and O-PND-DF are highly influenced by the time step, and the oscillation increases remarkably as Δt decreases. On the other hand, Figure 3.9(b) illustrates the very lower dependence of the proposed source terms TCPI-PND and TCPI-PND-DF in relation to the time step and the particle distance, showing remarkably improved time domain stability. Also, much lower standard deviations were obtained for small time

steps or larger particle distance, showing notable improvement achieved by the proposed source terms in extending the range of stable computation to higher time domain resolution or lower spatial resolution. The last one means increasing of the efficiency of the numerical modeling with lower processing demand for similar stable results. Finally, in this pure hydrostatic case, the TCPI-PND-DF source term provided excellent results by mitigating the spurious pressure oscillations and improving the time-stability of the results with a combination of the time scale correction with zero variation of the particle number density and divergence-free conditions.

Figure 3.9 - 2D hydrostatic tank. Standard deviation (Std) of pressure. (a) Original O-PND and O-PND-DF, (b) proposed TCPI-PND and TCPI-PND-DF source terms.



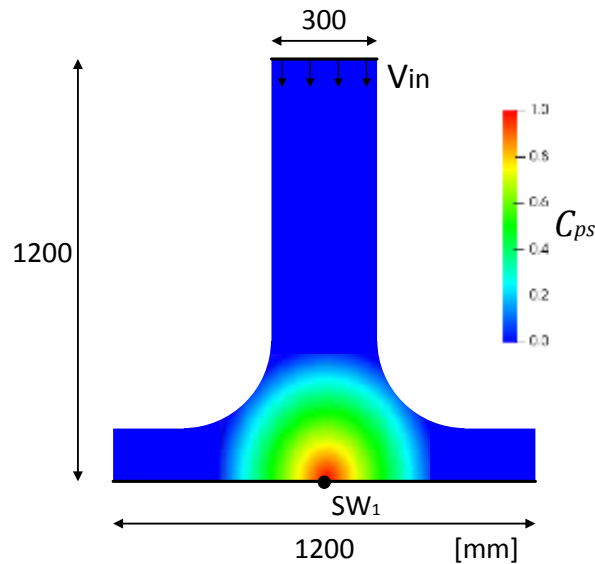
Source: the author.

3.6.2 2D WATER JET

Here a 2D case of hydrodynamic load due to a steady high velocity jet is considered. A flat wall is hit by perpendicular water jet of which the section width is $W_{jet} = 0.3\text{m}$, located $H_{jet} = 1.2\text{m}$ above the wall of length $L_{wall} = 1.2\text{m}$. The inflow velocity is set to $V_{in} = -4\text{m/s}$. A schematic drawing of the main dimensions, pressure field and shape of the water jet after reach the steady state is shown in Figure 3.10. The fluid properties adopted herein are density of $\rho_f = 1000\text{kg/m}^3$ and kinematic viscosity of $\nu_k = 0.0$ (inviscid). The gravity effects are neglected so that the load is pure hydrodynamic one.

Table 3.5 summarizes the numerical parameters used herein.

Figure 3.10 - 2D water jet. Main dimensions, shape of the water jet after reach the steady state and sensor position (SW_1). Pressure field in steady state flow.

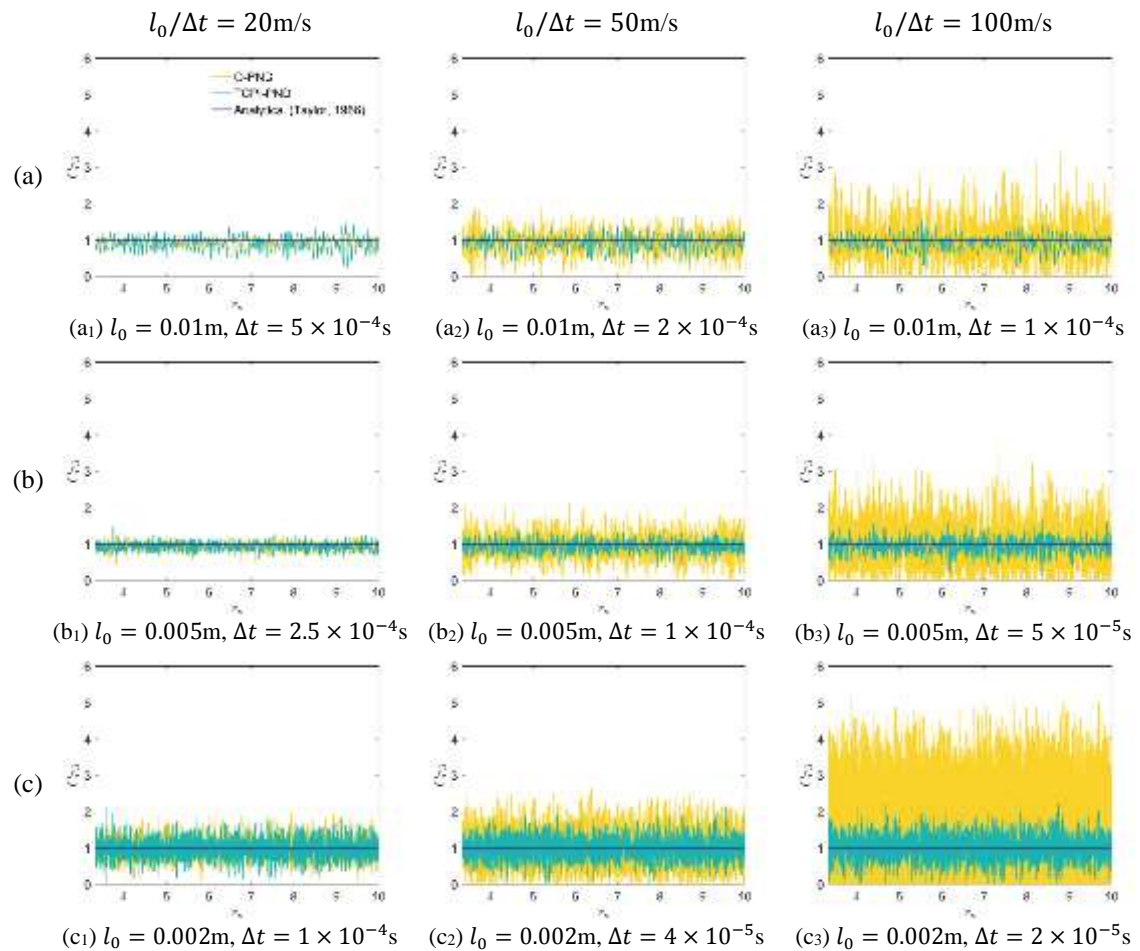


Source: the author.

The evolution of the non-dimensional pressure coefficient $C_{PS} = P/P_s$ computed at sensor SW_1 (see Figure 3.10) and the theoretical pressure coefficient $C_{PS} = 1$, represented by a blue solid line, are compared in the following analysis. $P_s = 0.5\rho_f V_{in}^2$ is the steady state analytical solution of the pressure at the stagnation point (null velocity) (Taylor, 1966). The dimensionless time (τ_u) is defined as $\tau_u = t|V_{in}|/H_{jet}$.

Figure 3.11 provides the time series of raw pressure coefficients computed by using O-PND and TCPI-PND source terms. The figure shows that computed pressure coefficients agree well with the analytical one. Similar to the previous results from the hydrostatic simulations, again higher pressure oscillations associated to the decrease of time step are computed when the original formulation O-PND is applied, whereas a better performance is achieved by the application of the proposed source term TCPI-PND ensuring a lower pressure oscillation, almost independent of the time step.

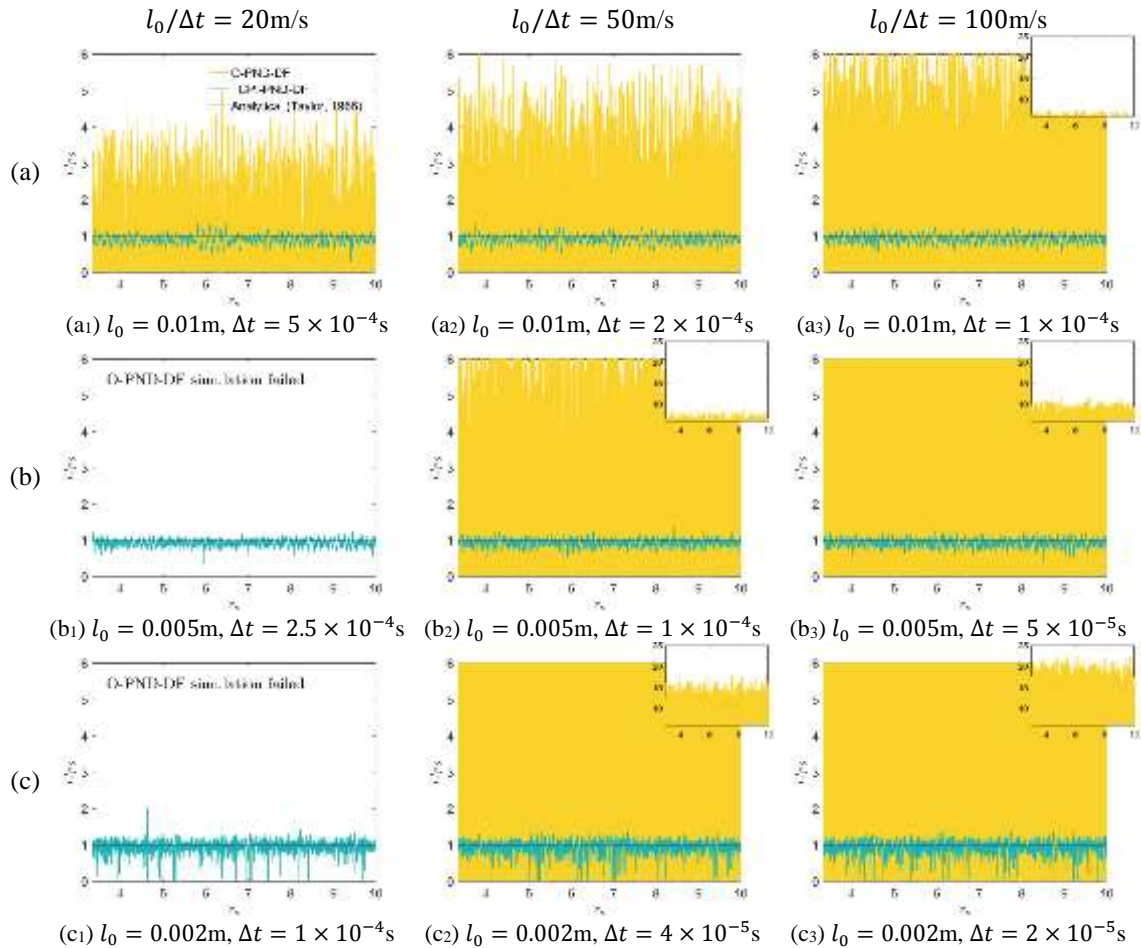
Figure 3.11 - Hydrodynamic pressure at sensor SW₁. Source terms with the zero variation of the particle number density O-PND and TCPI-PND.



Source: the author.

The time series of raw pressure coefficients computed by using O-PND-DF and TCPI-PND-DF source terms are presented in Figure 3.12. The amplitude of the spurious pressure oscillations computed by adopting O-PND-DF become significantly higher for smaller time steps, while they are almost independent of the time step when computed by using the TCPI-PND-DF source term. Moreover, the adoption of O-PND-DF do not only give higher spurious pressure oscillations but also cause unstable simulations for $l_0 = 0.005\text{ m}$ with $\Delta t = 2.5 \times 10^{-4}\text{ s}$, and $l_0 = 0.002\text{ m}$ with $\Delta t = 1 \times 10^{-4}\text{ s}$ (see Figure 3.12(b₁) and (c₁)).

Figure 3.12 - Hydrodynamic pressure at sensor SW₁. Source terms with the zero variation of the particle number density and velocity-divergence-free condition O-PND-DF and TCPI-PND-DF.



Source: the author.

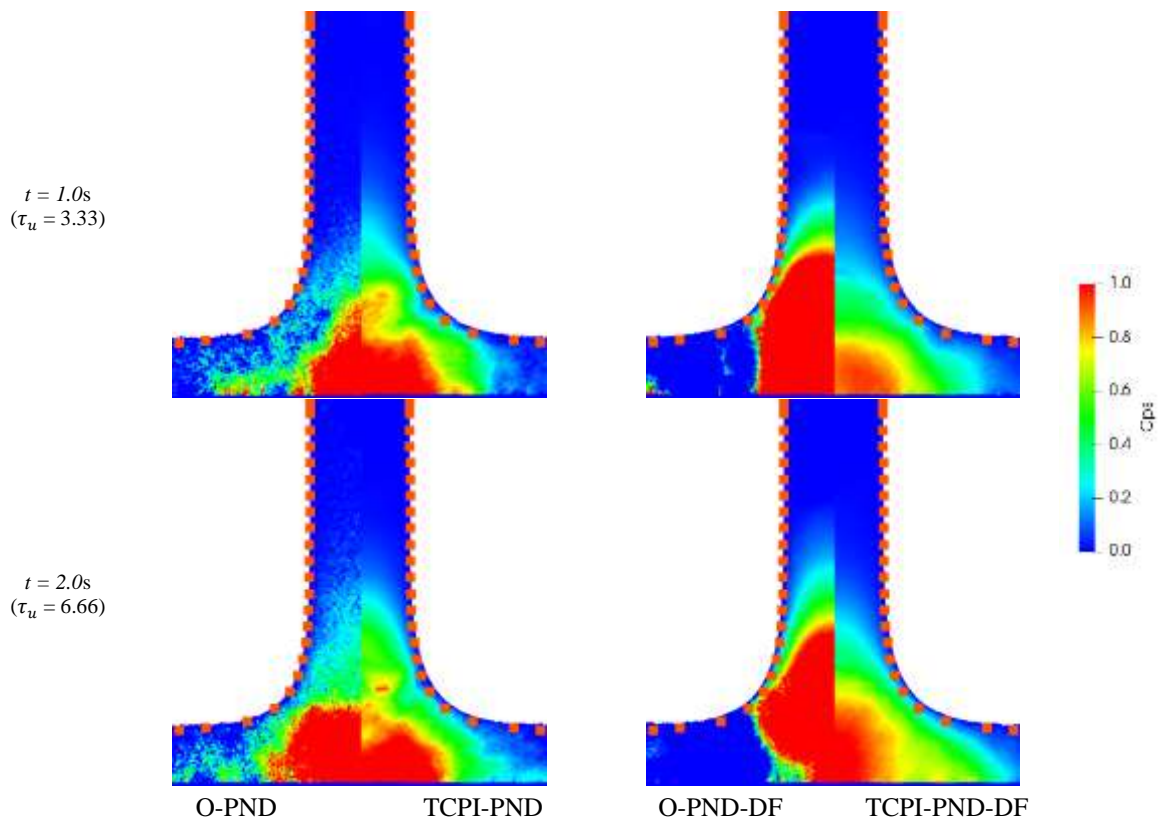
Figure 3.13 illustrates the computed pressure fields at the instants $t = 1.0$ and 2.0s ($\tau_u = 3.33$ and 6.66). Also, the contour shape (x_s, y_s) of jet, a perpendicular water jet impinging on a rigid wall obtained by the steady state analytical solution (Milne-Thomson, 1968) is marked by the orange squares:

$$y_s = L \left\{ \frac{1}{2} + \frac{1}{\pi} \ln \left(\coth \left[\frac{\pi}{4} \left(\frac{2x_s}{L} - 1 \right) \right] \right) \right\}. \quad (3.21)$$

In Figure 3.13, half of the symmetric water jet geometry represent the result with each of the source terms. The simulations with original sources O-PND and O-PND-DF are characterized by unphysical pressure distributions and significant oscillations in time. The adoption of the proposed approach results in improved pressure fields and smaller variation in time. Especially, TCPI-PND source term leads to better pressure distribution, although there still exist some numerical pressure oscillation. The proposed TCPI-PND-DF source term provides

significantly enhanced pressure field characterized by almost semi-ellipsoidal and distinctive smooth pressure contours at the high-pressure region in the vicinity of the stagnation point. All source terms capture the free surface solution in a satisfactory way.

Figure 3.13 - 2D water jet pressure field. Original O-PND and O-PND-DF, and proposed TCPI-PND and TCPI-PND-DF source terms. Distance between particles $l_0 = 0.01\text{m}$ and time step $\Delta t = 5 \times 10^{-4}\text{s}$. Evolution of water jet profile at times $t = 1.0$ and 2.0s ($\tau_u = 3.33$ and 6.66). The orange squares represent the free-surface steady state analytical solution (see Eq. (3.21)).

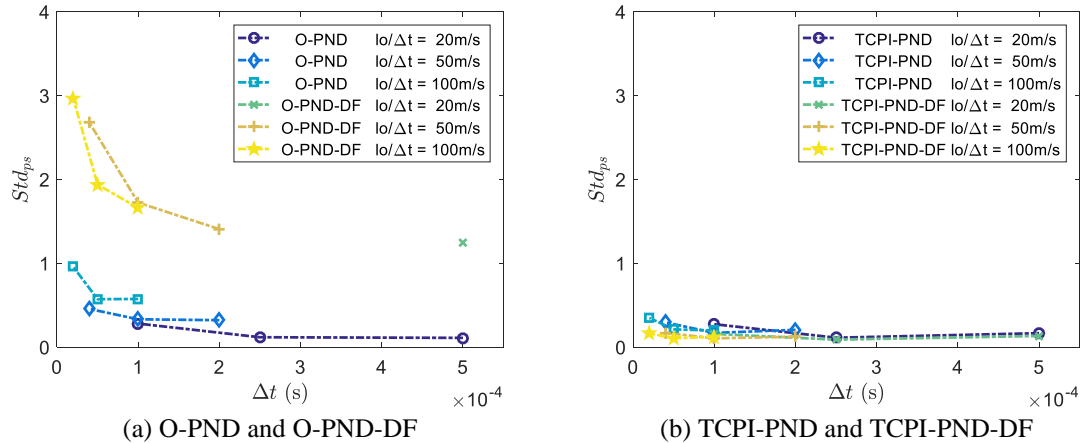


Source: the author.

In order to show how the pressure is affected by time step, the standard deviation (Std), see Eq. (3.17), of pressure coefficient between the instants $t = 1$ ($\tau_u = 3.33$) and 3s ($\tau_u = 10$), i.e. flow in steady state, is given in Figure 3.14. From the Figure 3.14(a), the standard deviations obtained O-PND and O-PND-DF increase with reduction of the time step, while in Figure 3.14(b), the numerical results demonstrated that the pressure oscillations become almost independent to both time step and particle distance after the adoption of the proposed source terms TCPI-PND and TCPI-PND-DF. As already commented, the simulations for $l_0 = 0.005\text{m}$ with $\Delta t = 2.5 \times 10^{-4}\text{s}$ and $l_0 = 0.002\text{m}$ with $\Delta t = 1 \times 10^{-4}\text{s}$ by using O-PND-DF

were unstable. Therefore, the standard deviations of these simulations are not computed and not plotted here.

Figure 3.14 - 2D water jet. Standard deviation (Std) of pressure. (a) Original O-PND and O-PND-DF, (b) proposed TCPI-PND and TCPI-PND-DF source terms.

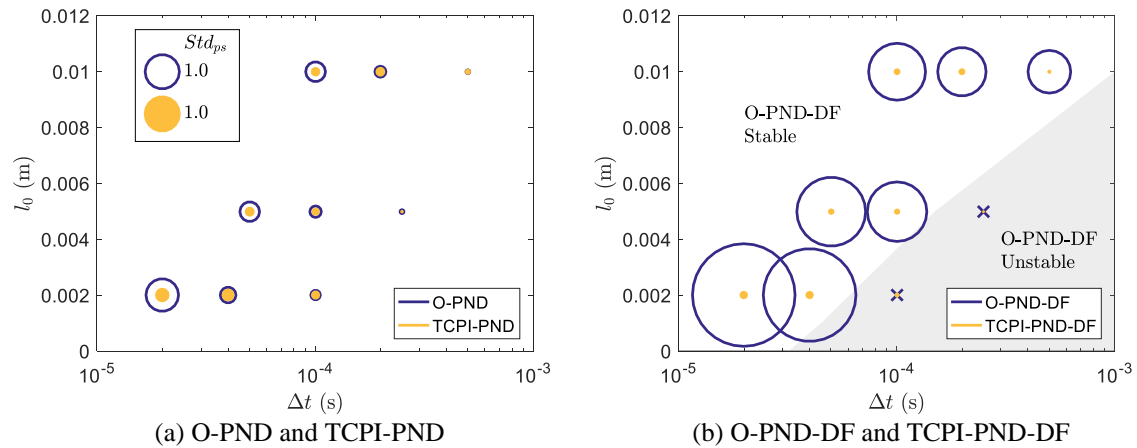


Source: the author.

Figure 3.15 gives an overview of the performances of the source terms in the pure hydrodynamic case.

The direct comparison between the results of O-PND with TCPI-PND provided by Figure 3.15(a) shows the improvements achieved by the proposed approach, which leads to much more stable pressure computation as the time step decreases. On the other hand, the direct comparison between the results of O-PND-DF with TCPI-PND-DF in Figure 3.15(b) shows clearly that, in this pure hydrodynamic case, the source term O-PND-DF produces the worst results, while TCPI-PND-DF achieved the most stable computation. The darker background shaded in Figure 3.15(b) are used to identify the region the O-PND-DF source term fails. As already commented, the simulations for $l_0 = 0.005$ m with $\Delta t = 2.5 \times 10^{-4}$ s, and $l_0 = 0.002$ m with $\Delta t = 1 \times 10^{-4}$ s by using O-PND-DF were unstable and are indicated by the cross markers. Underlying colors in Figure 3.15(b) are used to identify the region the O-PND-DF source term fails.

Figure 3.15 - 2D water jet. Standard deviation (Std) of pressure in spatial-time region. The magnitude of Std is represented by the circle's diameter and cross markers represent failed simulations. (a) O-PND and TCPI-PND, (b) O-PND-DF and TCPI-PND-DF source terms. Underlying colors are used to identify the region in which the O-PND-DF computations failed.



Source: the author.

3.6.3 2D DAM BREAKING

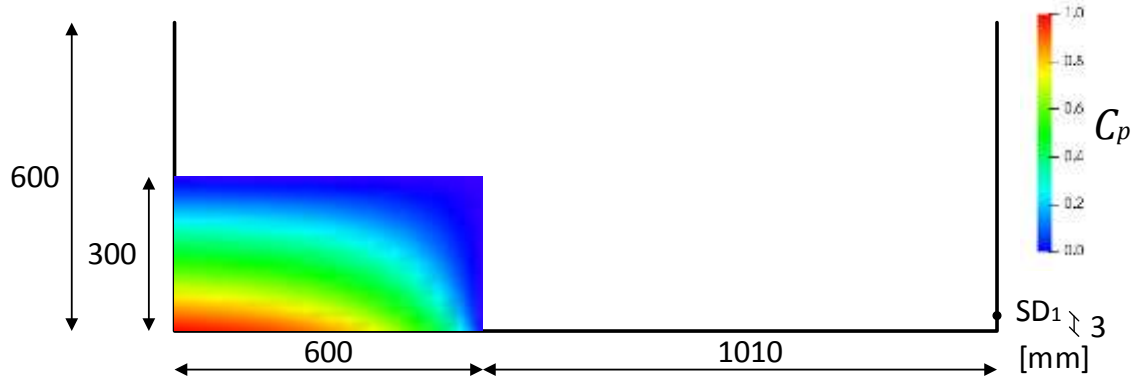
In order to verify the performance of the proposed source terms concerning the computation of transient hydrodynamic impact loads, the numerical simulation of a 2D dam-break flow is carried out. Figure 3.16 shows the main dimensions of the tank of height $H_T = 0.6\text{m}$ and length $L_T = 1.61\text{m}$, and the water column of height $H_F = 0.3\text{m}$, length $L_F = 0.6\text{m}$ (Lobovský et al., 2014) and initial hydrostatic pressure given by (Pohle, 1951; Cao et al., 2018):

$$P_0(x, y) = \rho_f g (H_F - y) - \frac{8\rho_f g H_F}{\pi^2} \sum_{k=0}^{100} \left[\frac{1}{(2k+1)^2} e^{\frac{(2k+1)\pi x}{2H_F}} \cos\left(\frac{2k+1}{2H_F} \pi y\right) \right]. \quad (3.22)$$

The fluid properties are density of $\rho_f = 997\text{kg/m}^3$ and kinematic viscosity of $\nu_k = 0.89 \times 10^{-6}\text{m}^2/\text{s}$. Numerical pressures computed by the original and proposed source terms are compared against experimental pressure at sensor SD_1 at bottom corner of the opposite side wall, 3mm height from the bottom. The numerical parameters presented in

Table 3.5 are adopted for all simulations.

Figure 3.16 - 2D dam breaking. Main dimensions and sensor position (Lobovský et al., 2014). Pressure field in the initial configuration (see Eq. (3.22)).

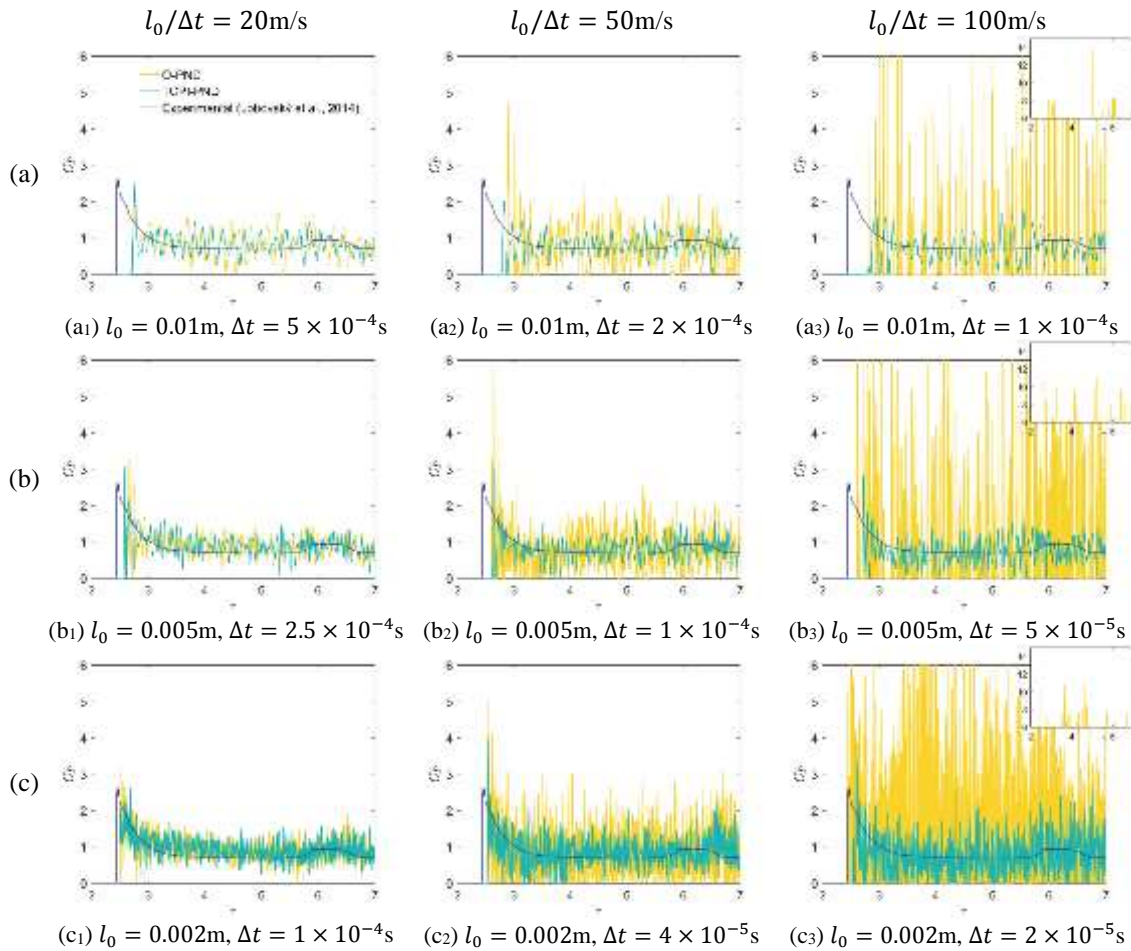


Source: the author.

The time histories of non-dimensional pressure coefficient $C_p = P/\rho_f gH$ at sensor SD₁, without any filtering technique, are shown in Figure 3.17. The dimensionless time (τ) is defined as $\tau = t\sqrt{g/H_F}$. According to Figure 3.17, the decrease of time step or increase of the ratio $l_0/\Delta t$ increases the amplitude of pressure oscillations computed by using O-PND. On the other hand, despite some oscillations still remains, much lower oscillation magnitudes, whose values are almost independent to the numerical parameters, were obtained by using TCPI-PND, following the same tendency obtained in the previous simulations for the hydrostatic (see Figure 3.7(a₃), (b₃) and (c₃)) and the hydrodynamic cases (see Figure 3.11(a₃), (b₃) and (c₃)).

The dam-break problem is also simulated by using O-PND-DF and TCPI-PND-DF source terms. Figure 3.18 depicts the time histories of raw pressure coefficient at sensor SD₁ computed by source terms O-PND-DF and TCPI-PND-DF, which are presented together with the pressure measured in the experiment (Lobovský et al., 2014). Again, the decrease of time step, keeping the particle distance constant, produces higher pressure oscillations computed by O-PND-DF, while the pressure oscillations computed by TCPI-PND-DF are much smaller. Furthermore, within the relatively wide range of the numerical parameters analyzed herein, the magnitude of pressure oscillations computed by TCPI-PND-DF are essentially independent of time step and particle distance, showing very stable results. Moreover, since the propagation speed used in the former hydrostatic case was also adopted in this case, the results show that the straightforward calibration of c_s also works relatively well for this dynamic case.

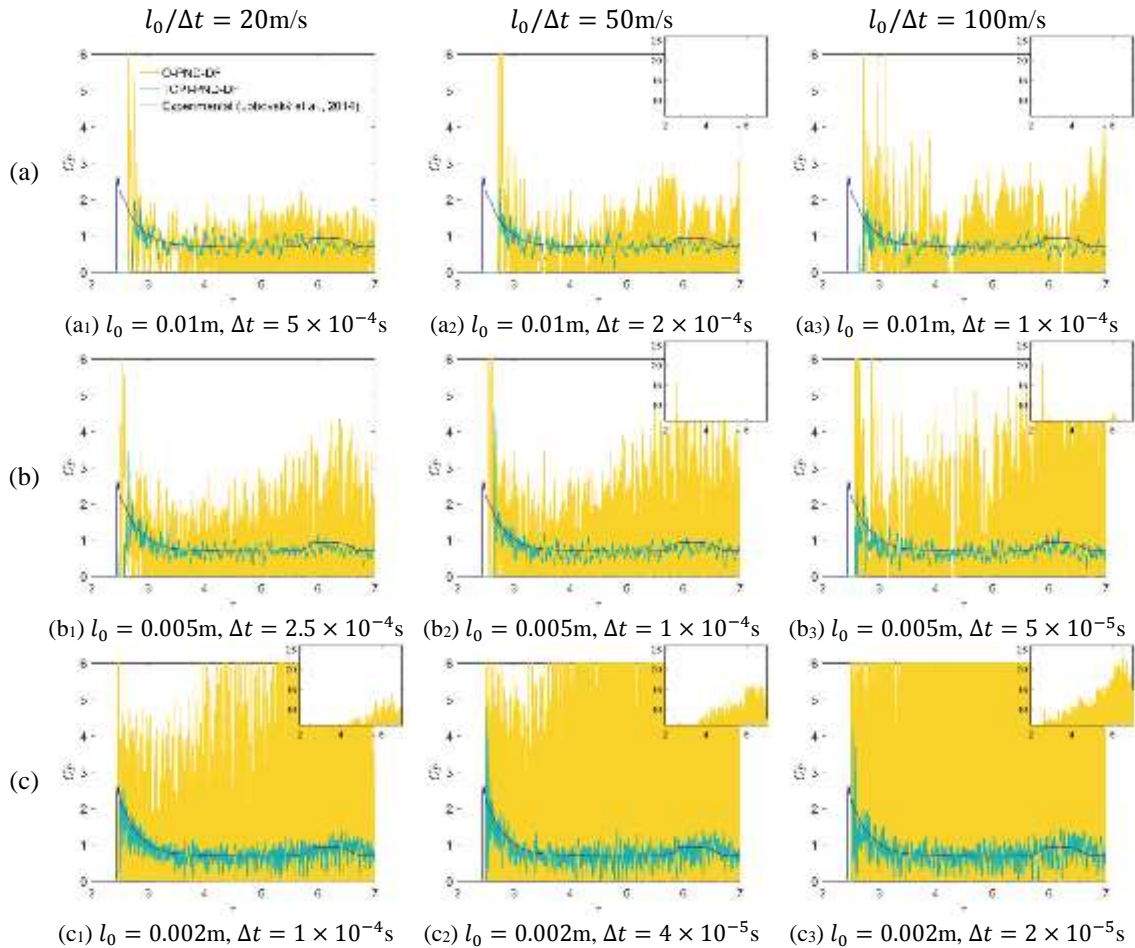
Figure 3.17 - 2D dam breaking. Pressure at sensor SD₁. Source terms with the zero variation of the particle number density and velocity-divergence-free condition O-PND and TCPI-PND.



Source: the author.

Figure 3.19 illustrates the snapshots showing free-surface profile of the collapsing water column obtained from the simulations using the O-PND and TCPI-PND, whereas Figure 3.20 presents the snapshots from O-PND-DF and TCPI-PND-DF source terms, all with distance between particles of $l_0 = 0.005\text{m}$ and time step of $\Delta t = 5 \times 10^{-5}\text{s}$. The color scale is associated to pressure magnitude. The pressure field near the stagnation point is also highlighted. The simulation carried out using O-PND leads to a rough pressure field with numerical oscillations and disordered particles. Although some unphysical pressure oscillations remained in the TCPI-PND simulations, smoother pressure field were obtained. The significant improvement achieved by adopting TCPI-PND-DF (see Figure 3.20(b)) is evidenced by a continuous and smooth pressure fields over the unphysically oscillating pressure fields obtained using O-PND or O-PND-DF.

Figure 3.18 - 2D dam breaking. Pressure at sensor SD₁. Source terms with the zero variation of the particle number density and velocity-divergence-free condition O-PND-DF and TCPI-PND-DF.



Source: the author.

In order to quantify the pressure oscillation and the error in relation to the experimental pressure, the normalized root mean square deviation (NRMSD) was calculated between the instants $\tau_1 = 3.0$ and $\tau_2 = 5.0$ and the results are shown in Figure 3.21. The NRMSD is defined here as:

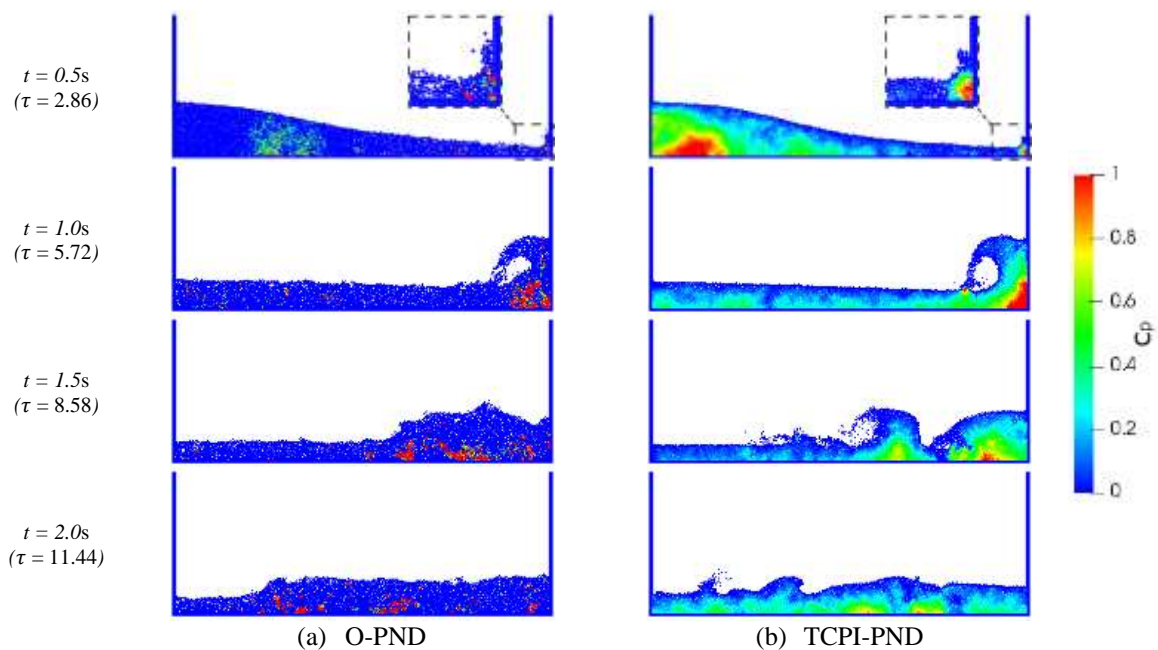
$$NRMSD = \frac{RMSD}{|\bar{p}_n|} = \frac{1}{|\bar{p}_n|} \sqrt{\frac{1}{n_v} \sum_{i=1}^{n_v} |p_{n,i} - p_{e,i}|^2}, \quad (3.23)$$

where RMSD denotes the root mean square deviation, \bar{p}_n is the mean of the computed numerical results p_n , p_e stands for the experimental results and n_v signifies the number of values computed during a time interval.

Figure 3.21(a) shows that in the case of dam breaking, the magnitude of computed pressure oscillations (NRMSD) obtained by O-PND is almost constant for a fixed $l_0/\Delta t$, when $\frac{l_0}{\Delta t} \leq 50\text{m/s}$. According to the figure, increasing of $l_0/\Delta t$ by decreasing time step or increasing the particle distance leads to higher computed pressure oscillations. On the other hand, Figure 3.21(b) shows that the influence of $l_0/\Delta t$, as well as time step and particle distance on pressure oscillations computed by using TCPI-PND is almost negligible. For all the cases analyzed herein, which cover a wide range of the numerical modeling parameters, the magnitude of pressure oscillations (NRMSD) computed by TCPI-PND is as small as the best result achieved by O-PND.

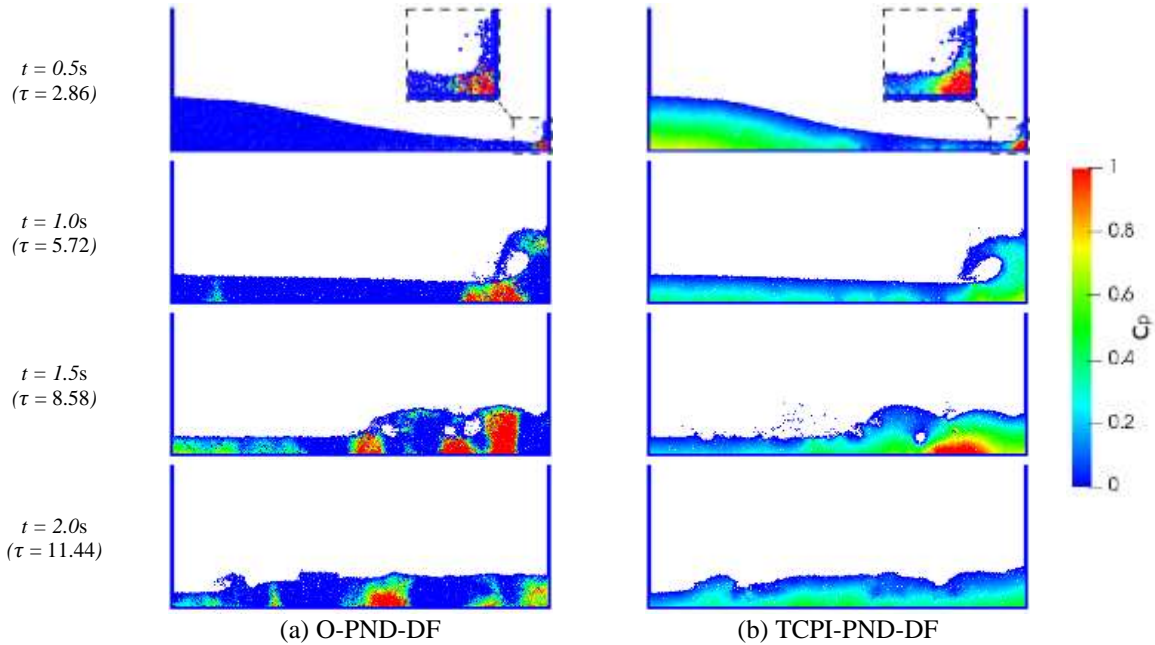
Regarding the source terms with the zero variation of the particle number density and velocity-divergence-free condition (O-PND-DF and TCPI-PND-DF) the pressure oscillations computed by O-PND-DF are very strongly influenced by the time step, meanwhile the results obtained by TCPI-PND-DF are much more stable and almost independent to both time step and particle distance.

Figure 3.19 - 2D dam breaking. Original O-PND and proposed TCPI-PND source terms. Distance between particles $l_0 = 0.005\text{m}$ and time step $\Delta t = 5 \times 10^{-5}\text{s}$. Evolution of free-surface profile at times $t = 0.50, 1.00, 1.50$ and 2.0s ($\tau = 2.86, 5.72, 8.58$ and 11.44)



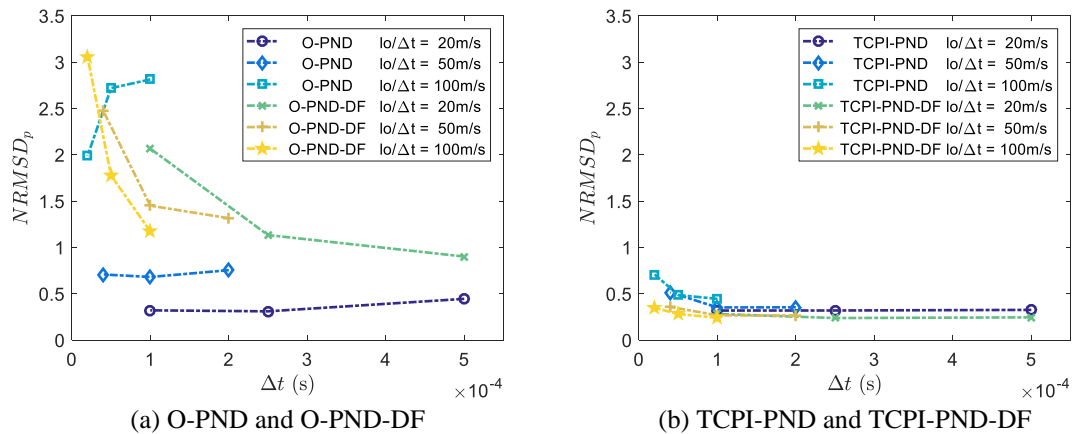
Source: the author.

Figure 3.20 - 2D dam breaking. Original O-PND-DF and proposed TCPI-PND-DF source terms. Distance between particles $l_0 = 0.005\text{m}$ and time step $\Delta t = 5 \times 10^{-5}\text{s}$. Evolution of free-surface profile at times $t = 0.50, 1.00, 1.50$ and 2.0s ($\tau = 2.86, 5.72, 8.58$ and 11.44).



Source: the author.

Figure 3.21 - 2D dam breaking. Normalized root mean square deviation (NRMSD) of pressure. (a) Original O-PND and O-PND-DF, (b) proposed TCPI-PND and TCPI-PND-DF source terms.



Source: the author.

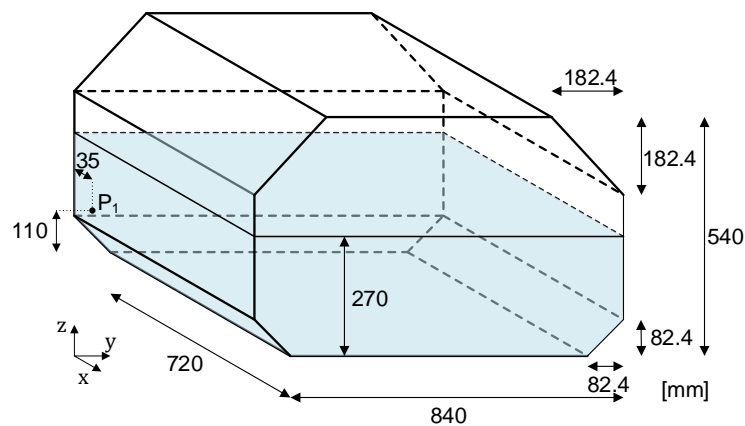
3.6.4 3D SLOSHING IN PRISMATIC TANK

The last case consists of 3D sloshing in a prismatic tank under translational coupled surge-sway (X and Y axis) motions. Figure 3.22 gives the geometry and the dimensions of the prismatic tank that have ceiling inclinations of 45 degrees with the vertical side walls. The

main dimensions of the tank are the height $H_T = 0.54\text{m}$, width $W_T = 0.84\text{m}$ and length $L_T = 0.72\text{m}$. In order to avoid hydroelastic effects, the tank was manufactured with Plexiglass of thickness $e_T = 30\text{mm}$. The performance of the proposed approach for the assessment of violent impact loads was evaluated for a filling ratio of 50% ($H_F = 0.27\text{m}$). The periods of surge and sway rotations are both selected to be $T_s = 1.25\text{s}$ with amplitude motions of $A_x = 0.0144\text{m}$ ($0.02 \times \text{length}$) and $A_y = 0.0168\text{m}$ ($0.02 \times \text{width}$). The experiment was carried out by the authors and the dynamic pressure at P_1 was measured by a piezoelectric pressure sensor (Kistler 211B6) and the sloshing wave motions were captured by a video camera.

In the numerical simulations, an initial particle spacing $l_0 = 0.01\text{m}$ and four time steps $\Delta t = 5, 2, 1, 0.5 \times 10^{-4}\text{s}$ were adopted. The fluid properties are density $\rho_f = 1000\text{kg/m}^3$, and kinematic viscosity of $\nu_k = 1.0 \times 10^{-6}\text{m}^2/\text{s}$. The relaxation parameter $\gamma = 0.01$ and the propagation speed of the perturbations $c_s = 2\text{m/s}$ were used herein. The simulations were carried out up to 20s, i.e., 16 cycles of excitations.

Figure 3.22 - Schematic view of 3D sloshing. Main dimensions of tank, filling height and sensor position P_1 .

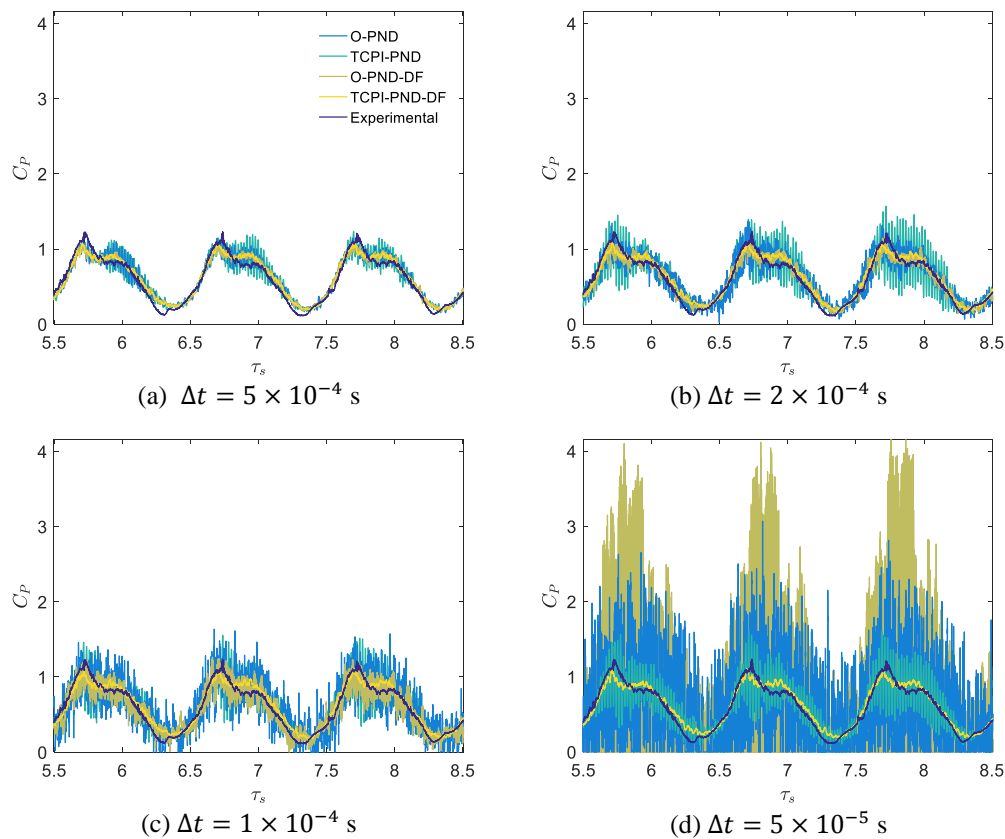


Source: the author.

The non-dimensional pressure coefficient $C_p = P/\rho_f gH$ at P_1 measured experimentally and computed numerically are shown in Figure 3.23. Both the experimental and numerical results consist of raw data, along the dimensionless time defined as $\tau_s = t/T_s$, obtained from the measurements and computations without any filtering technique. The results show that the general behaviors of the source terms regarding the time-stability of the pressure computation in the 3D cases are similar to the former 2D cases. For $\Delta t \geq 1 \times 10^{-4}\text{s}$, pressures computed by O-PND and TCPI-PND present similar oscillations. Nevertheless, when the time step is

reduced to 5×10^{-5} s, much higher pressure oscillations were computed by O-PND than TCPI-PND. On the other hand, significant improvements have been achieved by adopting TCPI-PND-DF, which lead to a very robust computation due to its stable results regardless of the variation of the numerical parameters. This robustness is followed by TCPI-PND-DF, and then original formulations O-PND and O-PND-DF, with the last one being the worst one very sensitive to the reduction of time step. In addition to this, the pressures computed by TCPI-PND-DF are in fairly good agreement with the experimental result, even for the coarse particle distance adopted here.

Figure 3.23 - 3D sloshing in prismatic tank. Pressure at sensor P₁. Source terms with the zero variation of the particle number density (O-PND and TCPI-PND) and velocity-divergence-free condition (O-PND-DF and TCPI-PND-DF). Cases simulated with $l_0 = 0.01$ m.



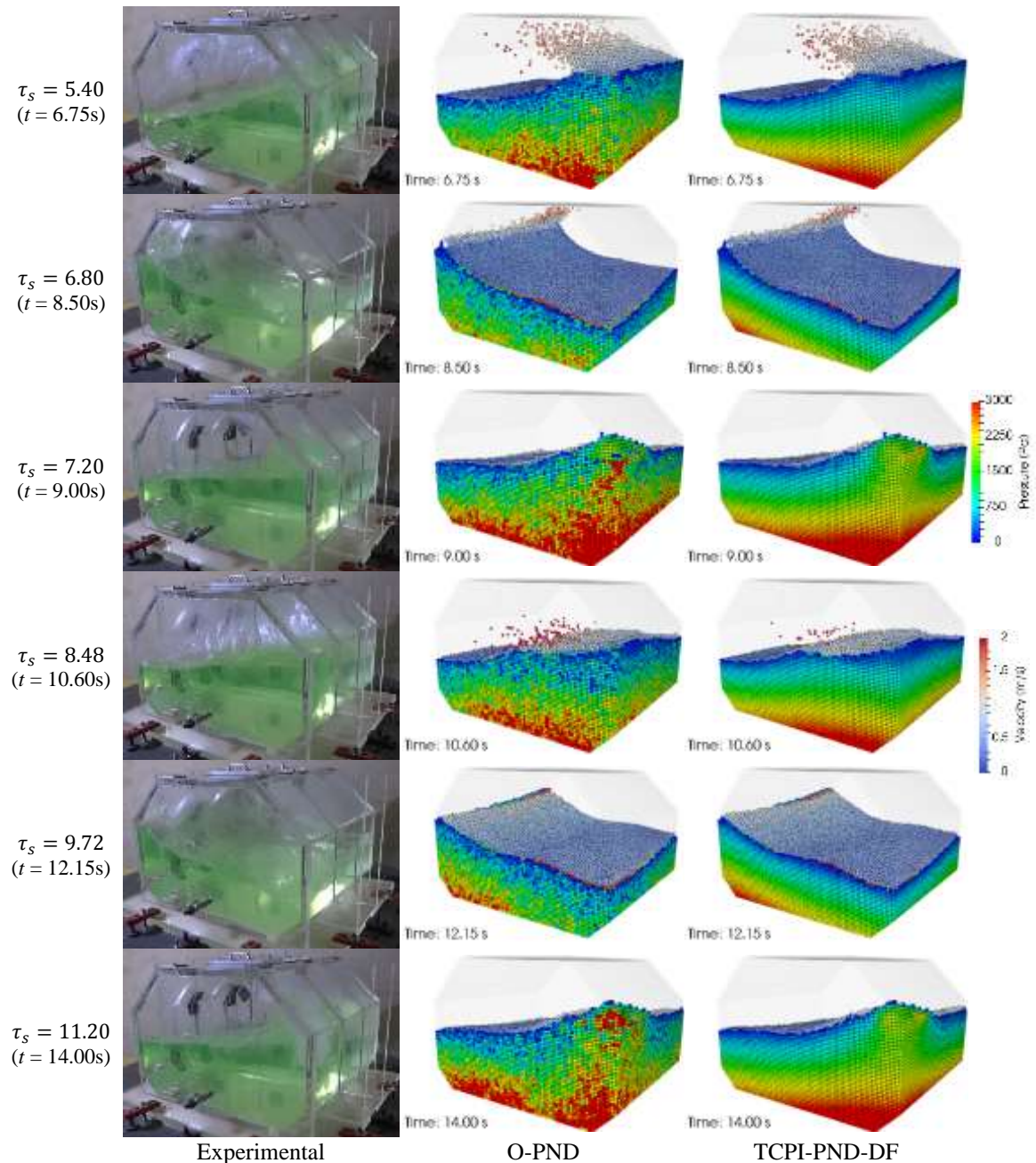
Source: the author.

Sloshing wave profiles at different instants, obtained experimentally and computed by using O-PND and TCPI-PND source terms with the distance between particles $l_0 = 0.01$ m and time step $\Delta t = 1 \times 10^{-4}$ s, are presented in

Figure 3.24. In the numerical results, the pressure distributions on the walls and velocity field on the free surface are also shown according the color scales. Both simulations capture the highly deformed sloshing waves involving fluid fragmentation and merging. The superposition of the wave components in the length and width directions of the tank generates a swirling wave motion. The swirling wave hits one corner of the tank at the instants $\tau_s = 5.40, 7.20$ and 11.20 , whereas another corner is hit at $\tau_s = 6.80$ and 9.72 , approximately. At the instant $\tau_s = 8.48$, the splashing collapses and impacts on the main water body. Compared to O-PND, the TCPI-PND-DF simulation has substantially reduced pressure fluctuations, thereby providing a more smooth and realistic pressure distribution.

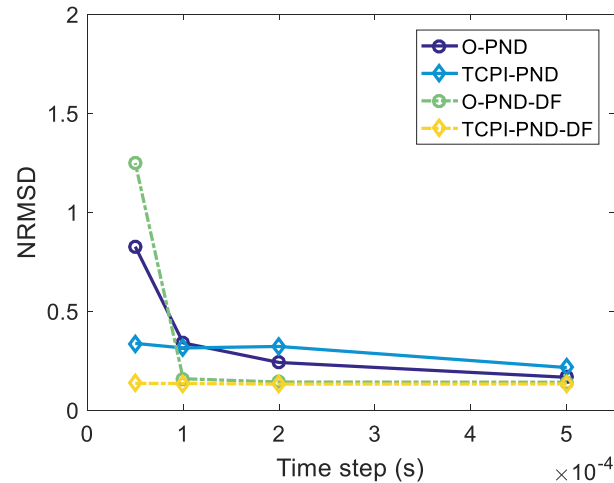
Figure 3.25 illustrates the normalized root mean square deviations (NRMSD), see Eq. (3.23), calculated between the instants $\tau_s = 6.4$ and 7.4 (7th cycle). Both original source terms O-PND and O-PND-DF are influenced by the time step. Especially for $\Delta t \leq 1 \times 10^{-4}$ s, the computed pressures become very unstable with very large oscillation magnitudes. In contrast, as in the previous 2D simulations, the proposed source terms TCPI-PND and TCPI-PND-DF lead a very lower dependence in relation to the time step. For O-PND with fine-tuned relaxation parameter γ , the magnitude of pressure oscillation might be slightly lower than TCPI-PND when relatively larger time steps are adopted. However, it important to emphasize that with such large time steps generally the numerical stability criteria (Eq. (3.1)) might be a concern for the computation. Finally, it is interesting to point out the lower pressure oscillation obtained by TCPI-PND-DF compared to another source terms, indicating that for this specific situation, with high-impulsive cyclic loads, the adoption of the divergence-free condition is highly recommended.

Figure 3.24 - Experimental and numerical simulations of 3D sloshing. Original O-PND and proposed TCPI-PND-DF source terms. Distance between particles $l_0 = 0.01\text{m}$ and time step $\Delta t = 1 \times 10^{-4}\text{s}$. Evolution of free-surface profile at times $t = 6.75, 8.50, 9.00, 10.60, 12.15$ and 14.0s ($\tau_s = 5.40, 6.80, 7.20, 8.48, 9.72$ and 11.20).



Source: the author.

Figure 3.25 - 3D sloshing in prismatic tank. Normalized root mean square deviation (NRMSD) of pressure. Original O-PND and O-PND-DF, and proposed TCPI-PND and TCPI-PND-DF source terms. Distance between particles of $l_0 = 0.01\text{m}$.



Source: the author.

3.7 CONCLUDING REMARKS

By considering the momentum conservation of the particle-level collision/impact, a correction between numerical and physical duration of the impulses is proposed. Then, relying on so-called time-scale correction of particle-level impulses (TCPI), which introduces a correction factor for the computation impulsive loads, new formulations for the source terms of the pressure Poisson equation (PPE) were derived based on density and divergency free criteria. As a result, TCPI-PND and TCPI-PND-DF source terms, directly dependents of the spatial discretization, are also proposed for more time-consistent computations that leads to more stable and robust computations.

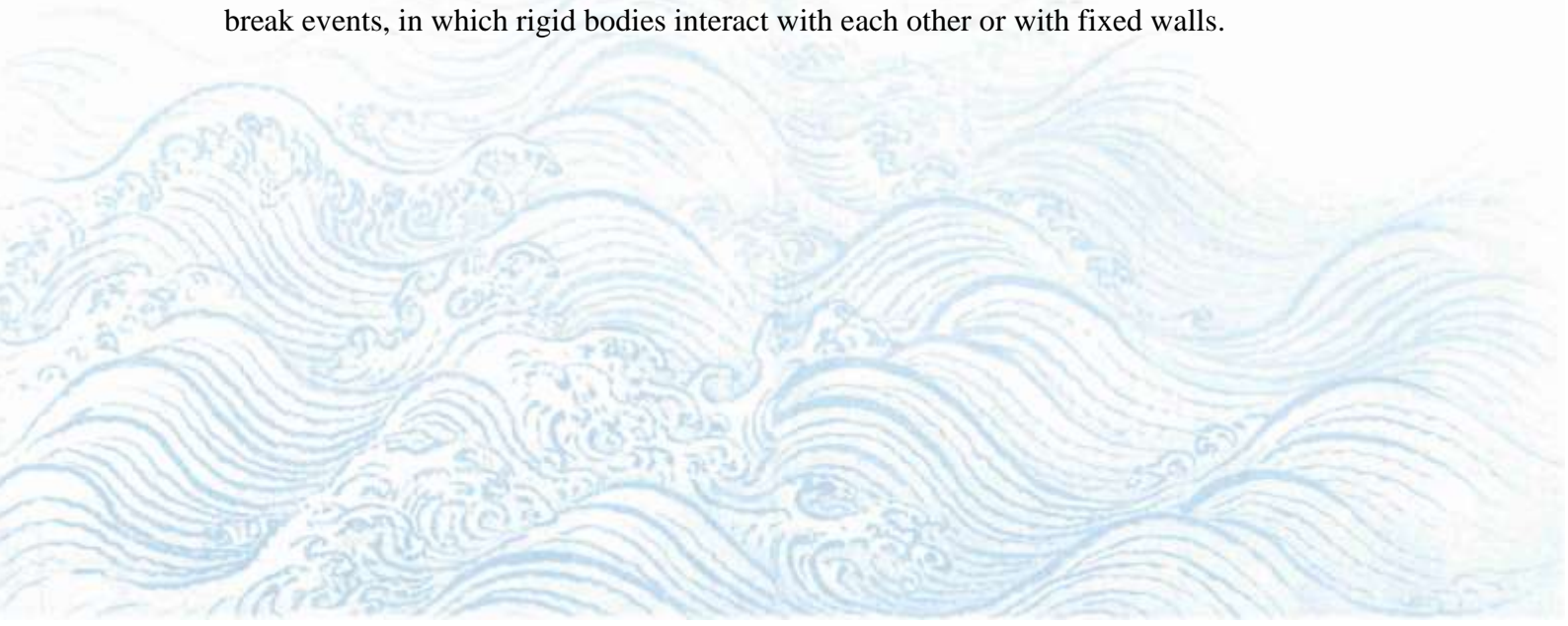
The comparison between the raw computed pressures obtained by the proposed source terms and those from original source terms, analytical or experimental ones show that the proposed source terms are more stable, with computed pressure nearly independent to time steps. As a result, beside increasing remarkably the robustness of the numerical method by extended the range of stable computation, they lead to significant improvement on the stability of the pressure computation by mitigating unphysical oscillations. Especially regarding the new TCPI-PND-DF source term, it achieved the most stable results with smooth pressure fields in all the situations tested in the presented study and is recommended for further applications. These features confirmed the effectiveness of the proposed time-scale correction of the particle-level impulses (TCPI) in the improvement of the stability of the computation.

From the viewpoint of practical engineering applications, instead of pressure relaxation coefficient that requires empirically calibration and adjustment, the only numerical parameter required in the proposed source terms is the propagation speed of the perturbations c_s , of which the calibration is much more straightforward due to its physical meaning. The calibration of the coefficient c_s was conducted and a range of reference value was provided for hydrodynamic problems dominated by gravitational forces, e.g., water wave motions. Also, in comparison to other spurious pressure oscillation mitigation strategies, the proposed approach is of extremely simple implementation and, the most relevant point, no additional computational effort is demanded to the already compute-intensive numerical method. Moreover, the proposed approach can be easily combined with the other strategies to further improve the stability and accuracy of pressure assessment.

CHAPTER 4

RIGID BODIES CONTACT FOR PARTICLE-BASED METHODS

Many problems of fluid–structure interaction with free-surface flow and multiple bodies are highly nonlinear phenomena, which is challenging for computational modeling and simulation. Particle-based methods have been proven to provide a substantial potential for simulation of free-surface fluid flows and their interactions with multiple solids that are often encountered in fluvial and coastal mechanics fields, due to their benefits from using Lagrangian tracking scheme and meshless nature. When contact between solids occurs, a numerical modeling to detect it and prevent penetration between bodies is required to avoid numerical inconsistencies. The objective of this work is to propose a solid-solid contact model that relays on contact mechanics theories and, by an effective way to determine the normal direction of contact, as well as the distance between bodies faces, eliminates the numerical instabilities induced by non-smooth modeling of bodies surfaces in the particle-based methods. The model adopts a penalty-based method that uses a nonlinear spring and dashpot concept, and thus reproducing the macroscopic properties of the multiple bodies interactions. To avoid very small time step for all the domain, a dynamic sub-cycling algorithm for rigid bodies contact is adopted. First, the present fluid solver, based on the moving particle semi-implicit (MPS) method, is validated by hydrodynamic and fluid-structure interaction problems. Then, analytical and numerical results are compared, demonstrating the improvements achieved by the proposed model. Finally, the present model is validated via three-dimensional (3D) dam-break events, in which rigid bodies interact with each other or with fixed walls.



4.1 BACKGROUND

Fluid-structure interactions (FSI) comprising free-surface flow and multiple bodies are highly nonlinear hydrodynamic phenomena, and they are challenging problems for computational modeling and simulation. Among the effective numerical methods used to simulate the complex free-surface flow with moving bodies, an important approach is the meshless Lagrangian particle-based method, in which the physical domain is represented by a set of points (particles). As the representatives of the meshless Lagrangian particle-based method for fluid and solid modeling, we have smoothed particle hydrodynamics (SPH) method (Gingold & Monaghan, 1977; Lucy, 1977), and moving particle semi-implicit (MPS) method (Koshizuka & Oka, 1996). Nowadays, there are innumerable variations of these two methods (Li et al., 2020; Lind et al., 2020). Besides the difference between the discrete operators adopted by these two methods, essentially most of the existing SPH methods use equation of state and explicit algorithm that are suitable for flow with limited compressibility, while MPS methods are based on semi-implicit algorithm with the solution of the pressure Poisson equation (PPE), which models perfectly the incompressible flow. However, despite the easy implementation and flexibility of these methods, one of the relevant topics for the modeling of FSI with multiple bodies is concerning the numerical treatment of contacts among rigid bodies.

Based on contact mechanics theories, the objective of this work is to propose a solid–solid contact model for the particle-based methods, especially for the MPS method, by adopting a nonlinear spring and dashpot model for solid–solid contact, similar to that adopted by Canelas et al. (2016), but with newly defined normal direction and distance of contact vectors to improve the numerical stability, and therefore reproducing the macroscopic properties of the multiple bodies interactions in transient incompressible flows involving free surface and impulsive hydrodynamic loads. Although the proposed model can be applied in other particle-based methods, in this work we use only in the MPS because it is generally expected to provide higher accuracy in terms of hydrodynamic load calculation and also to contribute toward the increase in work on solid-solid contact in MPS. Adopting the original idea of Koshizuka et al. (1998), the shell of a rigid body is represented by a cluster of particles whose relative positions remain unchanged. The overall contact force on the rigid body is calculated by summation of contributions due to the contact between particles belonging to different rigid bodies, similar to multi-sphere approach (Favier et al., 1999).

Using finite number of particles to represent only the shell of the rigid bodies enables the easy modeling of complex body shapes, with their precision dependent of the model resolution. However, it may induce some geometrical anomalies such as non-smooth modeling of a plane. As a result, oscillations in the computation of distance between pair of nearest particles belonging to different bodies with relative motion might lead to incorrect contact detection. In order to address this issue, beside a simple way to accurately determine the normal direction of contact, an approach based on the faces of the bodies and contact force computed taken into account the normal vectors of solid walls is proposed in the present work. The proposed approach improves significantly the stability and provides a relatively robust behavior for the solid-solid contact, besides its simple implementation.

Following this introduction, a concise summary of relevant published works is provided in Sect. 4.2. The main features of the numerical model and validations of the fluid solver are outlined in Sect. 4.3. The Sect. 4.4 contemplates the contact model and its improvements by comparing numerical and analytical energy and linear momentum of a collision between three bodies, and numerical and analytical position and velocity of a block subject to gravity and slides on a slope. Validations of the contact model by high complex interactions of fluid with multiple bodies, such as 3D dam-break events, in which heavy cubic bodies interact with each other and with fixed walls (Canelas et al., 2016) are illustrated in Sect. 4.6. Numerical results of solid position obtained by the proposed model are compared with available experimental and numerical results. The Sect. 4.7 provides some conclusions about the proposed model.

4.2 RELATED WORK

Recently, different techniques have been proposed for particle-based methods to deal with the contact between solids. Regarding the SPH method, several works on the contact among solids can be found. Harada et al. (2007) proposed real-time coupling of fluid and rigid body problems where the contact between rigid bodies is computed by repulsive forces composed of linear springs proportional to the overlap between particles, and dashpots proportional to the relative velocities of colliding particles, similar to the model adopted in the discrete element method (DEM) (Cundall & Strack, 1979). An impulse-based boundary force to solve rigid body interaction has been proposed by Oh et al. (2009). Compared to previous potential-based forces used in SPH, the impulse-based boundary force leads more stable and accurate results in rigid body interactions. Amicarelli et al. (2015) adapted the boundary force particles to treat contact among solids in the SPH. Validations of the model were carried out by bi-dimensional (2D) and three-dimensional (3D) benchmark test cases, which include a dam

breaking with 3D body transport. SPH method has also been adopted by Asai and Chandra (2016) to study wash-out phenomenon of bridge upper structure during tsunami, where the initial contact between girder and pier bridge has been modeled by using a penalty-based model composed of nonlinear springs and linear dashpots. A coupling of the SPH and a variation of the DEM method with distributed contact formulation, similar in concept to those employed by both Zhang et al. (2009) and Ren et al. (2014), was proposed by Canelas et al. (2016), in which a nonlinear spring dashpot model was applied for the solid–solid interactions. In addition to the previous works, SPH-DEM coupling has also been adopted by many researchers on the multiphase fluid-solid interaction in granular materials, i.e., no bond between rigid particles (Robb et al., 2016; Tang et al., 2018). Except the algorithm proposed by Tanaka et al. (2007), based on linear spring dashpot model, the DEM-MPS hybrid model introduced by Gotoh et al. (2009) to predict the motions of armor blocks and to study the interaction between fluid flow and sediment particles in the formation process of ripples on the swash zone (Harada et al., 2018), to the best knowledge of the authors, there is almost no study reporting numerical approaches to deal with contact between rigid bodies in the incompressible MPS method, which solves more rigorously the incompressible hydrodynamic problems.

4.3 NUMERICAL METHOD

4.3.1 MOVING PARTICLE SEMI-IMPLICIT (MPS) METHOD

To solve the incompressible viscous flow, the semi-implicit algorithm already detailed in the Chapter 2 was used herein. Since the implementations and investigations of this thesis were carried out at the same time, an original source term was used in the present simulations instead of the proposed source terms presented in the previous chapter. The numerical operators adopted in the cases illustrated in this chapter are given in Table 3.1.

The artificial compressibility factor $\alpha_c = 10^{-8} \text{ ms}^2/\text{kg}$ was adopted for all simulations of this chapter. The relaxation coefficient was chosen in the range $0.01 \leq \gamma \leq 0.05$ (Lee et al., 2011).

Table 4.1: Numerical operators applied in the problems presented in this chapter.

Numerical operator	Equation
Weight function	$\omega_{ij} = \begin{cases} \frac{r_e}{\ \mathbf{r}_{ij}\ } - 1 & \ \mathbf{r}_{ij}\ \leq r_e \\ 0 & \ \mathbf{r}_{ij}\ > r_e \end{cases}$
Particle number density	$n_i = \sum_{j \in \mathbb{P}_i} \omega_{ij}$
Pressure gradient	$\langle \nabla P \rangle_i = \left[\sum_{j \in \mathbb{P}_i} \frac{\mathbf{r}_{ij}}{\ \mathbf{r}_{ij}\ } \otimes \frac{\mathbf{r}_{ij}^T}{\ \mathbf{r}_{ij}\ } \omega_{ij} \right]^{-1} \sum_{j \in \mathbb{P}_i} \frac{P_j - \hat{P}_i}{\ \mathbf{r}_{ij}\ ^2} \mathbf{r}_{ij} \omega_{ij}$
Divergent of velocity	$\langle \nabla \cdot \mathbf{u} \rangle_i = \frac{dim}{n^0} \sum_{j \in \mathbb{P}_i} \frac{\mathbf{u}_j - \mathbf{u}_i}{\ \mathbf{r}_{ij}\ ^2} \cdot \mathbf{r}_{ij} \omega_{ij}$
Laplacian of velocity	$\langle \nabla^2 \mathbf{u} \rangle_i = \frac{2dim}{\lambda_i n^0} \sum_{j \in \mathbb{P}_i} (\mathbf{u}_j - \mathbf{u}_i) \omega_{ij}$
PPE	$\langle \nabla^2 P \rangle_i^{t+\Delta t} - \frac{\rho_f}{\Delta t^2} \alpha_c P_i^{t+\Delta t} = \gamma \frac{\rho_f}{\Delta t^2} \frac{n^0 - n_i^t}{n^0} + (1 - \gamma) \frac{\rho_f}{\Delta t} \langle \nabla \cdot \mathbf{u}^{**} \rangle_i$

Source: the author.

4.3.2 RIGID BODY DYNAMICS

For the rigid body dynamics, the governing equations of motion are those of translational motion and rotational motion expressed as:

$$m_s \frac{D\mathbf{u}_s}{Dt} = \mathbf{f}_h + \mathbf{f}_g + \mathbf{f}_c = - \iint_{\mathcal{A}} P d\mathbf{a} + m\mathbf{g} + \mathbf{f}_c = - \sum_{k \in \Omega_p} P_k(l_0)^{dim-1} \mathbf{n}_k + m\mathbf{g} + \mathbf{f}_c, \quad (4.1)$$

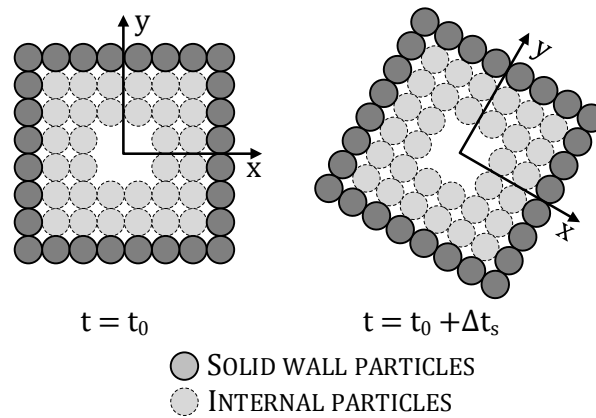
$$\mathbf{I}_s \cdot \frac{D\boldsymbol{\omega}_s}{Dt} + \boldsymbol{\omega}_s \times (\mathbf{I}_s \cdot \boldsymbol{\omega}_s) = \mathbf{T}_h + \mathbf{T}_c = - \iint_{\mathcal{A}} \mathbf{r}_s \times P d\mathbf{a} + \mathbf{T}_c = - \sum_{k \in \Omega_p} P_k(l_0)^{dim-1} \mathbf{r}_{ck} \times \mathbf{n}_k + \mathbf{T}_c, \quad (4.2)$$

where m_s is the total mass of the rigid body, \mathbf{u}_s represents the velocity vector at the center of mass (CM) of the rigid body, \mathbf{I}_s is the inertia matrix, $\boldsymbol{\omega}_s$ stands for the angular velocity vector about the principal axes of the rigid body, \mathbf{g} designates the gravity and dim is the number of spatial dimensions. The hydrodynamic forces on the rigid surface \mathbf{f}_h , gravitational force \mathbf{f}_g , contact forces between the rigid bodies \mathbf{f}_c , hydrodynamic torque \mathbf{T}_h and contact torque \mathbf{T}_c are taken into consideration for the motion of rigid bodies. The vector \mathbf{r}_s denotes the position vector from the CM of the rigid body and $d\mathbf{a}$ is the face vector of the of the rigid body surface, whose magnitude is the area of the discrete face and direction is normal to the body surface.

\mathbf{n}_k represents the normal vector of the wall at the wall particle k , \mathbf{r}_{ck} denotes the position vector between the CM of the rigid body p and the particle k , and Ω_p is the domain with solid wall particles. Focusing the impulsive hydrodynamic loads on the rigid solid, the contribution due to fluid shear forces was assumed to be negligible in the present study.

Here an approach similar to the multi-sphere DEM technique is used, in which the shell of a rigid bodies are represented by a collection of wall and internal (dummy) spherical particles whose relative positions remain unchanged, following Koshizuka et al. (1998), see Figure 4.1.

Figure 4.1 - Rigid body represented by a collection of solid wall and internal (dummy) particles in 2D space.



Source: the author.

4.3.3 TIME STEP

The Courant–Friedrichs–Lewy (CFL) condition (Courant et al., 1967) is adopted as stability criterion for fluid domain:

$$\Delta t_f < \frac{l_0 C_r}{|u_{max}|}, \quad 0 < C_r \leq 1, \quad (4.3)$$

where Δt_f is the time step of the fluid domain, u_{max} is the maximum velocity and C_r is the Courant number.

The transient response for the contact among rigid bodies requires a much smaller time step than that adopted for incompressible flows. To avoid the use of very small time step for the fluid domain, which increases computational cost, a dynamic sub-cycling algorithm for rigid bodies is adopted during the simulation. The hydrodynamic loads (force \mathbf{f}_h and moment \mathbf{T}_h) are assumed to be constant during this sub-cycling and only contact loads and solid motions are updated. Considering the duration t_c of a typical contact among rigid bodies, based on Hertz's contact theory (Johnson, 1985), and ensured that at least one hundred time steps are

used during the rigid bodies contact ($t_c/100$), the variable time step for the solid domain is adopted as $\Delta t_s = N_{dt}\Delta t_f$, where N_{dt} denotes an integer, since the Δt_s satisfies

$$\Delta t_s \leq \min_{\Omega_p} \left(\frac{t_c}{100} \right) \leq \min_{\Omega_p} \left(\frac{2.87}{100} \left[\frac{m_{ij}^2}{l_{0,ij} E_{ij}^2 \|\mathbf{u}_j - \mathbf{u}_i\|} \right]^{\frac{1}{5}} \right), \quad (4.4)$$

where E_{ij} and m_{ij} are the effective Young's modulus and mass between colliding particles i and j , respectively (shown later in Eq. (4.8)). In the absence of contact between rigid solids, $\Delta t_s = \Delta t_f$.

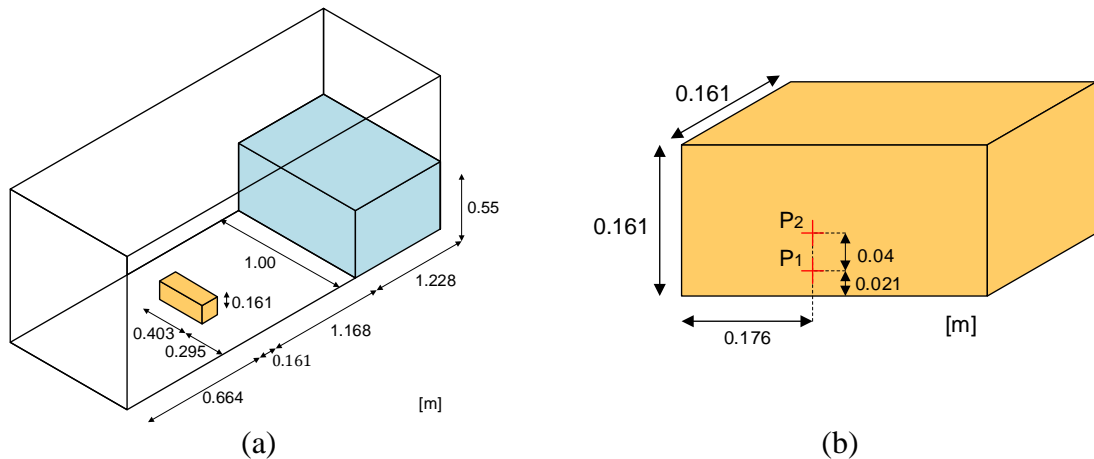
4.3.4 VALIDATION OF THE HYDRODYNAMIC MODELING

In this section, the present MPS is validated on a sequence of test cases. A benchmark case of 3D dam-break problem, where a collapsing water column hits a block, was simulated, and the computed pressures on the block are compared to the experimental ones (Kleefsman et al., 2005). The fluid-structure interaction is verified by a second test consisting of a 2D rigid block rotating and sinking in viscous fluid, of which the computed solid motions are compared with numerical results available in the literature (Barcarolo, 2013).

4.3.4.1 3D DAM BREAKING

The initial geometry and main dimensions of the benchmark case of 3D dam breaking, performed by Kleefsman et al. (2005), is shown in Figure 4.2(a) while the main dimensions and sensors positions on the block are presented in Figure 4.2(b). P1 and P2 correspond to the pressure sensors used in the experiment.

Figure 4.2 - (a) Initial geometry and main dimensions of the 3D dam breaking. (b) Pressure sensors P₁ and P₂ on the block.

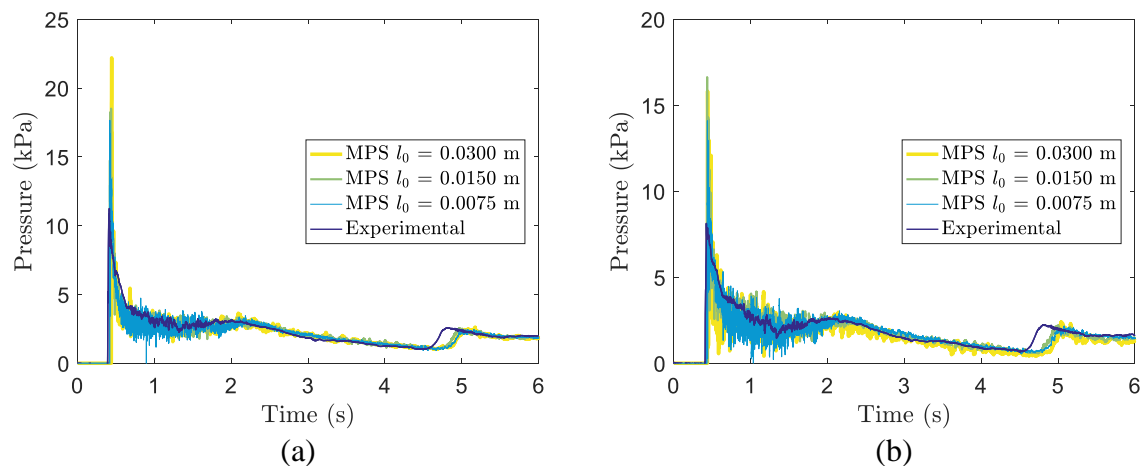


Source: (Amaro Jr et al., 2019).

The density and kinematic viscosity of the fluid are $\rho_f = 1000 \text{ kg/m}^3$ and $\nu_k = 10^{-6} \text{ m}^2/\text{s}$, respectively. The gravity acceleration is $g = 9.81 \text{ m/s}^2$. Three distances of particles were considered, namely $l_0 = 0.03, 0.015$ and 0.0075 m . Considering the dam-break problem and its theoretically predicted velocity of the wave front $u_w = 2\sqrt{gH_w}$, the canonical solution of the analytical formulation based on shallow water waves (Ritter, 1892), as the maximum velocity, where H_F is the water column height, and by adopting the Courant number of $C_r = 0.2$, the time step of the fluid domain is limited by $\Delta t_f < 0.1l_0/\sqrt{gH_w}$. Therefore, the time steps $\Delta t_f = 0.0012, 0.0006$ and 0.0003 s were considered in the validation study. The effective radius $r_e = 2.1l_0$ was used for all discrete operators and particle number density calculations. The relaxation coefficient $\gamma = 0.01$ was adopted herein.

In Figure 4.3(a)-(b), the pressure time series at, respectively, P1 and P2, computed with the present MPS method are compared with the experimental data (Kleefsman et al., 2005). The overall trends of computed and experimental pressure time series at P1 and P2 agree well in all three resolutions but the peak pressure is over predicted by MPS simulations. Despite this, the magnitude of the impact pressure is better predicted by the higher resolution ($l_0 = 0.0075 \text{ m}$) simulation. The numerical pressure oscillation is almost the same for all resolutions between the instants $t = 0.5$ and 2.0 s , but the increase of the resolution reduces the pressure oscillation after $t = 2.0 \text{ s}$. The numerical dissipation inherent of particle-based methods leads to a reduction wave front velocity, resulting in a slight delay between computed and experimental pressure time series between the instants $t = 4.6$ and $t = 5.0 \text{ s}$.

Figure 4.3 – Pressure computed by present MPS and measured by Kleefsman et al. (2005) at pressure sensors (a) P1 and (b) P2.

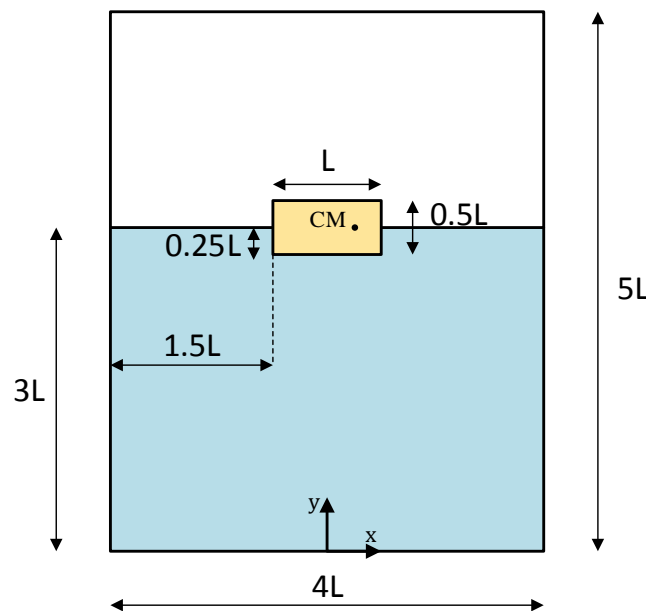


Source: (Amaro Jr et al., 2019).

4.3.4.2 FLUID-STRUCTURE INTERACTION VERIFICATION

In this section, a 2D rigid block rotating and sinking in viscous fluid, as adopted by Barcarolo et al. (2013), was simulated. The initial geometry and main dimensions of the body with an asymmetric mass distribution and partially immersed in a viscous flow is shown in Figure 4.4(a). The characteristic length is $L = 1\text{ m}$. The center of mass (CM) of the rigid block initially locates at position $(x, y) = (0.25, 3.0)$. The mass and moment of inertia of the rigid block are $M_s = 1\text{ kg}$ and $I_s = 0.083\text{ kgm}^2$, respectively. The density and kinematic viscosity of the fluid are $\rho_f = 1\text{ kg/m}^3$ and $\nu_k = 0.002\text{ m}^2/\text{s}$, respectively. The gravity acceleration is $g = 1\text{ m/s}^2$. In order to verify the convergence of the modeling for fluid-structure interaction, three distances of particles $l_0 = 0.04, 0.02$ and 0.01 m , which correspond respectively to ratios $L/l_0 = 25, 50$ and 100 , were considered. The time step of $\Delta t = 0.001\text{ s}$ was used for all simulations. The effective radius $r_e = 2.1l_0$ was used for the gradient, divergence and particle number density computation, whereas $r_e = 4.0l_0$ was used for the Laplacian operator. The relaxation coefficient $\gamma = 0.02$ was adopted herein.

Figure 4.4 - Main dimensions and initial position of the floating block with an asymmetric mass distribution immersed in a viscous flow.

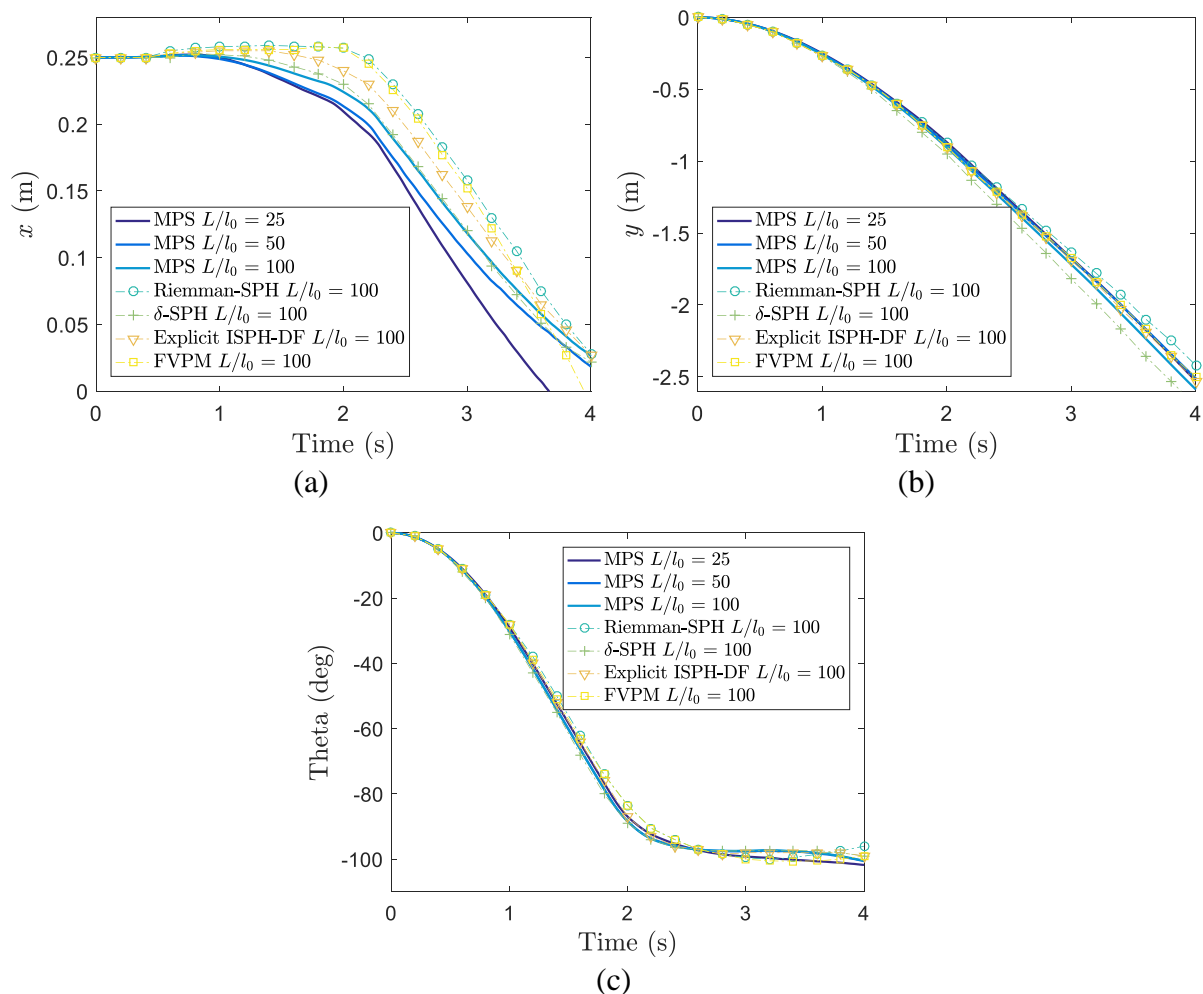


Source: (Amaro Jr et al., 2019).

Time history curves of horizontal (x), vertical (y) and rotational (Θ) motions at the center of mass of the rigid block are shown in Figure 4.5(a)-(c), respectively. The results of present MPS are compared with the results by using the finer resolution ($L/l_0 = 100$) of Riemman-SPH (Vila, 1999), δ -SPH (Antuono et al., 2010), explicit incompressible smoothed particle

hydrodynamics with free divergence condition (ISPH-DF) (Barcarolo, 2013) and finite volume particle method (FVPM) (Nestor et al., 2009) providing in Barcarolo et al. (2013). Vertical (Figure 4.5(b)) and rotational (Figure 4.5(c)) motions computed by present MPS, for all resolutions, are in very good agreement with numerical methods provided in Barcarolo et al. (2013). Only for the horizontal motion (Figure 4.5(a)), the resolution adopted in the present MPS affects the results. The coarse resolution provides slightly lower motions than the reference numerical data. Moreover, Figure 4.5(a) depicts that as the particle model resolution increases, the horizontal motion computed by the present MPS converges to the results obtained by δ -SPH.

Figure 4.5 - (a) Horizontal, (b) vertical and (c) rotational time series of the solid computed with present MPS for the resolutions $L/l_0 = 25, 50$ and 100 , and Riemman-SPH, δ -SPH, explicit ISPH and FVPM in Barcarolo et al. (2013) for resolution of $L/l_0 = 100$.



Source: (Amaro Jr et al., 2019).

4.4 SOLID-SOLID CONTACT MODEL

4.4.1 CONTACT FORCE

The contact force between the rigid bodies \mathbf{f}_c can be decomposed into normal \mathbf{f}_n and tangential \mathbf{f}_t components. In the present study, both components are modeled by using a penalty-based spring dashpot model inspired by the DEM formulation. They are decomposed into a repulsion force \mathbf{f}^r , which is proportional to the penetration between particles, and a damping force \mathbf{f}^d , representing the energy dissipation during the deformation. Here, subscript c stands for the contact, n is the normal and t denotes tangential. The superscripts r and d refer to repulsion and damping, respectively.

The pair of closest particles kl is defined considering a wall particle k belonging to a body and particle l , which is the wall particle belonging to another body and closest to the particle k . The pair is in contact when the distance of contact (see Sect. 4.4.4) is smaller than initial distance between particles l_0 .

4.4.1.1 NORMAL FORCES BETWEEN CLOSEST PARTICLES

The normal forces between the pair of closest particle k and l belonging respectively to the surface of two different rigid bodies in contact, can be described following a nonlinear Hertz's elastic contact theory (Johnson, 1985):

$$\mathbf{f}_{n,kl} = \mathbf{f}_{n,kl}^r + \mathbf{f}_{n,kl}^d = k_{n,kl} \delta_{kl}^{3/2} \mathbf{n}_c + c_{n,kl} \delta_{kl}^{1/4} \dot{\delta}_{kl} \mathbf{n}_c, \quad (4.5)$$

where $k_{n,kl}$ is the normal stiffness constant of pair kl , δ_{kl} is the overlap (penetration) between two wall particles belonging to two different bodies, $\dot{\delta}_{kl}$ is the rate of normal penetration, $c_{n,kl}$ is the normal damping constant and \mathbf{n}_c is the contact normal vector, explained in Sect. 0. It should be highlighted that nonlinear Hertz's elastic contact deformation relates the (circular) contact area of a sphere-sphere or sphere-plane with the elastic deformation of the materials. Since the proposed solid-solid contact model represents the contact area as a smooth plane, the Hertz circular contact area is not rigorously modeled herein.

The particle overlap and the rate of normal penetration are defined as:

$$\delta_{kl} = l_0 - \|\mathbf{r}_{kl,\perp}\|, \quad \dot{\delta}_{kl} = (\mathbf{u}_l - \mathbf{u}_k) \cdot \mathbf{n}_c, \quad (4.6)$$

where $\mathbf{r}_{kl,\perp}$ stands for the distance of contact vector, further explained in Sect. 4.4.4.

The stiffness and damping constants in Eq. (4.7) are defined as (Johnson, 1985):

$$k_{n,kl} = \frac{4}{3} E_{kl} \sqrt{l_{0,kl}}, \quad c_{n,kl} = \xi_n \sqrt{6 m_{kl} E_{kl} \sqrt{l_{0,kl}}}, \quad (4.7)$$

where ξ_n is the contact ratio, which must be provided, and E_{kl} , m_{kl} and $l_{0,kl}$ are given by:

$$E_{kl} = \frac{E_k E_l}{(1 - \nu_k^2) E_k + (1 - \nu_l^2) E_l}, \quad m_{kl} = \frac{m_k m_l}{m_k + m_l}, \quad l_{0,kl} = \frac{l_{0,k} l_{0,l}}{l_{0,k} + l_{0,l}}, \quad (4.8)$$

with E_k , E_l and ν_k , ν_l as the Young's modulus and the Poisson's ratio of particles k and l , respectively. In the present work, only one distance between particles l_0 is used for all domain, thus leading to $l_{0,kl} = l_0/2$. In case l is a particle belonging to a fixed rigid wall, $m_l \rightarrow \infty$, implying that $m_{kl} = m_k$.

4.4.1.2 TANGENTIAL FORCES BETWEEN CLOSEST PARTICLES

For the computation of the tangential forces between the pair of closest particles ($\mathbf{f}_{t,kl}$), two components are considered:

- i.) the first one is due to Coulomb's friction law ($\mathbf{f}_{t,kl}^c$),
- ii.) the second one is due to tangential repulsive ($\mathbf{f}_{t,kl}^r$) and damping forces ($\mathbf{f}_{t,kl}^d$),

and the tangential force is given by one of the two components with smaller absolute value:

$$\mathbf{f}_{t,kl} = \begin{cases} \mathbf{f}_{t,kl}^c & \|\mathbf{f}_{t,kl}^c\| \leq \|\mathbf{f}_{t,kl}^r + \mathbf{f}_{t,kl}^d\| \\ \mathbf{f}_{t,kl}^r + \mathbf{f}_{t,kl}^d & \|\mathbf{f}_{t,kl}^c\| > \|\mathbf{f}_{t,kl}^r + \mathbf{f}_{t,kl}^d\| \end{cases} \quad (4.9)$$

The Coulomb's law, as a function of the normal force, is modified with a sigmoidal function in order to make it continuous in the origin regarding the tangential velocity (Vetsch, 2011):

$$\mathbf{f}_{t,kl}^c = \mu_{kl} \|\mathbf{f}_n\| \tanh(8 \delta_{kl}^t) \mathbf{t}_c. \quad (4.10)$$

Here μ_{kl} is the friction coefficient for the pair of particles k and l , δ_{kl}^t is the tangential relative velocity, \mathbf{t}_c is the tangential contact vector. It should be highlighted that in the present work, the same value of friction coefficient μ_{kl} is adopted for both static and kinetic frictions.

The repulsion and damping forces can be modeled by assuming a linear spring dashpot model, and are given by:

$$\mathbf{f}_{t,kl}^r = k_{t,kl} \delta_{kl}^t \mathbf{t}_c, \quad (4.11)$$

$$\mathbf{f}_{t,kl}^d = c_{t,kl} \delta_{kl}^t \mathbf{t}_c, \quad (4.12)$$

where δ_{kl}^t is the relative sliding.

Assuming the same time scales of the normal and frictional contacts, the tangential stiffness and damping constants are given by (Hoomans, 2000):

$$k_{t,kl} = \frac{2}{7} k_{n,kl} \sqrt{l_0}, \quad c_{t,kl} = \frac{2}{7} c_{n,kl} (l_0)^{1/4}. \quad (4.13)$$

The tangential contact vector is calculated as:

$$\mathbf{t}_c = \frac{\mathbf{u}_l^t - \mathbf{u}_k^t}{\|\mathbf{u}_l^t - \mathbf{u}_k^t\|}, \quad (4.14)$$

where the tangential relative velocity of k and l is obtained with:

$$\mathbf{u}_l^t - \mathbf{u}_k^t = (\mathbf{u}_l - \mathbf{u}_k) - ((\mathbf{u}_l - \mathbf{u}_k) \cdot \mathbf{n}_c) \mathbf{n}_c. \quad (4.15)$$

The tangential deformation and the rate of tangential deformation are expressed as:

$$\delta_{kl}^t = (\mathbf{u}_l^t - \mathbf{u}_k^t) \cdot \mathbf{t}_c \Delta t_s, \quad \dot{\delta}_{kl}^t = (\mathbf{u}_l^t - \mathbf{u}_k^t) \cdot \mathbf{t}_c, \quad (4.16)$$

where Δt_s is the time step used in the solid domain.

4.4.1.3 CONTACT FORCES BETWEEN RIGID BODIES

After calculating all contacts between the pairs of closest particles belonging to different bodies, the resultant contact forces for each rigid body p can be calculated by:

$$\mathbf{f}_{n,p} = \sum_{q \in NB} \left(\sum_{pcp \in NP} (\mathbf{f}_{n,kl})_{pcp} \right), \quad \mathbf{f}_{t,p} = \sum_{q \in NB} \left(\sum_{pcp \in NP} (\mathbf{f}_{t,kl})_{pcp} \right), \quad (4.17)$$

where NP is the number of pairs of closest particles (pcp) belonging to the shell of the rigid bodies $q \in [1, NB]$, and NB is the number of bodies in contact with the body p .

4.4.2 CONTACT TORQUES

The torques that act on the solid center of mass generated by the contact forces between a pair of particles are evaluated as:

$$\mathbf{T}_{c,kl} = (\bar{\mathbf{r}}_{kl} - \mathbf{r}_{CM}) \times (\mathbf{f}_{n,kl}^r + \mathbf{f}_{n,kl}^d + \mathbf{f}_{t,kl}), \quad (4.18)$$

where $\bar{\mathbf{r}}_{kl} = (\mathbf{r}_k + \mathbf{r}_l)/2$ represents the average position vector of particle k and l and \mathbf{r}_{CM} symbolizes the position vector of the solid center of mass. The average position $\bar{\mathbf{r}}_{kl}$ is used to ensure the conservation of angular momentum. Accordingly, after calculating all torques due to contacts between particles, the contact torques for each rigid body p can be obtained by:

$$\mathbf{T}_{c,p} = \sum_{q \in NB} \left(\sum_{pcp \in NP} (\mathbf{T}_{c,kl})_{pcp} \right). \quad (4.19)$$

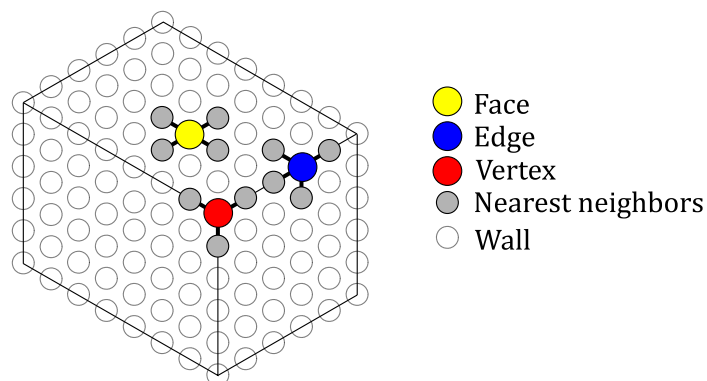
4.4.3 IMPROVED CONTACT NORMAL VECTOR

In the present work, in order to avoid the inaccurate calculation of surface normal of the wall particles at vertex or edge of body face, the contact normal vector \mathbf{n}_c is computed from the particle features at the moment just before the contact. A particle feature can be a *vertex*, an *edge* or a *face* of the rigid body, depending on its location, as shown in Figure 4.6. For sake of simplicity, box shaped rigid body is taken into account here. The identification of the features of a wall particle k is carried out based on the arrangements of the nearest wall particles at the initial instant $t = 0$, of which the number of neighbors and alignment of the distance vectors of the particle k to the neighbors l are used as criteria.

The identification process starts from the verification of the number of wall particles within the radius of $1.1 \times l_0$ (gray circles, see Figure 4.6). For the box shaped body with cubic particle arrangement considered in the present study, the particle k is *vertex* if the number of neighbors is 3, otherwise it might be *edge* or a *face*. Identification of *edge* or a *face* can be done based on the alignment of the four vectors \mathbf{r}_n , the vectors of the distance between the particle k and its neighbors within the radius of $1.1 \times l_0$. From the combination of the four vectors, 6 cross products between pairs of the four vectors can be carried out. If more than one cross product is zero, the particle is *face* because it means more than one pair of collinear vectors.

Although only box shaped bodies are used in the present study, the approach proposed herein can also be applied to solid faces parallel to the diagonal planes of square or cubic lattice particle arrangement.

Figure 4.6 - Schematic representation of rectangular parallelepiped geometry and respective wall particle model. Features highlight as: face particle (yellow circle), edge particle (blue circle), vertex particle (red circle), and neighbors (gray circle) within the radius of $1.1 \times l_0$.



Source: (Amaro Jr et al., 2019).

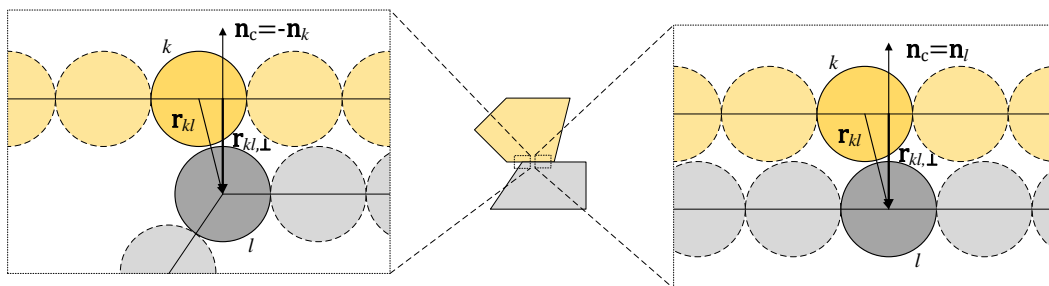
During the simulations, the contact normal vector between a pair of particles k and l is defined as follows:

- i.) If particle l is *face*, the normal of l is used as \mathbf{n}_c .
- ii.) If particle l is not *face*, but k is *face*, the reverse of the normal of k is used as \mathbf{n}_c .
- iii.) Neither particles are *face*, the reverse of the unit distance vector between the particles $\mathbf{r}_{kl}/\|\mathbf{r}_{kl}\|$ is used as \mathbf{n}_c .

4.4.4 IMPROVED DISTANCE OF CONTACT

In the particle-based modeling, the surfaces of the rigid bodies are discretized by a finite number of particles so that the detection of contact between two rigid bodies is generally performed based on the distance between pair of nearest particles k and l belonging respectively to the surfaces of two rigid bodies, as in the studies of (Canelas et al., 2016; Qiu et al., 2017; Rastgoftar et al., 2018), and called here as nearest particles distance criterion. However, with this simplified approach, mismatch between contact distances computed in the particle level and the body level might occur. Figure 4.7 illustrates the wall particles of two rigid bodies, represented by yellow and gray, respectively.

Figure 4.7 - Wall particles of two rigid bodies and the distance of contact vector $\mathbf{r}_{kl,\perp}$ between particle k and the closest wall particle l .



Source: (Amaro Jr et al., 2019).

In Figure 4.7, considering horizontal relative motion between the bodies, in particle level, the distance \mathbf{r}_{kl} between the particles k of the yellow body, and l , which belongs to the gray body and closest one to particle k , is minimum when the particles k and l are aligned in the normal direction of the wall. The distance increases when the particles are misaligned in the normal direction due to the relative motion, meanwhile the distance between the two bodies' faces remain unchanged. In this way, beside the numerical error by adopting only particle positions to calculate the distance between solids, the variation of the value of \mathbf{r}_{kl} might affect the contact detection, as well as the computation of the contact forces, provoking unstable computation.

In order to address this issue, in the method proposed here, the distance used in the contact detection and contact forces are based on the actual distance between the surfaces of the bodies by taking into account the normal vectors of solid walls.

First, the candidate pairs of particles in contact are selected. For a given wall particle i , the neighbor wall particle j , from a different body, is selected if

$$\begin{cases} \|\mathbf{r}_{ij}\| \leq \sqrt{1.25} \times l_0, & 2D \\ \|\mathbf{r}_{ij}\| \leq \sqrt{1.50} \times l_0, & 3D \end{cases} \quad (4.20)$$

is verified. The values $\sqrt{1.25} \times l_0$ and $\sqrt{1.50} \times l_0$, which represent the distances between two particles in the arrangement shown in Figure 4.8, were adopted here as the cutoff radius in which contact can occur for 2D and 3D simulations, respectively.

After that, in order to find all the pairs of closest wall particles k and l , from different bodies, the candidates that provide the vectors with minimum absolute value

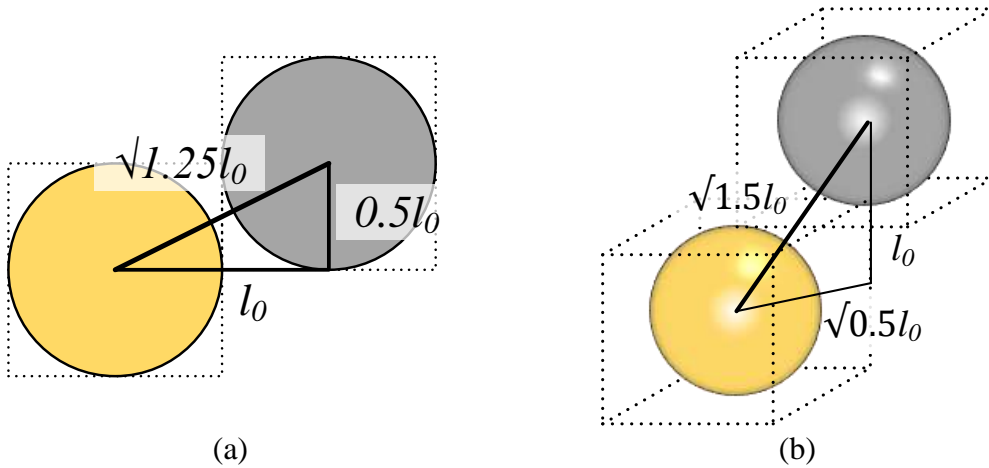
$$\|\mathbf{r}_{kl}\| = \operatorname{argmin}_{j \in \Omega_i} (\|\mathbf{r}_{ij}\|), \quad (4.21)$$

are selected. Then, for each closest pair kl , the distance of contact vector $\mathbf{r}_{kl,\perp}$ is obtained as the projection of the vector \mathbf{r}_{kl} on the contact normal \mathbf{n}_c , i.e. if k and/or l are/is face, then $\mathbf{r}_{kl,\perp}$ is the distance from a point to a plane. Otherwise, $\mathbf{r}_{kl,\perp}$ is the distance between points:

$$\mathbf{r}_{kl,\perp} = \mathbf{r}_{kl} \cdot \mathbf{n}_c. \quad (4.22)$$

Contact is detected when, at least one of the values $\|\mathbf{r}_{kl,\perp}\|$ is smaller than initial distance between particles l_0 .

Figure 4.8 - Cutoff radius adopted for select candidate pairs of particles in contact in (a) 2D and (b) 3D space.



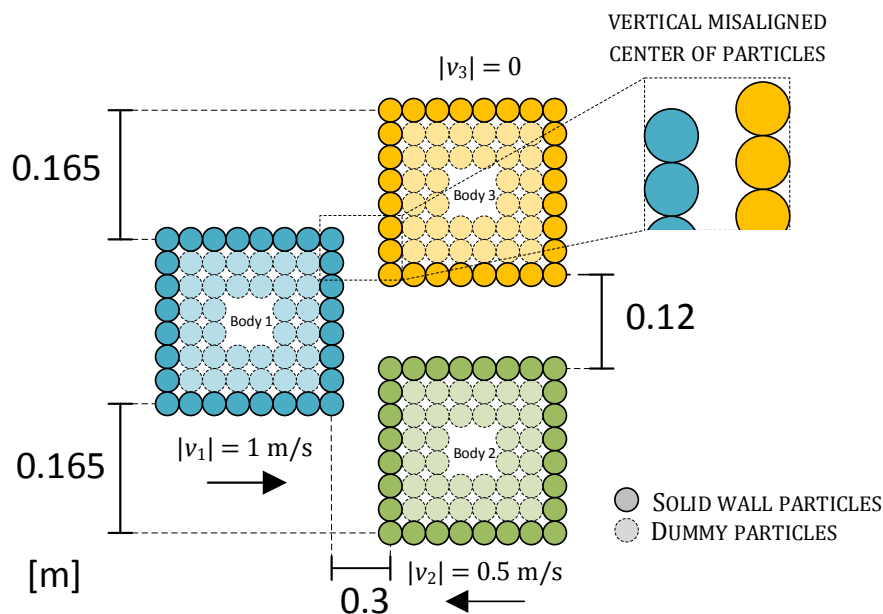
Source: (Amaro Jr et al., 2019).

4.4.5 VALIDATION OF THE SOLID-SOLID CONTACT MODEL

4.4.5.1 COLLISION ENERGY AND LINEAR MOMENTUM

In order to verify the improvements of the present solid-solid contact model regarding the conservation of kinetic energy (K) and linear momentum (Q), a collision between 3 cubic solids of length $L = 0.20\text{ m}$ and homogeneous material was simulated and the computed results are compared to the analytical ones. The initial configuration and main dimensions of the case are given in Figure 4.9. It is important to point out that initially, as shown in the figure, the positions of the wall particles of the three cubes are not aligned horizontally. The velocities $v_1 = 1\text{ m/s}$ and $v_2 = -0.5\text{ m/s}$ were imposed to bodies 1 (blue) and 2 (green), respectively, whereas no velocity was imposed to body 3 (yellow). The mass and moment of inertia of the cubes are: $m_1 = 1.5\text{ kg}$ and $I_1 = 0.01\text{ kgm}^2$, $m_2 = 1.2\text{ kg}$ and $I_2 = 0.008\text{ kgm}^2$, $m_3 = 3\text{ kg}$ and $I_3 = 0.02\text{ kgm}^2$. For all cubes, Young's modulus $E = 15\text{ MPa}$, Poisson's ratio $\nu = 0.3$, collision ratio $\xi_n = 0$, numerical kinetic friction coefficient $\mu_{kl} = 0$ and the initial distance between particles $l_0 = 0.04\text{ m}$ were considered. Since the gravity was neglected in this case and the damping and friction of the bodies are set to zero, there is no variation of energy due to gravity, damping or friction effects, and the total energy (U) is the sum of the kinetic (U_K) and elastic energy during the contact (U_E).

Figure 4.9 - Initial configuration and main dimensions of a collision between three rigid cubes.



Source: (Amaro Jr et al., 2019).

Figure 4.10(a)-(b) give the horizontal velocities $v_{1,x}$, $v_{2,x}$ and $v_{3,x}$, dimensionless energy (U/U_0) and linear momentums with respect to horizontal (Q_x/Q_{x0}) and vertical motions (Q_y/Q_{y0}) computed by using the nearest particles distance criterion and the proposed model of the combination of contact normal (\mathbf{n}_c) and distance of contact ($\mathbf{r}_{kl,\perp}$) vectors, respectively. The kinetic, elastic energies and linear momentum are calculated as:

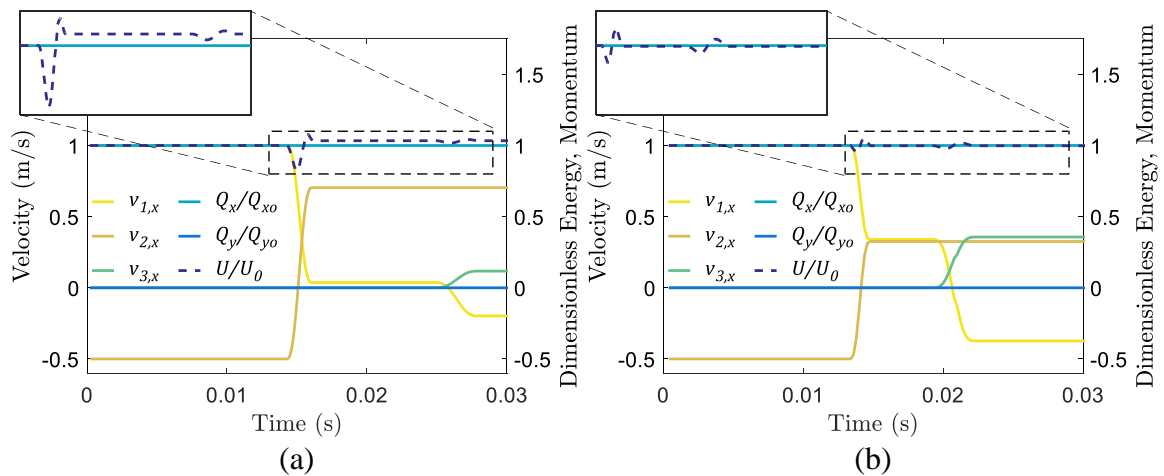
$$U_K = \sum_{p=1}^{NB} \left(\frac{m_p \|\mathbf{v}_p\|^2}{2} + \frac{I_p \|\boldsymbol{\omega}_p\|^2}{2} \right), \quad (4.23)$$

$$U_K = \sum_1^{NC} \int \mathbf{f}_{n,kl} d\mathbf{r} = \sum_1^{NC} \int k_{n,kl} \delta_{kl}^{3/2} \mathbf{n}_c \cdot d\mathbf{r} = \sum_1^{NC} \int k_{n,kl} \delta_{kl}^{3/2} d\delta = \sum_1^{NC} \frac{2}{5} k_{n,kl} \delta_{kl}^{5/2}, \quad (4.24)$$

$$\mathbf{Q} = \sum_{p=1}^{NB} (m_p \mathbf{v}_p), \quad (4.25)$$

where the subscript p refers to the body, NB denotes the number of bodies and NC is the number of pairs of closest particles belonging to the shell of the rigid bodies. The conservation of the horizontal and vertical linear momentum is assured by both approaches. The energy remains constant for the simulation computed by the present approach, except only between the instants of solid contact. On the other hand, after the first collision at the instant $t = 0.014$ s, the kinetic energy conservation is violated in the simulation using the nearest particles distance criterion, in which the kinetic energy increase.

Figure 4.10 - Horizontal velocities of the cubes (v_1 , v_2 and v_3) and dimensionless energy (U/U_0) and linear momentum (Q/Q_0) computed only with (a) the nearest particles distance criterion and (b) the combination of contact normal (\mathbf{n}_c) and distance of contact ($\mathbf{r}_{kl,\perp}$) vectors.

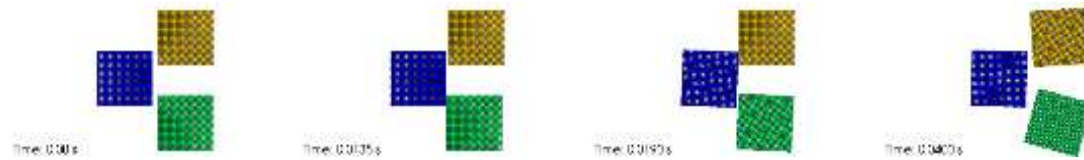


Source: (Amaro Jr et al., 2019).

The simulation obtained by the present approach are shown in Figure 4.11. The cubes 1 (blue) and 2 (green) collide at the instant $t = 0.0135$ s, consequently, repelling and beginning

rotational motions in addition to translational ones. After the collision between the cubes 1 (blue) and 3 (yellow) at the instant $t = 0.019$ s, the cube 1 moves backward, while the cube 3 starts its translational and rotational motions.

Figure 4.11 - Evolution of the collision between 3 cubes by using the proposed contact model.

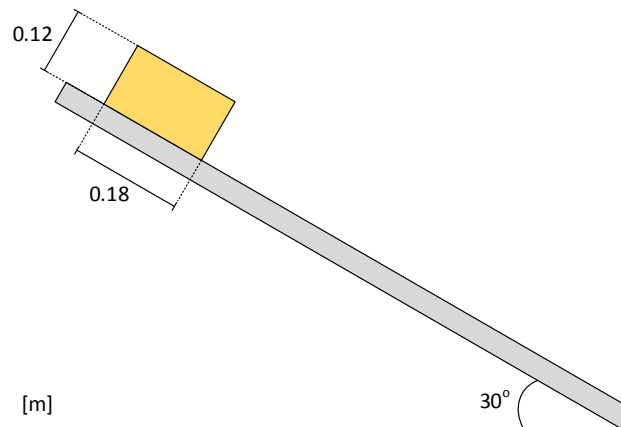


Source: (Amaro Jr et al., 2019).

4.4.5.2 FRICTIONAL FORCE

In order to verify the present friction model, a simple case of a solid sliding on a sloped surface is considered. The solid is a block with dimensions of $0.18 \times 0.18 \times 0.12$ m³, and the surface is a plane with an inclination angle of 30 degrees in relation to horizontal plane, as shown in Figure 4.12. The block has no initial velocity, and only gravitational, normal and frictional forces act on its motion. For the comparison with the analytical results, in which the body is assumed as an ideal point mass, the contact torque is set to zero. The numerical parameters and material properties are given in Table 4.2.

Figure 4.12 - Main dimensions of the sloped surface and the sliding block.



Source: (Amaro Jr et al., 2019).

Table 4.2 - Sliding block. Numerical parameters and material properties.

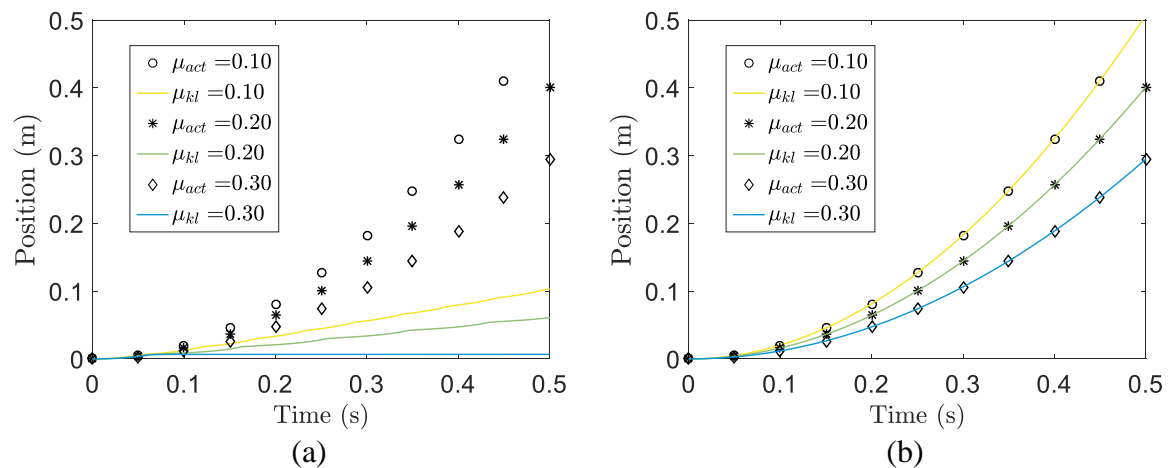
Solid	l_0 (m)	L/l_0	m (kg)	ν	E (MPa)	ξ_n
Block	0.012	15	3.5	0.3	10	0.05
Plane	-	-	∞	0.3	10	-/-

Source: (Amaro Jr et al., 2019).

Three cases using different values of numerical friction coefficients, $\mu_{kl} = 0.10, 0.20$ and 0.30 were simulated. In order to show the effects of the improvements on contact normal and distance computation, the positions and velocities of the sliding block computed using only the nearest particles distance criterion and obtained by using the combination of contact normal and the distance between two bodies face vectors (proposed approach) are presented in Figure 4.13 and Figure 4.14, respectively. Analytical results for actual friction coefficients $\mu_{act} = 0.10, 0.20$ and 0.30 are also provided in Figure 4.13 and Figure 4.14. A very good fitting is obtained for the proposed approach, showing that the features of the motions and velocities are precisely reproduced, as illustrated in Figure 4.13(b) and Figure 4.14(b). On the other hand, the solid motions computed by using only the nearest particles distance criterion are clearly lower than the analytical ones, as shown in Figure 4.13(a). The orientation of the contact normal as the unit distance vector between the particles leads to the incorrect contribution of normal forces in the tangential sliding solid velocity, with abrupt variations over time, as shown in Figure 4.14(a), thus increasing the frictional force.

Figure 4.13 - Position of the sliding block computed using (a) the nearest particles distance criterion and (b) the combination of contact normal (\mathbf{n}_c) and distance of contact ($\mathbf{r}_{kl,\perp}$) vectors.

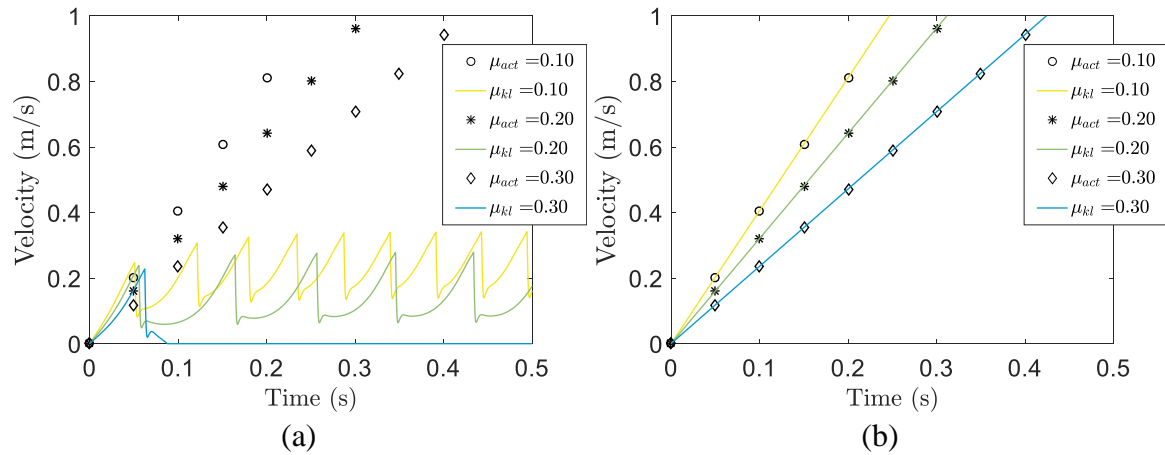
Symbols represent analytical solutions, and solid lines are computed results.



Source: (Amaro Jr et al., 2019).

Figure 4.14 - Velocity of the sliding block computed using (a) the nearest particles distance criterion and (b) the combination of contact normal (\mathbf{n}_c) and distance of contact ($\mathbf{r}_{kl,\perp}$) vectors.

Symbols represent analytical solutions, and solid lines are computed results.



Source: (Amaro Jr et al., 2019).

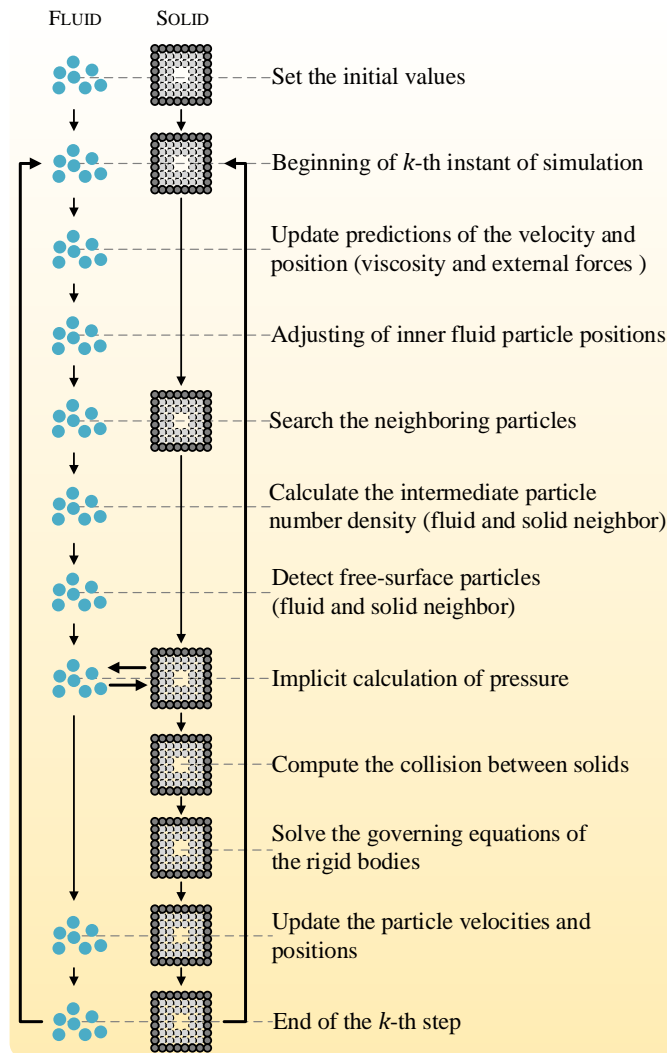
4.5 ALGORITHM

A brief summary of the algorithm implemented, as illustrated in Figure 4.15, proceeds as follows:

1. Set the initial values for all fluid particles and solid elements, including the search of the neighboring particles.
2. Beginning of the k -th instant of simulation.
3. Update the predictions of the velocity and position of fluid particles by using viscosity and external forces based on Eqs. (2.38) and (2.39), respectively.
4. Apply Eq. (2.41) to fluid particles adjusting their final positions.
5. Find neighboring fluid and solid particles.
6. Calculate the intermediate particle number density n_i considering the neighboring fluid and solid particles, see Eq. (2.4).
7. Detect free-surface particles by Eq. (2.35).
8. Solve Eq. (2.63) to obtain the pressure at particles (fluid and solid wall).
9. Solve the governing equations of the rigid solids under the fluid loads and solid collision loads given by Eqs. (4.1) and (4.2).
10. Calculation of the velocity, Eq. (2.42), and position, Eq. (2.43), of fluid particles by using the pressure gradient given by Eq. (2.29). Update velocities and positions of solid wall particles by Eqs. (4.1) and (4.2).

11. End of the k -th instant of simulation. Return to step (2) for the next time instant of simulation ($k+1$ -th).

Figure 4.15 - Schematic diagram of the FSI numerical algorithm.



Source: (Amaro Jr et al., 2019).

4.6 RESULTS AND DISCUSSIONS

4.6.1 3D DAM-BREAK FLOW HITTING ONE CUBE

The performance of the present solid-solid contact model for MPS is investigated considering a dam-break flow hitting a heavy cubic solid, as shown in Figure 4.16. The problem has been investigated in Canelas et al. (2016) which provides experimental data regarding trajectories of the body mass center. The position of the cube is referred to a reference frame with origin

Material properties provided in Canelas et al. (2016), as density, Poisson's ratio and Young's modulus, and numerical parameters are presented in Table 4.3. Since the collision ratio (ξ_n) is unknown, and the actual kinetic friction coefficient between the cube and the base is also not provided in the reference, some numerical tests of the dam-break problem were carried out first using different collision ratios (ξ_n) and numerical kinetic friction coefficients (μ_{kl}) to achieve appropriate value of these parameters. As a result, $\xi_n = 0.05$, and kinetic friction coefficient cube-base $\mu_{kl} = 0.05$ provide the computed motions close to experimental results and were adopted for the simulations.

Table 4.3 - 3D dam breaking with one cube. Numerical and materials properties.

Solid	ρ (kg/m³)	m (kg)	ν	E (GPa)	ξ_n	μ
Cube	800	2.7	0.3	3	0.05	-
Wall	∞	∞	0.3	210	-	0.05

Source: (Amaro Jr et al., 2019).

In order to find the compromise resolution between accuracy and processing time, five resolutions were considered in the first case: distances of particles $l_0 = 0.025, 0.0125, 0.01, 0.0075$ and 0.006 m which correspond to ratio $L/l_0 = 6, 12, 15, 20$ and 25 , respectively. The distance between particles and respective time steps are listed in Table 5.3.

Table 4.4 - 3D dam breaking with one cube. Spatial and temporal discretization.

l_0 [mm]	25.0	12.5	10.0	7.5	6.0
L/l_0	6	12	15	20	25
Simulation time [s]			2.0		
Number of particles	173172	1005168	1819758	3943866	7425150
Fluid time step [s]	1×10^{-3}	5×10^{-4}	4×10^{-4}	2.5×10^{-4}	2.5×10^{-4}
Computation time*	0d00h06m	0d02h00m	0d06h40m	0d19h30m	2d00h30m

*Intel® Xeon® Processor E5 v2 Family, processor base frequency of 2.80GHz, 25 MB cache, 20 cores and 126GB of memory.

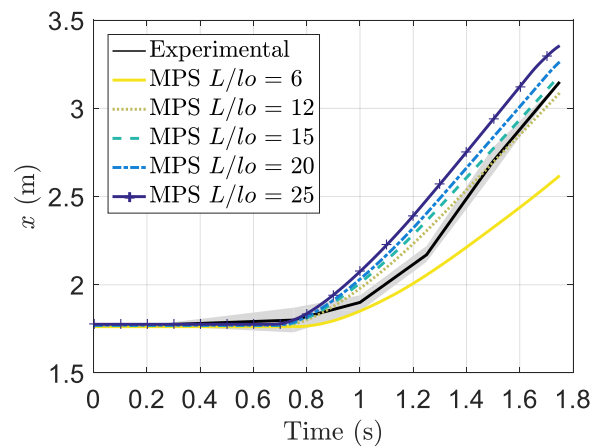
Source: (Amaro Jr et al., 2019).

Figure 4.17 provides the longitudinal motion of the solid (x), respectively, for the five resolutions, and the experimental data (Canelas et al., 2016). The shadowed area represents the symmetrical error region obtained by considering the variation between consecutive experimental tests, plus the variation between measurements in the same test.

The longitudinal position computed by the coarse resolution $L/l_0 = 6$ ($l_0 = 0.025$ m) shows an initial tendency similar to the experimental result. However, the computed motion of the coarse case slows down and is deviated from the experimental one. This deviation becomes

clear from $t = 1.3$ s. For the resolutions $L/l_0 \geq 12$, the computed longitudinal motions are close to experimental data. Due to slightly larger numerical dissipation associated to the coarse cases, the motion of the wave front computed by the present MPS simulations with larger distance between particles is slower, as well as the motion of the cube transported by the wave. In this way, considering the computational time, the distances between particles $l_0 = 0.01$ m ($L/l_0 = 15$) and/or $l_0 = 0.0075$ m ($L/l_0 = 20$) were adopted in the following simulations.

Figure 4.17 - 3D dam breaking with one cube. Longitudinal motion obtained by experimental test (Canelas et al., 2016) and present MPS modeling.

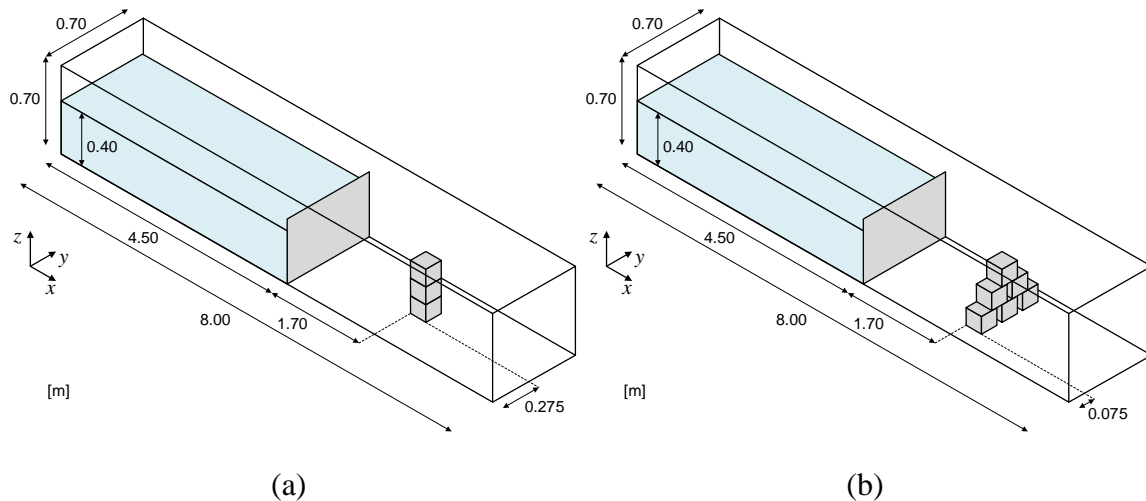


Source: (Amaro Jr et al., 2019).

4.6.2 3D DAM-BREAK FLOW HITTING STACKED CUBES

Two highly complex cases of multiple bodies motion in transient free-surface flow, whose experimental and numerical results were also provided by Canelas et al. (2016), were also simulated in order to assess the performance of the proposed model. The two cases consist of a dam-break event, in which heavy cubic solids, in different stacking configurations, interact with each other and fixed walls. Figure 4.18(a)-(b) show the initial geometry and the main dimensions of the dam-break event with three cubes stacked and aligned vertically and six cubes in triangle formation (pyramid), respectively. The tank is the same detailed in Sect. 4.6.1. In the case of the three cubes stacked vertically, the centers of mass of the cubes are in the central plane of the canal. For the triangle formation, the central cube also has its center of mass aligned with the central plane of the canal, and gaps of 0.05 m separate the cubes of the same level.

Figure 4.18 - Initial geometry and main dimensions of the 3D dam breaking with (a) three cubes stacked and aligned vertically and (b) six cubes in triangle formation (pyramid).



Source: (Amaro Jr et al., 2019).

Again, as the actual friction coefficients are not available, the numerical kinetic friction coefficient between cubes (μ_{kl}) was determined through numerical experiments using the case of dam-break flow with three cubes stacked and aligned vertically. As a result, the numerical kinetic friction coefficient between cubes $\mu_{kl} = 0.20$ provided a good agreement between the computed cube's motion and the experimental results and therefore was adopted for both stacking configurations. Material properties provided in Canelas et al. (2016) and numerical kinetic friction coefficients are listed in Table 4.5, whereas numerical parameters used in the following simulations are presented in Table 4.6.

Table 4.5 - 3D dam breaking with multiple cubes. Materials properties.

Solid	ρ (kg/m ³)	m (kg)	ν	E (GPa)	ξ_n	μ
Cube	800	2.7	0.3	3	0.05	0.2
Wall	∞	∞	0.3	210	-	0.05

Source: (Amaro Jr et al., 2019).

Table 4.6 - 3D dam breaking with multiple cubes. Numerical parameters.

Number of bodies	3		6	
l_0 [mm]	10	7.5	10	7.5
L/l_0	15	20	15	20
Simulation time [s]	2			
Number of particles	1803888	3968526	1811826	3986184
Fluid time step [s]	4.0×10^{-4}	2.5×10^{-4}	4.0×10^{-4}	2.5×10^{-4}
Computation time	0d06h00m	0d21h00m	0d05h30m	0d22h40m

Source: (Amaro Jr et al., 2019).

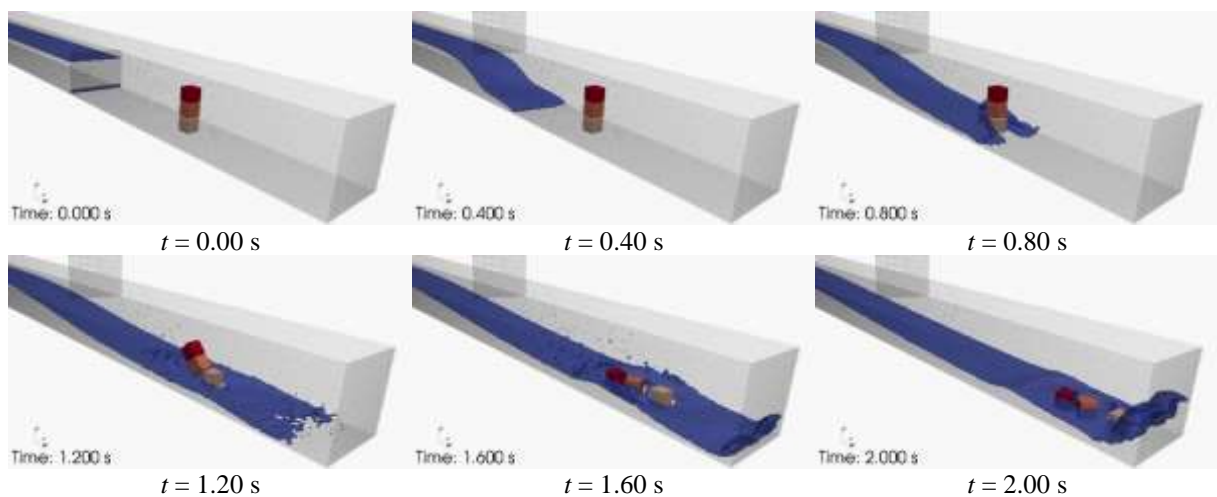
4.6.2.1 THREE STACKED CUBES ALIGNED VERTICALLY

Figure 5.19 shows the 3D dam breaking wave surface evolution, the gate motion and the cubes at the instants $t = 0.0, 0.4, 0.8, 1.2, 1.6, 2.0$ s computed using the particle distance $l_0 = 10$ mm. All the snapshots were rendered after simulations. Delaunay triangulation filter of the open-source Paraview (Ahrens et al., 2005) is used to represent the cubes as a mesh of triangle polygons. The free-surface particles are represented by a smooth surface by using the tools *VDB from Particle Fluid* and *Remesh* of the software Houdini SideFX (SideFX, 2018).

Figure 4.20 shows a sequence of frames from the experiment (Canelas et al., 2016), and the simulation carried in the present study for the configuration of three stacked cubes aligned vertically. Two resolutions were considered to simulate this case: $l_0 = 0.01$ and 0.0075 m. At the instant $t = 0.98$ s, the water hits and moves downstream the cube in the base of the stack with the formation of upward splash and deviation of the flow. In the experiment, the remaining two cubes fall, and the wave hits the upper cube at the instant $t = 1.28$ s, whereas the numerical simulations present a delay, and the remaining two cubes just start to fall at this instant. At the instant $t = 1.41$ s, the cubes are in contact with the bottom of the canal and transported by the wave front in the experiment, while the cubes still are falling in the numerical simulations. Despite these local differences, the error between the positions of the cubes obtained numerically and by the experimental test is an order of magnitude smaller than the cube length, thereby indicating that the numerical results are in overall good agreement with the experiment.

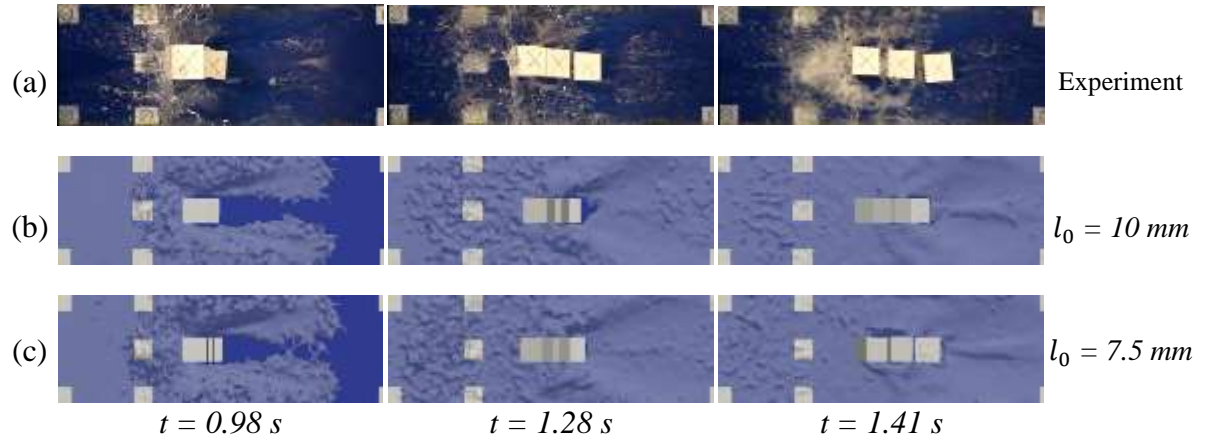
Figure 4.19 - Snapshots of the numerical simulations of 3D dam breaking with three cubes.

Initial particle distance $l_0 = 10$ mm.



Source: the author.

Figure 4.20 - Snapshots of the 3D dam breaking with three cubes. (a) Experiment (Canelas et al., 2016) and the simulations carried in the present study with (b) $l_0 = 10 \text{ mm}$ and (c) $l_0 = 7.5 \text{ mm}$.



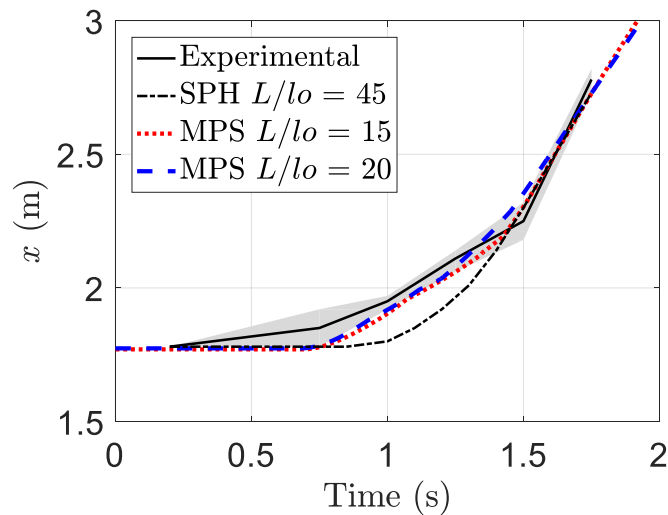
Source: (Amaro Jr et al., 2019).

The motion of the cube in the base of stack along the longitudinal direction (x) is presented in Figure 4.21. The motions of the cube computed by the SPH (Canelas et al., 2016) and present MPS start after the experimental data. From the experimental data, the wave motion starts to move the cube at the instant $t = 0.2 \text{ s}$, whereas the cube starts its motion at the instant $t = 0.71 \text{ s}$ for the present simulation and $t = 0.85 \text{ s}$ for the SPH simulation. Due to the action of the cube-cube plus cube-base friction forces, the computed velocity of the cube is lower until the instant $t = 1.25 \text{ s}$, when the middle and top cubes starts to fall and the stacked cubes become to lose the cube-cube contact and, therefore, decreasing mainly the friction force on the cube in the base. This is in agreement with the experimental trends, but at different instants, i.e. the experimental motion presents this behavior earlier between $t = 0.2 \text{ s}$ and $t = 1.00 \text{ s}$. The motion computed in the present study is closer to the experimental measurements than the SPH result.

The motions of the top cube along the longitudinal (x) and vertical direction (z) are shown in Figure 4.22(a)-(b), respectively. After the fluid hits the cube in the base of stack, the cube at the top starts to move along the longitudinal axis at the instant $t = 0.80 \text{ s}$. Experimentally measured and numerically computed motions along the longitudinal direction are in good agreement (see Figure 4.22(a)). The cube begins to fall (drop) at the instant $t = 1.00 \text{ s}$ for both experimental and computed by the present MPS. Contrary to the monotonic falling motions of the present numerical results and experimentally measured one, the SPH result presents an up and down motion from $t = 1.00 \text{ s}$ to $t = 1.30 \text{ s}$. This error is supposed to be a consequence of the adoption of the nearest particles distance criterion used in the SPH. In the

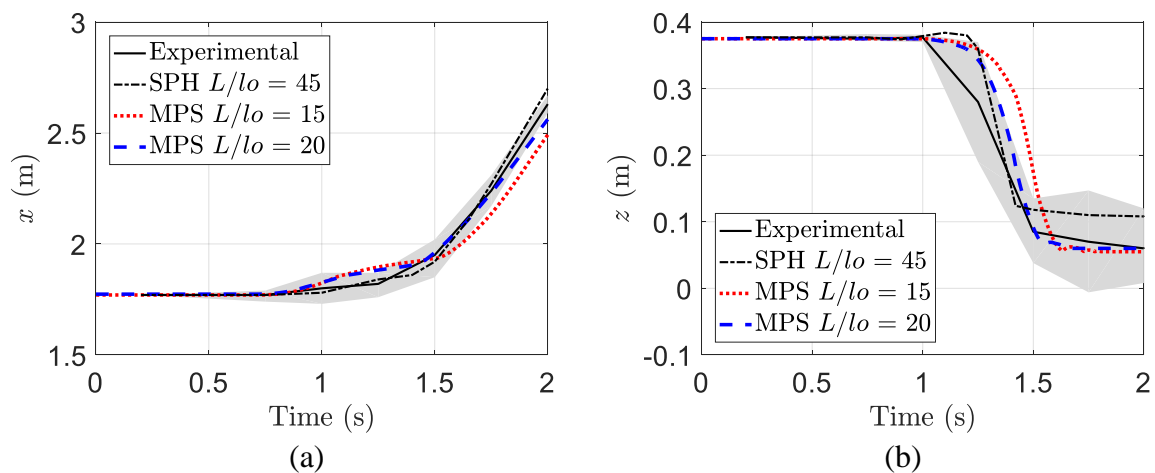
numerical simulation, however, the cubes interactions undergo a fall time longer than the experimental ones. Despite the initial delay on the motion of the cube in the base of the stack, a satisfactory agreement between experimental and computed motions is obtained. Concerning the top cube, a generally good agreement between experimental and computed motions is demonstrated, especially for the initial distance between particles $l_0 = 0.0075 \text{ m}$ ($L/l_0 = 20$).

Figure 4.21 - 3D dam breaking with three cubes. Motion of the cube on the base along the longitudinal direction. Experiment, SPH simulation (Canelas et al., 2016) and the present MPS simulations.



Source: (Amaro Jr et al., 2019).

Figure 4.22 - 3D dam breaking with three cubes. Motion of the top cube along the (a) longitudinal and (b) vertical direction. Experiment, SPH simulation (Canelas et al., 2016) and the present MPS simulations.



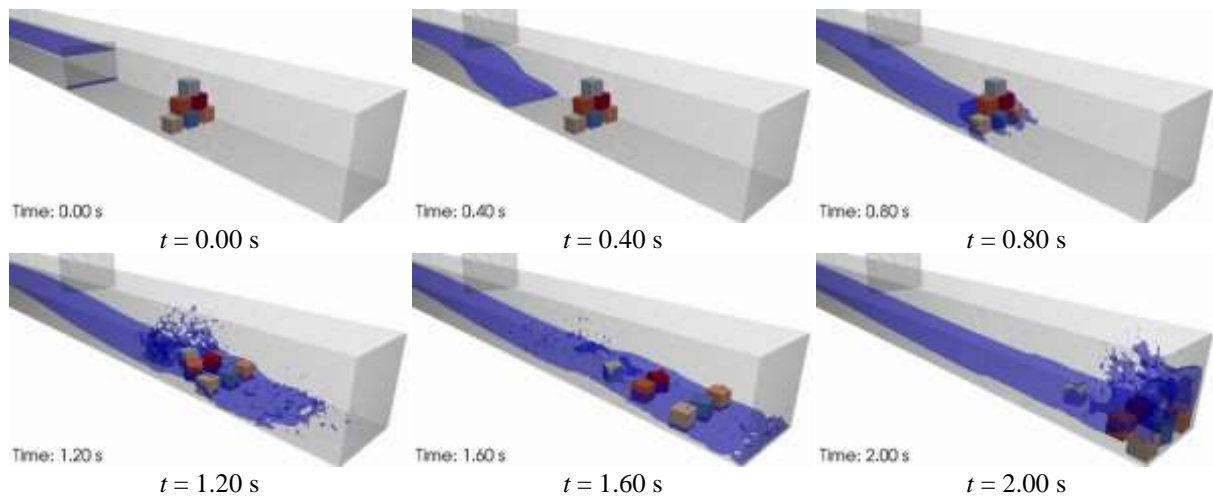
Source: (Amaro Jr et al., 2019).

4.6.2.2 SIX CUBES STACKED IN TRIANGLE FORMATION (PYRAMID)

Snapshots of the present simulation of the 3D dam breaking wave surface evolution, the gate motion and the six cubes at the instants $t = 0.0, 0.4, 0.8, 1.2, 1.6, 2.0$ s using the particle distance $l_0 = 10$ mm are presented in Figure 4.23. All the snapshots were rendered after simulations.

Figure 4.23 - Snapshots of the numerical simulations of 3D dam breaking with six cubes.

Initial particle distance $l_0 = 10$ mm.



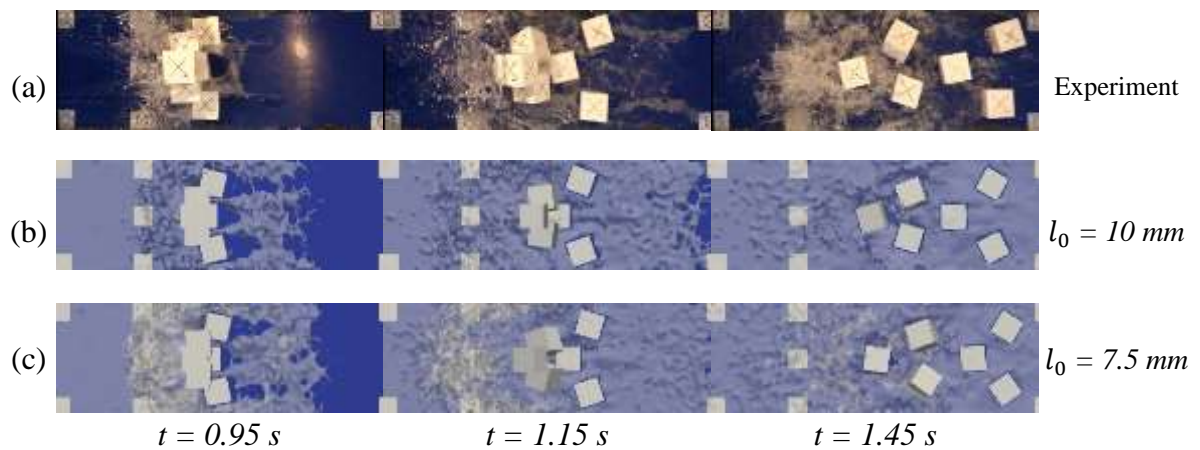
Source: the author.

A sequence of frames for the configuration of six cubes stacked in triangle formation (pyramid) obtained from the experiment (Canelas et al., 2016) and the simulation carried in the present study are given in Figure 4.24. At the instant $t = 0.95$ s, the wave front hits the cubes and begins to transport them downstream generating a large splash close the initial weather side of the cubes. The cubes in the base of the stack are transported by the wave front while the remaining cubes fall at the instant $t = 1.15$ s. After this, all the cubes are carried by the wave, with significant differences only between computed and experimental rotations of the cubes. Moreover, during this time interval, the differences of almost all the experimental and computed positions of the cubes are an order of magnitude smaller than the cube length. For this case, the numerical method is in very good agreement with the experiment, especially for the initial distance between particles $l_0 = 0.0075$ m ($L/l_0 = 20$).

Figure 4.25(a) illustrates the displacement of the top cube along the longitudinal (x) direction. After the fluid hits the cubes in the base of stack, the top cube starts the motion along the longitudinal axis at the instant $t = 0.85$ s. The computed and experimental motion follows the same tendency until the instant $t = 1.10$ s. For the simulations of the present MPS, the

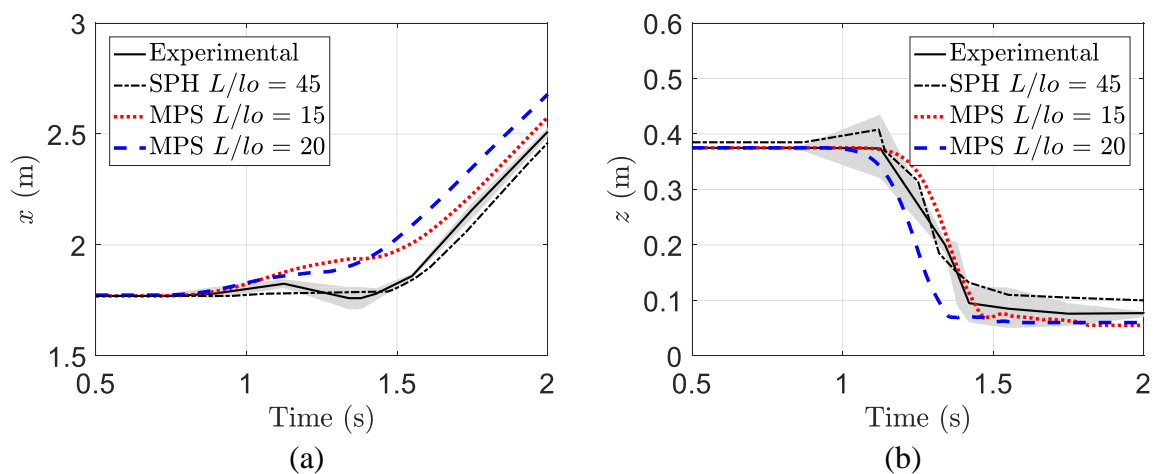
top cube is transported due to the friction force between the cubes contact surfaces, and, after the instant $t = 1.30$ s, by the wave. On the other hand, for the experimental test, the cube slumped to the base backward and is transported downstream, after the instant $t = 1.50$ s. In the simulation obtained by SPH, the top cube presents a very small motion until the instant $t = 1.50$ s, when is transported by the wave. After the instant $t = 1.60$ s, both experimental, SPH computed motion and present computed motions show a similar tendency although the motion computed by the present MPS occurs earlier.

Figure 4.24 - Snapshots of the 3D dam breaking with six cubes. (a) Experiment (Canelas et al., 2016) and the present simulations with (b) $l_0 = 10$ mm and (c) $l_0 = 7.5$ mm.



Source: (Amaro Jr et al., 2019).

Figure 4.25 - 3D dam breaking with six cubes. Motion of the top cube along the (a) longitudinal and (b) vertical direction. Experiment, SPH simulation (Canelas et al., 2016) and the present MPS simulations.



Source: (Amaro Jr et al., 2019).

The vertical motion of the top cube (z) is shown in Figure 4.25(b). In the experiment, the cube falls between the instants $t = 1.07$ and 1.40 s, while those computed by the present MPS are

slightly shifted. The motion obtained by the present MPS with $l_0 = 0.0075 \text{ m}$ presents a maximum advance of 0.10 s , approximately, whereas the motion obtained with $l_0 = 0.01 \text{ m}$ presents a maximum delay of 0.05 s , approximately. The up and down motion computed by the SPH between the instants $t = 0.87$ and 1.12 s , appears to be similar to the previous case, which is presumed due to the adoption of the nearest particles distance criterion.

Experimental and computed motions present a similar tendency demonstrating that the present model is able to reproduce the main behaviors of the complex problem. However, experimental and computational results still present some small discrepancies, and further investigations and improvements on the model are necessary.

4.7 CONCLUDING REMARKS

Numerical pressures computed by the present fluid solver, based on the MPS method, were validated by experimental results of a benchmark 3D dam break problem. After that, the fluid-structure interaction approach was verified by the comparisons between the computed rotational, horizontal and vertical solid motions with available numerical results obtained by other numerical methods.

The contact model was initially verified by two cases. Considering a collision between three cubes, the computed energy was compared against the analytical ones and linear momentum conservation is verified. Linear momentum and energy computed by the proposed model fit exactly the analytical results, with exception only during the solid contact. On the other hand, the contact detection based on the distance between the pair of nearest particles, as adopted in the existing works, violates the energy conservation.

The simulations of a solid sliding on a sloped surface showed the improvements of the contact computation stability achieved by the proposed model with the suppression of non-physical discontinuities in the collision distance, which may lead to incorrect contribution of normal forces on the tangential solid motion.

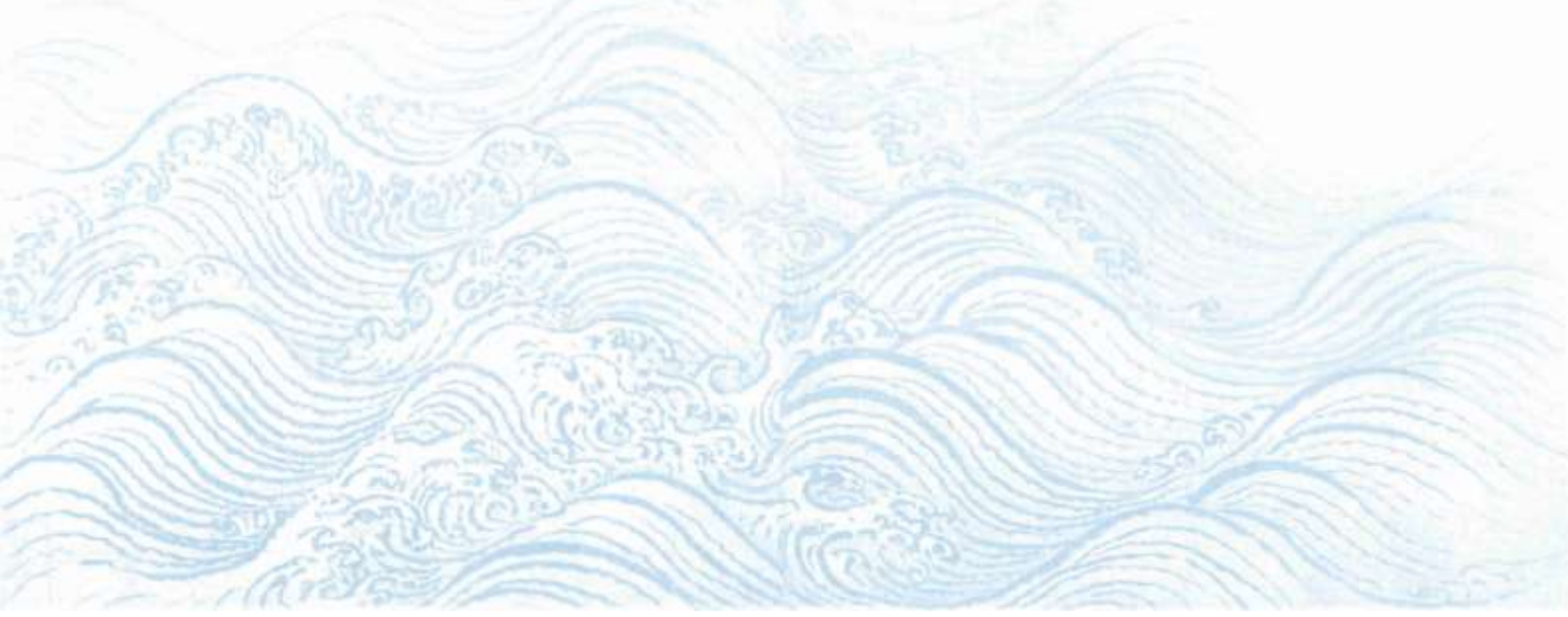
Finally, the proposed model was validated by highly complex 3D dam breaking flow hitting a cubic solid, three stacked cubes and six stacked cubes. First, the results of the dam breaking flow hitting a cube show that the compromised resolutions ranges from $L/l_0 = 15$ to $L/l_0 = 20$. After that, the positions of the cubes obtained from the present method and experiment are compared, exhibiting errors with order of magnitude smaller than the cube length.

The results suggest that the present model, which is of relatively easy implementation, is effective to reproduce the main behaviors of complex nonlinear fluid-structure interaction (FSI) problems.

CHAPTER 5

3D COUPLED WC-MPS-FE PARTICLE-MESH MODEL FOR FSI PHENOMENA

A novel 3D fluid-structure coupling between weakly-compressible moving particle semi-implicit (WC-MPS) and finite element (FE) methods is developed with its application to violent free-surface flows interacting with geometrically nonlinear thin-walled structures. As a powerful and very effective method to solve the hydrodynamic equations of free-surface flow, WC-MPS is used to model the domain covering the fluid, while a geometrically exact shell model is applied to nonlinear structural dynamic. In WC-MPS, a regularization technique is adopted to suppress the so-called tensile instability and a conservative pressure gradient formulation is integrated to improve computational accuracy. In order to avoid the excessive spurious non-physical pressure oscillations, the particle number density is obtained by using the continuity equation including a tuning-free diffusive term. Aiming to contribute towards the development of polygon wall boundary models, discrete divergence operators are derived and applied for the formalism of the explicitly represented polygon (ERP) model, as well as a repulsive Lennard-Jones force is introduced, with significant impact on the numerical stability. Simulations of structures under quasi-hydrostatic loads are conducted to verify the accuracy of the coupled model as well as its robustness, and the efficiency in highly nonlinear phenomena is demonstrated by solving transient fluid-structure interaction (FSI) problems with free-surface and structures that undergo large rotations and displacements.



5.1 BACKGROUND

Fluid-structure interaction (FSI) phenomena have attracted increasing interest due to wide range of its application in several scientific and engineering areas, as well as being of main importance in various industrial sectors such as biomedical, aerospace, automotive, etc. In most applications of engineering, the design of mechanical systems by considering FSI phenomena is of great importance due to safety, reliability, efficiency or durability issues. Among many phenomena involving fluid and structure motions in extreme conditions, hydrodynamic slamming/green-water on ships, sloshing in liquid storage systems, tsunami/storm/flood impact on structures, etc., are examples characterized by violent free-surface flows with abrupt hydrodynamic loads. Since these problems present an intrinsic complexity, analytical approaches are generally limited by simplified considerations, while laboratory experiments might be expensive, time consuming and even unfeasible. With the remarkable advances in high-performance computing (HPC) systems, numerical simulations provide an economical alternative to deal with complex large-scale models under different scenarios making it possible to perform parametric and even probabilistic studies.

The mesh-free particle-based (Lagrangian) methods, such as the smoothed particle hydrodynamics (SPH) (Gingold & Monaghan, 1977; Lucy, 1977) and the moving particle semi-implicit (MPS) (Koshizuka & Oka, 1996), are very effective to model violent free-surface flows with large interfacial deformation and fragmentations. These methods have been widely applied to solve FSI problems (Chikazawa et al., 2001) (Antoci et al., 2007) (Rafiee & Thiagarajan, 2009) (Amini et al., 2011) (Amaro Junior & Cheng, 2013) (Hwang et al., 2014) (Hwang et al., 2016) (Falahaty et al., 2018) (Khayyer et al., 2018) (Nasar et al., 2019) (Sun et al., 2019) (Wang et al., 2019) (Zhan et al., 2019) (Liu et al., 2020). Nevertheless, a uniform spatial resolution is usually adopted, which demands a huge amount of required computational power for large-scale FSI problems involving complex or thin structures, since high-resolution is necessary. In that case, some authors adopted multi-resolution techniques (Khayyer et al., 2019; Sun et al., 2019), in which high-resolution is used only near the structures or local critical areas, while low-resolution is used in the far field. However, these formulations are generally complex, especially for three-dimensional (3D) problems, and demands a considerable coding implementation effort. Since the finite element method (FEM), a robust and consolidated method for structural dynamic simulations, can handle with complex or thin structures and allows independent fluid and solid resolutions,

many researchers have taken benefit from meshless particle-based methods along with mesh-based methods aiming to develop coupled FSI solvers.

Since a significant range of FSI problems is represented by free-surface flow and thin-walled structures undergoing large deformations, the main objective of the present work is to propose a versatile and efficient FSI solver, by coupling a particle-based method and geometrically exact shell model to handle with highly nonlinear transient applications in the presence of free-surface flow and complex structures subjected to large rotations and displacements.

In the present work, the weakly-compressible MPS (WC-MPS) (Shakibaeinia & Jin, 2010) and the nonlinear FE solver Giraffe (Generic Interface Readily Accessible For Finite Elements) (Gay Neto, 2016) are coupled adopting the explicitly represented polygon (ERP) wall boundary model. The partitioned conventional sequential staggered (CSS) scheme (Felippa et al., 2001), in which each subdomain is solved separately and sequentially at a given time level, is adopted here. It is well known that particle-based modeling of fluid domain suffers from numerical noise on the pressure field. This can be highly dangerous when a particle method is dynamically coupled with a structural solver (Molteni & Colagrossi, 2009). In this way, a regularization technique and conservative pressure gradient formulation (Jandaghian & Shakibaeinia, 2020) are integrated to improve the computation of the pressure field. Furthermore, the particle number density is calculated herein by using the continuity equation with the introduction of a proper tuning-free diffusive term (Fernández-Gutiérrez & Zohdi, 2020), which improves the smoothness and the accuracy of pressure field. As a contribution to polygon wall boundary modeling, discrete divergence operators, considering free-slip or no-slip boundary conditions, are derived, and applied for the formalism of the ERP. In addition to that, a repulsive force based on Lennard-Jones potential (1994) is introduced in the ERP formulation, and since a little or no tuning is required for this force, the stability of the method is significantly improved. Moreover, since zero-thickness polygon walls can lead to incorrect interaction between particles placed at opposite sides of the wall, a simple but effective technique is proposed herein to overcome this shortcoming.

The chapter structure follows the sequence: Section 5.3 highlights the main features and the numerical modeling of fluid and shell structure as well as the polygon wall boundary model. Next, Sections 5.5 and 5.6 report respectively the evaluation of the fluid and structural solvers by comparing their results with those obtained by analytical solutions, laboratory measurements and numerical models reported in the literature. The verification and validation of the coupled model are presented in Section 5.7. Finally, Section 5.8 provides the concluding remarks.

5.2 RELATED WORKS

Several works have been applied the SPH-FEM approach to FSI problems with hydrodynamic impact loads. De Vuyst (2005) coupled the SPH to an explicit FEM solver (LLNL-DYNA3D). The FSI was estimated by particle-particle contact approach, in which the exterior layer of FE nodes was treated as SPH particles. In this approach, the elements require particles of same size scale. The performance of the algorithm was illustrated by the simulation of impact problems involving solid-solid and fluid-solid interaction. In Groenenboom and Cartwright (2010), a SPH solver was coupled to an explicit FEM solver (PAM-CRASH). The interaction between the fluid and structures was modeled by one of the sliding interface algorithms, based on the penalty formulation, available in PAM-CRASH. The size of elements and particles had almost the same scale in their solver. They demonstrated the robust nature of the proposed model to address complex applications such as flexible cylinder falling onto calm water, wave environment at the entrance to the well dock of an amphibious transport ship and the release of an offshore mooring structure from a ship. In Yang et al. (2012), the coupling of the fluid and structural models was realized through the Monaghan repulsive boundary condition (Monaghan, 1994; Monaghan, 2005), and the motion of the exterior layer of the FE nodes were used to update interface SPH particles. The proposed model was validated by a clamped elastic beam in mid-depth oil sloshing and dam-break flow of water through an elastic gate. The so-called striped-point-in-box (S-PIB) searching algorithm was proposed by Hu et al. (2014) aimed to improve the computational efficiency of neighbor and contact searching for a coupled SPH-FEM model. In the S-PIB, the entire domain is divided in striped subsets, followed by the three steps of PIB, namely sorting points, searching bounds and listing intersection. Numerical and experimental examples of dam breaking over elastic structures were used to validate the proposed model. A numerical framework to couple SPH-ALE (arbitrary Lagrangian–Eulerian) (Vila, 1999) and FE methods was proposed by Li et al. (2014) considering small structural deformation and displacement. Their work focused to ensure the zero algorithmic interface energy condition for the partitioned solution coupling procedure, then improving the numerical stability and order of accuracy. By comparing their numerical results with analytical ones from one-dimensional test cases, they showed that their coupling approach can preserve the order of accuracy in time for the coupled system, and correctly calculate the interface status when a shock wave impacts onto the fluid-structure interface. Also, 3D numerical results had a good agreement with those obtained by using coupled mesh-meshless and mesh-based software. After, Li et al.

(2015) extended their code to consider large structural deformation. In both works of Li the FE size was close to the fluid particle size. Subsequently, in order to optimize the efficiency and stability of the code, the so-called GC method (Gravouil & Combescure, 2001) was incorporated by Nunez-Ramirez et al. (2017), allowing simulations with different time-steps in each sub-domain. Nevertheless, the techniques adopted in Li et al. (2014; 2015) and Nunez-Ramirez et al. (2017), are not generic since they are strongly linked to the FE model, and considerable coding implementation effort within the solid solver is required. Aimed to ensure the conservation of linear and angular momentum, by adjusting positions and normal velocities of particles and FE nodes, Long et al. (2016) introduced a particle-element contact algorithm based on master-slave scheme into coupling of FEM-ISPH (incompressible SPH) and FEM-SPH. The effectiveness and accuracy of the proposed algorithm were verified for benchmark tests of hydrostatic tank, water column with an elastic gate and dam breaking on elastic plate. Two coupling algorithms were adopted by Fourey et al. (2017) to couple SPH and FE methods: conventional parallel staggered (CPS) procedure for parallel algorithm, in which both solvers update synchronously the solution to the next time step; and CSS for sequential algorithm, in which the solvers progress alternatively (Felippa et al., 2001). By simulating hydrostatic water column on an elastic bottom, hydroelastic slamming and water column with an elastic gate, they concluded that CSS algorithm is more stable than the CPS one, although CPS showed a better performance in terms of CPU time saving. Later, Hermange et al. (2019) extended the formalism developed in Fourey et al. (2017) to a 3D model and, by adopting the CPS algorithm, applied it to hydroplaning phenomenon. Recently, Ogino et al. (2019) developed a partitioned coupling of SPH-FE methods by adopting interface marker on fluid-structure boundaries and a dummy mesh for fluid analysis domain. Numerical results of dam-break problem with an elastic plate were compared with the proposed method, given acceptable agreement.

Regarding the efforts on the coupling of MPS and FE methods to deal with FSI problems with violent free-surface flows and impulsive hydrodynamic loads, the earliest attempt was the work of Lee et al. (2007). Pseudo fluid particles were placed at the FE nodes and a weak coupling was adopted, where the pressure computed by the MPS is first applied to the shell elements and then the interface velocity of the shell is given to the fluid particles. The same resolution for both the fluid and structural domains was adopted. Maximum amplitude responses of two-dimensional (2D) sloshing in rigid and elastic tanks were numerically compared. Similarly, Mitsume et al. (2014a) coupled the explicit MPS (EMPS) (Oochi et al., 2010) and FE methods by overlapping wall boundary particles and FE nodes in order to

exchange of physical values on fluid-structure interfaces. Subsequently, Mitsume et al. (2014b) improved their model by using a polygon wall boundary model (Yamada et al., 2011) instead of wall particles in order to deal with complex shaped fluid-structure boundaries. In both works of Mitsume, the models were verified against numerical results from collapse of water column on an elastic plate. A weak coupling of MPS-FEM was proposed by Rao et al. (2017), aimed to investigate a 2D interaction between a solitary wave and an elastic structure. Afterwards, Zhang and Wan (2018) improved the coupled model by the inclusion of a particle group scheme (Hwang et al., 2016). In the particle group scheme, solid particles located within the same transverse section are grouped and hydrodynamic forces of the sections are applied on the correspondent structural beam nodes. Then, the displacements of beam elements computed by FEM are applied to the correspondent particle group. The improved model was used to investigate sloshing flows in an elastic tank (Zhang & Wan, 2018) and the dynamic responses of rigid and elastic structures when subject to wave slamming (Zhang et al., 2019). In Zhang and Wan (2019) and Chen et al. (2019) the model was extended to solve 3D problems. A kernel function-based interpolation (KFBI) was proposed to transfer the summation of weighted forces on the neighbor particles to the FE nodes and summation of weighted neighbor nodal displacements to the boundary particles. The model was applied to a dam-break flow (Zhang & Wan, 2019) and sloshing phenomenon (Chen et al., 2019) interacting with elastic tanks, and the influence of structural elasticity on the evolution of free-surface flow was investigated. A partitioned one-way coupling of EMPS-FEM was considered in Zheng et al. (2018) and Zheng and Shioya (2019). They assumed an infinitesimal deformation of structures, which means that the motion of the fluid flow influences the solid structure, but the reaction of a solid upon fluid is negligible. Also, different interpolations methods were investigated, which concluded that the force on the FE nodes obtained by numerical integration of pressure on the surface element by using the Gauss numerical integration formula provided more accurate results. In both works, the stress on the turbine building of Fukushima Daiichi Nuclear Power Station Unit 1, due to tsunami loading, was estimated with the proposed approach.

5.3 NUMERICAL METHODS

An enhanced WC-MPS is adopted to solve the hydrodynamic equations of incompressible viscous flow. Thin-walled structures undergoing large displacements and rotations are modeled following a geometrically exact shell model, a robust formulation for nonlinear

structural dynamic simulations. For the coupling of fluid and solid subdomains, ERP wall boundary model and a partitioned CSS scheme are employed.

5.3.1 WEAKLY COMPRESSIBLE MPS (WC-MPS) METHOD - FLUID SUBDOMAIN

In the present study we adopted the fully explicit algorithm of the enhanced WC-MPS method, already detailed in the Item 0.

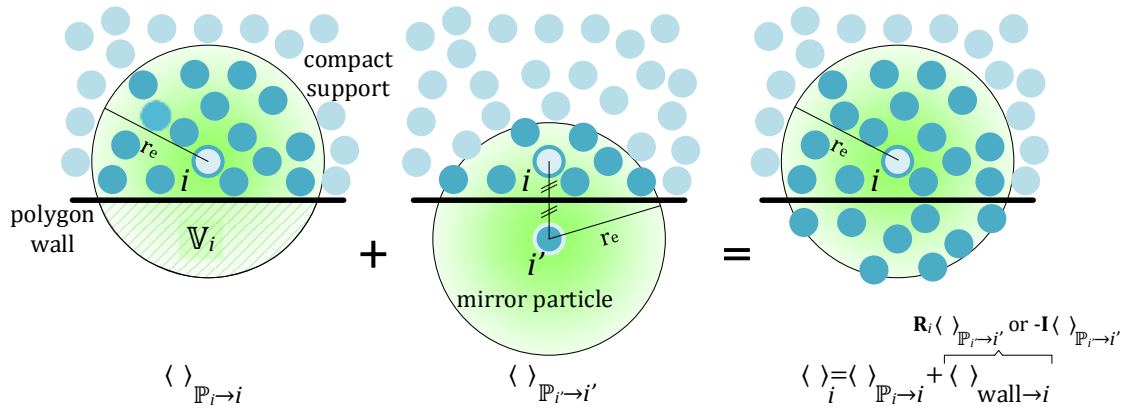
5.3.1.1 EXPLICITLY REPRESENTED POLYGON (ERP) WALL BOUNDARY MODEL

The explicitly represented polygon (ERP) wall boundary model (Mitsume et al., 2015) was adopted to represent solid boundaries as triangular polygons. From a practical point of view, polygon wall models are more flexible to model the surface of the complex-shaped bodies compared with conventional particle-based representation. Some advantages of the ERP are:

- i.) The generation of neighbor virtual particles are not required;
- ii.) Neumann boundary condition for pressure and the free-slip or no-slip condition for velocities on the walls are satisfied;
- iii.) Since reciprocal forces are computed at the interface between fluid and solid subdomains, Newton's third law is assured and, as a consequence, higher accuracy and stability are expected;
- iv.) No specific treatment is required for the coupling at discrete interface between fluid and structure subdomains with different particle and mesh resolutions.

Aiming to accelerate the search for the fluid particles to be mirrored and calculation of their distances to the closest polygons, an axis-aligned bounding box (AABB) hierarchy, implemented using the C++ library libigl (Jacobson et al., 2018), was used in the present work. Since the solid walls are represented by polygons in the ERP model, the compact support of fluid particles near the walls is not fully filled with particles. Hence, the numerical operators of these particles are divided into the contribution due to neighbor fluid particles $\langle \cdot \rangle_{\mathbb{P}_i \rightarrow i}$ and the virtual neighboring particles \mathbb{V}_i , represented by the closest polygon wall $\langle \cdot \rangle_{\text{wall} \rightarrow i}$, as illustrated in Figure 5.1. To calculate the numerical operators $\langle \cdot \rangle_{\text{wall} \rightarrow i}$, first, the position of the mirror particle i' corresponding to particle i is computed. After that, the numerical operators of particle i' are calculated considering the original particle i and its neighbors inside the neighbor region of i' . Finally, these operators are transformed, by the multiplication of the transformation matrix $\mathbf{R}_i^{\text{ref}}$ or the negative value of the identity matrix $-\mathbf{I}$, and added to the numerical operators $\langle \cdot \rangle_{\mathbb{P}_i \rightarrow i}$.

Figure 5.1 - ERP model. Contribution of fluid particles and polygon walls to the calculation of numerical operators.



Source: the author.

The pressure gradient and the Laplacian of the velocity terms of fluid particles close to polygon wall boundary are calculated as:

$$\langle \nabla P \rangle_i = \langle \nabla P \rangle_{\mathbb{P}_{i \rightarrow i}} + \langle \nabla P \rangle_{\text{wall} \rightarrow i}, \quad (5.1)$$

$$\langle \nabla^2 \mathbf{u} \rangle_i = \langle \nabla^2 \mathbf{u} \rangle_{\mathbb{P}_{i \rightarrow i}} + \langle \nabla^2 \mathbf{u} \rangle_{\text{wall} \rightarrow i}, \quad (5.2)$$

where $\langle \rangle_{\mathbb{P}_{i \rightarrow i}}$ denotes the contribution of fluid particles in the same way of the standard MPS. Here, we adapted the pressure gradient operator proposed by Mitsume et al. (2015), following Jandaghian and Shakibaeinia (2020):

$$\langle \nabla P \rangle_{\text{wall} \rightarrow i} = \mathbf{R}_i^{\text{ref}} \frac{\text{dim}}{n^0} \sum_{j \in \mathbb{P}_{i'}} \left(\frac{n_j}{n_j} P_j + \frac{n_j}{n_i} P_i \right) \frac{(\mathbf{r}_j - \mathbf{r}_{i'})}{\|\mathbf{r}_j - \mathbf{r}_{i'}\|^2} \omega_{i'j}. \quad (5.3)$$

The operators $\langle \rangle_{\text{wall} \rightarrow i}$ for the Laplacian of the velocity for the free-slip (Eq. (5.4)) and no-slip boundary (Eq. (5.5)) condition are computed via a weighted sum over neighboring fluid particles $\mathbb{P}_{i'}$ of the mirror particle i' (Mitsume et al., 2015):

$$\langle \nabla^2 \mathbf{u} \rangle_{\text{wall} \rightarrow i} = \mathbf{R}_i^{\text{ref}} \frac{2\text{dim}}{\lambda^0 n^0} \sum_{j \in \mathbb{P}_{i'}} (\mathbf{u}_j - \mathbf{u}_{i'}) \omega_{i'j}, \quad \mathbf{u}_{i'} = \mathbf{R}_i^{\text{ref}} \mathbf{u}_i, \quad (5.4)$$

$$\langle \nabla^2 \mathbf{u} \rangle_{\text{wall} \rightarrow i} = -\mathbf{I} \frac{2\text{dim}}{\lambda^0 n^0} \sum_{j \in \mathbb{P}_{i'}} (\mathbf{u}_j - \mathbf{u}_{i'}) \omega_{i'j}, \quad \mathbf{u}_{i'} = -\mathbf{u}_i + 2[\mathbf{u}_i^{\text{wall}} - (\mathbf{n}_i^{\text{wall}} \cdot \mathbf{u}_i^{\text{wall}}) \mathbf{n}_i^{\text{wall}}], \quad (5.5)$$

where $\mathbf{u}_i^{\text{wall}}$ is the velocity vector of the wall at the point where the force of particle i is applied and $\mathbf{n}_i^{\text{wall}}$ is the unit normal vector of the wall pointing to the particle i .

The position of the mirror particle i' corresponding to particle i is obtained as:

$$\mathbf{r}_{i'} = \mathbf{r}_i + 2(\mathbf{r}_i^{\text{wall}} - \mathbf{r}_i), \quad (5.6)$$

where $\mathbf{r}_i^{\text{wall}}$ is the closest point on the polygon to particle i .

The transformation matrix $\mathbf{R}_i^{\text{ref}}$ for reflection across the plane is expressed as:

$$\mathbf{R}_i^{\text{ref}} = \mathbf{I} - 2\mathbf{n}_i^{\text{wall}} \otimes \mathbf{n}_i^{\text{wall}}, \quad (5.7)$$

where \mathbf{I} denotes the identity matrix.

A repulsive force $\mathbf{f}_i^{\text{rep}}$, perpendicular to the boundary, is added to Eq. (5.3) to prevent penetrations of the free-surface particles at walls or inner fluid particles at curved knuckled surfaces. Instead the original repulsive force proposed by Mitsume et al. (2015), with a specific coefficient which should be tuned for each simulation, or the repulsive force proposed by Harada (2008), which is proportional to $1/\Delta t^2$, i.e., noticeably sensitive to any change on Δt , we introduced a repulsive force based on Lennard-Jones potential (1994) in the ERP formulation:

$$\mathbf{f}_i^{\text{rep}} = \begin{cases} -\frac{D_{\text{rep}}}{\|\mathbf{r}_{iw}\|} \left[\left(\frac{0.5l^0}{\|\mathbf{r}_{iw}\|} \right)^{n_1} - \left(\frac{0.5l^0}{\|\mathbf{r}_{iw}\|} \right)^{n_2} \right] \mathbf{n}_i^{\text{wall}} & \|\mathbf{r}_{iw}\| \leq 0.5l^0, \\ 0 & \|\mathbf{r}_{iw}\| > 0.5l^0 \end{cases}, \quad (5.8)$$

where n_1 and n_2 are integer coefficients that should satisfy $n_1 > n_2$ and are usually taken as $n_1 = 12$ and $n_2 = 4$, or $n_1 = 4$ and $n_2 = 2$ (Monaghan, 1994), $D_{\text{rep}} = \rho C_{\text{rep}} |V_{\text{MAX}}|^2$ with V_{MAX} the maximum velocity in the domain, and $\mathbf{r}_{iw} = \mathbf{r}_i - \mathbf{r}_i^{\text{wall}}$. The coefficient C_{rep} denotes a dimensionless constant in the range $C_{\text{rep}} \in [1.0, 10.0]$. In the present work, the values $n_1 = 4$, $n_2 = 2$ and $C_{\text{rep}} = 1$ are used for all simulations. Since D_{rep} is proportional to the instantaneous flow field, the Eq. (5.8) is dynamically adjusted, i.e., a little or no tuning of the coefficient C_{rep} is required, thereby improving significantly the numerical stability for a wide range of simulations.

Similar the gradient of pressure given by Eq. (2.30), the contribution of the closest polygon wall on the gradient of the concentration (Eq.(2.72)) can be approximated by:

$$\langle \nabla C \rangle_{\text{wall} \rightarrow i} = \mathbf{R}_i^{\text{ref}} \frac{d}{n^0} \sum_{j \in \mathbb{P}_i} \frac{C_i + C_j}{\|\mathbf{r}_{i'j}\|^2} \mathbf{r}_{i'j} \omega_{i'j}, \quad (5.9)$$

Thanks to the following relation $\mathbf{r}_{i'j} = \mathbf{R}_i^{\text{ref}} \mathbf{r}_{ij}$, the deviation σ_i (see Eq. (2.36)) of fluid particles close to polygon walls is rewritten as:

$$\sigma_i = \frac{|\sum_{j \in \mathbb{P}_i} (\omega_{ij} \mathbf{r}_{ij}) + \mathbf{R}_i^{\text{ref}} \sum_{j \in \mathbb{P}_i} (\omega_{i'j} \mathbf{r}_{i'j})|}{\sum_{j \in \mathbb{P}_i} \omega_{ij} + \sum_{j \in \mathbb{P}_i} \omega_{i'j}}, \quad (5.10)$$

The particle number density n_i also is partitioned into the contribution due to the fluid particles $n_{\mathbb{P}_i \rightarrow i}$, see Eq. (2.66), and the polygon walls $n_{\text{wall} \rightarrow i}$. As emphasized in Jandaghian

and Shakibaeinia (2020), the diffusive term D_i , see Eq. (2.67), is added to smoothed continuity equation (2.65) only between the fluid particles to exclude the effects of the solid boundary particles on the conservation features of the system. Hence, the particle number density due to the polygon walls $n_{\text{wall} \rightarrow i}$ is calculated by:

$$n_{\text{wall} \rightarrow i} = -n_i \Delta t \langle \nabla \cdot \mathbf{u} \rangle_{\text{wall} \rightarrow i}. \quad (5.11)$$

Since the divergence of the velocity over the polygon wall boundary is required in Eq. (5.11), discrete divergence operators for ERP were derived in the present work.

5.3.1.1.1 Divergence of the velocity - Free-slip boundary condition

Following Jandaghian and Shakibaeinia (2020), the divergence of the velocity associated to the virtual neighboring particles \mathbb{V}_i (see Figure 5.1), considering the free-slip boundary condition, can be obtained by:

$$\langle \nabla \cdot \mathbf{u} \rangle_{\text{wall} \rightarrow i} = \frac{\text{dim}}{n^0} \sum_{j' \in \mathbb{V}_i} \left(\frac{n_j}{n_i} \right) \frac{(\mathbf{R}_j^{\text{ref}} \mathbf{u}_j - \mathbf{u}_i) \cdot \mathbf{r}_{ij'}}{\|\mathbf{r}_{ij'}\|^2} \omega_{ij'}. \quad (5.12)$$

Assuming that the nearest polygon wall of the particle i and its neighboring particle j have the same unit normal vector $\mathbf{n}_j^{\text{wall}} \approx \mathbf{n}_i^{\text{wall}}$, one gets $\mathbf{R}_j^{\text{ref}} \approx \mathbf{R}_i^{\text{ref}}$, and Eq. (5.12) can be rewritten as:

$$\langle \nabla \cdot \mathbf{u} \rangle_{\text{wall} \rightarrow i} = \frac{\text{dim}}{n^0} \sum_{j \in \mathbb{P}_{i'}} \left(\frac{n_j}{n_i} \right) \frac{(\mathbf{R}_i^{\text{ref}} \mathbf{u}_j - \mathbf{u}_i) \cdot (\mathbf{R}_i^{\text{ref}} \mathbf{r}_{i'j})}{\|\mathbf{r}_{i'j}\|^2} \omega_{i'j}. \quad (5.13)$$

Taking into account the orthogonal properties $\mathbf{R}_i^{\text{ref}} = (\mathbf{R}_i^{\text{ref}})^T = (\mathbf{R}_i^{\text{ref}})^{-1}$ and $\mathbf{R}_i^{\text{ref}} \mathbf{R}_i^{\text{ref}} = \mathbf{I}$ of the transformation matrix, Eq. (5.13) yields:

$$\langle \nabla \cdot \mathbf{u} \rangle_{\text{wall} \rightarrow i} = \frac{\text{dim}}{n^0} \sum_{j \in \mathbb{P}_{i'}} \left(\frac{n_j}{n_i} \right) \frac{\mathbf{R}_i^{\text{ref}} (\mathbf{u}_j - \mathbf{u}_{i'}) \cdot (\mathbf{R}_i^{\text{ref}} \mathbf{r}_{i'j})}{\|\mathbf{r}_{i'j}\|^2} \omega_{i'j}, \quad (5.14)$$

with $\mathbf{u}_{i'}$ provided in Eq. (5.4). Given that the dot product between two vectors fulfills the commutative property, after simple algebraic manipulations, Eq. (5.14) can be slightly simplified as:

$$\langle \nabla \cdot \mathbf{u} \rangle_{\text{wall} \rightarrow i} = \frac{\text{dim}}{n^0} \sum_{j \in \mathbb{P}_{i'}} \left(\frac{n_j}{n_i} \right) \frac{(\mathbf{u}_j - \mathbf{u}_{i'}) \cdot \mathbf{r}_{i'j}}{\|\mathbf{r}_{i'j}\|^2} \omega_{i'j}. \quad (5.15)$$

5.3.1.1.2 Divergence of the velocity - No-slip boundary condition

When the no-slip boundary condition is imposed on a wall, the velocity of the neighbor mirror particle j' is defined by:

$$\mathbf{u}_{j'} = -\mathbf{u}_j + 2[\mathbf{u}_j^{\text{wall}} - (\mathbf{n}_j^{\text{wall}} \cdot \mathbf{u}_j^{\text{wall}})\mathbf{n}_j^{\text{wall}}], \quad (5.16)$$

where $\mathbf{u}_j^{\text{wall}}$ is the velocity of the wall at the point at which it is acted on by the force of particle j . Then, the wall part of the gradient of the velocity can be rewritten as follows:

$$\langle \nabla \cdot \mathbf{u} \rangle_{\text{wall} \rightarrow i} = -\frac{\text{dim}}{n^0} \sum_{j' \in \mathbb{V}_i} \left(\frac{n_j}{n_i} \right) \frac{\{\mathbf{u}_j - (-\mathbf{u}_i + 2[\mathbf{u}_j^{\text{wall}} - (\mathbf{n}_j^{\text{wall}} \cdot \mathbf{u}_j^{\text{wall}})\mathbf{n}_j^{\text{wall}}])\} \cdot \mathbf{r}_{ij'}}{\|\mathbf{r}_{ij'}\|^2} \omega_{ij'}. \quad (5.17)$$

Assuming that $\mathbf{u}_j^{\text{wall}} \approx \mathbf{u}_i^{\text{wall}}$, Eq. (5.17) reads:

$$\langle \nabla \cdot \mathbf{u} \rangle_{\text{wall} \rightarrow i} = -\frac{\text{dim}}{n^0} \sum_{j \in \mathbb{P}_{i'}} \left(\frac{n_j}{n_i} \right) \frac{(\mathbf{u}_j - \mathbf{u}_{i'}) \cdot (\mathbf{R}_i^{\text{ref}} \mathbf{r}_{i'j})}{\|\mathbf{r}_{i'j}\|^2} \omega_{i'j}. \quad (5.18)$$

5.3.1.2 PARTICLE INTERACTION ACROSS ZERO-THICKNESS WALLS

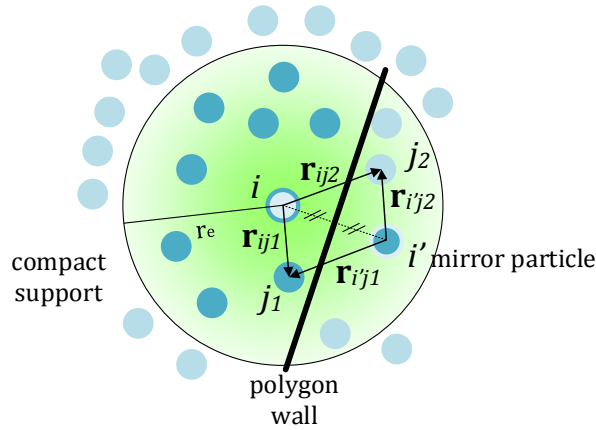
The adoption of zero-thickness polygon walls can lead to incorrect interaction between particles placed at opposite sides of the wall, i.e., the definition of a neighboring particle j inside the compact support of a particle i even if a wall boundary separate them. To overcome this problem, here a simple but effective technique is proposed.

Since the wall is equidistant to a particle i and its mirror i' , a potential neighboring particle j belongs to the neighboring domain \mathbb{P}_i when it is closer to i than i' , i.e., the following criterion can be adopted:

$$\begin{cases} \text{If } \|\mathbf{r}_j - \mathbf{r}_i\| < \|\mathbf{r}_j - \mathbf{r}_{i'}\| & \rightarrow j \in \mathbb{P}_i \\ \text{otherwise} & \rightarrow j \notin \mathbb{P}_i \end{cases} \quad (5.19)$$

To clarify the proposed criterion, Figure 5.2 illustrates a generic situation in which the particle j_1 is regarded as a neighboring particle of i , while j_2 is not defined as a neighbor, although both are within the compact support of i . It must be highlighted that since the ERP model assumes that the polygon is a flat wall in the compact support, approximation errors occur when the exact boundary geometry in the compact support region is a curved knuckled surface. In this way, the proposed technique may not always work properly for curved boundary geometries in the compact support region.

Figure 5.2 - Neighboring particle detection in the presence of zero-thickness walls.



Source: the author.

5.3.2 FINITE ELEMENT METHOD (FEM) – SOLID SUBDOMAIN

The section aims to show briefly the main assumptions and some relevant characteristics of the geometrically exact shell theory. This was developed in many previous works. In the light of the application in present work, our choice was to use the Rodrigues parameters to describe the finite rotations. In this context, the seminal ideas may be found in (Campello et al., 2003; Moreira, 2009; Campello et al., 2011; Ota et al., 2016).

5.3.2.1 KINEMATIC DESCRIPTION

The middle surface of the shell is assumed as a plane at the initial (reference) configuration r . Let $\{\mathbf{e}_1^r; \mathbf{e}_2^r; \mathbf{e}_3^r\}$ be an orthonormal system, with corresponding coordinates $\{\xi_1; \xi_2; \zeta\}$, the vectors \mathbf{e}_1^r and \mathbf{e}_2^r are placed on the middle surface and \mathbf{e}_3^r is normal to this plane, as shown in Figure 5.3.

The position $\boldsymbol{\xi}$ of any shell material point in the reference configuration can be described by:

$$\boldsymbol{\xi} = \boldsymbol{\zeta} + \mathbf{a}^r, \quad (5.20)$$

where the vector $\boldsymbol{\zeta} = \xi_\alpha \mathbf{e}_\alpha^r$, ($\alpha = 1, 2$), defines a point on the reference middle surface and $\mathbf{a}^r = \zeta \mathbf{e}_3^r$ is the shell director at this point, with $\zeta \in H = [-h^b, h^t]$ the thickness coordinate and $h = h^b + h^t$ being the shell thickness in the reference configuration.

In the current configuration t the position \mathbf{x} of any material point can be represented by:

$$\mathbf{x}^t = \mathbf{z}^t + \mathbf{a}^t, \quad (5.21)$$

where \mathbf{z} denotes the current position of a point in the middle surface and $\mathbf{a} = \mathbf{Q}\mathbf{a}^r$ the current director at this point, with \mathbf{Q}^t as the rotation tensor:

$$\mathbf{Q}^t = \mathbf{I} + \frac{4}{4 + \|\boldsymbol{\alpha}\|^2} \left(\mathbf{A} + \frac{1}{2} \mathbf{A}^2 \right), \quad (5.22)$$

in which \mathbf{I} stands for the identity tensor, $\mathbf{A} = \text{skew}(\boldsymbol{\alpha})$ and $\boldsymbol{\alpha}$ is the Rodrigues rotation vector (Pimenta & Campello, 2001), given by:

$$\boldsymbol{\alpha} = \frac{(\tan\|\boldsymbol{\theta}\|/2)}{\|\boldsymbol{\theta}\|/2} \boldsymbol{\theta}, \quad (5.23)$$

where $\boldsymbol{\theta}$ is the Euler rotation vector representing an arbitrary finite rotation on 3D Euclidean space.

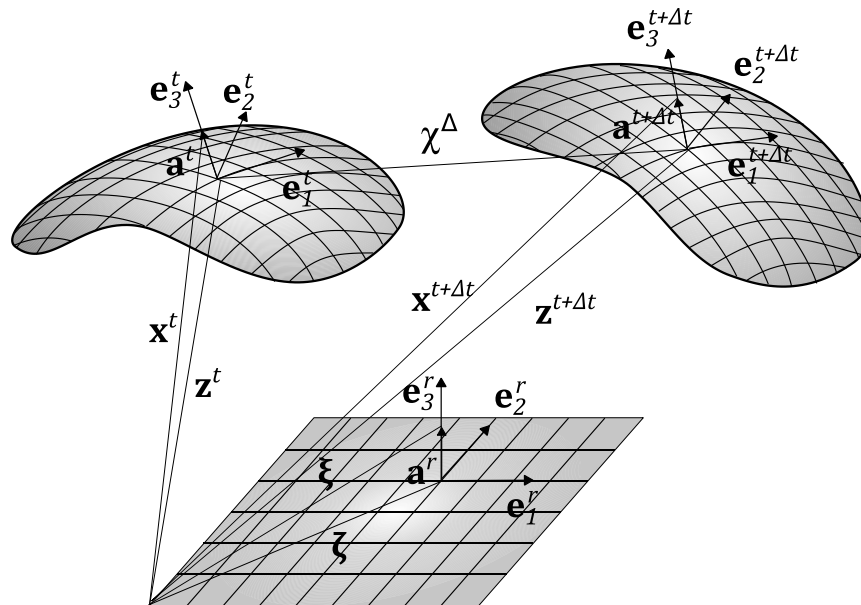
Similarly, the position of any material point at the end of the present time step, $t + \Delta t$, is given by:

$$\mathbf{x}^{t+\Delta t} = \mathbf{z}^{t+\Delta t} + \mathbf{a}^{t+\Delta t}. \quad (5.24)$$

Here $\mathbf{a}^{t+\Delta t} = \mathbf{Q}^\Delta \mathbf{a}^t$, where the superscript Δ stands for the quantities related to the interval $[t, t + \Delta t]$. Since $\mathbf{a}^t = \zeta \mathbf{e}_3^t$, Eq. (5.24) can be rewritten as:

$$\mathbf{x}^{t+\Delta t} = \mathbf{z}^{t+\Delta t} + \zeta \mathbf{Q}^\Delta \mathbf{e}_3^t. \quad (5.25)$$

Figure 5.3 - Shell description and basic kinematical configurations through time evolution (adapted from Moreira (2009)).



Source: the author.

The rotation tensor \mathbf{Q}^Δ stands for the incremental rotation from configuration t to $t + \Delta t$ and is evaluated similarly to Eq. (5.22), but employing the incremental Rodrigues rotation vector. Moreover, one may also evaluate the total rotation by the multiplicative decomposition as $\mathbf{Q}^{t+\Delta t} = \mathbf{Q}^\Delta \mathbf{Q}^t$.

5.3.2.2 STRAIN MEASURES

Adopting the notation $(\cdot)_{,\alpha} = \partial(\cdot)/\partial\xi_\alpha$ for derivatives, the translational strain vector $\boldsymbol{\eta}_\alpha$ at instant $t + \Delta t$ is given by:

$$\boldsymbol{\eta}_\alpha^{t+\Delta t} = \mathbf{z}_{,\alpha}^{t+\Delta t} - \mathbf{e}_\alpha^{t+\Delta t}. \quad (5.26)$$

By multiplying both sides of Eq. (5.26) by $\mathbf{Q}^{t+\Delta t^T}$, its back-rotated counter part reads:

$$\boldsymbol{\eta}_\alpha^{t+\Delta t^r} = \mathbf{Q}^{t+\Delta t^T} \mathbf{z}_{,\alpha}^{t+\Delta t} - \mathbf{e}_\alpha^r. \quad (5.27)$$

Similarly, the back-rotated specific rotation vector $\boldsymbol{\kappa}_\alpha^r$ at instant $t + \Delta t$ can be expressed by:

$$\boldsymbol{\kappa}_\alpha^{t+\Delta t^r} = \mathbf{Q}^{t^r} \boldsymbol{\Xi}^{\Delta^T} \boldsymbol{\alpha}_{,\alpha}^\Delta + \boldsymbol{\kappa}_\alpha^{t^r}, \quad (5.28)$$

with $\boldsymbol{\Xi}^\Delta$ given by (Pimenta & Campello, 2001):

$$\boldsymbol{\Xi}^\Delta = \frac{4}{4 + \|\boldsymbol{\alpha}^\Delta\|^2} \left(\mathbf{I} + \frac{1}{2} \mathbf{A}^\Delta \right), \quad (5.29)$$

where \mathbf{A}^Δ is the skew-symmetric tensor of $\boldsymbol{\alpha}^\Delta$ (the incremental Rodrigues rotation vector).

The generalized back-rotated strain vector $\boldsymbol{\varepsilon}^{t+\Delta t^r}$ can be represented as:

$$\boldsymbol{\varepsilon}^{t+\Delta t^r} = \begin{bmatrix} \boldsymbol{\varepsilon}_1^{t+\Delta t^r} \\ \boldsymbol{\varepsilon}_2^{t+\Delta t^r} \end{bmatrix}, \quad \text{with} \quad \boldsymbol{\varepsilon}_\alpha^{t+\Delta t^r} = \begin{bmatrix} \boldsymbol{\eta}_\alpha^{t+\Delta t^r} \\ \boldsymbol{\kappa}_\alpha^{t+\Delta t^r} \end{bmatrix}. \quad (5.30)$$

5.3.2.3 WEAK FORM OF THE EQUATIONS OF MOTION

Starting from the principle of virtual work, the weak form of the internal (δW_{int}) and external (δW_{ext}) virtual works for the shell, due to the internal stresses and external forces, respectively, can be expressed by:

$$\delta W_{int} = \int_{\Omega_s} (\boldsymbol{\sigma}^{t+\Delta t^r} \cdot \delta \boldsymbol{\varepsilon}^{t+\Delta t^r}) d\Omega, \quad (5.31)$$

$$\delta W_{ext} = \int_{\Omega_s} (\bar{\mathbf{q}} \cdot \delta \mathbf{d}^\Delta) d\Omega, \quad (5.32)$$

where Ω_s is the solid subdomain. Here the symbol δ represents virtual quantities.

The generalized cross-sectional stress vector $\boldsymbol{\sigma}^r$ is calculated as:

$$\boldsymbol{\sigma}^{t+\Delta t^r} = \begin{bmatrix} \boldsymbol{\sigma}_1^{t+\Delta t^r} \\ \boldsymbol{\sigma}_2^{t+\Delta t^r} \end{bmatrix}, \quad \text{with} \quad \boldsymbol{\sigma}_\alpha^{t+\Delta t^r} = \begin{bmatrix} \mathbf{n}_\alpha^{t+\Delta t^r} \\ \mathbf{m}_\alpha^{t+\Delta t^r} \end{bmatrix}, \quad (5.33)$$

in which $\mathbf{n}_\alpha^{t+\Delta t^r}$ designates the back-rotated cross-sectional forces and $\mathbf{m}_\alpha^{t+\Delta t^r}$ denotes the back-rotated cross-sectional moments (per unit length). They are obtained by the integration of the back-rotated stress vectors $\boldsymbol{\tau}_\alpha^r$ along the shell thickness, which act on the cross-sectional planes whose normal on the reference configuration are \mathbf{e}_m^r , $m = (1, 2, 3)$:

$$\mathbf{n}_\alpha^r = \int_H \boldsymbol{\tau}_\alpha^r d\zeta \quad \text{and} \quad \mathbf{m}_\alpha^{t+\Delta t^r} = \int_H \mathbf{a}^r \times \boldsymbol{\tau}_\alpha^r d\zeta. \quad (5.34)$$

The generalized external forces vector $\bar{\mathbf{q}}$ is written as:

$$\bar{\mathbf{q}} = \begin{bmatrix} \bar{\mathbf{n}} \\ \boldsymbol{\Xi}^T \bar{\mathbf{m}} \end{bmatrix}, \quad (5.35)$$

where $\bar{\mathbf{n}}$ is the vector of applied external forces per unit reference area of the middle surface and $\bar{\mathbf{m}}$ represents the vector of external moments per unit reference area.

The vector \mathbf{d}^Δ is defined as:

$$\mathbf{d}^\Delta = \begin{bmatrix} \boldsymbol{\chi}^\Delta \\ \boldsymbol{\alpha}^\Delta \end{bmatrix}, \quad (5.36)$$

where $\boldsymbol{\chi}^\Delta$ is the incremental displacement vector associated with any point of mid-surface of the shell.

Let δT be the virtual variation of the kinetic energy, the principle of virtual work renders:

$$\delta W_{int} - \delta W_{ext} + \delta T = 0, \quad (5.37)$$

with

$$\delta T = \delta T_1 + \delta T_2, \quad (5.38)$$

and δT_1 and δT_2 written as (Ota et al., 2016):

$$\delta T_1 = \rho_s h \int_{\Omega_s} \ddot{\boldsymbol{\chi}}^\Delta \cdot \delta \boldsymbol{\chi}^\Delta d\Omega, \quad (5.39)$$

$$\delta T_2 = \frac{\rho_s h^3}{12} \int_{\Omega_s} \boldsymbol{\Xi}^T \left[\mathbf{E}_3^{t+\Delta t^T} \mathbf{E}_3^{t+\Delta t} \dot{\boldsymbol{\omega}} + \mathbf{E}_3^{t+\Delta t^T} (\boldsymbol{\omega} \times \mathbf{E}_3^{t+\Delta t} \boldsymbol{\omega}) \right] \cdot \delta \boldsymbol{\alpha}^\Delta d\Omega, \quad (5.40)$$

where ρ_s is the solid density, $\boldsymbol{\omega}$ designates the angular velocity vector, $\dot{\boldsymbol{\omega}}$ denotes the angular acceleration vector and $\mathbf{E}_3^{t+\Delta t} = \text{skew}(\mathbf{e}_3^{t+\Delta t})$. As pointed out in Ota et al. (2016), the term $\mathbf{E}_3^{t+\Delta t^T} \mathbf{E}_3^{t+\Delta t} \dot{\boldsymbol{\omega}}$ quantifies the angular acceleration effects, whereas the term $\boldsymbol{\omega} \times \mathbf{E}_3^{t+\Delta t} \boldsymbol{\omega}$ describes the gyroscopic effects on kinetic energy. The angular vectors $\boldsymbol{\omega}$ and $\dot{\boldsymbol{\omega}}$ can be obtained by:

$$\boldsymbol{\omega} = \boldsymbol{\Xi} \dot{\boldsymbol{\alpha}}, \quad (5.41)$$

$$\dot{\boldsymbol{\omega}} = \dot{\boldsymbol{\Xi}} \dot{\boldsymbol{\alpha}} + \boldsymbol{\Xi} \ddot{\boldsymbol{\alpha}}, \quad (5.42)$$

with the more compact notation $\boldsymbol{\Xi} = \boldsymbol{\Xi}^\Delta$, see Eq. (5.29), and $\dot{\boldsymbol{\Xi}}$ given by:

$$\dot{\boldsymbol{\Xi}} = \frac{2}{4 + \|\boldsymbol{\alpha}\|^2} [\dot{\mathbf{A}} - (\boldsymbol{\alpha} \cdot \dot{\boldsymbol{\alpha}}) \boldsymbol{\Xi}]. \quad (5.43)$$

Consistent linearization of Eq. (5.37) leads naturally to the tangent operator:

$$\Delta(\delta W) = \Delta(\delta W_{int}) - \Delta(\delta W_{ext}) + \Delta(\delta T). \quad (5.44)$$

The components of the tangent operator $\Delta(\delta W_{int})$ and $\Delta(\delta W_{ext})$ are fully developed in Campello et al. (2003) and Moreira (2009). The kinetic energy component $\Delta(\delta T)$, on the other hand, is an innovative contribution of Ota et al. (2016). The material formulation employed here is the same presented in Campello et al. (2003) and Tiago (2007). It is a hyperplastic material that, under small strain conditions, recovers linear elastic isotropic behavior.

The tangent operator can be obtained by:

$$\begin{aligned} \Delta(\delta T) = \Delta(\delta T_1) + \Delta(\delta T_2) = \rho_s h \int_{\Omega_s} \left(\mathbf{f}_{\chi, \chi} \Delta \boldsymbol{\chi}^\Delta + \mathbf{f}_{\chi, \alpha} \Delta \boldsymbol{\alpha}^\Delta \right) \cdot \delta \boldsymbol{\chi}^\Delta d\Omega \\ + \frac{\rho_s h^3}{12} \int_{\Omega_s} \left(\mathbf{f}_{\alpha, \chi} \Delta \boldsymbol{\chi}^\Delta + \mathbf{f}_{\alpha, \alpha} \Delta \boldsymbol{\alpha}^\Delta \right) \cdot \delta \boldsymbol{\alpha}^\Delta d\Omega, \end{aligned} \quad (5.45)$$

with

$$\mathbf{f}_{\chi} = \ddot{\boldsymbol{\chi}}, \quad (5.46)$$

$$\mathbf{f}_{\alpha} = \boldsymbol{\Xi}^T \left[\mathbf{E}_3^{t+\Delta t T} \mathbf{E}_3^{t+\Delta t} \dot{\boldsymbol{\omega}} + \mathbf{E}_3^{t+\Delta t T} (\boldsymbol{\omega} \times \mathbf{E}_3^{t+\Delta t} \boldsymbol{\omega}) \right]. \quad (5.47)$$

Then, the Eq. (5.45) can be organized in matrix form, as follows:

$$\Delta(\delta T) = \begin{bmatrix} \rho_s h \int_{\Omega_s} \mathbf{N}^T \mathbf{f}_{\chi, \chi} \mathbf{N} d\Omega & \rho_s h \int_{\Omega_s} \mathbf{N}^T \mathbf{f}_{\chi, \alpha} \mathbf{N} d\Omega \\ \frac{\rho_s h^3}{12} \int_{\Omega_s} \mathbf{N}^T \mathbf{f}_{\alpha, \chi} \mathbf{N} d\Omega & \frac{\rho_s h^3}{12} \int_{\Omega_s} \mathbf{N}^T \mathbf{f}_{\alpha, \alpha} \mathbf{N} d\Omega \end{bmatrix} \begin{bmatrix} \Delta \boldsymbol{\chi}^\Delta \\ \Delta \boldsymbol{\alpha}^\Delta \end{bmatrix} \cdot \begin{bmatrix} \delta \boldsymbol{\chi}^\Delta \\ \delta \boldsymbol{\alpha}^\Delta \end{bmatrix}, \quad (5.48)$$

where \mathbf{N} is the matrix of element shape functions constructed using standard Lagrange polynomials.

5.3.2.4 TIME INTEGRATION SCHEME

Here, accelerations and velocities related to instant $t + \Delta t$ can be obtained by the Newmark method (Newmark, 1959):

$$\ddot{\chi}^{t+\Delta t} = \alpha_1 \chi^\Delta - \alpha_2 \dot{\chi}^t - \alpha_3 \ddot{\chi}^t, \quad (5.49)$$

$$\dot{\chi}^{t+\Delta t} = \alpha_4 \chi^\Delta + \alpha_5 \dot{\chi}^t + \alpha_6 \ddot{\chi}^t, \quad (5.50)$$

$$\dot{\omega}^{t+\Delta t} = \mathbf{Q}^\Delta (\alpha_1 \alpha^\Delta - \alpha_2 \omega^t - \alpha_3 \dot{\omega}^t), \quad (5.51)$$

$$\omega^{t+\Delta t} = \mathbf{Q}^\Delta (\alpha_4 \alpha^\Delta + \alpha_5 \omega^t + \alpha_6 \dot{\omega}^t), \quad (5.52)$$

with the coefficients α_1 - α_6 :

$$\alpha_1 = \frac{1}{\beta_N \Delta t^2}, \quad \alpha_2 = \frac{1}{\beta_N \Delta t}, \quad \alpha_3 = \frac{1 - 2\beta_N}{2\beta_N},$$

$$\alpha_4 = \frac{\gamma_N}{\beta_N \Delta t}, \quad \alpha_5 = 1 - \frac{\gamma_N}{\beta_N}, \quad \alpha_6 = \left(1 - \frac{\gamma_N}{2\beta_N}\right) \Delta t, \quad (5.53)$$

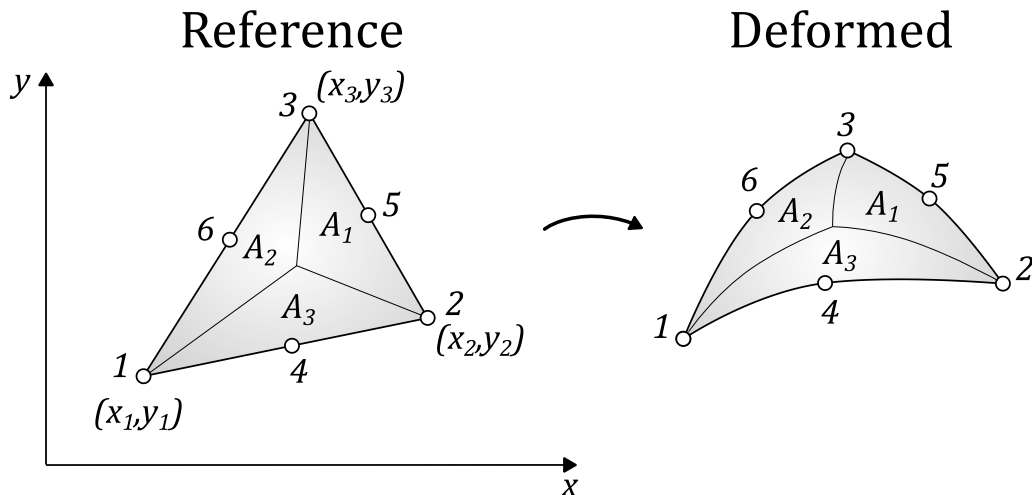
where $\beta_N \in [0.0, 0.5]$ and $\gamma_N \in [0.0, 1.0]$. In the present work, we used $\beta_N = 0.3$ and $\gamma_N = 0.5$. One can refer to Wriggers (2008) for more details.

Therefore, the weak form is a function only of unknown generalized displacements χ^Δ and rotations α^Δ , and the initial conditions for each time step $\dot{\chi}^t$, $\dot{\chi}^t$, $\dot{\omega}^t$ and ω^t .

5.3.2.5 TRIANGULAR SHELL FINITE ELEMENT

The spatial discretization was done using the so-called t6-3i finite element (Campello et al., 2003), see Figure 5.4, a six-node triangular element with quadratic shape functions for interpolation of the displacement field (nodes 1-6) and linear shape functions for interpolation of the rotation field at the mid-points of the edges of the triangle (nodes 4, 5 and 6).

Figure 5.4 - Six-node triangular element in reference and deformed configurations. Nodes, subareas and barycentric coordinate.



Source: the author.

Let \mathbf{p}^Δ be a vector associated with each nodal degrees-of-freedom, containing both displacements and rotations, the proposed shape functions for kinematic quantities are given by:

$$\begin{bmatrix} \boldsymbol{\chi}^\Delta \\ \boldsymbol{\alpha}^\Delta \end{bmatrix} = \mathbf{N} \mathbf{p}^\Delta. \quad (5.54)$$

Let the points 1, 2, 3, be the vertices and 4, 5 and 6 the mid-points of the edges of a triangle, \mathbf{N} and \mathbf{p}^Δ can be rewritten as:

$$\mathbf{N} = [\mathbf{N}_1^\chi \quad \mathbf{N}_2^\chi \quad \mathbf{N}_3^\chi \quad \mathbf{N}_4^\chi \quad \mathbf{N}_5^\chi \quad \mathbf{N}_6^\chi \quad \mathbf{N}_4^\alpha \quad \mathbf{N}_5^\alpha \quad \mathbf{N}_6^\alpha], \quad (5.55)$$

$$\mathbf{p}^\Delta = [\boldsymbol{\chi}_1^c \quad \boldsymbol{\chi}_2^c \quad \boldsymbol{\chi}_3^c \quad \boldsymbol{\chi}_4^c \quad \boldsymbol{\chi}_5^c \quad \boldsymbol{\chi}_6^c \quad \boldsymbol{\alpha}_4^c \quad \boldsymbol{\alpha}_5^c \quad \boldsymbol{\alpha}_6^c]^T, \quad (5.56)$$

in which the superscript c represents a given configuration that may assume any of such points. The shape functions related to $\boldsymbol{\chi}$ are given by:

$$\begin{aligned} N_1^\chi &= (2L_1 - 1)L_1, & N_2^\chi &= (2L_2 - 1)L_2, & N_3^\chi &= (2L_3 - 1)L_3, \\ N_4^\chi &= 4L_1L_2, & N_5^\chi &= 4L_2L_3, & N_6^\chi &= 4L_3L_1, \end{aligned} \quad (5.57)$$

If A is the total area of the element and A_j is the subareas indicated in Figure 5.4, we have:

$$L_j = \frac{A_j}{A}, \quad j = 1, 2, 3, \quad (5.58)$$

where in cartesian coordinates reads:

$$L_j = \frac{1}{2A}(a_j + b_j x + c_j y), \quad j = 1, 2, 3, \quad (5.59)$$

with

$$\begin{aligned} a_1 &= x_2 y_3 - x_3 y_2 & b_1 &= y_2 - y_3 & c_1 &= x_3 - x_2 \\ a_2 &= x_3 y_1 - x_1 y_3 & b_2 &= y_3 - y_1 & c_2 &= x_1 - x_3 \\ a_3 &= x_1 y_2 - x_2 y_1 & b_3 &= y_1 - y_2 & c_3 &= x_2 - x_1 \end{aligned} \quad (5.60)$$

For $\boldsymbol{\alpha}$ we have:

$$N_4^\alpha = 1 - 2L_3, \quad N_5^\alpha = 1 - 2L_1, \quad N_6^\alpha = 1 - 2L_2, \quad (5.61)$$

For a more detailed description of the shell modeling, the reader is referred to Campello et al. (2003) and Ota et al. (2016).

5.3.3 COUPLING SCHEME

The partitioned CSS scheme is adopted here, i.e., each subdomain is solved separately and sequentially at a given time level. At the initial of the step, the fluid solver receives the structural positions and velocities, and afterwards the solution of the fluid subdomain is

updated. The hydrodynamic loads are sent to the structural nodes, and then the structure responses are evaluated. Forces induced by the fluid particles are distributed on the FE nodes through linear shape functions. On the other hand, nodal positions are update, then imposing a new configuration of the wall boundary around the fluid. The same values of time steps for fluid and structure solvers are adopted herein. Such couple scheme can be summarized as below:

1. The force from a fluid particle i to each finite element \mathbb{E}_e , $\mathbf{f}_{i \rightarrow \mathbb{E}_e}$, can be determined based on the normal and tangential components due to the pressure gradient and shear stress, respectively, at the fluid-structure interface, i.e., the reaction to the wall parts of the pressure gradient (Eq. (5.3)), viscous term (Eq. (5.4) or Eq. (5.5)) and repulsive force (Eq. (5.8)):

$$\mathbf{f}_{i \rightarrow \mathbb{E}_e} = -\mathbf{f}_{\text{wall} \rightarrow i} = -(l^0)^{\text{dim}}(-\langle \nabla P \rangle_{\text{wall} \rightarrow i} + \rho_f \nu_f \langle \nabla^2 \mathbf{u} \rangle_{\text{wall} \rightarrow i} - \mathbf{f}_i^{\text{rep}}). \quad (5.62)$$

2. The force $\mathbf{f}_{i \rightarrow \mathbb{E}_e}$ is divided into three parts and transferred to the j -th vertices of the finite elements ($j = 1, 2, 3$) by using linear shape functions $L_j^i = A_j^i/A$, related to the closest point $\mathbf{r}_i^{\mathbb{E}_e}$ on the finite element \mathbb{E}_e to particle i :

$$\mathbf{f}_{i \rightarrow \mathbb{E}_{e,1}} = L_1^i \mathbf{f}_{i \rightarrow \mathbb{E}_e}, \quad \mathbf{f}_{i \rightarrow \mathbb{E}_{e,2}} = L_2^i \mathbf{f}_{i \rightarrow \mathbb{E}_e}, \quad \mathbf{f}_{i \rightarrow \mathbb{E}_{e,3}} = L_3^i \mathbf{f}_{i \rightarrow \mathbb{E}_e}. \quad (5.63)$$

3. Since one vertex (node) can be shared by m elements, the total force on each j -th vertex, is obtained by the following sum:

$$\mathbf{f}_{\mathbb{P}_{\mathbb{E}} \rightarrow j} = \sum_{e \in m} \sum_{i \in \mathbb{P}_{\mathbb{E}_e}} \mathbf{f}_{i \rightarrow \mathbb{E}_{e,j}}, \quad (5.64)$$

where $\mathbb{P}_{\mathbb{E}}$ denotes all the neighboring particles belonging to the m elements \mathbb{E} that share the vertex j , and $\mathbb{P}_{\mathbb{E}_e}$ denotes the neighboring particles of a specific finite element \mathbb{E}_e , i.e., $\|\mathbf{r}_i - \mathbf{r}_i^{\mathbb{E}_e}\| < r_e$

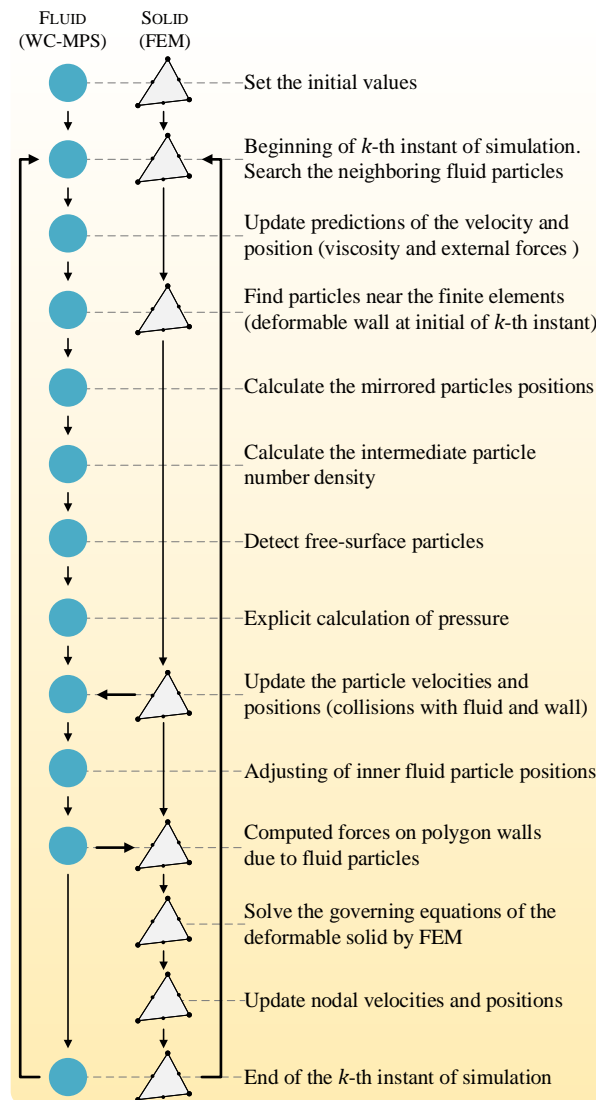
4. Updated nodal positions are provided by the FE solver. Consequently, a new configuration of the wall boundary around the fluid particles are determined.

5.4 ALGORITHM

A brief summary of the algorithm implemented, also illustrated in the schematic diagram of Figure 5.5, proceeds as follows:

1. Set the initial values for all fluid particles and solid elements. This step is evaluated only at the beginning of the simulation.
2. Beginning of the k -th instant of simulation. Search the neighboring fluid particles by a bucket-based domain decomposition (Murotani et al., 2015).
3. Update the predictions of the velocity and position by using viscosity and external forces based on Eqs. (2.38) and (2.39), respectively.
4. Find particles near the polygons, considering the deformable wall configuration at the initial of the step.
5. Calculate the positions of the mirrored particles (Eq. (5.6)).
6. Calculate the intermediate particle number density considering the neighboring fluid particles n_i , see Eq. (2.66), and the neighboring polygon $n_{\text{wall} \rightarrow i}$, see Eq (5.11).
7. Detect free-surface particles by Eq. (2.35).
8. Solve Eq. (2.68) to obtain the pressure at particles.
9. Calculation of the velocity and position by using the pair-wise collision contribution given by Eq. (2.37), pressure gradient due to fluid particles given by Eq. (2.30), and the wall part of pressure gradient and Laplacian of velocity based on Eqs. (5.3) and (5.4) or (5.5), respectively.
10. Apply Eq. (2.70) to inner fluid particles adjusting their final positions.
11. Forces on polygon walls due to fluid particles are calculated by Eq. (5.62).
12. Solve the governing equations of the deformable solid under the fluid forces on the FE nodes given by Eq. (5.64).
13. Update nodal velocities and positions by using nodal displacements and rotations given by Eq. (5.54), resulting in a new configuration of the deformable wall boundary.
14. End of the k -th instant of simulation. Return to step (2) for the next time instant of simulation ($k+1$ -th).

Figure 5.5 - Schematic diagram of the WC-MPS-FEM numerical algorithm.



Source: the author.

5.5 VERIFICATION OF THE WC-MPS METHOD

In order to evaluate the performance of the present WC-MPS method, i.e., only the fluid solver, two benchmark tests were considered. First, 3D hydrostatic tank was simulated and the computed pressures of all particles within a control volume are compared to analytical results. After, 3D dam-break event is simulated and the wave profiles and pressure at sensors are compared against experimental data. To illustrate the improvement on the pressure field by using the smoothed continuity equation (2.66) to compute the particle number density n_i , the numerical results from WC-MPS adopting the Eq. (2.4) and Eq. (2.66) are also compared for both benchmark tests. We assumed no-slip boundary condition for all tests, i.e., Eq. (5.5) and

Eq. (5.18) were used for all cases. The fluid properties defined in Table 5.1 and the gravity acceleration $g = 9.81\text{m/s}^2$ were used for all simulations.

Table 5.1 - Physical properties of the fluid.

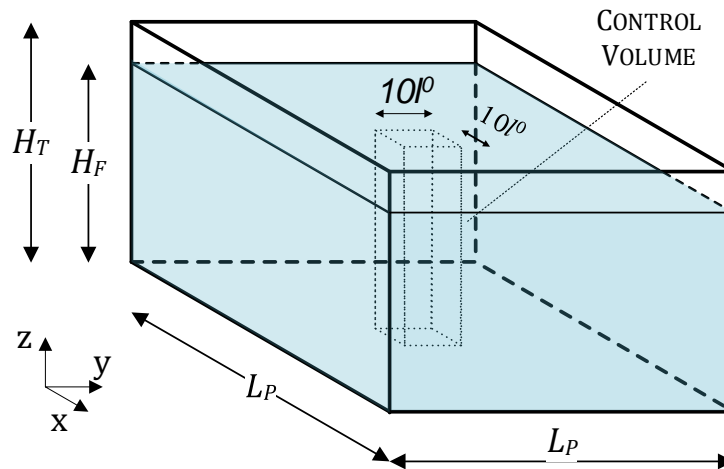
Property	Value
Density ρ_f (kg/m ³)	1000
Kinematic viscosity ν_f (m ² /s)	10^{-6}

Source: the author.

5.5.1 3D PLATE SUBJECT TO GRAVITY

This case consists of a 3D hydrostatic water column of height $H_F = 0.2\text{m}$ in a rigid tank of height $H_T = 0.22\text{m}$ and square bottom of side length $L_p = 0.2\text{m}$, see Figure 5.6. The parameters adopted in the simulations are given in Table 5.2. Aimed to reach a quasi-static state, the dimensionless coefficient $A_F = 1$ was adopted herein. Simulations considering three initial distance between particles, $l_0 = 20, 10$ and 5mm , were performed during 1 second. We conduct a quantitative evaluation of the present WC-MPS adopting the Weight Function, see Eq. (2.4), which is named as WF-WC-MPS, and using the smoothed Continuity equation with Diffusive term, see Eq. (2.66), hereinafter referred to as CD-WC-MPS. Computational times are present in Table 5.3.

Figure 5.6 - Hydrostatic water column of height $H_F = 0.2\text{m}$ in a tank of height $H_T = 0.22\text{m}$ and square bottom of side length $L_p = 0.2\text{m}$. Control volume of square cross section of side l_0 and height $H_F = 0.2\text{m}$.



Source: the author.

Table 5.2 - Hydrostatic tank. Simulation parameters of the fluid.

Parameter	Value	Parameter	Value
Particle distance l_0 (m)	0.02, 0.01, 0.005	Mach number Ma	0.1
Time step Δt (s)	$5.0, 2.5, 1.25 \times 10^{-4}$	Dimensionless number A_F	1
Effective radius r_e (m)	$2.1 \times l^0$	Dimensionless constant C_{rep}	1
Sound speed c_0 (m/s)	15	Surface threshold β	0.98
Courant number C_r	0.2	Surface threshold ϱ	0.2

Source: the author.

Table 5.3 - Hydrostatic tank. Computational time.

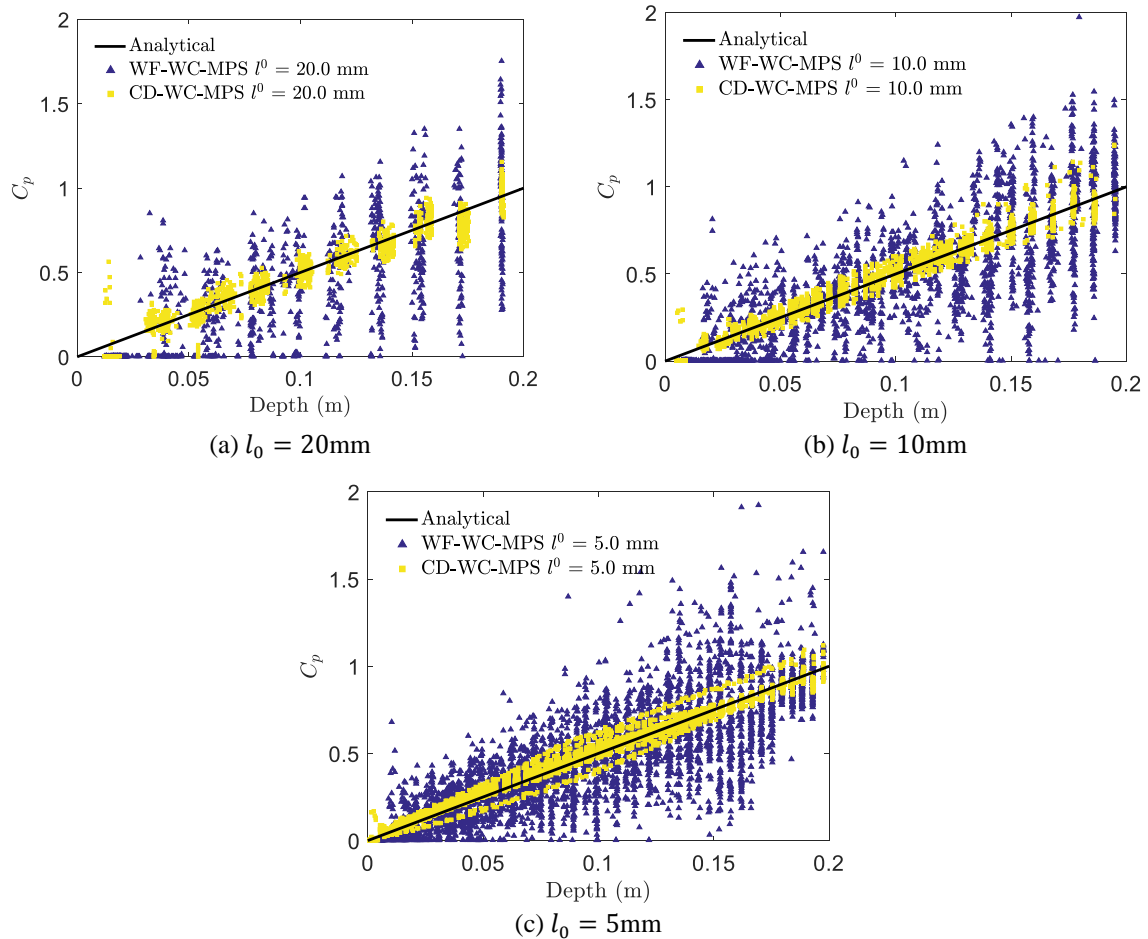
l_0 (mm)	20.0	10.0	5.0
Simulation time (s)		1.0	
Number of particles	1000	8000	64000
Time step (s)	5.0×10^{-4}	2.5×10^{-4}	1.25×10^{-4}
Computation time*	0d00h04m	0d00h55m	0d11h00m

*Intel® Core™ Processor i7-4510U, processor base frequency of 2.00GHz, 4 MB cache, 2 cores and 8GB of memory. Source: the author.

Figure 5.7 depicts the non-dimensional pressure coefficient $C_p = P/\rho g H_F$ computed between the instants $t = 0.7$ and 1.0s (steady-state) for all particles within the control volume of square cross section of side $10l^0$ and height H_F (see Figure 5.6). The theoretical pressure coefficient represented by the black solid line, is also shown. Due to some numerical inconsistencies related to the truncation of the weight function at the free-surface particles close the tank walls and the dynamic nature of the WC-MPS, variations of the pressure field are expected even for still water tank. Despite out of the scope of the present work, the reader can find some works that have adopted different solutions to obtain an exact linear pressure field in the context of particle-based methods (Jandaghian & Shakibaeinia, 2020; Macià et al., 2020).

Figure 5.7 shows that the smoothed continuity equation (2.66) remarkable improves the computed pressure, since much lower non-physical oscillations are obtained compared to the computed pressure by using the original equation (2.4). Moreover, the magnitude of the pressure dispersion is almost the same for all resolutions adopted. Hence, the accuracy of the present CD-WC-MPS is verified for all resolutions simulated in this quasi-static test.

Figure 5.7 - Non-dimensional pressure (C_p) at the particles in the control volume (see Figure 5.6) between the instants $t = 0.7$ and 1.0s. Comparison between the analytical and numerical results computed with the WF-WC-MPS and CD-WC-MPS methods

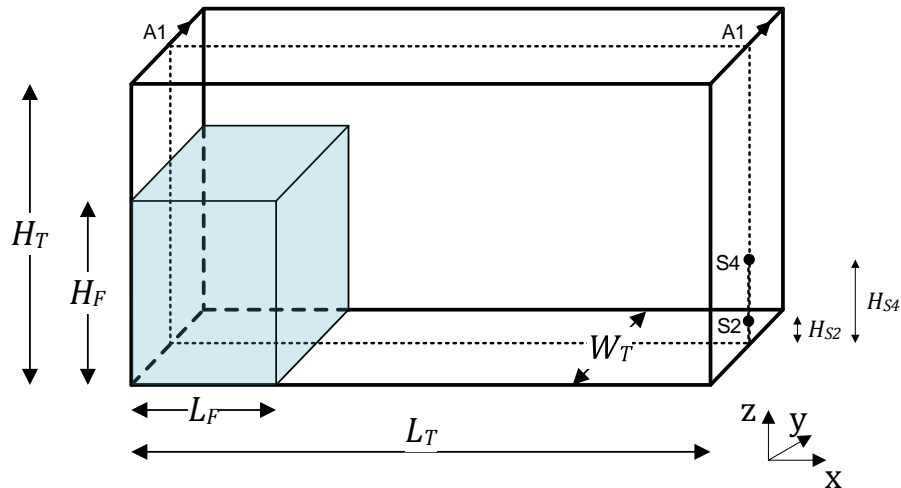


Source: the author.

5.5.2 DYNAMIC PRESSURE UNDER DAM-BREAK EVENT

Aiming to verify the improvements on the hydrodynamic simulations, the benchmark dam-break experiment conducted by Lobovský et al. (2014) was simulated. Figure 5.8 shows the initial configuration of the water column of height $H_F = 0.3\text{m}$ and length $L_F = 0.6\text{m}$, rigid tank of length $L_T = 1.61\text{m}$, width $W_T = 0.15\text{m}$ and height $H_T = 0.6\text{m}$, and the sensors S2 and S4 placed at the heights $H_{S2} = 0.015\text{m}$ and $H_{S4} = 0.08\text{m}$, respectively. Three initial distance between particles, $l_0 = 20, 10$ and 5mm , were adopted. The simulation parameters and computational times are shown respectively in Table 5.4 and Table 5.5. Similar to the previous case, the computed results by using the present WF-WC-MPS and CD-WC-MPS are qualitative and quantitative compared against the experimental data.

Figure 5.8 - Schematic drawing of the tank of length $L_T = 1.61\text{m}$, width $W_T = 0.15\text{m}$ and height $H_T = 0.6\text{m}$, initial water column of height $H_F = 0.3\text{m}$ and length $L_F = 0.6\text{m}$, and the sensors S2, placed at the height $H_{S2} = 0.015\text{m}$ and S4, placed at the height $H_{S4} = 0.08\text{m}$ (Lobovský et al., 2014). The section A1-A1 denotes the middle cross-sectional view.



Source: the author.

Table 5.4 - Dam break. Simulation parameters of the fluid.

Parameter	Value	Parameter	Value
Particle distance l_0 (m)	0.02, 0.01, 0.005	Mach number Ma	0.1
Time step Δt (s)	$2.5, 2.5, 1.25 \times 10^{-4}$	Dimensionless number A_F	2
Effective radius r_e (m)	$2.1 \times l^0$	Dimensionless constant C_{rep}	1
Sound speed c_0 (m/s)	15	Surface threshold β	0.98
Courant number C_r	0.2	Surface threshold ϱ	0.2

Source: the author.

Table 5.5 - Dam break. Computational time.

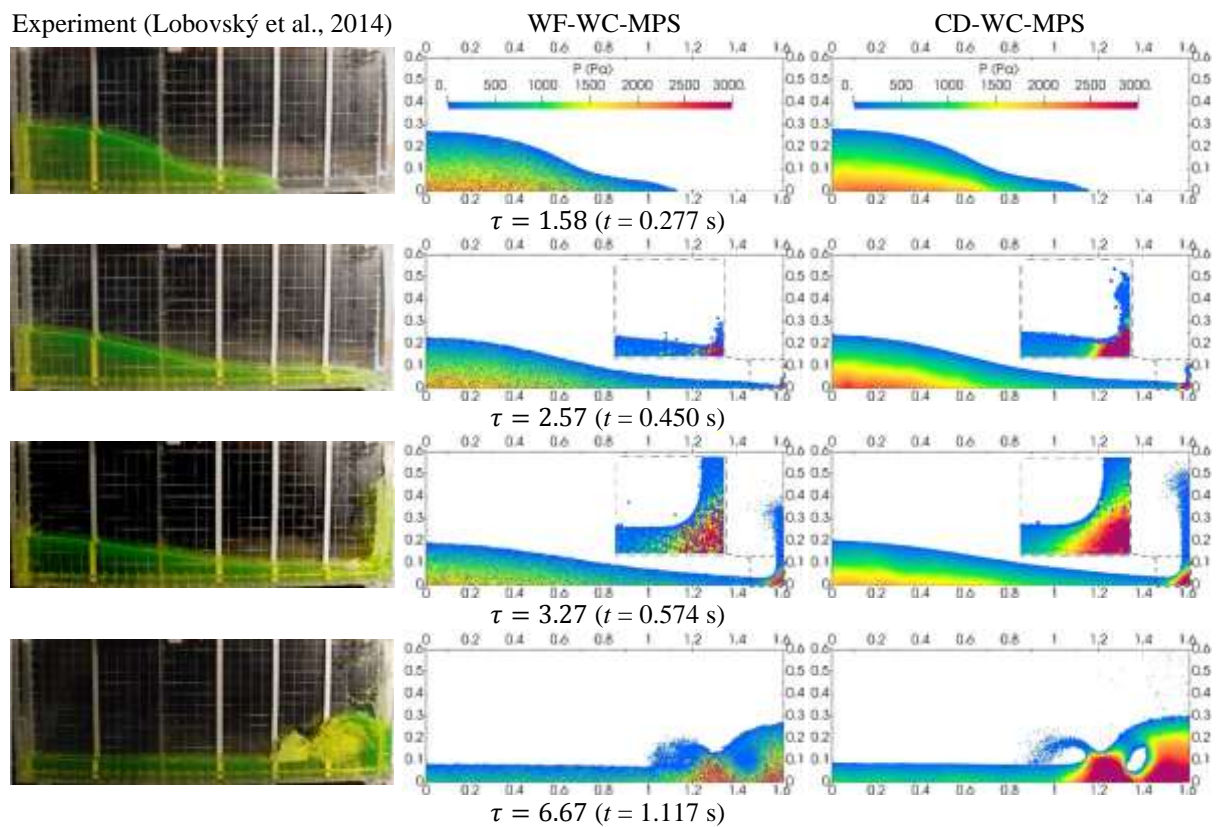
l_0 (mm)	20.0	10.0	5.0
Simulation time (s)		1.5	
Number of particles	3150	27000	216000
Time step (s)	2.5×10^{-4}	2.5×10^{-4}	1.25×10^{-4}
Computation time*	0d00h28m	0d03h40m	2d00h00m

*Intel® Core™ Processor i7-4510U, processor base frequency of 2.00GHz, 4 MB cache, 2 cores and 8GB of memory. Source: the author.

Figure 5.9 illustrates the snapshots showing the free-surface profile of the collapsing water column at synchronized instants with the experiment and obtained from the simulations with the present WC-MPS, distance between particles $l_0 = 5\text{mm}$ and time step $\Delta t = 1.25 \times 10^{-4}\text{s}$.

The color scale is associated to pressure field behind the middle cross-sectional view A1-A1 (see Figure 5.8). Also, the pressure near the stagnation point is highlighted. The dimensionless time (τ) is defined as $\tau = t\sqrt{g/H_F}$. The overall wave profile computed with the present WC-MPS applying the Eq. (2.4) and Eq. (2.66) are in good agreement with the experiment. However, the simulation carried out using WC-MPS with Eq. (2.4) leads to a rough pressure field. On the other hand, much smoother and continuous pressure field is obtained by applying the Eq. (2.66), resulting in a more stable and accurate calculation.

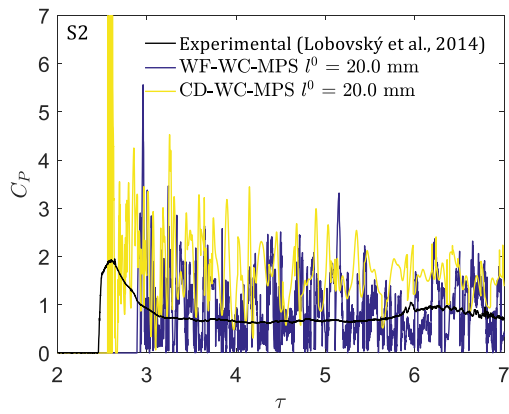
Figure 5.9 - Dam break. Snapshots of the experiment (Lobovský et al., 2014) and numerical simulations (middle cross-sectional view A1-A1, see Figure 5.8) at the instants $t = 0.40, 0.80, 1.20, 1.60, 2.00, 2.40$ s (non-dimensional times $\tau = 1.58, 2.57, 3.27, 6.67$). WF-WC-MPS and CD-WC-MPS using the particle distance $l_0 = 5$ mm. The colors on the fluid particles are related to its pressure magnitude.



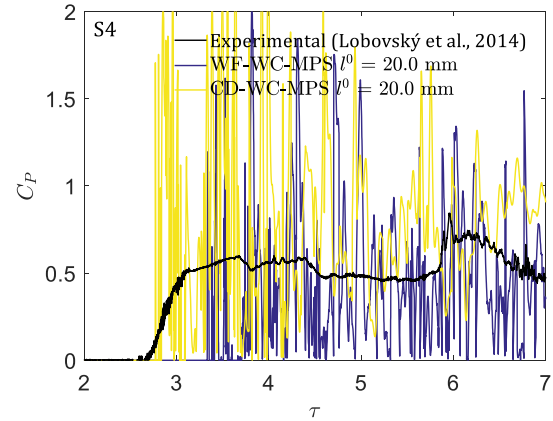
Source: the author and (Lobovský et al., 2014).

Figure 5.10 depicts the time histories of non-dimensional pressure coefficient $C_p = P/\rho g H_F$ measured in the experiment and numerically computed at sensors S2 and S4. It should be clarified how the computed pressure time series were obtained. The raw data of the pressure calculated at the fluid particle that is closest one to the sensor position was considered.

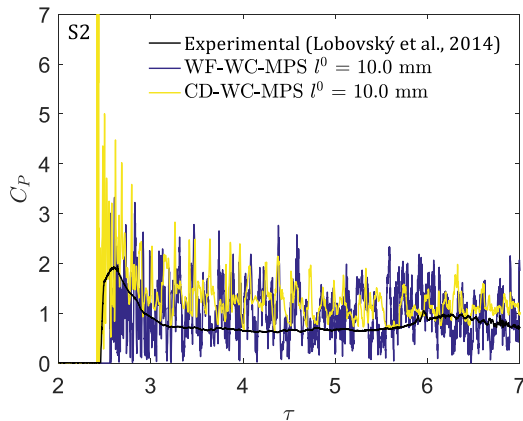
Figure 5.10 - Comparison between the experimental (Lobovský et al., 2014) and numerical pressures computed with WF-WC-MPS and CD-WC-MPS. Pressures at sensors S2 and S4.



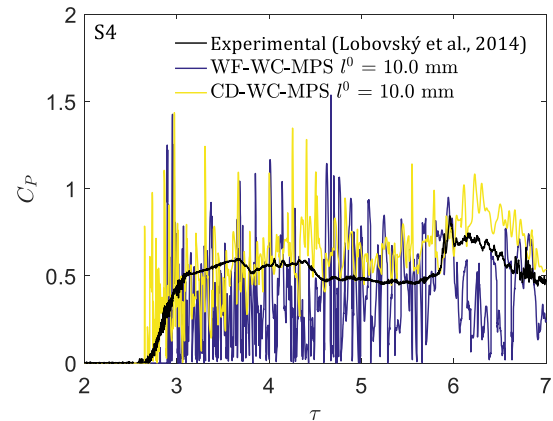
(a₁) Sensor S2, $l_0 = 20\text{mm}$



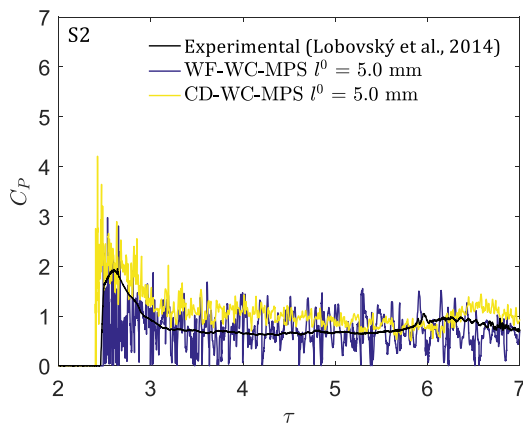
(a₂) Sensor S4, $l_0 = 20\text{mm}$



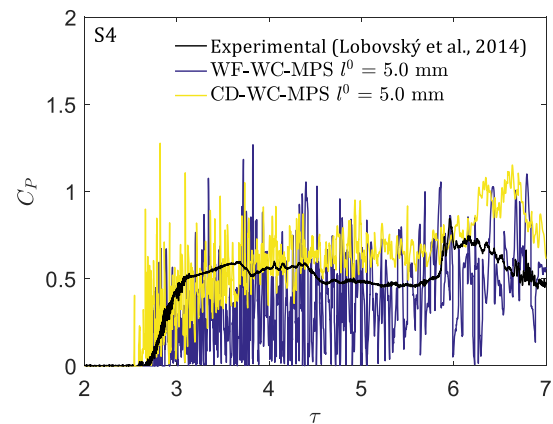
(b₁) Sensor S2, $l_0 = 10\text{mm}$



(b₂) Sensor S4, $l_0 = 10\text{mm}$



(c₁) Sensor S2, $l_0 = 5\text{mm}$



(c₂) Sensor S4, $l_0 = 5\text{mm}$

Source: the author.

For both simulations using $l_0 = 20\text{mm}$, see Figure 5.10(a₁) and (a₂), the initial instant of the impact is delayed, although the delay in the simulation using WF-WC-MPS is lower than

0.02s ($\tau = 0.12$). Considerable pressure oscillations are computed by the present WC-MPS, showing that this resolution is not enough to accurately reproduce the physics of the problem. The numerical results are improved by using $l_0 = 10\text{mm}$, as shown in Figure 5.10(b₁) and (b₂). The initial instant of the impact still is delayed when WF-WC-MPS is used, but lower than 0.02s ($\tau = 0.12$), and the presence of pressure oscillations still remains. Regarding the results from CD-WC-MPS, experimental and numerical instant of the impact are in very good agreement. The first pressure peak at sensor S2 is overestimated, but the overall trends of computed and experimental pressure time series at S2 and S4 agree well. Moreover, the pressure oscillation is reduced. The best results are obtained by using $l_0 = 5\text{mm}$, as illustrated in Figure 5.10(c₁) and (c₂). Although pressure oscillations still are computed with WF-WC-MPS, a noticeable improvement on the accuracy of the results is obtained when CD-WC-MPS is adopted, since the reduction of oscillations are remarkable. One should note that between the instants $\tau = 2.5$ and 5.6, and after $\tau = 6$, approximately, the numerical results are slightly higher than experimental ones. Such discrepancy, also observed in other particle-based simulations (Cercos-Pita et al., 2016; Meringolo et al., 2019; Jandaghian & Shakibaeinia, 2020; Fernández-Gutiérrez & Zohdi, 2020), can be related to the weakly compressibility, boundary effects and/or neglect of air-phase, as pointed out in Jandaghian and Shakibaeinia (2020). Despite of these overestimations, the adoption of the present CD-WC-MPS ensures stable and acceptable predictions of hydrodynamic problems.

5.6 VERIFICATION OF THE GEOMETRICALLY EXACT SHELL MODEL

In this section the accuracy and reliability of the geometrically exact shell model is analyzed by means of static equilibrium and dynamic response of shells under distributed loads.

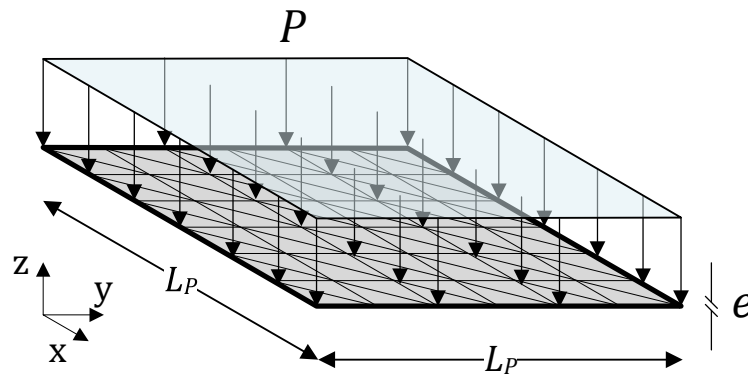
5.6.1 STATIC RESPONSE OF PLATE CLAMPED AT ALL EDGES UNDER UNIFORM PRESSURE

An elastic square plate of side length $L_p = 0.2\text{m}$ and thickness $e = 0.002\text{m}$, clamped at all edges and under uniform pressure $P = 2000\text{ Pa}$, as shown in Figure 5.11, was simulated using 4, 8, 16 and 32 element divisions per side in order to verify the numerical convergence. The physical properties and numerical parameters are given in Table 5.6 and Table 5.7, respectively. Table 5.8 illustrates the computational times. Aimed to achieve the static equilibrium, a high structural numerical damping was adopted by using the Rayleigh coefficient $\beta_R = 0.025$. More details about the Rayleigh damping can be found in Bathe (1996). The numerical results of the vertical displacement at the center of the plate are

compared with the analytical solution v_{MAX} obtained by (Timoshenko & Woinowsky-Krieger, 1959):

$$v_{MAX} = \alpha \frac{PL_P}{D_s}, \quad D_s = \frac{E_s e^3}{12(1 - \nu_s^2)}, \quad \alpha = 0.00126. \quad (5.65)$$

Figure 5.11 - Square plate of side length $L_p = 0.2\text{m}$ and thickness $e = 0.002\text{m}$, clamped at all edges and under uniform pressure $P = 2000\text{ Pa}$.



Source: the author.

Table 5.6 - Square plate clamped at all edges and under uniform pressure. Physical properties of the elastic plate.

Property	Value
Density ρ_s (kg/m ³)	1000
Young's modulus E_s (GPa)	200
Poisson's ratio ν_s	0.3
Thickness e (m)	0.002

Source: the author.

Table 5.7 - Square plate clamped at all edges and under uniform pressure. Simulation parameters of the elastic plate.

Parameter	Value
Mesh elements	4×4, 8×8, 16×16, 32×32
Time step Δt_s (s)	5×10^{-4}
Rayleigh damping β_R	0.025
Newmark coefficient β_N	0.3
Newmark coefficient γ_N	0.5

Source: the author.

Table 5.8 - Square plate clamped at all edges and under uniform pressure. Computational time.

Mesh elements	4×4	8×8	16×16	32×32
Simulation time (s)	0.4			
Time step (s)	5×10^{-4}	5×10^{-4}	5×10^{-4}	5×10^{-4}
Computation time* (min)	1	6	11	45

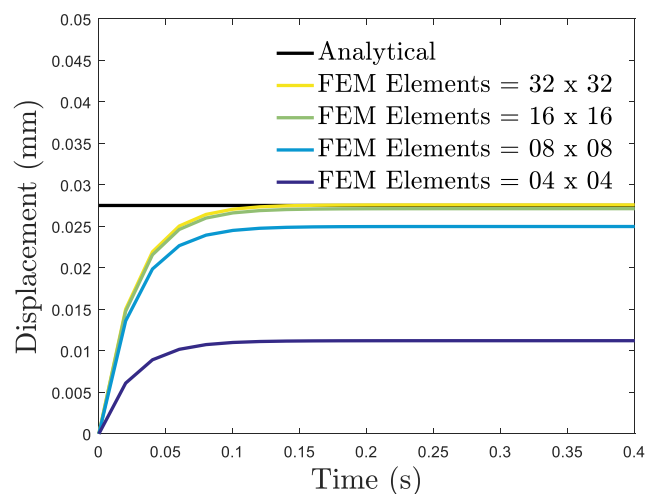
*Intel® Core™ Processor i7-4510U, processor base frequency of 2.00GHz, 4 MB cache, 2 cores and 8GB of memory. Source: the author.

Figure 5.12 shows the analytical and numerical time series of the vertical displacement at the center of the plate. For all simulations, the static equilibrium was obtained at the instant $t = 0.15$ s, approximately. Concerning the mesh discretization, the adoption of 4 or 8 elements per side was not enough to represent the correct response of the plate since the discrepancies between the numerical and analytical results are considerable. On the other hand, the numerical displacements from the simulations with 16 or 32 elements per side are in very good agreement with the analytical one. Table 5.12 presents the displacements and the error defined here as:

$$\text{Error} = \left| \frac{X_n - X_a}{X_a} \right|, \quad (5.66)$$

where X_a means the analytical result at the static equilibrium and X_n stands for the numerical one. Table 5.9 shows that the numerical results properly converge to the analytical one since the increase of the mesh refinement leads to the decrease of the error.

Figure 5.12 - Plate's mid-span vertical displacement. Analytical and numerical results computed with the present FEM for different number of elements 4×4, 8×8, 16×16, 32×32.



Source: the author.

Table 5.9 - Analytical and numerical plate's mid-span vertical displacement computed with the present FEM for different number of elements 4×4, 8×8, 16×16, 32×32.

	Vertical displacement v_{MAX} (mm)	Error (%)
Analytic solution	0.0275	-
Present FEM (04×04 elements)	0.0112	59.27
Present FEM (08×08 elements)	0.0250	9.09
Present FEM (16×16 elements)	0.0271	1.27
Present FEM (32×32 elements)	0.0276	0.36

Source: the author.

5.6.2 DYNAMIC RESPONSE OF PLATE CLAMPED AT ONE EDGE AND SUBJECTED TO INITIAL VELOCITY DISTRIBUTION PERPENDICULAR TO THE PLATE

In this example, an elastic square plate of side length $L_p = 0.2\text{m}$, thickness $e = 0.002\text{m}$ and clamped at one edge, as shown in Figure 5.13, was simulated with 16 elements per side. The physical properties and numerical parameters are given in Table 5.10 and Table 5.11, respectively. A velocity distribution $v_y(x)$ perpendicular to the plate is applied only at the initial instant $t = 0$ and the plate is free to oscillate without any structural numerical damping imposed. The velocity along the x-axis is expressed as follow:

$$v_y(x) = v_{L0} c_0 \frac{f(x)}{f(L_p)}, \quad c_0 = \sqrt{\frac{K_s}{\rho_s}}, \quad (5.67)$$

with $v_{L0} = 0.01$, the maximum velocity at the free-end, and

$$f(x) = [\cos(kL_p) + \cosh(kL_p)][\cosh(kx) - \cos(kx)] + [\sin(kL_p) - \sinh(kL_p)][\sinh(kx) - \sin(kx)], \quad (5.68)$$

where $kL_p = 1.875$.

Table 5.10 - Square plate clamped at one edge and subjected to initial velocity. Physical properties of the elastic plate.

Property	Value
Density ρ_s (kg/m ³)	1000
Young's modulus E_s (MPa)	2.00
Bulk modulus K_s (MPa)	3.25
Poisson's ratio ν_s	0.40
Thickness e (m)	0.002

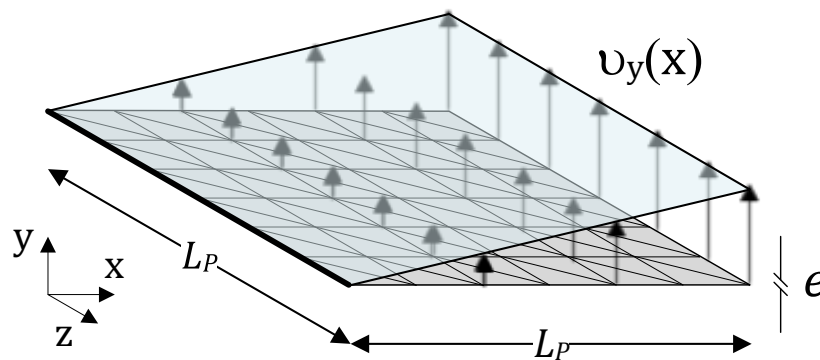
Source: the author.

Table 5.11 - Square plate clamped at one edge and subjected to initial velocity. Simulation parameters of the elastic plate.

Parameter	Value
Mesh elements	16×16
Time step Δt_c (s)	5×10^{-3}
Simulation time (s)	1.0
Computational time* (min)	3
Rayleigh damping β_R	0.0
Newmark coefficient β_N	0.3
Newmark coefficient γ_N	0.5

*Intel® Core™ Processor i7-4510U, processor base frequency of 2.00GHz, 4 MB cache, 2 cores and 8GB of memory. Source: the author.

Figure 5.13 - Square plate of side length $L_p = 0.2\text{m}$ and thickness $e = 0.002\text{m}$, clamped at one edge and subjected to initial ($t = 0$) velocity distribution $v_y(x)$ perpendicular to the plate.



Source: the author.

Table 5.12 gives the analytic solution (Landau & Lifšits, 1979) of the non-dimensional amplitude motion A_{fe}/L_p at the free-end and period T_{c_0}/L_p , as well as the numerical results computed with the particle-based methods SPH (Gray et al., 2001; Antoci et al., 2007; Rafiee & Thiagarajan, 2009) and MPS (Hwang et al., 2014), and the present FEM. Moreover, Table 5.12 also presents the error defined in Eq. (5.66). With the exceptions of the non-dimensional results obtained with the MPS by Hwang et al. (2014), the accuracy of the present FEM is better than that achieved with SPH, since the error of the present simulations remains below 4.35%, i.e., less than the smaller error of 7.87% reported in Antoci et al. (2007). In addition to the previous results of the benchmark static test, the results of the dynamic benchmark case demonstrated that the present shell model provides reliable and very accurate predictions of the structural motions.

Table 5.12 - Square plate clamped at one edge and subjected to initial velocity. Analytical and numerical results from the particle methods SPH (Gray et al., 2001; Antoci et al., 2007; Rafiee & Thiagarajan, 2009), MPS (Hwang et al., 2014) and present FEM.

	Dimensionless amplitude A_{fe}/L_p	Error (%)	Dimensionless period Tc_0/L_p	Error (%)
Analytic solution	0.115	-	72.39	-
SPH (Gray et al., 2001)	0.125	8.70	82.00	13.28
SPH (Antoci et al., 2007)	0.124	7.83	81.50	12.59
SPH (Rafiee & Thiagarajan, 2009)	0.126	9.57	82.20	13.55
MPS (Hwang et al., 2014)	0.113	1.74	72.40	0.0
Present FEM (16×16 elements)	0.120	4.35	74.11	2.38

Source: the author.

5.7 RESULTS AND DISCUSSIONS

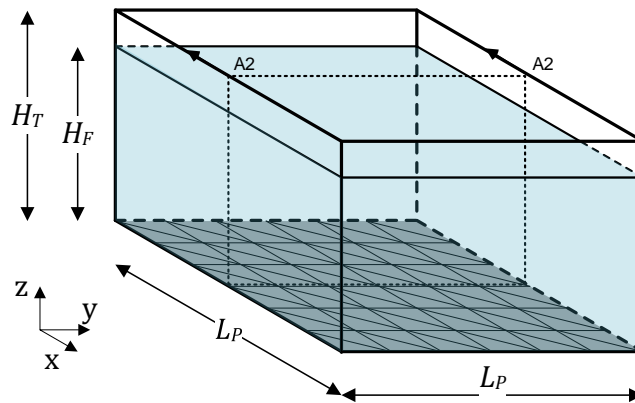
In order to illustrate the performance and robustness of the proposed coupled WC-MPS-FE model, a set of FSI problems are investigated from two perspectives: (i) quasi-static FSI benchmark tests involving small deformations and (ii) dynamic benchmark experiments with free-surface flow and thin-walled structures undergoing large changes in shape. The first two cases are clamped plates subjected to hydrostatic pressure. The numerical results of the maximum displacements are compared to the theoretical ones. The idea behind this study is to evaluate the accuracy of the coupling scheme using the ERP wall boundary model and linear shape functions to determine the forces at the FE nodes, see Eq. (5.63). The third case, a classical benchmark validation test case for FSI solvers (Amini et al., 2011; Yang et al., 2012; Hwang et al., 2014; Fourey et al., 2017; Khayyer et al., 2018; Falahaty et al., 2018; Liu et al., 2020), consists of an experiment involving the interaction between water column and an elastic gate (Antoci et al., 2007). The last case, also used for FSI validations (Martínez-Ferrer et al., 2018; Khayyer et al., 2019; Sun et al., 2019), represents the experiment conducted by Liao et al. (2015), in which complex dam-breaking flow interacts with a clamped elastic plate. Since the present WC-MPS with Eq. (2.66), here named as CD-WC-MPS, provides more accurate predictions for free-surface flows, it is used in all FSI cases. The no-slip boundary condition was adopted for all simulations, i.e., Eq. (5.5) and Eq. (5.18) were used, and the gravity acceleration was assigned as $g = 9.81\text{m/s}^2$. Furthermore, considering the results of the static and dynamic benchmark tests, FE mesh with 16 elements per side were considered for all FSI problems based on a compromise between accuracy and efficiency.

5.7.1 SQUARE PLATE CLAMPED AT ALL EDGES AND UNDER HYDROSTATIC PRESSURE

In this example, we consider a hydrostatic water column of height $H_F = 0.2\text{m}$ in a tank of height $H_T = 0.22\text{m}$ and square elastic bottom of side length $L_p = 0.2\text{m}$, thickness $e = 0.002\text{m}$ and clamped at all edges, according to Figure 5.14. Simulations were performed for 2 seconds and the numerical convergence was evaluated for three initial distance between particles, namely $l_0 = 20, 10$ and 5mm . The physical properties and numerical parameters are summarized in Table 5.13 and Table 5.14, respectively. The computational times are presented in Table 5.15. To achieve the quasi-static equilibrium, we adopted the dimensionless number $A_F = 1$ and a high structural numerical damping $\beta_R = 0.025$. The computed results are compared to the analytical solution of the central deflection v_{MAX} given by (Timoshenko & Woinowsky-Krieger, 1959):

$$v_{MAX} = \alpha \frac{\rho_f g H_F L_p}{D_s}, \quad D_s = \frac{E_s e^3}{12(1 - \nu_s^2)}, \quad \alpha = 0.00126. \quad (5.69)$$

Figure 5.14 - Square plate of side length $L_p = 0.2\text{m}$, clamped at all edges and under hydrostatic water column of height $H_F = 0.2\text{m}$ in a tank of height $H_T = 0.22\text{m}$. The section A2-A2 is the middle cross-sectional view.



Source: the author.

Table 5.13 - Square plate clamped at all edges and under hydrostatic water column. Physical properties of the fluid and elastic plate.

Fluid		Elastic plate	
Property	Value	Property	Value
Density ρ_f (kg/m ³)	1000	Density ρ_s (kg/m ³)	1000
Kinematic viscosity ν_f (m ² /s)	10^{-6}	Young's modulus E_s (GPa)	200
		Poisson's ratio ν_s	0.3
		Thickness e (m)	0.002

Source: the author.

Table 5.14 - Square plate clamped at all edges and under hydrostatic water column.
Simulation parameters of the fluid and elastic plate.

Fluid		Elastic plate	
Parameter	Value	Parameter	Value
Particle distance l_0 (m)	0.02, 0.01, 0.005	Mesh elements	16×16
Time step Δt_f (s)	5, 1.25, 1.25×10^{-4}	Time step Δt_s (s)	Δt_f
Effective radius r_e (m)	$2.1 \times l^0$	Rayleigh damping β_R	0.025
Sound speed c_0 (m/s)	15	Newmark coefficient β_N	0.3
Courant number C_r	0.2	Newmark coefficient γ_N	0.5
Mach number Ma	0.1		
Dimensionless number A_F	1		
Dimensionless constant C_{rep}	1		
Surface threshold β	0.98		
Surface threshold ϱ	0.2		

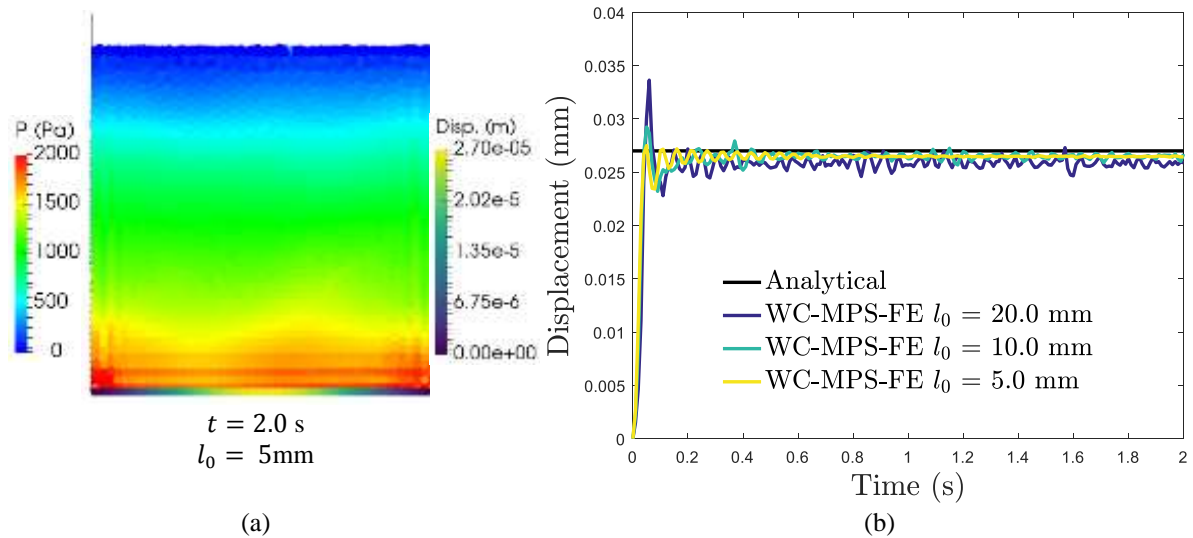
Source: the author.

Table 5.15 - Square plate clamped at all edges and under hydrostatic water column.
Computational time.

l_0 (mm)	20.0	10.0	5.0
Simulation time (s)		2.0	
Number of particles	1000	8000	64000
Time step (s)	5×10^{-4}	1.25×10^{-4}	1.25×10^{-4}
Computation time*	0d02h35m	0d15h40m	5d00h00m

*Intel® Core™ Processor i7-4510U, processor base frequency of 2.00GHz, 4 MB cache, 2 cores and 8GB of memory. Source: the author.

Figure 5.15 - (a) Pressure field in the fluid and the field of the displacement in the elastic plate at $t = 2.0\text{s}$ using $l_0 = 5\text{mm}$ (middle cross-sectional view A2-A2, see Figure 5.14). (b) Time history of the plate's mid-span vertical displacement. Analytical and numerical results computed with the present WC-MPS-FE for different particle distances $l_0 = 20, 10, 5\text{mm}$.



Source: the author.

Figure 5.15(a) illustrates the pressure field in the fluid and the displacement in the elastic plate, both behind the middle cross-sectional view A2-A2 (see Figure 5.14), at the instant $t = 2.0\text{s}$ and adopting $l_0 = 5\text{mm}$. Given the intrinsic difficulties to obtain a quasi-static state with particle-based methods, the theoretical hydrostatic tank is numerically well-predicted, although it does not match exactly the theoretical solution.

Figure 5.15(b) shows the evolution in time of the vertical displacements of the solid plate's central point. The plate presents a large oscillation until $t = 0.15\text{s}$ in response to the suddenly change of the hydrostatic pressure field on the fluid particles. Approximately after $t = 0.2\text{s}$, the plate response becomes more stable and the computed displacement agrees very well with the analytical one. The computed results using the initial particle distances $l_0 = 20, 10$ and 5 mm oscillate around the maximum displacements $0.0259, 0.0265$ and 0.0265mm , respectively. Compared to the theoretical maximum displacement 0.027 mm , the simulations using $l_0 \leq 10\text{mm}$ show a very small error of 1.85% , illustrating that the accuracy increases with the decrease of the particle distance, i.e., indicating the numerical convergence of the proposed model. The error was computed following the Eq. (5.66), but the variable X_n defined as the mean of the numerical result after reach the quasi-static equilibrium, namely $t \geq 0.5\text{s}$. The quantitative comparison between the analytical and present results is provided in Table 5.16.

Table 5.16 - Square plate clamped at all edges and under hydrostatic water column. Analytical and numerical results computed with the present WC-MPS-FE for different particle distances

$$l_0 = 20, 10, 5\text{mm.}$$

	Vertical displacement v_{MAX} (mm)	Error (%)
Analytical solution	0.0270	-
Present WC-MPS-FE ($l_0 = 20$ mm)	0.0259	4.07
Present WC-MPS-FE ($l_0 = 10$ mm)	0.0265	1.85
Present WC-MPS-FE ($l_0 = 5$ mm)	0.0265	1.85

Source: the author.

5.7.2 VERTICAL PLATE CLAMPED AT THE BOTTOM SUBJECT TO HYDROSTATIC PRESSURE

In this case we simulated a still water column of height $H_F = 0.18\text{m}$ in a cubic tank of length $L_T = 0.2\text{m}$. Among the four side walls, three are rigid while one is an elastic square plate of side length $L_p = 0.2\text{m}$, thickness $e = 0.002\text{m}$ and clamped at the bottom edge, as seen in Figure 5.16. Simulations were performed for 1 seconds and three initial distance between particles were evaluated, namely $l_0 = 20, 10$ and 5 mm. The physical properties and numerical parameters are summarized in Table 5.13 and Table 5.14, respectively. The computational times are shown in Table 5.19. To achieve the quasi-static equilibrium, we adopted the dimensionless number $A_F = 1$ and the structural numerical damping $\beta_R = 0.025$. The computed results are compared to the analytical solution of the horizontal displacement v_{TIP} of the plate's tip (Timoshenko & Woinowsky-Krieger, 1959):

$$v_{TIP} = \frac{\rho_f g H_F}{D_s} \left[\frac{H_F^4}{30} + \frac{(H_P - H_F) H_F^3}{24} \right], \quad D_s = \frac{E_s e^3}{12(1 - \nu_s^2)}. \quad (5.70)$$

Table 5.17 - Square plate clamped at one edge and under hydrostatic water column. Physical properties of the fluid and elastic plate.

Fluid		Elastic plate	
Property	Value	Property	Value
Density ρ_f (kg/m ³)	1000	Density ρ_s (kg/m ³)	1000
Kinematic viscosity ν_f (m ² /s)	10^{-6}	Young's modulus E_s (GPa)	200
		Poisson's ratio ν_s	0.3
		Thickness e (m)	0.002

Source: the author.

Table 5.18 - Square plate clamped at one edge and under hydrostatic water column.
Simulation parameters of the fluid and elastic plate.

Fluid		Elastic plate	
Parameter	Value	Parameter	Value
Particle distance l_0 (m)	0.02, 0.01, 0.005	Mesh elements	16×16
Time step Δt_f (s)	5, 1.25, 1.25×10^{-4}	Time step Δt_s (s)	Δt_f
Effective radius r_e (m)	$2.1 \times l_0$	Rayleigh damping β_R	0.025
Sound speed c_0 (m/s)	15	Newmark coefficient β_N	0.3
Courant number C_r	0.2	Newmark coefficient γ_N	0.5
Mach number Ma	0.1		
Dimensionless number A_F	1		
Dimensionless constant C_{rep}	1		
Surface threshold β	0.98		
Surface threshold ϱ	0.2		

Source: the author.

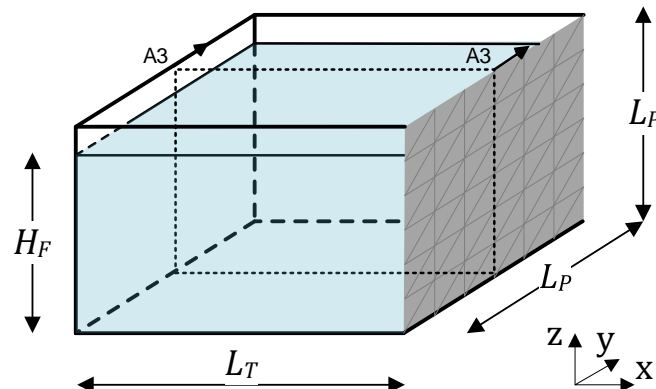
Table 5.19 - Square plate clamped at one edge and under hydrostatic water column.
Computational time.

l_0 (mm)	20.0	10.0	5.0
Simulation time (s)		1.0	
Number of particles	900	7200	57600
Time step (s)	5×10^{-4}	1.25×10^{-4}	1.25×10^{-4}
Computation time*	0d01h00m	0d05h30m	2d00h00m

*Intel® Core™ Processor i7-4510U, processor base frequency of 2.00GHz, 4 MB cache, 2 cores and 8GB of memory. Source: the author.

Figure 5.16 - Square plate of side length $L_P = 0.20\text{m}$, clamped at one edge and under hydrostatic water column of height $H_F = 0.18\text{m}$ in a cubic tank of side length $L_T = 0.2\text{m}$.

The section A3-A3 is the middle cross-sectional view.

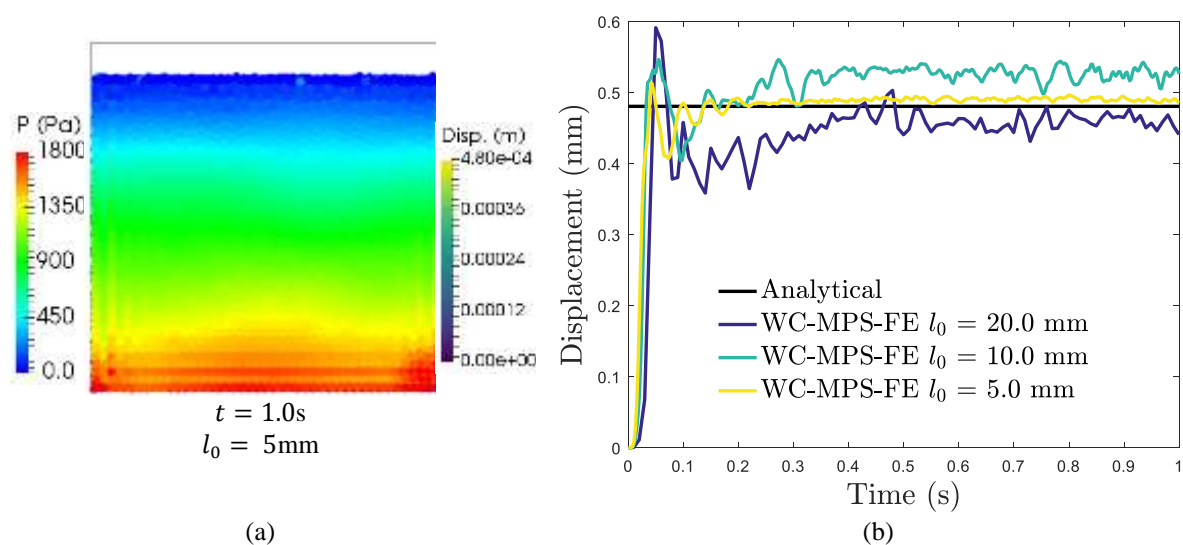


Source: the author.

The pressure field in the fluid particles and the displacement in the elastic plate, both behind the middle cross-sectional view A3-A3 (see Figure 5.16), at the instant $t = 1.0s$, and using $l_0 = 5mm$, is shown in Figure 5.17(a). As previously mentioned, since the particle-based methods present inherent difficulties to obtain quasi-static pressure field, the hydrostatic pressure fields obtained by the present model are reasonable accurate.

Figure 5.17(b) shows the time series of the horizontal displacement of the elastic plate's tip. A large oscillation until approximately $t = 0.15s$ can be seen in response to the suddenly change of the hydrostatic pressure field, similarly to the previous case. Afterwards, the quasi-static motion is achieved, and the computed displacement remains close to the analytical one. The mean of computed displacements with $l_0 = 20$ and $10mm$, after reach the quasi-static equilibrium, namely $t \geq 0.5s$, are 0.046 and $0.052mm$ with the errors of roughly 4.2 and 8.3% , respectively. A noticeable improvement is obtained with the high-resolution simulations using particle distances $l_0 = 5mm$, given the displacement around $0.049mm$ and error of 2.08% . The Eq. (5.66) is used to calculate the error and the mean of each computed result, after reach the quasi-static equilibrium, is assigned to the variable X_n , which represents the numerical result. Table 5.20 summarizes the results and errors obtained herein.

Figure 5.17 - (a) Pressure field in the fluid and the field of the displacement in the elastic plate at $t = 1.0s$ using $l_0 = 5mm$ (middle cross-sectional view A3-A3, see Figure 5.16). (b) Time series of horizontal displacement of the elastic plate's tip. Analytical and numerical results computed with the present WC-MPS-FE for different particle distances $l_0 = 20, 10, 5mm$.



Source: the author.

Table 5.20 - Square plate clamped at all edges and under hydrostatic water column. Analytical and numerical results computed with the present WC-MPS-FE for different particle distances

$$l_0 = 20, 10, 5\text{mm.}$$

	Horizontal displacement v_{TIP} (mm)	Error (%)
Analytical solution	0.048	-
Present WC-MPS-FE ($l_0 = 20$ mm)	0.046	4.17
Present WC-MPS-FE ($l_0 = 10$ mm)	0.052	8.33
Present WC-MPS-FE ($l_0 = 5$ mm)	0.049	2.08

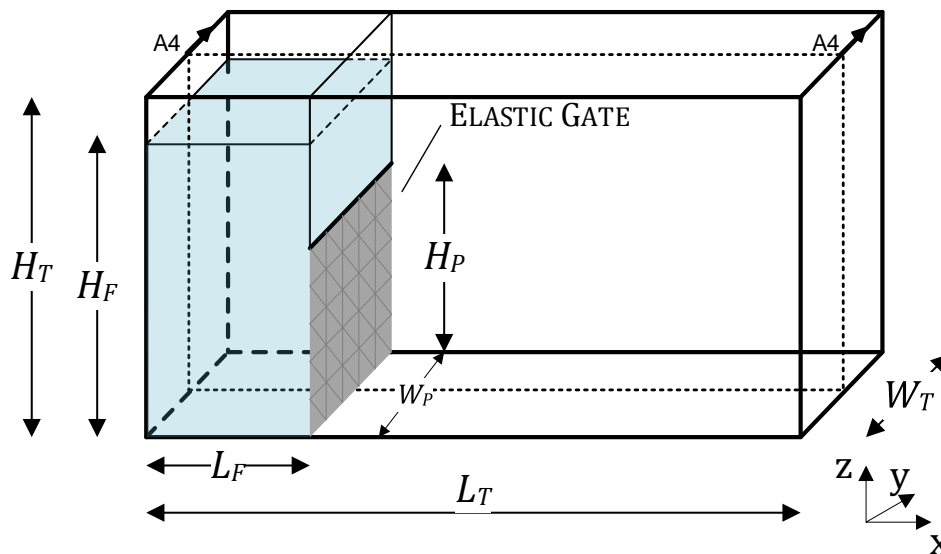
Source: the author.

5.7.3 WATER COLUMN WITH AN ELASTIC GATE CLAMPED AT TOP EDGE

This example has a fluid initially at rest and confined by a clamped elastic gate that is released suddenly to let the fluid flow. Despite the transient hydrodynamic nature, in this case, the gate deformation is essentially due to hydrostatic load of the water column instead of violent hydrodynamic impact load. Figure 5.18 shows the initial configuration of the water column of height $H_F = 0.14\text{m}$ and length $L_F = 0.1\text{m}$, the tank of length $L_T = 0.5\text{m}$, width $W_T = 0.1\text{m}$ and height $H_T = 0.146\text{m}$, and the elastic gate of height $H_P = 0.079\text{m}$ and width $W_P = 0.098\text{m}$ clamped at the top (Antoci et al., 2007).

Figure 5.18 - Schematic drawing of the tank of length $L_T = 0.5\text{m}$, width $W_T = 0.1\text{m}$ and height $H_T = 0.146\text{m}$, water column of height $H_F = 0.14\text{m}$ and length $L_F = 0.1\text{m}$, and a clamped elastic gate of height $H_P = 0.079\text{m}$ and width $W_P = 0.098\text{m}$ (Antoci et al., 2007).

The section A4-A4 is the middle cross-sectional view.



Source: the author.

Once again, three initial distance between particles $l_0 = 10, 5$ and 2.5 mm were adopted. Table 5.21 and Table 5.22 present respectively the physical properties of the fluid and gate, and the simulation parameters. Table 5.23 gives the computational times.

Table 5.21 - Water column with a clamped gate. Physical properties of the fluid and elastic plate.

Fluid		Elastic plate (gate)	
Property	Value	Property	Value
Density ρ_f (kg/m ³)	1000	Density ρ_s (kg/m ³)	1100
Kinematic viscosity ν_f (m ² /s)	10^{-6}	Young's modulus E_s (MPa)	10
		Poisson's ratio ν_s	0.4
		Thickness e (m)	0.005

Source: the author.

Table 5.22 - Water column with a clamped gate. Simulation parameters of the fluid and elastic plate.

Fluid		Elastic plate	
Parameter	Value	Parameter	Value
Particle distance l_0 (m)	0.01, 0.005, 0.0025	Mesh elements	16×16
Time step Δt_f (s)	1, 1, 0.5×10^{-4}	Time step Δt_s (s)	Δt_f
Effective radius r_e (m)	$2.1 \times l^0$	Rayleigh damping β_R	0.0001
Sound speed c_0 (m/s)	15	Newmark coefficient β_N	0.3
Courant number C_r	0.2	Newmark coefficient γ_N	0.5
Mach number Ma	0.1		
Dimensionless number A_F	2		
Dimensionless constant C_{rep}	1		
Surface threshold β	0.98		
Surface threshold ϱ	0.2		

Source: the author.

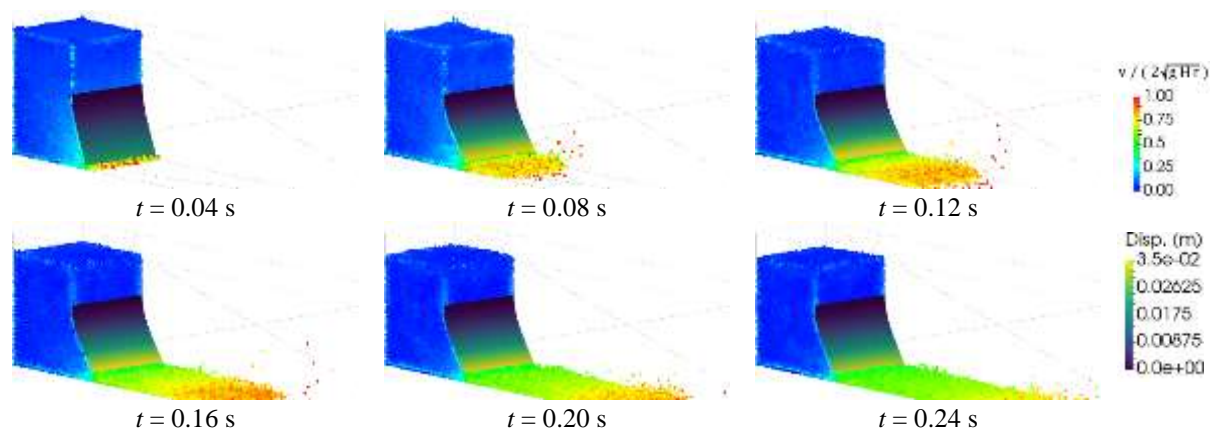
Table 5.23 - Water column with a clamped gate. Computational time.

l_0 (mm)	10.0	5.0	2.5
Simulation time (s)		0.4	
Number of particles	1400	11200	89600
Time step (s)	1×10^{-4}	1×10^{-4}	5×10^{-5}
Computation time*	0d01h00m	0d03h00m	4d00h00m

*Intel® Core™ Processor i7-4510U, processor base frequency of 2.00GHz, 4 MB cache, 2 cores and 8GB of memory. Source: the author.

Figure 5.19 shows the wave surface evolution and gate deformation at the instants $t = 0.04, 0.08, 0.12, 0.16, 0.20, 0.24$ s computed using the particle distance $l_0 = 2.5$ mm. The color scale of the fluid particles is related to its non-dimensional velocity $v/(2\sqrt{gH_F})$, where $2\sqrt{gH_F}$ stands for the maximum velocity given by the canonical solution of the analytical formulation based on shallow water waves (Ritter, 1892), while the color scale on the elastic gate refers to its displacement field. From the snapshots given in the Figure 5.19, the proposed model seems to be able to reproduce the main hydrodynamic characteristics of the free-surface flow as well as the structural dynamic behavior of the elastic gate.

Figure 5.19 - Water column with a clamped gate. Snapshots of the numerical simulations WC-MPS-FE for the particle distance $l_0 = 2.5$ mm at the instants $t = 0.04, 0.08, 0.12, 0.16, 0.20, 0.24$ s. The color scale of the fluid particles is related to its non-dimensional velocity $v/(2\sqrt{gH_F})$ and the color scale on the elastic plate refers to its displacement.

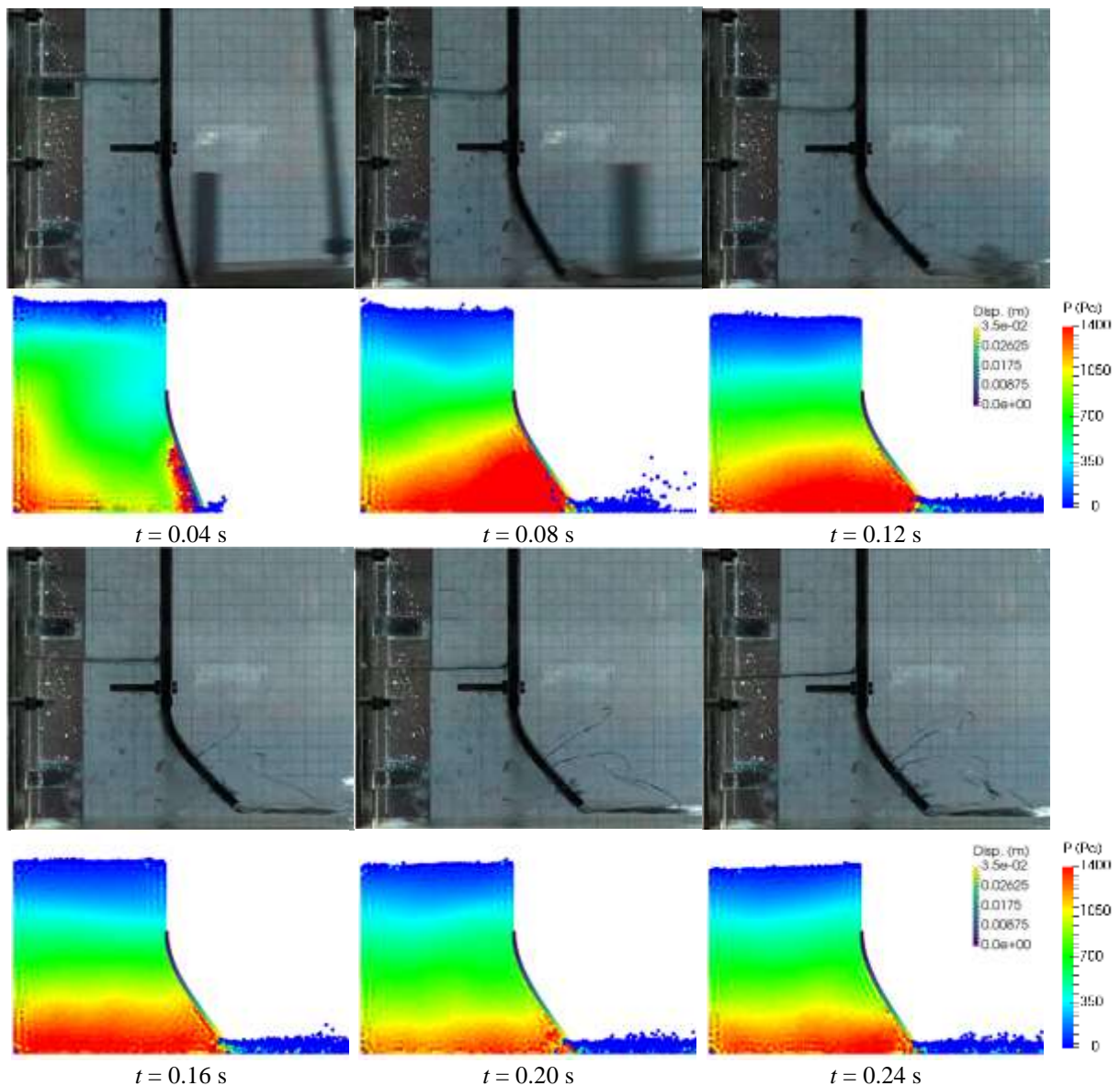


Source: the author.

The comparison between experimental and numerical evolutions of the fluid and gate deformation at several instants are shown in Figure 5.20. The color scale at the particles correspond to the pressure field while the color on the elastic gate refers to its displacement, both behind the middle cross-sectional view A4-A4 (see Figure 5.18). At the initial instants $t = 0.04$ s and $t = 0.08$ s, the experimental and numerical results are in very good agreement, although the fluid pressure field is degraded at $t = 0.04$ s. A possible explanation for this non-physical behavior is numerical instability in the coupling scheme that results to the rough pressure field near the fluid-structure interface. The numerical treatment to avoid such pressure instabilities near the interface is not an easy task, and this irregularity can be also seen for the same benchmark test simulated in Falahaty et al. (2018) and Khayyer et al. (2018). As pointed out in Hermange et al. (2019), such instabilities lead to high frequency displacements at the interface, being responsible for non-physical acoustic waves within the

fluid. In the subsequent instants, $t \geq 0.04\text{s}$, a smoother pressure field is numerically obtained, but the displacement of the gate is underestimated by the present model. Consequently, the experimental and numerical water level present some discrepancies. No perfect matching exists between the actual physical nonlinearities of the rubber gate material and the simple hyperplastic material model herein adopted for the shell model. Therefore, differences between experimental and numerical predictions are expected (Yang et al., 2012).

Figure 5.20 - Water column with a clamped gate. Snapshots of the experiment (Antoci et al., 2007) and numerical simulations (middle cross-sectional view A4-A4, see Figure 5.18) with WC-MPS-FE for the particle distance $l_0 = 2.5\text{mm}$ at the instants $t = 0.40, 0.80, 1.20, 1.60, 2.00, 2.40\text{s}$. The colors on the fluid particles are related to its pressure magnitude.

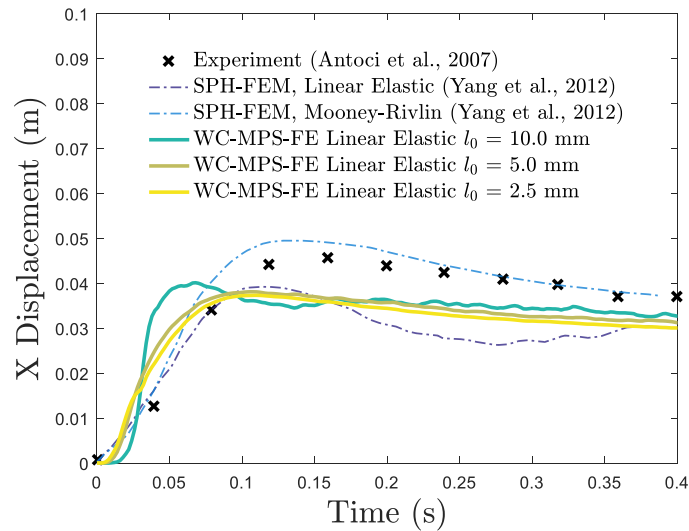


Source: the author.

Figure 5.21 shows the time series of the horizontal displacements of the free end of the elastic plate experimental measured (Antoci et al., 2007) and numerically computed with a SPH-FEM model (Yang et al., 2012) and the present coupled WC-MPS-FE model for initial distances between particles $l_0 = 10, 5, 2.5\text{mm}$. Apart from the computed results obtained with the coarse resolution of $l_0 = 10\text{mm}$, the overall trends of the displacements computed with the present model using finer resolutions $l_0 = 5$ and 2.5mm agree well with the experimental data. Nevertheless, after the instant $t = 0.1\text{ s}$, the present model underestimates the displacement. The main reason of these discrepancies is attributed to simplifications in material constitutive behavior modeling. Yang et al. (2012) pointed out that actual elastic rubber gate used in the experiment exhibits a non-linear stress-strain relation and the adoption of non-linear materials is crucial to numerically reproduce the same response of the gate. The numerical results of the simulations performed by Yang et al. (2012) using a SPH-FEM model with linear and non-linear (Mooney-Rivlin) elasticity are also plotted in Figure 5.21. While the results using the linear material underestimated the experimental data, results using the non-linear material are much closer the experimental one.

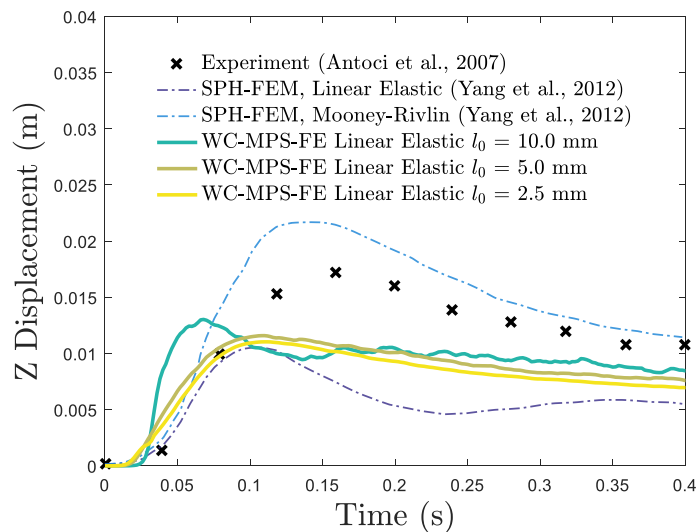
In Figure 5.22, the experimental (Antoci et al., 2007) and numerical vertical displacements of the free end of the elastic plate are shown. The numerical results of the simulations performed by Yang et al. (2012) are also presented. Once more, overall trends of the numerical results using higher resolutions $l_0 = 5$ and 2.5mm agree well with the experimental data. Moreover, as previously mentioned, the discrepancies between the present results and the experimental one arise from the fact that the present model assumes a simple material model, not considering on its behavior the actual rubber expected nonlinear behavior when large strains take place.

Figure 5.21 - Time series of the horizontal displacements of the free end of the elastic plate in the dam-break flow with an initial water column of height $H_F = 0.14\text{m}$. Experimental data from Antoci et al. (2007), numerical results of SPH-FEM with linear and non-linear (Mooney-Rivlin) elasticity (Yang et al., 2012) and present WC-MPS-FE with linear elasticity for different particle distances $l_0 = 10, 5, 2.5\text{mm}$.



Source: the author.

Figure 5.22 - Time series of the vertical displacements of the free end of the elastic plate in the dam-break flow with an initial water column of height $H_F = 0.14\text{m}$. Experimental data from Antoci et al. (2007), numerical results of SPH-FEM with linear and non-linear (Mooney-Rivlin) elasticity (Yang et al., 2012) and present WC-MPS-FE with linear elasticity for different particle distances $l_0 = 10, 5, 2.5\text{mm}$.



Source: the author.

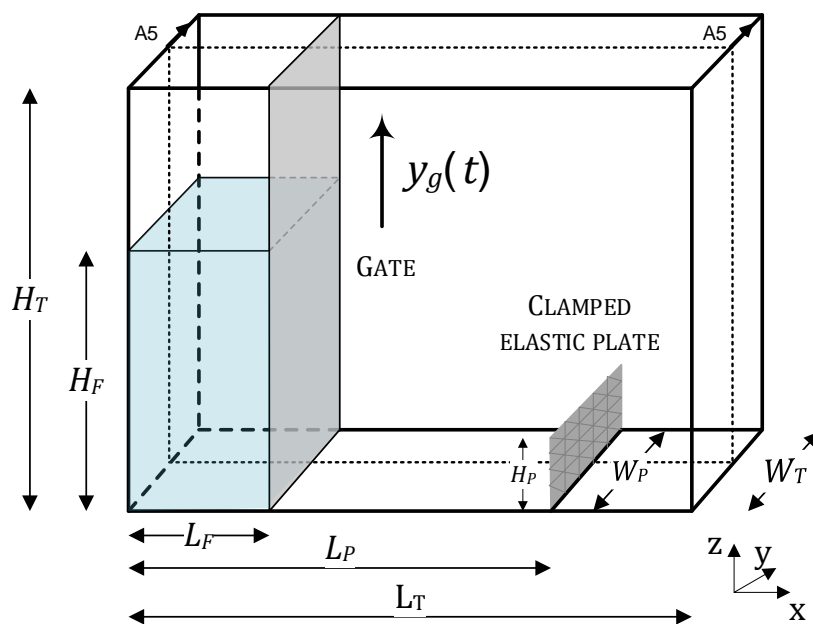
5.7.4 DAM BREAKING HITTING AN ELASTIC PLATE CLAMPED AT ONE EDGE

In the last case, we intend to demonstrate that the proposed coupled model can handle violent transient free-surface flow interacting with elastic structures undergoing large deformations. Figure 5.23 shows the initial configuration of the experiment conducted by Liao et al. (2015), represented by a tank of length $L_T = 0.8\text{m}$, width $W_T = 0.2\text{m}$ and height $H_T = 0.6\text{m}$, a water column of height $H_F = 0.4\text{m}$, length $L_F = 0.2\text{m}$ and confined by a rigid gate. An elastic plate of height $H_P = 0.1\text{m}$ and width $W_P = 0.1995\text{m}$ is clamped at the bottom and located $L_P = 0.6\text{m}$ downstream. Three distance between particles, $l_0 = 20, 10$ and 5mm , were adopted in the simulations. The physical properties of the fluid and elastic plate can be found in Table 5.24 and the simulation parameters are given in Table 5.25. The computational times are presented in Table 5.26.

In the present simulations, the vertical motion of the gate follows a smooth function $y_g(t)$ that approximately fits the experimental vertical motion provided in Liao et al. (2015):

$$y_g(t) = -300t^3 + 75t^2. \quad (5.71)$$

Figure 5.23 - Schematic drawing of the tank of length $L_T = 0.8\text{m}$, width $W_T = 0.2\text{m}$ and height $H_T = 0.6\text{m}$, water column of height $H_F = 0.4\text{m}$ and length $L_F = 0.2\text{m}$, clamped elastic plate of height $H_P = 0.1\text{m}$ and width $W_P = 0.1995\text{m}$ and a gate subjected to a upward motion $y_g(t)$ (Liao et al., 2015). The elastic plate is located $L_P = 0.6\text{m}$ downstream. The section A5-A5 represents the middle cross-sectional view.



Source: the author.

Table 5.24 - Dam breaking hitting a clamped plate. Physical properties of the fluid and elastic plate.

Fluid		Elastic plate	
Property	Value	Property	Value
Density ρ_f (kg/m ³)	1000	Density ρ_s (kg/m ³)	1161.54
Kinematic viscosity ν_f (m ² /s)	10^{-6}	Young's modulus E_s (MPa)	3.5
		Poisson's ratio ν_s	0.3
		Thickness e (m)	0.004

Source: the author.

Table 5.25 - Dam breaking hitting a clamped plate. Simulation parameters of the fluid and elastic plate.

Fluid		Elastic plate	
Parameter	Value	Parameter	Value
Particle distance l_0 (m)	0.02, 0.01, 0.005	Mesh elements	16×16
Time step Δt_f (s)	5, 2.5, 1.25×10^{-4}	Time step Δt_s (s)	Δt_f
Effective radius r_e (m)	$2.1 \times l^0$	Rayleigh damping β_R	0.001
Sound speed c_0 (m/s)	15	Newmark coefficient β_N	0.3
Courant number C_r	0.2	Newmark coefficient γ_N	0.5
Mach number Ma	0.1		
Dimensionless number A_F	2		
Dimensionless constant C_{rep}	1		
Surface threshold β	0.98		
Surface threshold ϱ	0.2		

Source: the author.

Table 5.26 - Dam breaking hitting a clamped plate. Computational time.

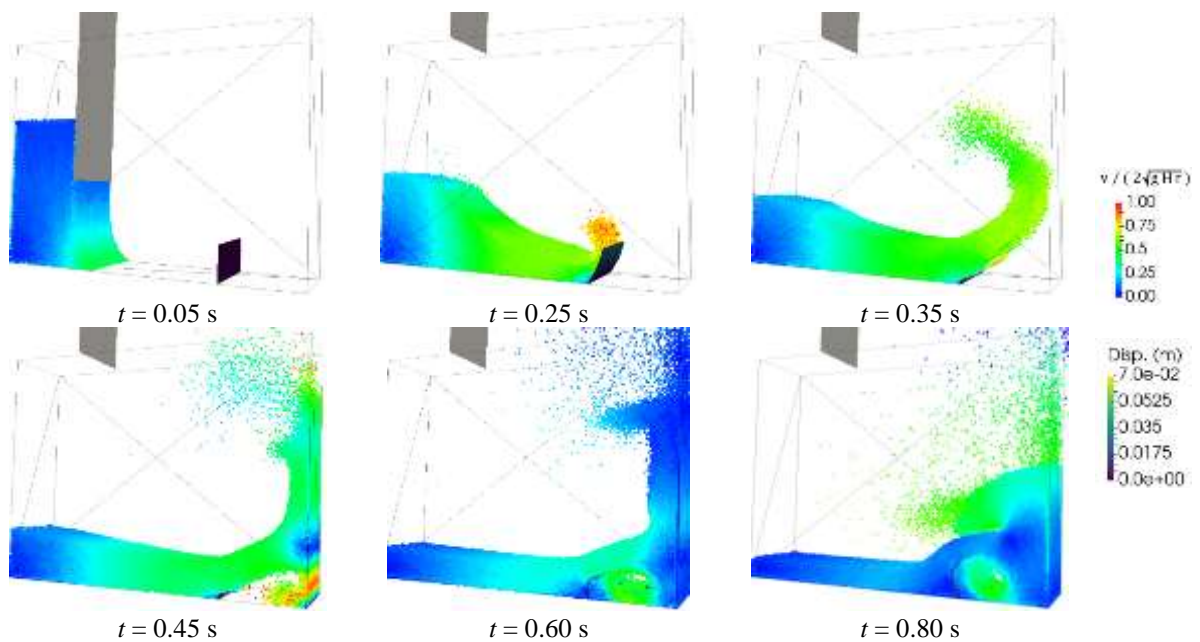
l_0 (mm)	20.0	10.0	5.0
Simulation time (s)		1.0	
Number of particles	2000	16000	128000
Time step (s)	5×10^{-4}	2.5×10^{-4}	1.25×10^{-4}
Computation time*	0d00h35m	0d03h50m	6d20h00m

*Intel® Core™ Processor i7-4510U, processor base frequency of 2.00GHz, 4 MB cache, 2 cores and 8GB of memory. Source: the author.

Figure 5.24 shows the sequences of the flow, at selected instants $t = 0.05, 0.25, 0.35, 0.45, 0.60, 0.80$ s, computed using particle distance $l_0 = 5$ mm. The colors scale of the fluid particles denotes the non-dimensional velocity $v/(2\sqrt{gH_F})$ and the color scale on the elastic plate refers to its displacement. As the fluid is released, the dam-break flow proceeds and the wave front hits the clamped plate at an instant just before to $t = 0.25$ s.

After that, the plate undergoes a large displacement and part of the fluid is deflected upward at $t = 0.35$ s. Subsequently, at $t = 0.45$ s, the wave impacts on the downstream wall generates a vertical run-up jet whereas a back flow of part of the fluid propagates along the tank bottom toward the largely deformed elastic plate. Afterwards, at the instants $t = 0.60$ s and $t = 0.85$ s, the splashed fluid falls due to the gravity, followed by a merging with the back flow near the elastic plate, creating a violent turbulent cavity flow. Concerning the elastic plate, a second impact on its right-side lead to a reverse deflection.

Figure 5.24 - Dam breaking hitting a clamped plate. Snapshots of the numerical simulations WC-MPS-FE for the particle distance $l_0 = 5$ mm at the instants $t = 0.05, 0.25, 0.35, 0.45, 0.60, 0.80$ s. The colors on the fluid particles are related to its non-dimensional velocity $v/(2\sqrt{gH_F})$ and the color on the elastic plate refers to its displacement.



Source: the author.

Free-surface profile and plate deformation at the instants $t = 0.25, 0.28, 0.30, 0.55, 0.60$ and 0.80 s from the experiment (Liao et al., 2015) and the simulation carried in the present study using the proposed WC-MPS-FE with particle distance $l_0 = 5$ mm are compared in Figure 5.25. The colors scale of the fluid particles denotes the non-dimensional velocity $v/(2\sqrt{gH_F})$ and the color scale of the elastic plate designates its displacement, both behind the middle cross-sectional view A5-A5 (see Figure 5.23). During the initial stages between the instants $t = 0.25$ and 0.30 s, the wave front hits the elastic plate and subsequently overtops it towards the downstream tank wall. The plate displacement suddenly changes during this stage. Overall,

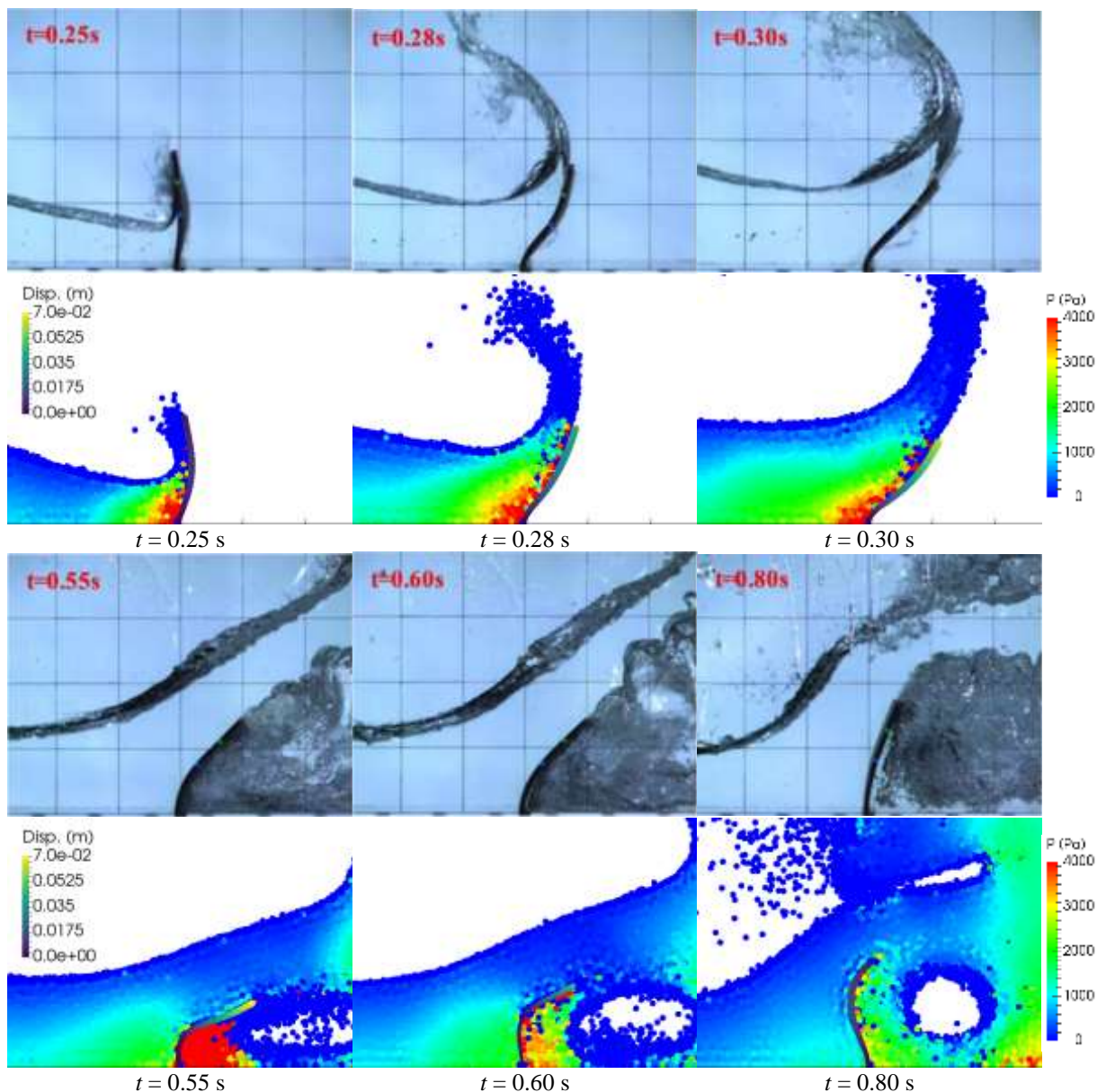
the experiment is well reproduced by the present simulations. Advancing in time, the back flow hits the right-side of the plate between the instants $t = 0.55$ and 0.60 s. As a result, an open cavity surrounded by the fluid is created, which increases the local turbulent intensity, followed by considerable change of the plate shape. Afterwards, at the instant $t = 0.85$ s, part of collapsed runup fluid merges with the back flow near the elastic plate, violent turbulent flow and the open cavity still remain, and the plate is deflected in the reverse direction compared to that due to the first wave impact. Although local free-surface profiles and the deformation of the elastic plate between the instants $t = 0.55$ s and $t = 0.85$ s are not exactly simulated by the present model, the main behaviors of this complex interaction are numerically reproduced. The main reasons of these differences might be the neglect of the air-phase and a proper turbulent model, such as a sub particle-scale (SPS) turbulence model for large eddy simulation (LES), in the present simulations.

Figure 5.26 provides the time histories of horizontal displacement of the free end of the elastic plate experimentally measured (Liao et al., 2015) and numerically computed with single-phase and multi-phase SPH (Sun et al., 2019), single-phase MPS (Khayyer et al., 2019), and present single-phase WC-MPS-FE using different initial particle distances $l_0 = 20, 10, 5$ mm. The wave front hits the bottom of the plate leading to a negative acceleration of the plate's tip, which is evidenced by the negative displacement approximately at $t = 0.25$ s. Despite both experimental and numerical displacements present the same initial trend, the experimental impact occurs at approximately $t = 0.27$ s while the numerical ones, computed by the present model, happen around $t = 0.25$ s. This discrepancy was also observed in Liao et al. (2015), which attributed to the neglect of the gate motion in the numerical simulation. However, since the present study numerically reproduced the gate motion, the explanation given by Liao et al. (2015) is not reasonable herein. A possible reason for this discrepancy might be attributed to the Laplacian operator used for the wall contribution (Eq. (5.5)) that overestimates the viscous forces. Nevertheless, in order to rigorously clarify such discrepancy further investigations should be considered. After the first wave impact, the displacement at the plate's tip suddenly increases. Between the instants $t = 0.4$ and 0.6 s, a small oscillation in the displacement was experimentally measured. However, such oscillation was not observed with the present model. As pointed by Liao et al. (2015), higher modes of structural vibration are caused by the presence of entrapped air near the elastic plate so that the numerical modeling of the air-phase is required to reproduce this physical phenomenon appropriately. Others results numerically computed with single-phase and multi-phase particle methods

(Khayyer et al., 2019; Sun et al., 2019) are plotted in Figure 5.26 and illustrates the importance of the air-phase modeling at this time interval.

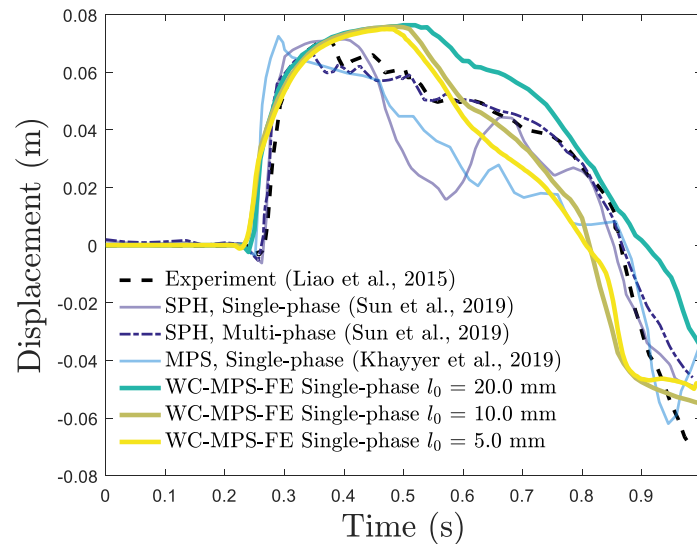
After the instant $t = 0.5\text{s}$, the displacement of the plate is gradually reduced due to the impact of the back flow. Besides small discrepancies, the overall trend of the displacement experimentally measured by Liao et al. (2015) is correctly reproduced by the proposed model, even for a coarse resolution.

Figure 5.25 - Dam breaking hitting a clamped plate. Snapshots of the experiment (Liao et al., 2015) and numerical simulations (middle cross-sectional view A5-A5, see Figure 5.23) with WC-MPS-FE for the particle distance $l_0 = 5\text{mm}$ at the instants $t = 0.25, 0.28, 0.30, 0.55, 0.60, 0.80\text{s}$. The colors on the fluid particles are related to its pressure magnitude.



Source: the author and Liao et al. (2015).

Figure 5.26 - Time series of the horizontal displacement of the free end of the elastic plate in the dam-break flow with an initial water column of height $H_F = 0.4\text{m}$. Experimental data from Liao et al. (2015), numerical results of single-phase and multi-phase SPH (Sun et al., 2019), single-phase MPS (Khayyer et al., 2019), and present single-phase WC-MPS-FE for different initial particle distances $l_0 = 20, 10, 5\text{mm}$.



Source: the author.

5.8 CONCLUDING REMARKS

Several benchmark tests covering static and dynamic phenomena were simulated and the fluid and solid solvers are verified against analytical solutions or other numerical models, and validated by laboratory measurements reported in the literature. The results show that the regularization technique applied to the WC-MPS reduces the tensile instability, and the computational accuracy is improved by conservative pressure gradient formulation. In addition to this, much more smooth and accurate pressure field is computed by using the particle number density obtained by tuning-free diffusive term.

A repulsive Lennard-Jones, using the same tuning parameter, and simple technique to avoid incorrect interactions between particles placed at opposite sides of thin shell solid modeling were adopted for all simulations involving quasi-static or dynamic events. As a result, more consistent and numerically stable fluid-solid coupling were achieved.

Transient fluid-structure interaction (FSI) problems with violent free-surface and structures that undergo small or large rotations and displacements were simulated and the results demonstrate the robustness, reliability, and efficiency of the proposed model.

CHAPTER 6

FINAL CONSIDERATIONS

Focusing on the investigation of FSI problems, we explored the applicability, robustness and accuracy of the meshless particle-based methods incompressible moving particle semi-implicit (MPS) and weakly-compressible moving particle semi-implicit (WC-MPS).

Several original contributions were reached in this work, specifically:

- i. New source terms dependent directly on the spatial discretization and independent to the time step.
- ii. Numerical solid-solid contact model that eliminates the numerical instabilities induced by non-smooth modeling of bodies surfaces in the particle-based methods.
- iii. A 3D fluid-structure coupling between WC-MPS and FE methods to solve the interaction between free-surface flows and geometrically nonlinear shell structures.

The main conclusions as well as the challenges and suggestions for future works are presented in this chapter.



6.1 CONCLUSIONS

This thesis was devoted to developing efficient computational solutions based on meshless particle-based methods for complex fluid-structure interaction (FSI) in free-surface flow from two different ways: using a i) truly incompressible or ii) weakly-compressible approach to solve free surface flow. Initially, the unstable nature of pressure computation focusing on truly incompressible flow modeling through the projection-based particle methods was investigated and consistent formulations in time domain for the pressure Poisson equation (PPE) were proposed for the moving particle semi-implicit (MPS) method. Because the adoption of particles to represent the shell of the rigid bodies may induce some geometrical anomalies such as non-smooth modeling of a plane, an approach based on the faces of the bodies and contact force computed taken into account the normal vectors of solid walls was derived. Finally, since a significant range of FSI problems is represented by free-surface flow and thin-walled structures undergoing large deformations, a novel 3D fluid-structure coupling between the weakly-compressible moving particle semi-implicit (WC-MPS) and finite element (FE) methods was developed.

6.1.1 TIME-CONSISTENCY AND STABILITY OF THE PARTICLE-BASED HYDRODYNAMIC PRESSURE

The main contributions in the context of the time-consistency computations of hydrodynamic pressure can be summarized as:

1. Based on the viewpoint of momentum conservation in particle-level collisions, a correction of the mismatch between numerical and physical time scales was introduced to derive new source terms for the PPE, namely time-scale correction of particle-level impulses (TCPI).
2. More stable pressure computations with drastic reduction of the spurious pressure oscillation and pressure magnitudes almost independent to time step, since the new formulations relying on the spatial discretization.
3. From the viewpoint of practical engineering applications, only the calibration the propagation speed of the perturbations c_s is required, which is much more straightforward due to its physical meaning.
4. The proposed formulation preserves advantages of the original particle-based methods such as:
 - a. flexibility;

- b. very easy in coding implementation;
- c. no additional computational effort on the already compute-intensive method;
- d. easy to incorporate other approaches to improve the stability and accuracy of pressure assessment.

6.1.2 RIGID BODIES CONTACT FOR PARTICLE-BASED METHODS

Concerning the contact between rigid bodies, the following contributions should be highlighted:

1. A simple way accurately determines the normal direction of contact.
2. Suppression of non-physical discontinuities in the collision distance.
3. An approach based on the faces of the bodies and contact force, taken into account the normal vectors of solid walls, improves significantly the stability and provides a relatively robust behavior for the solid-solid contact.
4. Exact computation of linear momentum and energy.
5. Coding implementation is very simple.

6.1.3 3D COUPLED WC-MPS-FE PARTICLE-MESH MODEL FOR FSI PHENOMENA

The key contributions in the context of the 3D fluid-structure coupling are:

1. A robust 3D coupled particle-mesh method to solve free-surface flows interacting with geometrically nonlinear thin-walled structures.
2. Introduction of a repulsive Lennard-Jones force in the explicitly represented polygon (ERP) wall boundary model improves the numerical stability.
3. Derivation of discrete divergence operators with appropriate modifications in the context of ERP.
4. Simple but effective technique avoids false interaction between particles placed at opposite sides of zero-thickness walls.
5. Spurious pressure oscillations are remarkably reduced by a free-tuning diffusive term.

6.2 PERSPECTIVES OF FUTURE WORKS

Further works that may be beneficial for the topics investigated in this thesis are suggested as follows.

6.2.1 TIME-CONSISTENCY AND STABILITY OF THE PARTICLE-BASED HYDRODYNAMIC PRESSURE

1. Adoption of high-order and/or modified discrete differential operators to enhance the accuracy of pressure assessment.
2. Introduction of regularization techniques for particle distribution to improve the numerical stability.
3. Extension for multi-resolution MPS techniques (Chen et al., 2016; Tang et al., 2016; Shibata et al., 2017; Tanaka et al., 2018; Khayyer et al., 2019), in which high-resolution is used only near the local critical areas, while low-resolution is used in the far-field.
4. Extension of the proposed source terms to other incompressible projection-based particle methods such as the incompressible smoothed particle hydrodynamics (ISPH) or the consistent particle method (CPM) (Koh et al., 2012).

6.2.2 RIGID BODIES CONTACT FOR PARTICLE-BASED METHODS

1. Implementation of solid-solid contact model based on impulse methods (Li et al., 2020), which require less or no parameter tuning.
2. Multi-resolution techniques could provide impressive gains in solving only local regions around solid walls, with remarkable reduction of the computational cost.
3. Integration of the present incompressible MPS solver with other multi-body libraries, e.g., GIRAFFE or CHRONO (Mazhar et al., 2013), to deal with discontinuous frictional contacts and large collection of kinematic constraints like joints and sliders.

6.2.3 3D COUPLED WC-MPS-FE PARTICLE-MESH MODEL FOR FSI PHENOMENA

1. Introduction of a multiphase and a proper turbulent model, e.g., sub particle-scale (SPS) turbulence model for large eddy simulation (LES), to capture the high frequencies of vibration experienced by the structures due entrapped air.
2. Extension of the FE solver to model more enhanced hyperelastic materials, improving the reproduction of highly non-linear hydroelastic problems.

3. Implementation of parallel fluid solver by high-performance computing (HPC) using many-core and graphics processing units (GPU) architectures, capable of handling practical large-scale problems.
4. Boundary walls represented by a scalar field with discrete signed distance functions (SDF) (Koschier & Bender, 2017), aiming to improve the efficiency in calculate the distances between the particles and polygons.
5. Accuracy improvement of the polygon wall formalism by adopting numerical boundary integrations (Chiron et al., 2019), semi-analytical boundary integrations (Kostorz & Esmail-Yakas, 2020) or analytical volume integrations (Matsunaga et al., 2020).
6. Extension for multi-resolution MPS techniques should also be evaluated with respect to adaptivity and versatility of our code.

CHAPTER 7

REFERENCES

Ahrens, J., Geveci, B. & Law, C., 2005. *ParaView: An End-User Tool for Large Data Visualization, Visualization Handbook*. Elsevier.

Alder, B.J. & Wainright, T.E., 1957. Phase transition for a hard sphere system. *Journal of Chemical Physics*, 27(5), pp.1208-09. Available at: <https://doi.org/10.1063/1.1743957>.

Amaro Jr, R.A., Cheng, L.-Y. & Osello, P.H.S., 2019. An improvement of rigid bodies contact for particle-based non-smooth walls modeling. *Computational Particle Mechanics*, 6(4), pp.561-80. Available at: <https://doi.org/10.1007/s40571-019-00233-4>.

Amaro Junior, R.A. & Cheng, L.-Y., 2013. Brittle Fracture and Hydroelastic Simulations based on Moving Particle Simulation. *Computer Modeling in Engineering & Sciences*, 95(2), pp.87-118. Available at: <http://dx.doi.org/10.3970/cmcs.2013.095.087>.

Amicarelli, A. et al., 2015. A Smoothed Particle Hydrodynamics model for 3D solid body transport in free surface flows. *Computers and Fluids*, 116, pp.205-28. Available at: <https://doi.org/10.1016/j.compfluid.2015.04.018>.

Amini, Y., Emdad, H. & Farid, M., 2011. A new model to solve fluid–hypo-elastic solid interaction using the smoothed particle hydrodynamics (SPH) method. *European Journal of Mechanics - B/Fluids*, 30(2), pp.184-94. Available at: <https://doi.org/10.1016/j.euromechflu.2010.09.010>.

Antoci, C., Gallati, M. & Sibilla, S., 2007. Numerical simulation of fluid structure interaction by SPH. *Computers & Structures*, 85(11-14), pp.879-90. Available at: <https://doi.org/10.1016/j.compstruc.2007.01.002>.

Antuono, M., Colagrossi, A. & Marrone, S., 2012. Numerical diffusive terms in weakly-compressible SPH schemes. *Computer Physics Communications*, 183(12), pp.2570–80. Available at: <https://doi.org/10.1016/j.cpc.2012.07.006>.

- Antuono, M., Colagrossi, A., Marrone, S. & Molteni, D., 2010. Free-surface flows solved by means of SPH schemes with numerical diffusive terms. *Computer Physics Communications*, 181(3), pp.532-49. Available at: <https://doi.org/10.1016/j.cpc.2009.11.002>.
- Asai, M. & Chandra, B., 2016. Numerical prediction of bridge wash-out during natural disaster by using a stabilized ISPH method. *Advances in Civil, Environmental and Materials Research*.
- Axisa, F. & Antunes, J., 2006. *Modelling of mechanical systems - Fluid structure interaction*. Elsevier Butterworth-Heinemann.
- Barcarolo, D.A., 2013. *Improvement of the precision and the efficiency of the SPH method: theoretical and numerical study*. Ph.D. Thesis. Ecole Centrale de Nantes.
- Bathe, K.-J., 1996. *Finite Element Procedures*. New Jersey: Prentice-Hall.
- Bazilevs, Y., Takizawa, K. & Tezduyar, T.E., 2013. *Computational Fluid-Structure Interaction: Methods and Applications*. John Wiley & Sons Ltd.
- Belytschko, T. & Mullen, R., 1981. Two-dimensional fluid-structure impact computations with regularization. *Computer Methods in Applied Mechanics and Engineering*, 27(2), pp.139-54. Available at: [https://doi.org/10.1016/0045-7825\(81\)90146-8](https://doi.org/10.1016/0045-7825(81)90146-8).
- Bhatia, H., Norgard, G., Pascucci, V. & Bremer, P.T., 2013. The Helmholtz-Hodge decomposition-a survey. *IEEE Transactions on Visualization And Computer Graphics*, 19(8), Available at: <https://doi.org/10.1109/TVCG.2012.316>.
- Bird, G.A., 1963. Approach to translational equilibrium in a rigid sphere gas. *The Physics of Fluids*, 6, pp.1518-19. Available at: <https://doi.org/10.1063/1.1710976>.
- Campello, E.M.B., Pimenta, P.M. & Wriggers, P., 2003. A triangular finite shell element based on a fully nonlinear shell formulation. *Computational Mechanics*, 31, pp.505-18. Available at: <https://doi.org/10.1007/s00466-003-0458-8>.
- Campello, E.M.B., Pimenta, P.M. & Wriggers, P., 2011. An exact conserving algorithm for nonlinear dynamics with rotational DOFs and general hyperelasticity. Part 2: shells. *Computational Mechanics*, 48, pp.195-211. Available at: <https://doi.org/10.1007/s00466-011-0584-7>.

- Canelas, R.B., Crespo, A.J.C., Domínguez, J.M. & Ferreira, R.M.L., 2016. SPH–DCDEM model for arbitrary geometries in free surface solid–fluid flows. *Computer Physics Communications*, 202, pp.131-40. Available at: <https://doi.org/10.1016/j.cpc.2016.01.006>.
- Cao, X.Y., Ming, F.R., Zhang, A.M. & Tao, L., 2018. Multi-phase SPH modelling of air effect on the dynamic flooding of a damaged cabin. *Computers & Fluids*, 163(15), pp.7-19. Available at: <https://doi.org/10.1016/j.compfluid.2017.12.012>.
- Cercos-Pita, J.L., Dalrymple, R.A. & Herault, A., 2016. Diffusive terms for the conservation of mass equation in SPH. *Applied Mathematical Modelling*, 40, pp.8722-36. Available at: <http://dx.doi.org/10.1016/j.apm.2016.05.016>.
- Cheng, L.-Y. & Arai, M., 2002. A Numerical treatment of the boundary conditions for stable assessment of hydrodynamic impact pressure. *21st International Conference on Offshore Mechanics and Arctic Engineering*, Available at: <https://doi.org/10.1115/OMAE2002-28266>.
- Chen, X., Sun, Z.G., Liu, L. & Xi, G., 2016. Improved MPS method with variable-size particles. *International Journal for Numerical Methods in Fluids*, 80(6), pp.358-74. Available at: <https://doi.org/10.1002/flid.4082>.
- Chen, X., Zhang, Y. & Wan, D., 2019. Numerical study of 3-D liquid sloshing in an elastic tank by MPS-FEM coupled method. *Journal of Ship Research*, 63(3), pp.143-53. Available at: <http://dx.doi.org/10.5957/JOSR.09180082>.
- Chikazawa, Y., Koshizuka, S. & Oka, Y., 2001. A particle method for elastic and viscoplastic structures and fluid-structures interactions. *Computational Mechanics*, 27(2), pp.97-106. Available at: <https://doi.org/10.1007/s004660000216>.
- Chiron, L., de Leffe, M., Oger, G. & Le Touzé, D., 2019. Fast and accurate SPH modelling of 3D complex wall boundaries in viscous and non viscous flows. *Computer Physics Communications*, 234, pp.93-111. Available at: <https://doi.org/10.1016/j.cpc.2018.08.001>.
- Chorin, A.J., 1967. The numerical solution of the Navier-Stokes equations for an incompressible fluid. *Bulletin of the American Mathematical Society*, 73(6), pp.928-31. Available at: <https://projecteuclid.org/euclid.bams/1183529112>.
- Chorin, A.J. & Bernard, P.S., 1973. Discretization of a vertex sheet, with an example of roll-up. *Journal of Computational Physics*, 13(3), pp.423-29. Available at: [https://doi.org/10.1016/0021-9991\(73\)90045-4](https://doi.org/10.1016/0021-9991(73)90045-4).

- Chow, A.D., Rogers, B.D. & Lind, S.J..S.P.K., 2018. Incompressible SPH (ISPH) with fast Poisson solver on a GPU. *Computer Physics Communications*, 226, pp.81-103. Available at: <https://doi.org/10.1016/j.cpc.2018.01.005>.
- Courant, R., Friedrichs, K. & Levy, H., 1967. On the Partial Difference Equations of Mathematical Physics. *IBM Journal of Research and Development*, 11(2), pp.215-34. Available at: <https://doi.org/10.1147/rd.112.0215>.
- Cummins, S.J. & Rudman, M., 1999. An SPH projection method. *Journal of Computational Physics*, 152(2), pp.584-607. Available at: <https://doi.org/10.1006/jcph.1999.6246>.
- Cundall, P.A. & Strack, O.D.L., 1979. A discrete numerical model for granular assemblies. *Geotechnique*, 29(1), pp.47-65. Available at: <https://doi.org/10.1680/geot.1979.29.1.47>.
- Dagum, L. & Menon, R., 1998. OpenMP: an industry standard API for shared-memory programming. *IEEE Computational Science and Engineering*, 5(1), pp.46-55. Available at: <https://doi.org/10.1109/99.660313>.
- De Vuyst, T., Vignjevic, R. & Campbell, J.C., 2005. Coupling between meshless and finite element methods. *International Journal of Impact Engineering*, 31(8), pp.1054-64. Available at: <https://doi.org/10.1016/j.ijimpeng.2004.04.017>.
- Duan, G., Chen, B., Zhang, X. & Wang, Y., 2017. A multiphase MPS solver for modeling multi-fluid interaction with free surface and its application in oil spill. *Computer Methods in Applied Mechanics and Engineering*, 320, pp.133-61. Available at: <https://doi.org/10.1016/j.cma.2017.03.014>.
- Duan, G. et al., 2018. An accurate and stable multiphase moving particle semi-implicit method based on a corrective matrix for all particle interaction models. *International Journal for Numerical Methods in Engineering*, 115(10), pp.1287-314. Available at: <https://doi.org/10.1002/nme.5844>.
- Evans, M.W. & Harlow, F.H., 1957. *The particle-in-cell method for hydrodynamic calculations*. Report LA-2139. Los Alamos National Laboratory.
- Falahaty, H., Khayyer, A. & Gotoh, H., 2018. Enhanced particle method with stress point integration for simulation of incompressible fluid-nonlinear elastic structure interaction. *Journal of Fluids and Structures*, 81, pp.325-60. Available at: <https://doi.org/10.1016/j.jfluidstructs.2018.04.012>.

- Favier, J.F., Abbaspour-Fard, M.H., Kremmer, M. & Raji, A.O., 1999. Shape representation of axi-symmetrical, non-spherical particles in discrete element simulation using multi-element model particles. *Engineering Computations*, 16(4), pp.467-80. Available at: <https://doi.org/10.1108/02644409910271894>.
- Felippa, C.A., Park, K.C. & Farhat, C., 2001. Partitioned analysis of coupled mechanical systems. *Computer Methods in Applied Mechanics and Engineering*, 190(24-25), pp.3247-70. Available at: [https://doi.org/10.1016/S0045-7825\(00\)00391-1](https://doi.org/10.1016/S0045-7825(00)00391-1).
- Fernandes, D.T., Cheng, L.-Y., Favero, E.H. & Nishimoto, K., 2015. A domain decomposition strategy for hybrid parallelization of moving particle semi-implicit (MPS) method for computer cluster. *Cluster Computing*, 18(4), pp.1363-77. Available at: <https://doi.org/10.1007/s10586-015-0483-3>.
- Fernández-Gutiérrez, D. & Zohdi, T.I., 2020. Delta Voronoi smoothed particle hydrodynamics, δ -VSPH. *Journal of Computational Physics*, 401, Available at: <https://doi.org/10.1016/j.jcp.2019.109000>.
- Fourey, G., Hermange, C., Le Touzé, D. & Oger, G., 2017. An efficient FSI coupling strategy between Smoothed Particle Hydrodynamics and Finite Element methods. *Computer Physics Communications*, 217, pp.66-81. Available at: <https://doi.org/10.1016/j.cpc.2017.04.005>.
- Frisch, U., Hasslacher, B. & Pomeau, Y., 1986. Lattice-gas automata for the Navier-Stokes equation. *Physical Review Letters*, 56(14), pp.1505-08. Available at: <https://doi.org/10.1103/PhysRevLett.56.1505>.
- Gaugain, F., 2013. *Analyse expérimentale et simulation numérique de l'interaction fluide-structure d'un hydrofoil élastique en écoulement subcavitant et cavitant*. France: Ecole nationale supérieure d'arts et métiers - ENSAM.
- Gay Neto, A., 2016. *Giraffe*. [Online] (2.0.37) Available at: <http://sites.poli.usp.br/p/alfredo.gay/giraffe.html> [Accessed 19 February 2020].
- Gentry, R.A., Martin, R.E. & Daly, B.J., 1966. An eulerian differencing method for unsteady compressible flow problems. *Journal of Computational Physics*, 1(1), pp.87-118. Available at: [https://doi.org/10.1016/0021-9991\(66\)90014-3](https://doi.org/10.1016/0021-9991(66)90014-3).
- Gingold, R.A. & Monaghan, J.J., 1977. Smoothed particle hydrodynamics: Theory and application to non-spherical stars. *Monthly Notices of the Royal Astronomical Society*, 181, pp.375-89. Available at: <https://doi.org/10.1093/mnras/181.3.375>.

Gotoh, H., Ikari, H. & Yasuoka, T., 2009. Simulation of Armor Blocks in front of Caisson Breakwater by DEM-MPS Hybrid Model. *The Nineteenth International Offshore and Polar Engineering Conference*.

Gotoh, H. & Khayyer, A., 2016. Current achievements and future perspectives for projection-based particle methods with applications in ocean engineering. *Journal of Ocean Engineering and Marine Energy*, 2(3), pp.251-78. Available at: <https://doi.org/10.1007/s40722-016-0049-3>.

Gotoh, H. & Khayyer, A., 2018. On the state-of-the-art of particle methods for coastal and ocean engineering. *Coastal Engineering Journal*, 60(1), pp.79-103. Available at: <https://doi.org/10.1080/21664250.2018.1436243>.

Gotoh, H., Khayyer, A. & Hori, C., 2009. New assessment criterion of free surface for stabilizing pressure field in particle method. *Journal of Japan Society of Civil Engineers, Ser. B2 (Coastal Engineering)*, 65(1), pp.21-25. Available at: <https://doi.org/10.2208/kaigan.65.21>.

Gotoh, H. et al., 2014. On enhancement of Incompressible SPH method for simulation of violent sloshing flows. *Applied Ocean Research*, 46, pp.104-15. Available at: <https://doi.org/10.1016/j.apor.2014.02.005>.

Gotoh, H., Okayasu, A. & Watanabe, Y., 2013. *Computational wave dynamics*. World Scientific Publishing Company. Available at: <https://doi.org/10.1142/8714>.

Gravouil, A. & Combescure, A., 2001. Multi-time-step explicit–implicit method for nonlinear structural dynamics. *International Journal for Numerical Methods in Engineering*, 50(1), pp.199-225. Available at: [https://doi.org/10.1002/1097-0207\(20010110\)50:1%3C199:AID-NME132%3E3.0.CO;2-A](https://doi.org/10.1002/1097-0207(20010110)50:1%3C199:AID-NME132%3E3.0.CO;2-A).

Gray, J.P., Monaghan, J.J. & Swift, R.P., 2001. SPH elastic dynamics. *Computer Methods in Applied Mechanics and Engineering*, 190(49), pp.6641-62. Available at: [https://doi.org/10.1016/S0045-7825\(01\)00254-7](https://doi.org/10.1016/S0045-7825(01)00254-7).

Groenenboom, P.H.L. & Cartwright, B.K., 2010. Hydrodynamics and fluid-structure interaction by coupled SPH-FE method. *Journal of Hydraulic Research*, 48(1), pp.61-73. Available at: <https://doi.org/10.1080/00221686.2010.9641246>.

Guo, D. et al., 2020. Numerical modeling of churning power loss of gear system based on moving particle method. *Tribology Transactions*, 63(1), pp.182-93. Available at: <https://doi.org/10.1080/10402004.2019.1682212>.

Guo, X., Rogers, B.D., Lind, S. & Stansby, P.K., 2018. New massively parallel scheme for Incompressible Smoothed Particle Hydrodynamics (ISPH) for highly nonlinear and distorted flow. *Computer Physics Communications*, 233, pp.16-28. Available at: <https://doi.org/10.1016/j.cpc.2018.06.006>.

Harada, E., Ikari, H., Khayyer, A. & Gotoh, H., 2018. Numerical simulation for swash morphodynamics by DEM–MPS coupling model. *Coastal Engineering Journal*, Available at: <https://doi.org/10.1080/21664250.2018.1554203>.

Harada, T., Koshizuka, S. & Shimazaki, K., 2008. Improvement of Wall Boundary Calculation Model for MPS Method. *Transactions of Japan Society for Computational Engineering and Science*, 2008.

Harada, T., Tanaka, M., Koshizuka, S. & Kawaguchi, Y., 2007. Real-time coupling of fluids and rigid bodies.

Harlow, F.H. & Welch, J.E., 1965. Numerical calculation of time-dependent viscous incompressible flow of fluid with a free surface. *The Physics of Fluids*, 8(12), pp.2182-89. Available at: <https://doi.org/10.1063/1.1761178>.

Henshaw, W.D. & Kreiss, H.-O., 1995. *Analysis of a difference approximation for the incompressible Navier-Stokes equations*. Research Report LA–UR–95–3536. Los Alamos National Laboratory.

Henshaw, W.D. & Petersson, N.A., 2003. A split-step scheme for the incompressible Navier-Stokes equations." Numerical simulations of incompressible flows. *Numerical simulations of incompressible flows*, pp.108-25. Available at: https://doi.org/10.1142/9789812796837_0007.

Hermange, C., Oger, G., Le Chenadec, Y. & Le Touzé, D., 2019. A 3D SPH–FE coupling for FSI problems and its application to tire hydroplaning simulations on rough ground. *Computer Methods in Applied Mechanics and Engineering*, 355, pp.558-90. Available at: <https://doi.org/10.1016/j.cma.2019.06.033>.

Hietel, D., Steiner, K. & Struckmeier, J., 2000. A finite volume particle method for compressible flows. *Mathematical Models and Methods in Applied Science*, 10(9), pp.1363-82. Available at: <https://doi.org/10.1142/S0218202500000604>.

Hirokazu, I., 1999. *Numerical analysis of fragmentation processes in vapor explosion using particle method*.

Hoogerbrugge, P.J. & Koelman, J.M.V.A., 1992. Simulating microscopic hydrodynamic phenomena with dissipative particle dynamics. *Europhysics Letters*, 19(3), pp.155-60. Available at: <https://doi.org/10.1209/0295-5075/19/3/001>.

Hoomans, B., 2000. *Granular dynamics of gas-solid two-phase flows*. PhD. Thesis. University of Twente.

Hori, C., Gotoh, H., Ikari, H. & Khayyer, A., 2011. GPU-acceleration for moving particle semi-Implicit method. *Computers & Fluids*, 51(1), pp.174-83. Available at: <https://doi.org/10.1016/j.compfluid.2011.08.004>.

Hu, X.Y. & Adams, N.A., 2007. An incompressible multi-phase SPH method. *Journal of Computational Physics*, 227(1), pp.264-78. Available at: <https://doi.org/10.1016/j.jcp.2007.07.013>.

Hu, D. et al., 2014. Fluid–structure interaction analysis by coupled FE–SPH model based on a novel searching algorithm. *Computer Methods in Applied Mechanics and Engineering*, 276, pp.266-86. Available at: <https://doi.org/10.1016/j.cma.2014.04.001>.

Hwang, Y.-H., 2011. A moving particle method with embedded pressure mesh (MPPM) for incompressible flow calculations. *Numerical Heat Transfer, Part B: Fundamentals: An International Journal of Computation and Methodology*, 60(5), pp.370-98. Available at: <https://doi.org/10.1080/10407790.2011.601178>.

Hwang, S.-C., Khayyer, A., Gotoh, H. & Park, J.-C., 2014. Development of a fully Lagrangian MPS-based coupled method for simulation of fluid–structure interaction problems. *Journal of Fluids and Structures*, 50, pp.497-511. Available at: <https://doi.org/10.1016/j.jfluidstructs.2014.07.007>.

Hwang, S.C. et al., 2016. Numerical simulations of sloshing flows with elastic baffles by using a particle-based fluid–structure interaction analysis method. *Ocean Engineering*, 118, pp.227-41. Available at: <https://doi.org/10.1016/j.oceaneng.2016.04.006>.

Idelsohn, S.R. & Oñate, E., 2006. To mesh or not to mesh. That is the question. *Computer Methods in Applied Mechanics and Engineering*, 195(37-40), pp.4681-96. Available at: <https://doi.org/10.1016/j.cma.2005.11.006>.

Ikeda, H., 1999. *Numerical analysis of fragmentation processes in vapor explosion using particle method*. Japan (in Japanese): Doctoral Thesis, Tokyo University.

- Ismagilov, J.T., 2006. Smooth volume integral conservation law and method for problems in Lagrangian coordinates. *Computational Mathematics and Mathematical Physics*, 46, pp.453-64. Available at: <https://doi.org/10.1134/S0965542506030110>.
- Isshiki, H., 2011. Discrete differential operators on irregular nodes (DDIN). *International Journal for Numerical Methods in Engineering*, 88(12), pp.1323-43. Available at: <https://doi.org/10.1002/nme.3225>.
- Itori, S., Iribe, T. & Nakaza, E., 2011. Development and application on new judging method of free water surface of MPS. *Journal of Japan Society of Civil Engineers, Ser. B3 (Ocean Engineering)*, 67(2), pp.274-79. Available at: https://doi.org/10.2208/jscejoe.67.I_274.
- Jacobson, A., Panozzo, D. & others, 2018. *libigl: A simple C++ geometry processing library*. [Online] (2.0) Available at: [Accessed 21 February 2020].
- Jandaghian, M. & Shakibaeinia, A., 2020. An enhanced weakly-compressible MPS method for free-surface flows. *Computer Methods in Applied Mechanics and Engineering*, 360, Available at: <https://doi.org/10.1016/j.cma.2019.112771>.
- Johnson, K.L., 1985. *Contact Mechanics*. Cambridge: Cambridge University Press.
- Karunasena, H.C.P., Senadeera, W., Gu, Y.T. & Brown, R.J., 2014. A coupled SPH-DEM model for micro-scale structural deformations of plant cells during drying. *Applied Mathematical Modelling*, 38(15-16), pp.3781-801. Available at: <https://doi.org/10.1016/j.apm.2013.12.004>.
- Khayyer, A. & Gotoh, H., 2008. Development of CMPS method for accurate water-surface tracking in breaking waves. *Coastal Engineering Journal*, 50(2), pp.179-207. Available at: <https://doi.org/10.1142/S0578563408001788>.
- Khayyer, A. & Gotoh, H., 2009. Modified moving particle semi-implicit methods for the prediction of 2D wave impact pressure. *Coastal Engineering*, 56(4), pp.419-40. Available at: <https://doi.org/10.1016/j.coastaleng.2008.10.004>.
- Khayyer, A. & Gotoh, H., 2010. A higher order Laplacian model for enhancement and stabilization of pressure calculation by the MPS method. *Applied Ocean Research*, 32(1), pp.124-31. Available at: <https://doi.org/10.1016/j.apor.2010.01.001>.
- Khayyer, A. & Gotoh, H., 2011. Enhancement of stability and accuracy of the moving particle semi-implicit method. *Journal of Computational Physics*, 230(8), pp.3093-118. Available at: <https://doi.org/10.1016/j.jcp.2011.01.009>.

Khayyer, A. & Gotoh, H., 2012. A 3D higher order laplacian model for enhancement and stabilization of pressure calculation in 3D MPS-based simulations. *Applied Ocean Research*, 37, pp.120-26. Available at: <https://doi.org/10.1016/j.apor.2012.05.003>.

Khayyer, A., Gotoh, H., Falahaty, H. & Shimizu, Y., 2018. An enhanced ISPH–SPH coupled method for simulation of incompressible fluid–elastic structure interactions. *Computer Physics Communication*, 232, pp.139-64. Available at: <https://doi.org/10.1016/j.cpc.2018.05.012>.

Khayyer, A., Gotoh, H. & Shao, S., 2009. Enhanced predictions of wave impact pressure by improved incompressible SPH methods. *Applied Ocean Research*, 31(2), pp.111-31. Available at: <https://doi.org/10.1016/j.apor.2009.06.003>.

Khayyer, A., Gotoh, H. & Shimizu, Y., 2017. Comparative study on accuracy and conservation properties of two particle regularization schemes and proposal of an optimized particle shifting schem in ISPH context. *Journal of Computational Physics*, 332, pp.236-56. Available at: <https://doi.org/10.1016/j.jcp.2016.12.005>.

Khayyer, A., Gotoh, H., Shimizu, Y. & Gotoh, K., 2017. On enhancement of energy conservation properties of projection-based particle methods. *European Journal of Mechanics - B/Fluids*, 66, pp.20-37. Available at: <https://doi.org/10.1016/j.euromechflu.2017.01.014>.

Khayyer, A., Tsuruta, N., Shimizu, Y. & Gotoh, H., 2019. Multi-resolution MPS for incompressible fluid-elastic structure interactions in ocean engineering. *Applied Ocean Research*, 82, pp.397-414. Available at: <https://doi.org/10.1016/j.apor.2018.10.020>.

Kleefsman, K.M.T. et al., 2005. A Volume-of-Fluid based simulation method for wave impact problems. *Journal of Computational Physics*, 206(1), pp.363-93. Available at: <https://doi.org/10.1016/j.jcp.2004.12.007>.

Koh, C.G., Gao, M. & Luo, C., 2012. A new particle method for simulation of incompressible free surface flow problems. *International Journal for Numerical Methods in Engineering*, pp.1582-604. Available at: <https://doi.org/10.1002/nme.3303>.

Kondo, M. & Koshizuka, S., 2011. Improvement of stability in moving particle semi-implicit method. *International Journal for Numerical Methods in Fluids*, 65(6), pp.638-54. Available at: <https://doi.org/10.1002/flid.2207>.

- Koschier, D. & Bender, J., 2017. Density maps for improved SPH boundary handling. In *Proceedings of the ACM SIGGRAPH / Eurographics Symposium on Computer Animation.*, 2017.
- Koshizuka, S., Nobe, A. & Oka, Y., 1998. Numerical analysis of breaking waves using the moving particle semi-implicit method. *International Journal for Numerical Methods in Fluids*, 26(7), pp.751-69. Available at: [https://doi.org/10.1002/\(SICI\)1097-0363\(19980415\)26:7<751::AID-FLD671>3.0.CO;2-C](https://doi.org/10.1002/(SICI)1097-0363(19980415)26:7<751::AID-FLD671>3.0.CO;2-C).
- Koshizuka, S. & Oka, Y., 1996. Moving-particle semi-implicit method for fragmentation of incompressible fluid. *Nuclear Science and Engineering*, 123(3), pp.421-34. Available at: <https://doi.org/10.13182/NSE96-A24205>.
- Kostorz, W. & Esmail-Yakas, A., 2020. A semi-analytical boundary integral method for radial functions with application to Smoothed Particle Hydrodynamics. *Journal of Computational Physics*, 417, Available at: <https://doi.org/10.1016/j.jcp.2020.109565>.
- Landau, L.D. & Lifšits, E.M., 1979. *Teoria dell'elasticità*.
- Lee, E.-S. et al., 2008. Comparisons of weakly compressible and truly incompressible algorithms for the SPH mesh free particle method. *Journal of Computational Physics*, 227(18), pp.8417-36. Available at: <https://doi.org/10.1016/j.jcp.2008.06.005>.
- Lee, C.J.K., Noguchi, H. & Koshizuka, S., 2007. Fluid–shell structure interaction analysis by coupled particle and finite element method. *Computers & Structures*, 85(11-14), pp.688-97. Available at: <https://doi.org/10.1016/j.compstruc.2007.01.019>.
- Lee, B.-H., Park, J.-C., Kim, M.-H. & Hwang, S.-C., 2011. Step-by-step improvement of MPS method in simulating violent free-surface motions and impact-loads. *Computer Methods in Applied Mechanics and Engineering*, 200(9-12), pp.1113-25. Available at: <https://doi.org/10.1016/j.cma.2010.12.001>.
- Li, L., 2020. A split-step finite-element method for incompressible Navier-Stokes equations with high-order accuracy up-to the boundary. *Journal of Computational Physics*, 408, Available at: <https://doi.org/10.1016/j.jcp.2020.109274>.
- Liao, K., Hu, C. & Makoto, S., 2015. Free surface flow impacting on an elastic structure: experiment versus numerical simulation. *Applied Ocean Research*, 50, pp.192-208. Available at: <https://doi.org/10.1016/j.apor.2015.02.002>.

- Li, Y., Asai, M., Chandra, B. & Isshiki, M., 2020. Energy-tracking impulse method for particle-discretized rigid-body simulations with frictional contact. *Computational Particle Mechanics*, Available at: <https://doi.org/10.1007/s40571-020-00326-5>.
- Li, G. et al., 2020. A review on MPS method developments and applications in nuclear engineering. *Computer Methods in Applied Mechanics and Engineering*, 367, Available at: <https://doi.org/10.1016/j.cma.2020.113166>.
- Li, S. & Kam, L.W., 2004. *Meshfree Particle Methods*. Springer-Verlag Berlin Heidelberg. Available at: <https://doi.org/10.1007/978-3-540-71471-2>.
- Li, Z., Leduc, J., Combescure, A. & Leboeuf, F., 2014. Coupling of SPH-ALE method and finite element method for transient fluid–structure interaction. *Computers & Fluids*, 103, pp.6-17. Available at: <https://doi.org/10.1016/j.compfluid.2014.06.028>.
- Li, Z. et al., 2015. A non-intrusive partitioned approach to couple smoothed particle hydrodynamics and finite element methods for transient fluid-structure interaction problems with large interface motion. *Computational Mechanics*, 55(4), pp.697-718. Available at: <https://doi.org/10.1007/s00466-015-1131-8>.
- Lind, S.J., Rogers, B.D. & Stansby, P.K., 2020. Review of smoothed particle hydrodynamics: towards converged Lagrangian flow modelling. *Proceedings of the Royal Society A*, 476(2241), Available at: <https://doi.org/10.1098/rspa.2019.0801>.
- Lind, S.J., Xu, R., Stansby, P.K. & Rogers, B.D., 2012. Incompressible smoothed particle hydrodynamics for free-surface flows: a generalised diffusion-based algorithm for stability and validations for impulsive flows and propagating waves. *Journal of Computational Physics*, 231(4), pp.1499-523. Available at: <https://doi.org/10.1016/j.jcp.2011.10.027>.
- Liu, G.-R. & Liu, M.-B., 2003. *Smoothed Particle Hydrodynamics A Meshfree Particle Method*. World Scientific Publishing Company.
- Liu, M.-B. & Liu, G.-R., 2015. *Particle Methods for Multi-Scale and Multi-Physics*. Singapore: World Scientific Publishing Company.
- Liu, X., Morita, K. & Zhang, S., 2018. An advanced moving particle semi-implicit method for accurate and stable simulation of incompressible flows. *Computer Methods in Applied Mechanics and Engineering*, 339, pp.467-87. Available at: <https://doi.org/10.1016/j.cma.2018.05.005>.

- Liu, Q.-x. et al., 2019. Numerical investigation of liquid dispersion by hydrophobic/hydrophilic mesh packing using particle method. *Chemical Engineering Science*, 202, pp.447-61. Available at: <https://doi.org/10.1016/j.ces.2019.03.046>.
- Liu, F., Yu, Y., Wang, Q. & Luo, Y., 2020. A coupled smoothed particle hydrodynamic and finite particle method: An efficient approach for fluid-solid interaction problems involving free-surface flow and solid failure. *Engineering Analysis with Boundary Elements*, 118, pp.143-55. Available at: <https://doi.org/10.1016/j.enganabound.2020.03.006>.
- Lobovský, L. et al., 2014. Experimental investigation of dynamic pressure loads during dam break. *Journal of Fluids and Structures*, 48, pp.407-34. Available at: <https://doi.org/10.1016/j.jfluidstructs.2014.03.009>.
- Long, T., Hu, D., Yang, G. & Wan, D., 2016. A particle-element contact algorithm incorporated into the coupling methods of FEM-ISPH and FEM-WCSPH for FSI problems. *Ocean Engineering*, 123, pp.154-63. Available at: <https://doi.org/10.1016/j.oceaneng.2016.06.040>.
- Lo, E.Y.M. & Shao, S., 2002. Simulation of near-shore solitary wave mechanics by an incompressible SPH method. *Applied Ocean Research*, 24(5), pp.275-86. Available at: [https://doi.org/10.1016/S0141-1187\(03\)00002-6](https://doi.org/10.1016/S0141-1187(03)00002-6).
- Lucy, L.B., 1977. A numerical approach to the testing of the fission hypothesis. *Astronomical Journal*, 82, pp.1013-24. Available at: <https://doi.org/10.1086/112164>.
- Macià, F., Merino-Alonso, P.E. & Souto-Iglesias, A., 2020. On the truncated integral SPH solution of the hydrostatic problem. *Computational Particle Mechanics*, Available at: <https://doi.org/10.1007/s40571-020-00333-6>.
- Maningo, J. et al., 2017. Smoothed particle hydrodynamics approach to aggregation of quadrotor unmanned aerial vehicle swarm. *Journal of Advanced Computational Intelligence and Intelligent Informatics*, 21(2), pp.181-88. Available at: <https://doi.org/10.20965/jaciii.2017.p0181>.
- Marrone, S., Colagrossi, A., Di Mascio, A. & Le Touzé, D., 2015. Prediction of energy losses in water impacts using incompressible and weakly compressible models. *Journal of Fluids and Structures*, 54, pp.802-22. Available at: <https://doi.org/10.1016/j.jfluidstructs.2015.01.014>.

- Martínez-Ferrer, P.J. et al., 2018. An efficient finite-volume method to study the interaction of two-phase fluid flows with elastic structures. *Journal of Fluids and Structures*, 83, pp.54-71. Available at: <https://doi.org/10.1016/j.jfluidstructs.2018.08.019>.
- Matsunaga, T., Södersten, A., Shibata, K. & Koshizuka, S., 2020. Improved treatment of wall boundary conditions for a particle method with consistent spatial discretization. *Computer Methods in Applied Mechanics and Engineering*, 358, Available at: <https://doi.org/10.1016/j.cma.2019.112624>.
- Matsunaga, T., Yuhashi, N., Shibata, K. & Koshizuka, S., 2020. A wall boundary treatment using analytical volume integrations in a particle method. *International Journal for Numerical Methods in Engineering*, pp.1-33. Available at: <https://doi.org/10.1002/nme.6429>.
- Mazhar, H. et al., 2013. CHRONO: a parallel multi-physics library for rigid-body, flexible-body, and fluid dynamics. 4(1), pp.49-64. Available at: <https://doi.org/10.5194/ms-4-49-2013>.
- Ma, Q.W., Zhou, Y. & Yan, S., 2016. A review on approaches to solving Poisson's equation in projection-based meshless methods for modelling strongly nonlinear water waves. *Journal of Ocean Engineering and Marine Energy*, 2(3), pp.279-99. Available at: <https://doi.org/10.1007/s40722-016-0063-5>.
- McNamara, G.R. & Zanetti, G., 1988. Use of the Boltzmann equation to simulate lattice-gas automata. *Physical Review Letters*, 61(20), pp.2332-35. Available at: <https://doi.org/10.1103/PhysRevLett.61.2332>.
- Meringolo, D.D., Colagrossi, A., Marrone, S. & Aristodemo, F., 2017. On the filtering of acoustic components in weakly-compressible SPH simulations. *Journal of Fluids and Structures*, 70, pp.1-23. Available at: <https://doi.org/10.1016/j.jfluidstructs.2017.01.005>.
- Meringolo, D.D., Marrone, S., Colagrossi, A. & Liu, Y., 2019. A dynamic δ -SPH model: How to get rid of diffusive parameter tuning. *Computers & Fluids*, 179, pp.334-55. Available at: <https://doi.org/10.1016/j.compfluid.2018.11.012>.
- Metropolis, N. & Ulam, S., 1949. The Monte Carlo method. *Journal of American Statistical Association*, 44(247), pp.335-41. Available at: <https://doi.org/10.2307/2280232>.
- Milne-Thomson, L.M., 1968. *Theoretical Hydrodynamics*. 5th ed. New York: Macmillan Press.

- Mitsume, N., Yoshimura, S., Murotani, K. & Yamada, T., 2014a. MPS–FEM Partitioned coupling approach for fluid–structure interaction with free surface flow. *International Journal of Computational Methods*, 11(4), Available at: <https://doi.org/10.1142/S0219876213501016>.
- Mitsume, N., Yoshimura, S., Murotani, K. & Yamada, T., 2014b. Improved MPS-FE fluid-structure interaction coupled method with MPS polygon wall boundary model. *Computer Modeling in Engineering and Sciences*, 101(4), pp.229-47. Available at: <https://doi.org/10.3970/cmcs.2014.101.229>.
- Mitsume, N., Yoshimura, S., Murotani, K. & Yamada, T., 2015. Explicitly represented polygon wall boundary model for the explicit MPS method. *Computational Particle Mechanics*, 2(1), pp.73-89. Available at: <https://doi.org/10.1007/s40571-015-0037-8>.
- Mokrani, C. & Abadie, S., 2016. Conditions for peak pressure stability in VOF simulations of dam break flow impact. *Journal of Fluids and Structures*, 62, pp.86-103. Available at: <https://doi.org/10.1016/j.jfluidstructs.2015.12.007>.
- Molteni, D. & Colagrossi, A., 2009. A simple procedure to improve the pressure evaluation in hydrodynamic context using the SPH. *Computer Physics Communications*, 180(6), pp.861-72. Available at: <https://doi.org/10.1016/j.cpc.2008.12.004>.
- Monaghan, J.J., 1992. Smoothed particle hydrodynamics. *Annual Review of Astronomy and Astrophysics*, 30, pp.543-74. Available at: <https://doi.org/10.1146/annurev.aa.30.090192.002551>.
- Monaghan, J.J., 1994. Simulating free surface flows with SPH. *Journal of Computational Physics*, 110(2), pp.399-406. Available at: <https://doi.org/10.1006/jcph.1994.1034>.
- Monaghan, J.J., 2005. Smoothed particle hydrodynamics. *Reports on Progress in Physics*, 68(8), pp.1703-59. Available at: <http://dx.doi.org/10.1088/0034-4885/68/8/R01>.
- Moreira, M.L.T., 2009. *Rotation parameterization in rod and shell theories (in Portuguese)*. Ph.D. thesis. Universidade de São Paulo.
- Murotani, K. et al., 2015. Performance improvements of differential operators code for MPS method on GPU. *Computational Particle Mechanics*, 2, pp.261-72. Available at: <https://doi.org/10.1007/s40571-015-0059-2>.
- Nasar, A.M.A., Rogers, B.D., Revell, A. & Stansby, P.K., 2019. Flexible slender body fluid interaction: Vector-based discrete element method with Eulerian smoothed particle

hydrodynamics. *Computers & Fluids*, 179, pp.563-78. Available at: <https://doi.org/10.1016/j.compfluid.2018.11.024>.

Nestor, R.M., Basa, M., Lastiwka, M. & Quinlan, N.J., 2009. Extension of the finite volume particle method to viscous flow. *Journal of Computational Physics*, 228(5), pp.1733-49. Available at: <https://doi.org/10.1016/j.jcp.2008.11.003>.

Newmark, N.M., 1959. A method of computation for structural dynamics. *Journal of the Engineering Mechanics Division*, 85(3), pp.67-94.

Ng, K.C., Hwang, Y.H. & Sheu, T.W.H., 2014. On the accuracy assessment of Laplacian models in MPS. *Computer Physics Communications*, 185(10), pp.2412-26. Available at: <https://doi.org/10.1016/j.cpc.2014.05.012>.

Ngo-Cong, D., Tran, C.-D., Mai-Duy, N. & Tran-Cong, T., 2015. Incompressible smoothed particle hydrodynamics-moving IRBFN method for viscous flow problems. *Engineering Analysis with Boundary Elements*, 59, pp.172-86. Available at: <https://doi.org/10.1016/jenganabound.2015.06.006>.

Ng, K.C., Sheu, T.W.H. & Hwang, Y.H., 2016. Unstructured moving particle pressure mesh (UMPPM) method for incompressible isothermal and non-isothermal flow computation. *Computer Methods in Applied Mechanics and Engineering*, 305, pp.703-38. Available at: <https://doi.org/10.1016/j.cma.2016.03.015>.

Nunez-Ramirez, J., Marongiu, J., Brun, M. & Combescure, A., 2017. A partitioned approach for the coupling of SPH and FE methods for transient nonlinear FSI problems with incompatible time-steps. *International Journal for Numerical Methods in Engineering*, 109(10), pp.1391-417. Available at: <https://doi.org/10.1002/nme.5331>.

Ogino, M., Iwama, T. & Asai, M., 2019. Development of a partitioned coupling analysis system for fluid–structure interactions using an in-house ISPH code and the adventure system. *International Journal of Computational Methods*, 16(4), Available at: <https://doi.org/10.1142/S0219876218430090>.

Oh, S., Kim, Y. & Roh, B.S., 2009. Impulse-based rigid body interaction in SPH. *Computer Animation and Virtual Worlds*, 20, pp.215-24. Available at: <https://doi.org/10.1002/cav.290>.

Oochi, M., Koshizuka, S. & Sakai, M., 2010. Explicit MPS algorithm for free surface flow analysis. *Transactions of the Japan Society for Computational Engineering and Science*, 2010, pp.185-93.

- Ota, N.S.N. et al., 2016. Nonlinear dynamic analysis of creased shells. *Finite Elements in Analysis and Design*, 121, pp.64-74. Available at: <https://doi.org/10.1016/j.finel.2016.07.008>.
- Pan, Z.H., Yan, J. & Zhao, C.Y., 2019. Numerical analyses and optimization of tubular thermochemical heat storage reactors using axisymmetric thermal lattice Boltzmann model. *Chemical Engineering Science*, 195, pp.737-47. Available at: <https://doi.org/10.1016/j.ces.2018.10.019>.
- Pimenta, P.M. & Campello, E.M.B., 2001. Geometrically nonlinear analysis of thin-walled space frames. In *Proceedings of the Second European Conference on Computational Mechanics, II ECCM*. Cracow, 2001.
- Pimenta, L.C.A. et al., 2013. Swarm coordination based on smoothed particle hydrodynamics technique. *IEEE Transactions on Robotics*, 29(2), pp.383-99. Available at: <https://doi.org/10.1109/TRO.2012.2234294>.
- Pohle, F.V., 1951. *The Lagrangian equations of hydrodynamics: solutions which are analytic functions of the time*. New York: New York University.
- Price, D.J., 2012. Smoothed particle hydrodynamics and magnetohydrodynamics. *Journal of Computational Physics*, 231(3), pp.759-94. Available at: <https://doi.org/10.1016/j.jcp.2010.12.011>.
- Qiu, L.-c. et al., 2017. Numerical simulation of submarine landslide tsunamis using particle based methods. *Journal of Hydrodynamics*, 29(4), pp.542-51. Available at: [https://doi.org/10.1016/S1001-6058\(16\)60767-9](https://doi.org/10.1016/S1001-6058(16)60767-9).
- Quentrec, B. & Brot, C., 1975. New method for searching for neighbors in molecular dynamics computations. *Journal of Computational Physics*, 13(3), pp.430-32. Available at: [https://doi.org/10.1016/0021-9991\(73\)90046-6](https://doi.org/10.1016/0021-9991(73)90046-6).
- Rafiee, A. & Thiagarajan, K.P., 2009. An SPH projection method for simulating fluid-hypoelastic structure interaction. *Computer Methods in Applied Mechanics and Engineering*, 198(33-36), pp.2785-95. Available at: <https://doi.org/10.1016/j.cma.2009.04.001>.
- Randles, P.W. & Libersky, L.D., 1996. Smoothed particle hydrodynamics: Some recent improvements and applications. *Computer Methods in Applied Mechanics and Engineering*, 139(1-4), pp.375-408. Available at: [https://doi.org/10.1016/S0045-7825\(96\)01090-0](https://doi.org/10.1016/S0045-7825(96)01090-0).

- Rao, C., Zhang, Y. & Wan, D., 2017. Numerical Simulation of the Solitary Wave Interacting with an Elastic Structure Using MPS-FEM Coupled Method. *Journal of Marine Science and Application*, 16(4), pp.395-404. Available at: <https://doi.org/10.1007/s11804-017-1430-x>.
- Rasio, F.A., 2000. Particle methods in astrophysical fluid dynamics. *Progress of Theoretical Physics Supplement*, 138, pp.609-21. Available at: <https://doi.org/10.1143/PTPS.138.609>.
- Rastgoftar, E., Jannat, M.R.A. & Banijamali, B., 2018. An integrated numerical method for simulation of drifted objects trajectory under real-world tsunami waves. *Applied Ocean Research*, 73, pp.1-16. Available at: <https://doi.org/10.1016/j.apor.2018.01.013>.
- Ren, B. et al., 2014. SPH-DEM Modeling of the Hydraulic Stability of 2D Blocks on a Slope. *Journal of Waterway, Port, Coastal, and Ocean Engineering*, 140(6), Available at: [https://doi.org/10.1061/\(ASCE\)WW.1943-5460.0000247](https://doi.org/10.1061/(ASCE)WW.1943-5460.0000247).
- Ritter, A., 1892. Die Fortpflanzung de Wasserwellen. *Zeitschrift Verein Deutscher Ingenieure*, 36(33), pp.947-54.
- Robb, D.M., Gaskin, S.J. & Marongiu, J.C., 2016. SPH-DEM model for free-surface flows containing solids applied to river ice jams. *Journal of Hydraulic Research*, 54(1), pp.27-40. Available at: <https://doi.org/10.1080/00221686.2015.1131203>.
- Sandim, M., Paiva, A. & Figueiredo, L.H., 2020. Simple and reliable boundary detection for meshfree particle methods using interval analysis. *Journal of Computational Physics*, Available at: <https://doi.org/10.1016/j.jcp.2020.109702>.
- Shakibaeinia, A. & Jin, Y.-C., 2010. A weakly compressible MPS method for modeling of open-boundary free-surface flow. *International journal for numerical methods in fluids*, 63(10), pp.1208-32. Available at: <https://doi.org/10.1002/flid.2132>.
- Shibata, K., Koshizuka, S., Matsunaga, T. & Massaie, I., 2017. The overlapping particle technique for multi-resolution simulation of particle methods. *Computer Methods in Applied Mechanics and Engineering*, 325, pp.434-62. Available at: <https://doi.org/10.1016/j.cma.2017.06.030>.
- SideFX, 2018. *Houdini*. [Online] Available at: <https://www.sidefx.com/>.
- Skillen, A., Lind, S., Stansby, P.K. & Rogers, B.D., 2013. Incompressible smoothed particle hydrodynamics (SPH) with reduced temporal noise and generalised Fickian smoothing applied to body–water slam and efficient wave–body interaction. *Computer Methods in*

- Applied Mechanics and Engineering*, 265, pp.163-73. Available at: <https://doi.org/10.1016/j.cma.2013.05.017>.
- Sulsky, D., Chen, Z. & Schreyer, H.L., 1994. A particle method for history dependent materials. *Computer Methods in Applied Mechanics and Engineering*, pp.179-96. Available at: [https://doi.org/10.1016/0045-7825\(94\)90112-0](https://doi.org/10.1016/0045-7825(94)90112-0).
- Sun, P.N., Le Touzé, D. & Zhang, A.-M., 2019. Study of a complex fluid-structure dam-breaking benchmark problem using a multi-phase SPH method with APR. *Engineering Analysis with Boundary Elements*, 104, pp.240-58. Available at: <https://doi.org/10.1016/j.enganabound.2019.03.033>.
- Sun, C., Shen, Z. & Zhang, M., 2019. Surface treatment technique of MPS method for free surface flows. *Engineering Analysis with Boundary Elements*, 102, pp.60-72. Available at: <https://doi.org/10.1016/j.enganabound.2019.02.004>.
- Sun, Y., Xi, G. & Sun, Z., 2019. A fully Lagrangian method for fluid–structure interaction problems with deformable floating structure. *Journal of Fluids and Structures*, 90, pp.379-95. Available at: <https://doi.org/10.1016/j.jfluidstructs.2019.07.005>.
- Suzuki, Y., 2008. *Studies on improvement in particle method and multiphysics simulator using particle method [doctoral thesis in Japanese]*. Tokyo, Japan: The University of Tokyo.
- Tamai, T. & Koshizuka, S., 2014. Least squares moving particle semi-implicit method. *Computational Particle Mechanics*, 1(3), pp.277-305. Available at: <https://doi.org/10.1007/s40571-014-0027-2>.
- Tanaka, M., Cardoso, R. & Bahai, H., 2018. Multi-resolution MPS method. *Journal of Computational Physics*, 359, pp.106-36. Available at: <https://doi.org/10.1016/j.jcp.2017.12.042>.
- Tanaka, M. & Masunaga, T., 2010. Stabilization and smoothing of pressure in MPS method by Quasi-Compressibility. *Journal of Computational Physics*, 229(11), pp.4279-90. Available at: <https://doi.org/10.1016/j.jcp.2010.02.011>.
- Tanaka, M., Sakai, M. & Koshizuka, S., 2007. Particle-based Rigid Body Simulation and Coupling with Fluid Simulation. *Transactions of the Japan Society for Computational Engineering and Science*.

- Tang, Y., Jiang, Q. & Zhou, C., 2018. A Lagrangian-based SPH-DEM model for fluid–solid interaction with free surface flow in two dimensions. *Applied Mathematical Modelling*, 62, pp.436-60. Available at: <https://doi.org/10.1016/j.apm.2018.06.013>.
- Tang, Z., Wan, D., Chen, G. & Xiao, Q., 2016. Numerical simulation of 3D violent free-surface flows by multi-resolution MPS method. *Journal of Ocean Engineering and Marine Energy*, 2, pp.355-64. Available at: <https://doi.org/10.1007/s40722-016-0062-6>.
- Taylor, G., 1966. Oblique impact of a jet on a plane surface. *Philosophical Transactions for the Royal Society of London. Series A, Mathematical and Physical Sciences*, 260(1110), pp.96-100. Available at: <http://www.jstor.org/stable/73541>.
- Temam, R., 1969. Sur l'approximation de la solution des équations de Navier-Stokes par la méthode des pas fractionnaires (II). *Archive for Rational Mechanics and Analysis*, 33(5), pp.377-85. Available at: <https://doi.org/10.1007/BF00247678>.
- Tiago, C., 2007. *Meshless methods: extending the linear formulation and its generalization to geometrically exact structural analysis*. Ph.D. thesis. Instituto Superior Técnico da Universidade Técnica de Lisboa.
- Timoshenko, S. & Woinowsky-Krieger, S., 1959. *Theory of Plates and Shells*. 2nd ed.
- Tsukamoto, M.M. et al., 2020. A numerical study of the effects of bottom and sidewall stiffeners on sloshing behavior considering roll resonant motion. *Marine Structures*, 72, Available at: <https://doi.org/10.1016/j.marstruc.2020.102742>.
- Tsukamoto, M.M., Cheng, L.-Y. & Motezuki, F.K., 2016. Fluid interface detection technique based on neighborhood particles centroid deviation (NPCD) for particle methods. *International Journal for Numerical Methods in Fluids*, pp.148-68. Available at: <https://doi.org/10.1002/flid.4213>.
- Tsuruta, N., Khayyer, A. & Gotoh, H., 2013. A short note on dynamic stabilization of moving particle semi-implicit method. *Computers & Fluids*, 82, pp.158-64. Available at: <https://doi.org/10.1016/j.compfluid.2013.05.001>.
- Vetsch, D., 2011. *Numerical simulation of sediment transport with meshfree methods*. Ph.D. thesis. ETH Zurich.
- Vila, J.P., 1999. On particle weighted methods and smooth particle hydrodynamics. *Mathematical Models and Methods in Applied Sciences*, 9(2), pp.161-209. Available at: <https://doi.org/10.1142/S0218202599000117>.

- Vorobyev, A., Kriventsev, V. & Maschek, W., 2011. Simulation of central sloshing experiments with smoothed particle hydrodynamics (SPH) method. *Nuclear Engineering and Design*, 241(8), pp.3086-96. Available at: <https://doi.org/10.1016/j.nucengdes.2011.05.020>.
- Wang, L., Jiang, Q. & Zhang, C., 2017. Improvement of moving particle semi-implicit method for simulation of progressive water waves. *International Journal for Numerical Methods in Fluids*, 85(2), pp.69-89. Available at: <https://doi.org/10.1002/fld.4373>.
- Wang, L. et al., 2019. Enhancement of pressure calculation in projection-based particle methods by incorporation of background mesh scheme. *Applied Ocean Research*, 86, pp.320-39. Available at: <https://doi.org/10.1016/j.apor.2019.01.017>.
- Wang, Z., Shibata, K. & Koshizuka, S., 2017. Verification and validation of explicit moving particle simulation method for application to internal flooding analysis in nuclear reactor building. *Journal of Nuclear Science and Technology*.
- Wang, L., Xu, F. & Yang, Y., 2019. Improvement of the tensile instability in SPH scheme for the FEI (Fluid-Elastomer Interaction) problem. *Engineering Analysis with Boundary Elements*, 106, pp.116-25. Available at: <https://doi.org/10.1016/j.enganabound.2019.04.032>.
- Wang, J. & Zhang, X., 2018. Modified particle method with integral Navier–Stokes formulation for incompressible flows. *Journal of Computational Physics*, 366(1), pp.1-13. Available at: <https://doi.org/10.1016/j.jcp.2018.03.043>.
- Wriggers, P., 2008. *Nonlinear Finite Element Methods*. Berlin: Springer. Available at: <https://doi.org/10.1007/978-3-540-71001-1>.
- Xu, R., Stansby, P.K. & Laurence, D., 2009. Accuracy and stability in incompressible SPH (ISPH) based on the projection method and a new approach. *Journal of Computational Physics*, 228(18), pp.6703-25. Available at: <https://doi.org/10.1016/j.jcp.2009.05.032>.
- Yamada, Y. et al., 2011. Numerical simulation of three-dimensional free-surface flows with explicit moving particle simulation method. *Transaction of the Atomic Energy Society of Japan*, 10(3), pp.185-93. Available at: <https://doi.org/10.3327/taesj.J10.033>.
- Yang, Q., Jones, V. & McCue, L., 2012. Free-surface flow interactions with deformable structures using an SPH-FEM model. *Ocean Engineering*, 55, pp.136-47. Available at: <https://doi.org/10.1016/j.oceaneng.2012.06.031>.

- Ye, T., Pan, D., Huang, C. & Liu, M., 2019. Smoothed particle hydrodynamics (SPH) for complex fluid flows: Recent developments in methodology and applications. *Physics of Fluids*, 31(1), Available at: <https://doi.org/10.1063/1.5068697>.
- Yoon, H.Y., Koshizuka, S. & Yoshiaki Oka, Y., 1999. A particle–gridless hybrid method for incompressible flows. *International Journal for Numerical Methods in Fluids*, 30(4), pp.407-24. Available at: [https://doi.org/10.1002/\(SICI\)1097-0363\(19990630\)30:4%3C407:AID-FLD846%3E3.0.CO;2-C](https://doi.org/10.1002/(SICI)1097-0363(19990630)30:4%3C407:AID-FLD846%3E3.0.CO;2-C).
- Zhang, L.W., Ademiloye, A.S. & Liew, K.M., 2019. Meshfree and particle methods in biomechanics: Prospects and challenges. *Archives of Computational Methods in Engineering*, 26, pp.1547-76. Available at: <https://doi.org/10.1007/s11831-018-9283-2>.
- Zhang, G., Chen, X. & Wan, D., 2019. MPS-FEM coupled method for study of wave-structure interaction. *Journal of Marine Science and Application*, Available at: <https://doi.org/10.1007/s11804-019-00105-6>.
- Zhang, S. et al., 2009. Simulation of solid–fluid mixture flow using moving particle methods. *Journal of Computational Physics*, 228(7), pp.2552-65. Available at: <https://doi.org/10.1016/j.jcp.2008.12.005>.
- Zhang, S., Morita, K., Fukuda, K. & Shirakawa, N., 2006. An improved MPS method for numerical simulations of convective heat transfer problems. *International Journal for Numerical Methods in Fluids*, 51(1), pp.31-47. Available at: <https://doi.org/10.1002/flid.1106>.
- Zhang, Y. & Wan, D., 2018. MPS-FEM coupled method for sloshing flows in an elastic tank. *Ocean Engineering*, 152, pp.416-27. Available at: <https://doi.org/10.1016/j.oceaneng.2017.12.008>.
- Zhang, Y. & Wan, D., 2019. MPS-FEM coupled method for fluid–structure interaction in 3d dam-break flows. *International Journal of Computational Methods*, 16(2), Available at: <https://doi.org/10.1142/S021987621846009X>.
- Zhan, L., Peng, C., Zhang, B. & Wu, W., 2019. A stabilized TL–WC SPH approach with GPU acceleration for three-dimensional fluid–structure interaction. *Journal of Fluids and Structures*, 86, pp.329-53. Available at: <https://doi.org/10.1016/j.jfluidstructs.2019.02.002>.
- Zheng, X., Ma, Q.-W. & Duan, W.-Y., 2014. Incompressible SPH method based on Rankine source solution for violent water wave simulation. *Journal of Computational Physics*, 276, pp.291-314. Available at: <https://doi.org/10.1016/j.jcp.2014.07.036>.

Zheng, H. & Shioya, R., 2019. Verifications for large-scale parallel simulations of 3d fluid–structure interaction using moving particle simulation (MPS) and finite element method (FEM). *International Journal of Computational Methods*, 15(3), Available at: <https://doi.org/10.1142/S0219876218400145>.

Zheng, H., Shioya, R. & Mitsume, N., 2018. Large-scale parallel simulation of coastal structures loaded by tsunami wave using FEM and MPS Method. *Journal of Advanced Simulation in Science and Engineering*, 5(1), Available at: <https://doi.org/10.15748/jasse.5.1>.